ON LINEAR AND NON-LINEAR INTERACTIONS OF LIGHT WITH TWO DIMENSIONAL MATERIALS

FÁBIO M. HIPÓLITO V. B.
(MSc, Universidade do Minho, Portugal)

A THESIS SUBMITTED

FOR THE DEGREE OF DOCTOR OF PHILOSOPHY
NUS GRADUATE SCHOOL FOR INTEGRATIVE SCIENCES AND ENGINEERING
NATIONAL UNIVERSITY OF SINGAPORE

2016

This page was intentionally left blank.

Declaration

I hereby declare that this thesis is my original work and it has been written by me in its entirety. I have duly acknowledged all the sources of information which have been used in the thesis.

This thesis has also not been submitted for any degree in any university previously.

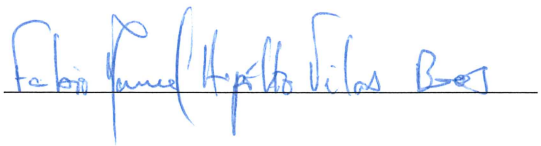

Fábio Manuel Hipólito Vilas Boas

9th May 2016

This page was intentionally left blank.

Acknowledgements

First and foremost, I would like to express my gratitude to my supervisors, professors Vítor M. Pereira and A. H Castro Neto, for their incredible support, advice and guidance throughout my entire PhD program. A special acknowledgement to professor Vítor M. Pereira, who was not only an outstanding supervisor, but also a wonderful mentor who guided me throughout my entire PhD program.

Words come short to express my gratitude to professor Nuno Peres, whose advices and mentoring have accompanied me since my undergraduate studies.

I also would like to express my gratitude to the NGS staff for the kind support and assistance provided along all these years. Among all members of NGS, I would like to acknowledgement professor Tang for all our exciting and highly formative discussions.

Some the conversations and debates with several guests of the Graphene Research Centre played a large role in my research path, I would like to specially thank professors Mikhail Vasilevskiy, Giovanni Vignale and Thomas Pedersen for their invaluable comments and recommendations.

A significant contribution can be traced to conversations with my fellow colleagues and research staff from the Graphene Research Centre. Miguel, let me thank you for your *double plus good* recommendations on all aspects of computing, in so many aspects of physics and our remarkable and enlightening discussions. João Nuno, your presence since the early stages of my PhD program was crucial in many aspects. Mirco, you are probably the physicist and friend with whom I most debated, physics and many more subjects. Sofia, it has been over ten years since we first discussed physics, let's keep it going.

Both outside and inside the context of academia, I had the opportunity to make great friendships, among all I must thank Abhinav and Rui my flatmates and great friends for over four years.

Inês, Carlos and Rui Santos your friendship, support and patience had an immeasurable effect on me, words come short to thank you properly.

To my friends Tânia, Paula, Lídia, Yuan Luo, Alex Pachoud, Aires, Mariana, Marta, Cao Jingnan, Duong, Navneeth, Jorge, Alex Rodin, Alfred, Alexandra, Christina, Bridgette, Sarah and Leonor you are great friends that I wont forget and in so many different ways inspired me.

To the family of Francisco, Ana, David and Alice for their exceptional friendship.

To Rose, Hans and Galen, who opened to the doors to your home and family, my kindest acknowledgement.

À minha família, em particular ao Daniel e ao André agradeço o vosso apoio e amizade.

Para ti Mãe, guardo o último e mais sentido agradecimento, sem o teu apoio não teria chegado aqui. Obrigado.

This page was intentionally left blank.

Contents

Summary

The main subject of this thesis is the interaction of light with two dimensional condensed matter systems, it encompasses the bulk of the contents in the thesis and spans from the first to third chapters. Chapter one is dedicated to the review of the formalism used to study this interactions. The second and third chapters concern applications on linear and quadratic response, respectively. The fourth and final chapter delves into the calculation of effective Hamiltonians for (quasi) two dimensional in the presence of spin-orbit interaction.

The response formalism is reviewed using multiple methods and is then applied to the calculation of the current response, setting the formal foundation for the core of the thesis. Both the linear and non-linear response are computed using both the minimal and direct couplings (the so-called velocity and length gauge) and compared against each other.

The exact optical conductivity of Graphene NanoRibbons (GNRs) is derived analytically. It is shown that an intraband response channel is opened, when the translational invariance along one direction is broken. This intraband channel generates a considerably large response exclusively along the direction of broken translational invariance. Therefore, having the potential to generate an highly anisotropic response. It is proposed a device to generate highly polarized light, by transmission of radiation through an array of ribbons encapsulated in a waveguide.

A comprehensive review of the generation of photocurrent in hexagonal lattices is presented. It starts with a phenomenological analysis of the photocurrent, taking into account multiple mechanism and symmetry considerations. The photocurrent is calculated for mono and bilayers of graphene as well as for hexagonal Boron Nitride (hBN), using the analytical results derived in the first chapter considering the direct coupling with radiation. The photocurrent exhibits, particularly in the Biased Bilayer Graphene (BBG), remarkable features, among which a high sensitivity to the chemical potential.

The Löwdin's Partitioning Technique (LPT) is reviewed and use to compute the effective Hamiltonians for several systems with the honeycomb lattice. The low energy effective Hamiltonians with intrinsic spin-orbit coupling are derived and analyzed. Furthermore, we apply the LPT to the estimate gap in buckled honeycomb lattices.

This page was intentionally left blank.

List of Figures

This page was intentionally left blank.

List of Tables

This page was intentionally left blank.

List of Acronyms

2D Two Dimensional

BBG Biased Bilayer Graphene

BZ Brillouin zone

CNT Carbon NanoTube

DC Direct Current

DM Density Matrix

DFG Difference Frequency Generation

DoS Density of States

GNR Graphene NanoRibbon

GF Green's Function

hBN hexagonal Boron Nitride

HP Heisenberg's Picture

KS Keldysh Space

LR Langreth's rules

LPT Löwdin's Partitioning Technique

NEF Non-Equilibrium Formalism

OC Optical Conductivity

OR Optical Rectification

PE Perturbative Expansion

PG Point Group

SE Schrödinger's Equation

TDSE Time Dependent Schrödinger's Equation

SFG Sum Frequency Generation

SG Space Group

SHG Second Harmonic Generation

SK Slater–Koster

SO Spin–Orbit

SOC Spin–Orbit Coupling

SPP Surface Plasmon-Polariton

SP Schrödinger's Picture

TB Tight-Binding

TE Topologically Equivalent

CTI Connected and Topologically Inequivalent

VHs Van Hove singularity

vNE von Neumann's Equation

WS Wigner–Seitz

WT Wick's Theorem

Introduction

Context

Interaction of light and matter has been an area of intense and exciting research for well over a century. Throughout this period, the field of atomic physics has dominated the advances on light-matter interactions, particularly non-linear effects. In the field of condensed matter, research on light-matter interactions, both in the theoretical and experimental perspectives, has been progressing at a slower pace, when compared with the field of atomic physics. To a large extent, the slower pace can be attributed to the additional complexity of condensed matter systems, where phenomena associated with temperature, phonons, plasmons and the role of disorder cannot be neglected. Moreover, the large absorption associated with bulk materials introduces an additional challenge which contributed significantly for the slow pace of research.

Over the last decade, the discovery of the zoo of (quasi) two dimensional materials has invigorated the research on light matter interactions in condensed matter systems [1–7]. From the theoretical point of view, the understanding of light-matter interactions in condensed matter systems, has experienced significant advances over the past decades, such as the calculation of linear and non-linear susceptibility of semiconductors [8–10]. To this date, the calculation of the susceptibility relies on the recursive integration of the density matrix or a Green's function in the context of the independent particle approximation. Notwithstanding these advances, open questions remain without answer. For instance, the correct choice for parametrization of the coupling with radiation [8, 11–13]

One of the central objectives of our research, is to determine a versatile and robust method to address linear and non-linear response to radiation, starting from a sound microscopic model for the system. In the field of condensed matter systems, interactions

with phonons, excitons or other phenomena are usually present and can play a significant role on the properties of systems. Diagrammatic techniques have been successfully used to incorporate interactions with these phenomena into microscopic models of the system. Thus, providing an useful tool to accurately determine the properties of the system under consideration, *e.g.* transport properties. In addition, these techniques have been particularly effective within the context of non-equilibrium formalism.

It appears to be reasonable to dedicate effort into reviewing the response formalism for light-matter interactions within this framework, as it may provide an useful tool to analyze effects arising from multiple interactions.

Besides electron-electron or electron-photon interactions, two dimensional materials have sparked a large interest in other fields, such as the emerging field of spintronics. Introducing interactions with light, particularly circularly polarized light, on materials with large spin-orbit coupling expands even further the realm of interesting phenomena and possible applications.

Outline of the thesis

The kernel of this thesis is the study of linear and non-linear interactions of light with matter. The first chapter lays theoretical foundations of the methods used to study the linear and non-linear response in chapters two and three, respectively.

The second chapter concerns the linear interaction of light with graphene nanoribbons. Based on the exact calculation of the optical conductivity we analyse its anisotropic nature and the respective effects on the propagation of light. Chapter three address the subject of quadratic response in (quasi) two dimensional materials. It begins with a phenomenological review of the generation of photocurrents. Followed by our results on the photocurrent generation in two dimensional hexagonal lattices.

The last chapter is dedicated to spin orbit coupling in (quasi) two dimensional materials, more specifically the construction and analysis of effective Hamiltonians. It begins with a review of the method used compute the effective Hamiltonians, the so-called Löwdin's partitioning technique. Followed by the application of the method to the calculation several effective Hamiltonians and respective analysis.

Original content and external material

The work presented in this thesis is accompanied by extensive usage of computational techniques, for both numerical and algebraic calculation. Apart from internal functions and libraries (LAPACK, ARPACK and derived routines) associated with each programming language (FORTRAN 90, Mathematica and MATLAB), the author wrote all code from blank files. In addition, all figures and tables shown in this thesis were prepared by author.

This page was intentionally left blank.

Chapter 1

Perturbative methods

This chapter is concerned with the calculation of response functions to external perturbations. It begins with a review of the "standard" approach to the calculation of a response function in the context of quantum mechanics, namely solving the Time Dependent Schrödinger's Equation (TDSE) [14–20]. The second section is concerned with the evaluation of a particular response function, the current density response in the so-called length gauge [10, 21]. Section three presents a review of the more general review of the response function. The response function is computed in the context of the *Keldysh–Schwinger* contour formalism for non-equilibrium dynamics [20, 22, 23]. The fourth section presents a review of the definition of the current response function, adopted throughout this thesis.

1.1 Response functions

The purpose of this section is to review the definition of the response function and its connection with either the Perturbative Expansion (PE) of a Green's Function (GF) or the recursive integration of von Neumann's Equation (vNE) for the Density Matrix (DM).

In general, we can define a response function $\mathtt{R}_i(t)$ as a series expansion on a given external force or potential $\mathtt{F}_j(t)$

$$\begin{aligned}\mathtt{R}_i(t) = \mathtt{T}^{(0)}(t) + \int_{-\infty}^{t} \mathrm{d}t_1\, \mathtt{T}^{(1)}_{ij}(t,t_1)\mathtt{F}_j(t_1) + \int_{-\infty}^{t,t_1} \mathrm{d}t_1\mathrm{d}t_2\, \mathtt{T}^{(2)}_{ijk}(t-t_1,t-t_2)\mathtt{F}_j(t_1)\mathtt{F}_k(t_2) \\ + \int_{-\infty}^{t,t_1,t_2} \mathrm{d}t_1\mathrm{d}t_2\mathrm{d}t_3\, \mathtt{T}^{(3)}_{ijkl}(t-t_1,t-t_2,t-t_3)\mathtt{F}_j(t_1)\mathtt{F}_k(t_2)\mathtt{F}_l(t_3) + \cdots, \end{aligned} \tag{1.1}$$

where the n^{th} order coefficients define the respective, $n+1^{\text{th}}$ rank tensor $\mathtt{T}^{(n)}$. In addition, to condense the expressions, we make use of the following shorthand notation $\int_{-\infty}^{t,t_1,\ldots,t_{k-1}} \mathrm{d}t_1 \mathrm{d}t_2 \ldots \mathrm{d}t_k \equiv \int_{-\infty}^{t} \mathrm{d}t_1 \int_{-\infty}^{t_1} \mathrm{d}t_2 \ldots \int_{-\infty}^{t_{k-1}} \mathrm{d}t_k$. Within the limits of classical electromagnetism, we may choose several response functions to characterize the response to an external electromagnetic field.

1.1.1 Current response function

The freedom of choice for the parametrization of the electric field and definition of conductivity tensor can cause significant confusion and lead to apparently different relations. We dedicate this subsection to lay out our parametrization and definitions. First, the external field is parametrized as

$$E_\alpha(t) = \frac{1}{2}\sum_{\omega_m} E^\alpha_{\omega_m} e^{-i\omega_m t} \quad ; \qquad A_\alpha(t) = \frac{1}{2}\sum_{\omega_m} A^\alpha_{\omega_m} e^{-i\omega_m t} \tag{1.2}$$

where the sum includes positive and negative frequencies. Second, the $n\text{th}$ order current density response will generically be

$$\begin{aligned} J^{(n)}_\lambda(t) &= \int_{-\infty}^{t} \mathrm{d}t_1 \cdots \mathrm{d}t_n \, \sigma^{(n)}_{\lambda\alpha\ldots\beta}\Big(t, t-t_1, t-t_2, \ldots, t-t_n\Big)\, E_\alpha(t_1)\cdots E_\beta(t_n) \\ &= \frac{1}{2^n}\sum_{\{\omega_k\}} \int_0^\infty \mathrm{d}\tau_1 \cdots \mathrm{d}\tau_n \; \sigma^{(n)}_{\lambda\alpha\ldots\beta}(\tau_1,\ldots,\tau_n)\; e^{i(\omega_1\tau_1+\cdots+\omega_n\tau_n)}\times \\ &\times E^\alpha_{\omega_1}\ldots E^\alpha_{\omega_n} e^{-i(\omega_1+\ldots+\omega_n)t} \,, \end{aligned} \tag{1.3}$$

where we introduce the n^{th} order conductivity tensor $\sigma^{(n)}_{\lambda\alpha\ldots\beta}$. In the last line there is a summation over all ω_1 to ω_n, and each ω_k can take the values that define the harmonic content of the field. Hence,

$$J^{(n)}_\lambda(t) = \sum_{\{\omega_k\}} \sigma^{(n)}_{\lambda\alpha\ldots\beta}(\omega_1,\ldots,\omega_n)\, E^\alpha_{\omega_1}\ldots E^\beta_{\omega_n} e^{-i(\omega_1+\cdots+\omega_n)t} \,, \tag{1.4}$$

with

$$\sigma^{(n)}_{\lambda\alpha\ldots\beta}(\omega_1,\ldots,\omega_n) \equiv \frac{1}{2^n}\int_0^\infty \mathrm{d}\tau_1\cdots\mathrm{d}\tau_n\, \sigma^{(n)}_{\lambda\alpha\cdots\beta}(\tau_1,\ldots,\tau_n) e^{i(\omega_1\tau_1+\cdots\omega_n\tau_n)} \,. \tag{1.5}$$

To identify each spectral component of the response field we may write it as

$$J_\lambda(t) = \sum_{\omega_s} J_\lambda(\omega_s) e^{-i\omega_s t} \,, \tag{1.6}$$

where

$$j_\lambda(\omega_s) \equiv \sum_{\omega_1 \dots \omega_n | \omega_s} \sigma^{(n)}_{\lambda\alpha\cdots\beta}(\omega_s; \omega_1, \dots, \omega_n)\, E^\alpha_{\omega_1} \dots E^\beta_{\omega_n} \,, \tag{1.7}$$

and $\sum_{\omega_1 \dots \omega_n | \omega_s} \equiv \sum_{\omega_1 \dots \omega_n} \delta_{\omega_1 + \cdots + \omega_n, \omega_s}$ means a summation retaining only those combinations of frequencies for which $\omega_s = \omega_1 + \omega_2 \cdots + \omega_n$. As a definite example, in second order we have

$$J^{(2)}_\lambda(\omega_s) = \sum_{\omega_1, \omega_2} \delta_{\omega_1 + \omega_2, \omega_s}\, \sigma^{(2)}_{\gamma\alpha\beta}(\omega_s;\, \omega_1, \omega_2)\, E^\alpha_{\omega_1} E^\beta_{\omega_2} \,, \tag{1.8}$$

and the explicit time dependence is

$$J^{(2)}_\lambda(t) = \sum_{\omega_s} j_\lambda(\omega_s) e^{-i\omega_s t} = \sum_{\omega_1, \omega_2} \sigma^{(2)}_{\gamma\alpha\beta}(\omega_s; \omega_1, \omega_2)\, E^\alpha_{\omega_1} E^\beta_{\omega_2} e^{-i(\omega_1 + \omega_2)t} \,. \tag{1.9}$$

By evaluating explicitly the time dependence of the DM we may compute the current response function.

In addition to the current response functions, we may also characterize the response of a system by the polarization function. In the field of non-linear optics, this is a standard choice to study non-linear interactions [24, 25]. By the same token, the n-th order polarization response reads

$$\begin{aligned} P^{(n)}_\lambda(t) &= \int_{-\infty}^{t} \mathrm{d}t_1 \cdots \mathrm{d}t_n\, \varepsilon_0\, \chi^{(n)}_{\lambda\alpha\dots\beta}\Big(t, t - t_1, t - t_2, \dots, t - t_n\Big)\, E_\alpha(t_1) \cdots E_\beta(t_n) \\ &= \frac{1}{2^n} \sum_{\{\omega_k\}} \int_0^\infty \mathrm{d}\tau_1 \cdots \mathrm{d}\tau_n\, \varepsilon_0\, \chi^{(n)}_{\lambda\alpha\dots\beta}(\tau_1, \dots, \tau_n)\, e^{i(\omega_1\tau_1 + \cdots + \omega_n\tau_n)} \times \\ &\times E^\alpha_{\omega_1} \dots E^\alpha_{\omega_n} e^{-i(\omega_1 + \dots + \omega_n)t} \,, \end{aligned} \tag{1.10}$$

where we introduce the n^{th} order susceptibility tensor $\chi^{(n)}_{\lambda\alpha\dots\beta}$ The non-linear response to electric fields has been intensively studied in the field of atomic physics and optics [24, 25].

In atomic systems, the analysis has followed the traditional approach via the polar-

ization function. In condensed matter this method is particularly suited to insulators, as there are no free currents in the material and it reacts to the external electromagnetic field with a polarization. In metals the picture changes: currents are present and polarizations absent. Thus, the characterization of response system by a polarization function becomes ill-defined. Furthermore, the vast range of semiconductors and semimetals can support both currents or polarizations. However, the polarization response function is defined in the length gauge, whereas the current response function is defined in the velocity gauge. Recently, it was shown that both response functions are equivalent and predict the same physical properties [13].

Moreover, the time evolution of the electric displacement field generates an electric (displacement) current in material, *i.e.*

$$\begin{aligned}\mathbf{J}(t) &= \frac{\partial \mathbf{D}(t)}{\partial t} = \frac{\partial}{\partial t}\Big[\varepsilon_0 \mathbf{E}(t) + \mathbf{P}(t)\Big] = \frac{\partial}{\partial t}\Big[\varepsilon_0 \mathbf{E}(t) + \mathbf{P}^{\mathrm{L}}(t) + \mathbf{P}^{\mathrm{NL}}(t)\Big] \\ &= \frac{\partial}{\partial t}\Big[\mathbf{D}^{\mathrm{L}}(t) + \mathbf{P}^{\mathrm{NL}}(t)\Big], \end{aligned} \tag{1.11}$$

where we separated the usual linear order terms in the polarization from the non-linear contributions. By Fourier transforming this relation to frequency domain, it reads

$$\mathbf{J}^{\mathrm{L}}(\omega) = -i\omega \mathbf{D}^{\mathrm{L}}(\omega) = -i\omega\, \varepsilon_0 \left[1 + \chi^{\mathrm{L}}(\omega)\right] \mathbf{E}^{\mathrm{L}}(\omega), \tag{1.12a}$$

$$\mathbf{J}^{\mathrm{NL}}(\omega) = -i\omega \mathbf{P}^{\mathrm{NL}}(\omega) = -i\omega\, \varepsilon_0\, \chi^{\mathrm{NL}}(\omega) \mathbf{E}^{\mathrm{NL}}(\omega). \tag{1.12b}$$

From previous results and the PE of the current in the electric field, we can extract the relation between the Fourier components of the tensors $\sigma(\omega)$ and $\chi(\omega)$

$$\sigma^{\mathrm{L}}(\omega) = -i\omega\, \varepsilon_0 \big[1 + \chi^{\mathrm{L}}(\omega)\big]\,, \tag{1.13a}$$

$$\sigma^{\mathrm{NL}}(\omega) = -i\omega\, \varepsilon_0\, \chi^{\mathrm{NL}}(\omega)\,, \tag{1.13b}$$

with the simplified notation $\sigma^{(n)}(\omega;\, \omega_1 + \ldots + \omega_n) \equiv \sigma^{(n)}(\omega)$ and $\chi^{(n)}(\omega;\, \omega_1 + \ldots + \omega_n) \equiv \chi^{(n)}(\omega)$.

As was pointed out in the previous section, our aim is to compute the response function using either the recursive integration of the DM or Non-Equilibrium Formalism (NEF). Having computed the current response both in the length and velocity gauges, we proceed with applications of these results. First, we address the linear res-

ponse in GNRs and then proceed with the study of a specific case of the quadratic response, Optical Rectification (OR), in hexagonal crystals.

1.2 Response formalism

Concerning the calculation of *response function* to a weak external perturbation, we start with a concise review of the zero temperature formalism. To facilitate the comparison with literature, the notation adopted in this section follows that of Fetter and Walecka [14].

Consider Schrödinger's Equation (SE) $i\hbar\partial_t |\Psi_S(t)\rangle = \hat{H} |\Psi_S(t)\rangle$ and the following trial function $|\Psi_S(t)\rangle = e^{-i\hat{H}t} |\Psi_S(0)\rangle$. By introducing an external perturbation $\hat{V}$ (without explicit time dependency) at time $t = t_0$, SE reads $i\hbar\partial_t |\Psi_S(t)\rangle = \hat{H}_t |\Psi_S(t)\rangle$, where the total Hamiltonian is $\hat{H}_t = \hat{H} + \hat{V}$. This can be solved by generalizing the trial function to $|\Psi_S(t)\rangle = e^{-i\hat{H}t}\hat{A}(t) |\Psi_S(0)\rangle \; : \hat{A}(t) = \mathbb{1} \, \forall \, t < t_0$. Solving SE with this trial function yields

$$\begin{aligned} i\partial_t e^{-i\hat{H}t}\hat{A}(t) |\Psi_S(0)\rangle &= \hat{H}_t \, e^{-i\hat{H}t}\hat{A}(t) |\Psi_S(0)\rangle \\ e^{-i\hat{H}t}\big[\hat{H} + i\partial_t\hat{A}(t)\big] |\Psi_S(0)\rangle &= \hat{H}_t \, e^{-i\hat{H}t}\hat{A}(t) |\Psi_S(0)\rangle \\ i\partial_t\hat{A}(t) &= e^{i\hat{H}t}\,\hat{V}e^{-i\hat{H}t}\hat{A}(t) = \hat{V}(t)\hat{A}(t)\,, \end{aligned} \tag{1.14}$$

with the following integral solution $\hat{A}(t) = \mathbb{1} - i\int_{t_0}^{t} \mathrm{d}t'\hat{V}(t')\hat{A}(t')$. By recursive evaluation, the auxiliary operator reads

$$\hat{A}(t) = \mathbb{1} - i\int_{t_0}^{t} \mathrm{d}t' \, \hat{V}(t') + i^2 \int_{t_0,t_0}^{t,t'} \mathrm{d}t'\mathrm{d}t'' \, \hat{V}(t')\hat{V}(t'') + \dots \,. \tag{1.15}$$

Now, we take under consideration the expectation value of an observable $\hat{O}_S(t)$, *i.e.* $\langle\hat{O}_S(t)\rangle = \langle\Psi_S(t)| \hat{O}_S(t) |\Psi_S(t)\rangle$ and the time evolution of the states in the presence of the external perturbation $|\Psi_S(t)\rangle = e^{-i\hat{H}t}\hat{A}(t) |\Psi_S(0)\rangle$. Hence, the expectation value reads

$$\begin{aligned} \langle\hat{O}_S(t)\rangle &= \langle\Psi_S(0)| \, \hat{A}^\dagger(t) \, e^{i\hat{H}t}\hat{O}_S(t) \, e^{-i\hat{H}t}\hat{A}(t) |\Psi_S(0)\rangle \\ &= \langle\Psi_S(0)| \, \hat{A}^\dagger(t) \, \hat{O}_H(t) \, \hat{A}(t) |\Psi_S(0)\rangle \;, \end{aligned} \tag{1.16}$$

where the $\hat{O}_H(t) = e^{i\hat{H}t}\hat{O}_S(t)e^{-i\hat{H}t}$ is an operator in Heisenberg's Picture (HP).

Since $\hat{A}(t)$ is defined by a recursive equation, each occurrence of this operator contains all elements of the power series expansion of the interaction potential V. Hence, the product $\hat{A}^\dagger(t)\hat{O}_H(t)\hat{A}(t)$ can also be represented by a series expansion of the interaction potential. Collecting all terms up to second order

$$\begin{aligned}
\hat{A}^\dagger(t)\hat{O}_H(t)\hat{A}(t) &= \left[\mathbb{1} + i\int_{t_0}^{t} \mathrm{d}t'\, \hat{V}(t') + i^2 \int_{t_0,t_0}^{t,t'} \mathrm{d}t'\mathrm{d}t''\, \hat{V}(t'')\hat{V}(t') + \mathcal{O}(V^3)\right]\hat{O}_H(t) \\
&\times \left[\mathbb{1} - i\int_{t_0}^{t} \mathrm{d}t'\, \hat{V}(t') + i^2 \int_{t_0,t_0}^{t,t'} \mathrm{d}t'\mathrm{d}t''\, \hat{V}(t')\hat{V}(t'') + \mathcal{O}(V^3)\right] \\
&= \hat{O}_H(t) + i\int_{t_0}^{t}\mathrm{d}t'\hat{V}(t')\hat{O}_H(t) - i\hat{O}_H(t)\int_{t_0}^{t}\mathrm{d}t'\,\hat{V}(t') - \int_{t_0,t_0}^{t,t'}\mathrm{d}t'\mathrm{d}t''\,\hat{V}(t''\hat{V}(t')\hat{O}_H(t) \\
&+ \int_{t_0}^{t}\mathrm{d}t'\hat{V}(t')\hat{O}_H(t)\int_{t_0}^{t}\mathrm{d}t'\hat{V}(t') - \hat{O}_H(t)\int_{t_0,t_0}^{t,t'}\mathrm{d}t'\mathrm{d}t''\hat{V}(t')\hat{V}(t'') + \mathcal{O}(V^3)\,, \\
&= \hat{O}_H(t) - i\int_{t_0}^{t}\mathrm{d}t'\left[\hat{O}_H(t),\hat{V}(t')\right] - \int_{t_0,t_0}^{t,t'}\mathrm{d}t'\mathrm{d}t''\Big[\hat{V}(t'')\hat{V}(t')\hat{O}_H(t) + \\
&+ \hat{O}_H(t)\hat{V}(t')\hat{V}(t'')\Big] + \left(\int_{t_0,t_0}^{t,t'}\mathrm{d}t'\mathrm{d}t'' + \int_{t_0,t'}^{t,t}\mathrm{d}t'\mathrm{d}t''\right)\hat{V}(t')\hat{O}_H(t)\hat{V}(t'')\,. \qquad (1.17)
\end{aligned}$$

The first two terms provide us with the standard linear response calculation, as clearly demonstrated in references [14–20] [1]. To further simplify the results, consider the last element of the previous equation

$$I_1 + I_2 = \left(\int_{t_0,t_0}^{t,t'}\mathrm{d}t'\mathrm{d}t'' + \int_{t_0,t'}^{t,t}\mathrm{d}t'\mathrm{d}t''\right)\hat{V}(t')\hat{O}_H(t)\hat{V}(t'')\,. \qquad (1.18)$$

In its present form, the integration limits prevent a combination with the other second order terms. Figure 1.1 illustrates the integration regions for equation 1.18. The figure assists the reader to perform the necessary transformations to obtain the desired integration limits, namely $t'' \in [t_0, t']$. The grey triangles represent the integration regions for both integral present in equation 1.18 I_1 and I_2, grey and light grey respectively. According to the definition of I_2, the integral is evaluated by sweeping the integration from bottom to top. By inverting the integration order, we define and integral $I_3 = \int_{t_0,t_0}^{t,t''}\mathrm{d}t''\mathrm{d}t'\,\hat{V}(t')\,\hat{O}_H(t)\,\hat{V}(t'')$. Because the integrand is symmetric to an interchange of $t' \leftrightarrows t''$, $I_3 = I_2$. Therefore, to cast the integral to desired form, one

[1] Reference [17] uses extensively path integral formalism, hence it might not be immediately clear the equivalence between these results. Nonetheless, with a brief review of path integral formalism the reader should be able to verify the equivalence.

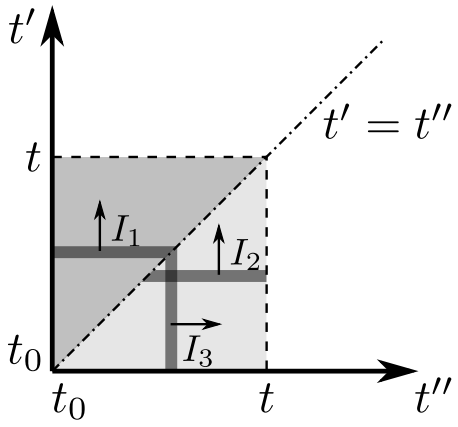

Figure 1.1: Integration regions for double integrals. The grey and light grey triangles represent the integrals shown in equation 1.18, I_1 and I_2 respectively. The dark grey bars (with infinitesimal width) represent the integration elements at a given point t' or t'', for horizontal and vertical elements respectively. Finally, the solid black arrows indicate the direction of the integrations.

replaces the integration variables as follow, $t' \leftrightarrows t''$, and the integral reads

$$I_2 = I_3 = \int_{t_0,t_0}^{t,t''} \mathrm{d}t'' \mathrm{d}t' \, \hat{V}(t') \, \hat{O}_H(t) \, \hat{V}(t'') = \int_{t_0,t_0}^{t,t'} \mathrm{d}t' \mathrm{d}t'' \, \hat{V}(t'') \, \hat{O}_H(t) \, \hat{V}(t') \, . \tag{1.19}$$

Hence, the operator product reads

$$\begin{aligned} \hat{A}^\dagger(t)\hat{O}_H(t)\hat{A}(t) &= \hat{O}_H(t) - i\int_{t_0}^{t} \mathrm{d}t' \left[\hat{O}_H(t), \hat{V}(t')\right] - \int_{t_0,t_0}^{t,t'} \mathrm{d}t' \mathrm{d}t'' \Big[\hat{V}(t'')\hat{V}(t')\hat{O}_H(t) \\ &+ \hat{O}_H(t)\hat{V}(t')\hat{V}(t'') - \hat{V}(t')\hat{O}_H(t)\hat{V}(t'') - \hat{V}(t'')\hat{O}_H(t)\hat{V}(t')\Big] \\ &= \hat{O}_H(t) - i\int_{t_0}^{t} \mathrm{d}t' \left[\hat{O}_H(t), \hat{V}(t')\right] + \int_{t_0,t_0}^{t,t'} \mathrm{d}t' \mathrm{d}t'' \Big[\Big[\hat{O}_H(t), \hat{V}(t'')\Big], \hat{V}(t')\Big] \, . \end{aligned} \tag{1.20}$$

Thus, the second order response can be defined by the last term in equation 1.20. Furthermore, the adiabatic approximation is obtained straightforwardly from this result by redefining the perturbation as $\hat{V}(t^i) \equiv e^{-\eta|t^i - t_0|}\hat{V}(t^i)$ and replacing the lower integration, t_0 by $-\infty$, and taking the limit $\eta \to 0^+$. The expansion of the lower limit is easily understood by considering the fact that, for any positive η, the adiabatic factor $e^{-\eta|t^i - t_0|}$ imposes a fully decoupled perturbation at $t^i = -\infty$, and a fully switched on (coupled) perturbation at $t^i = t_0$.

This section has reviewed the "standard" *response function* formalism for an external perturbation by means of a recursive solution of the TDSE, The following section addresses the calculation of a particular response function, the current density response in the length gauge.

1.3 Response in the length gauge

Regarding the interaction with an light, we consider the calculation of the current response with respect to an external electric field by considering direct coupling between the position operator with the external electric field $\mathbf{E}(t)$, *i.e.* the length gauge. The respective Hamiltonian and DM read

$$\hat{H} = \hat{H}_0 - q\hat{\mathbf{r}} \cdot \mathbf{E}\,. \tag{1.21}$$

$$\hat{\rho} = \sum_j p_j \big|j(t)\big\rangle\big\langle j(t)\big| = \sum_{mn} \rho_{mn}(t)|m\rangle\langle n|\,, \tag{1.22}$$

where we defined the time dependent DM elements $\rho_{mn}(t) = \sum_j p_j \left\langle m\middle|j(t)\right\rangle\left\langle j(t)\middle|n\right\rangle$. In addition, q is defined as the particle's charge. Hence, for electrons $q = -e$, where e is the elementary charge. The equation of motion for the DM is defined by vNE, $i\hbar\,\partial\hat{\rho}/\partial t = \left[\hat{H}, \hat{\rho}\right]$, also known as quantum Liouville equation. The equation of motion for the respective matrix elements reads

$$i\hbar\frac{\partial \rho_{mn}}{\partial t} = \epsilon_{mn}\,\rho_{mn} + \sum_l \Big(V_{ml}\,\rho_{ln} - \rho_{ml}\,V_{ln}\Big)\,. \tag{1.23}$$

In the context of crystals and Bloch state, the position operator is ill defined for intraband transitions. To address this, we follow the definition of the position matrix elements in a periodic lattice proposed by [10, 26]. These matrix elements can be computed in the position representation as

$$\langle m\mathbf{k}|\hat{\mathbf{x}}|n\mathbf{k}'\rangle = \int \mathrm{d}\mathbf{x}\,\mathbf{x}\,e^{-i(\mathbf{k}-\mathbf{k}')\cdot\mathbf{x}}\,u^*_{m\mathbf{k}}(\mathbf{x})u_{n\mathbf{k}'}(\mathbf{x})\,, \tag{1.24a}$$

where $|n\mathbf{k}'\rangle$ represents a Bloch state and $u_{n\mathbf{k}'}(\mathbf{x})$ is the respective periodic function. We identify the gradient with respect to the wavevector as $\mathbf{x}\,\exp[-i(\mathbf{k}-\mathbf{k}')\cdot\mathbf{x}] = -i\boldsymbol{\nabla}_{\mathbf{k}'}\exp[-i(\mathbf{k}-\mathbf{k}')\cdot\mathbf{x}]$. Introducing the gradient and making use of the product rule, the position matrix elements read

$$\begin{aligned}\langle m\mathbf{k}|\hat{\mathbf{x}}|n\mathbf{k}'\rangle = -i\int \mathrm{d}\mathbf{x}\Big(&\boldsymbol{\nabla}_{\mathbf{k}'}\Big[e^{-i(\mathbf{k}-\mathbf{k}')\cdot\mathbf{x}}u^*_{m\mathbf{k}}(\mathbf{x})u_{n\mathbf{k}'}(\mathbf{x})\Big]\\ &- e^{-i(\mathbf{k}-\mathbf{k}')\cdot\mathbf{x}}u^*_{m\mathbf{k}}(\mathbf{x})\boldsymbol{\nabla}_{\mathbf{k}'}\Big[u_{n\mathbf{k}'}(\mathbf{x})\Big]\Big).\end{aligned} \tag{1.24b}$$

In periodic systems the position variable can be redefined as $\mathbf{x} \equiv \mathbf{R}_N + \mathbf{r}$, where $\mathbf{R}_N$ are the translation vectors for the underlying lattice and $\mathbf{r}$ is the position vector confined to the unit cell. Moreover, $u_{n\mathbf{k}'}(\mathbf{r} + \mathbf{R}_N) = u_{n\mathbf{k}'}(\mathbf{r})$. Introducing the above-mentioned properties, the matrix elements read

$$\langle m\mathbf{k}|\hat{\mathbf{x}}|n\mathbf{k}'\rangle = -i\sum_{\mathbf{R}_N}\int_{\bar{V}} \mathrm{d}\mathbf{r}\Big(\boldsymbol{\nabla}_{\mathbf{k}'}\Big[e^{-i(\mathbf{k}-\mathbf{k}')\cdot(\mathbf{R}_N+\mathbf{r})}u^*_{m\mathbf{k}}(\mathbf{r})u_{n\mathbf{k}'}(\mathbf{r})\Big] - e^{-i(\mathbf{k}-\mathbf{k}')\cdot(\mathbf{R}_N+\mathbf{r})}u^*_{m\mathbf{k}}(\mathbf{r})\boldsymbol{\nabla}_{\mathbf{k}'}\big[u_{n\mathbf{k}'}(\mathbf{r})\big]\Big)\,. \tag{1.24c}$$

Evaluating the summations over all translations vectors $\mathbf{R}_N$, we identify Dirac delta functions in both terms on the *r.h.s.* of the previous equation. In the first term of the *r.h.s.* we obtain the gradient of the Dirac delta and in the second we get the product of the Dirac delta with the Berry connection

$$\langle m\mathbf{k}|\hat{\mathbf{x}}|n\mathbf{k}'\rangle = i\delta_{mn}\boldsymbol{\nabla}_{\mathbf{k}}\big[\delta(\mathbf{k}-\mathbf{k}')\big] + \delta(\mathbf{k}-\mathbf{k}')\boldsymbol{\mathcal{A}}_{mn}(\mathbf{k})\,, \tag{1.24d}$$

where the Berry connection matrix elements are defined as [10, 27, 28]

$$\boldsymbol{\mathcal{A}}_{mn} = \frac{i}{V_{WS}}\int \mathrm{d}\mathbf{r}\, u^*_{m\mathbf{k}}(\mathbf{r})\boldsymbol{\nabla}_{\mathbf{k}}\big[u_{n\mathbf{k}}(\mathbf{r})\big]\,. \tag{1.25}$$

The Bloch states and periodic functions are defined by $\langle\mathbf{r}|n\mathbf{k}\rangle = e^{i\mathbf{k}\mathbf{r}}u_{n\mathbf{k}}(\mathbf{r})$ and the V_{WS} is the volume of the unit cell. To proceed with this method, we separate the definition of intra and inter-band position operator in periodic systems as $\hat{\mathbf{r}} = \hat{\mathbf{r}}^{(i)} + \hat{\mathbf{r}}^{(e)}$, such that the respective matrix elements (evaluated on Bloch states) read

$$\mathbf{r}^{(e)}_{mn} = \langle m\,\mathbf{k}|\hat{\mathbf{r}}^{(e)}|n\,\mathbf{k}'\rangle = (1-\delta_{mn})\delta(\mathbf{k}-\mathbf{k}')\boldsymbol{\mathcal{A}}_{mn}\,, \tag{1.26a}$$

$$\mathbf{r}^{(i)}_{mn} = \langle m\,\mathbf{k}|\hat{\mathbf{r}}^{(i)}|n\,\mathbf{k}'\rangle = \delta_{mn}\Big[\delta(\mathbf{k}-\mathbf{k}')\boldsymbol{\mathcal{A}}_{mn} + i\boldsymbol{\nabla}_{\mathbf{k}}\delta(\mathbf{k}-\mathbf{k}')\Big]\,. \tag{1.26b}$$

Using equations 1.26, the perturbation part of the Hamiltonian is explicitly separated, reading $\hat{H} = \hat{H}_0 - q\hat{\mathbf{r}}^{(i)}\cdot\mathbf{E} - q\hat{\mathbf{r}}^{(e)}\cdot\mathbf{E}$. By the same token, the time evolution of the DM elements reads

$$i\hbar\frac{\partial\rho_{mn}}{\partial t} = \epsilon_{mn}\,\rho_{mn} - q\mathbf{E}(t)\cdot\sum_l\left(\mathbf{r}^{(e)}_{ml}\,\rho_{ln} - \rho_{ml}\,\mathbf{r}^{(e)}_{ln}\right) - q\mathbf{E}(t)\cdot\sum_l\left(\mathbf{r}^{(i)}_{ml}\,\rho_{ln} - \rho_{ml}\,\mathbf{r}^{(i)}_{ln}\right)$$

$$= \epsilon_{mn}\,\rho_{mn} - q\,\delta(\mathbf{k}-\mathbf{q})\sum_l \Big[(1-\delta_{ml})\boldsymbol{\mathcal{A}}_{ml}\,\rho_{ln} - \rho_{ml}(1-\delta_{ln})\boldsymbol{\mathcal{A}}_{ln}\Big]\cdot\mathbf{E}(t)$$
$$- iq\,\delta(\mathbf{k}-\mathbf{q})\Big[\boldsymbol{\nabla}_{\mathbf{k}}\rho_{mn} - i\rho_{mn}\Big(\boldsymbol{\mathcal{A}}_{mm} - \boldsymbol{\mathcal{A}}_{nn}\Big)\Big]\cdot\mathbf{E}(t)\,, \tag{1.27}$$

The combination of terms in the last line is gauge - invariant and appears frequently in the perturbative expansion to higher orders. It's useful to condense it in what has been named a "generalized derivative" [10]:

$$\langle n|\Big[\mathbf{r}^{(i)},\hat{S}\Big]|m\rangle = i\delta(\mathbf{k}-\mathbf{k}')\Big(S_{nm}\Big)_{;\mathbf{k}} = i\delta(\mathbf{k}-\mathbf{k}')\Big[\boldsymbol{\nabla}_{\mathbf{k}}\Big[S_{nm}\Big] - iS_{nm}\big(\boldsymbol{\mathcal{A}}_{nn}-\boldsymbol{\mathcal{A}}_{mm}\big)\Big]. \tag{1.28}$$

Considering the diagonal (populations) and non-diagonal (coherences) elements of the time evolution of the DM, equation 1.27, we can divide it into two more insightful equations. One equation for the time evolution of the populations and another for the time evolution of the coherences.

The time evolution of the diagonal elements reads

$$\frac{\partial\rho_{nn}}{\partial t} = \frac{iq}{\hbar}E^{\alpha}(t)\Big[\sum_l \bar{\delta}_{ln}\Big(\mathcal{A}^{\alpha}_{nl}\rho_{ln} - \rho_{nl}\mathcal{A}^{\alpha}_{ln}\Big) - i\frac{\partial\rho_{nn}}{\partial k_{\alpha}}\Big]\,, \tag{1.29a}$$

where we introduce the shorthand notation involving Kronecker deltas, $\bar{\delta}_{ln} = 1-\delta_{ln}$ and make use of Einstein's double index summation for Greek indices. The time evolution of the remaining elements of the DM, $m \neq n$, reads

$$\frac{\partial}{\partial t}\Big(\rho_{mn}e^{i\omega_{mn}t}\Big) = \frac{iq}{\hbar}E^{\alpha}(t)e^{i\omega_{mn}t}\;\bar{\delta}_{mn}\;\Big[\Big(\mathcal{A}^{\alpha}_{mn}\rho_{nn} - \rho_{mm}\mathcal{A}^{\alpha}_{mn}\Big) + \sum_l \bar{\delta}_{lm}\bar{\delta}_{ln}\Big(\mathcal{A}^{\alpha}_{ml}\rho_{ln}$$
$$- \rho_{ml}\mathcal{A}^{\alpha}_{ln}\Big) - i\Big(\frac{\partial\rho_{mn}}{\partial k_{\alpha}} - i\rho_{mn}\Big(\mathcal{A}^{\alpha}_{mm} - \mathcal{A}^{\alpha}_{nn}\Big)\Big)\Big]\,, \tag{1.29b}$$

where we transformed the initial linear differential equation in the form $dy(x)/dx + P(x)y = Q(x)$ to $dy(x)\exp\big[\int dxP(x)\big]/dx = \exp\big[\int dxP(x)\big]Q(x)$. Having computed the DM, we may compute the expectation value of an operator tracing the product of DM and the given operator $\langle\hat{O}\rangle = \mathrm{tr}\{\hat{\rho}\hat{O}\}$. The electric current density reads, in general, and for the case of non-interacting particles that we are considering

$$\langle\hat{\mathbf{J}}\rangle = \mathrm{tr}\Big\{\hat{\mathbf{j}}\,\hat{\rho}\Big\} = \frac{g}{L^D}\sum_{\mathbf{k}}\sum_{mn} q\,v_{nm}\,\rho_{mn}\,, \tag{1.30}$$

where g is the degeneracy and L^D is the volume (area) for a 3D (2D) system. The following subsection addresses the integration of these differential equations in the presence of an external AC field.

1.3.1 Integration of the equation of motion

We assume two initial conditions to solve these equations. First, the diagonal elements of DM in the absence of the external electric field are the equilibrium distribution functions, *i.e.* $\rho_{nn}(\mathbf{E}=0) \equiv f[\epsilon_n(\mathbf{k})-\mu] \equiv f_n$, where $\epsilon_n(\mathbf{k})$ is the energy dispersion for band n and μ is the chemical potential. Second, in the unperturbed system the non-diagonal elements of the DM are zero, *i.e.* there are no coherences $\rho_{mn}(\mathbf{E}=0)=0 \;\forall\; m \neq n$. The initial conditions can be condensed to $\rho_{mn}(\mathbf{E}=0) = f_m\delta_{mn}$. We are interested in the steady state response to an external perturbation, which can be achieved by invoking an adiabatic *switching on* of the interaction with an infinitesimal dampening parameter, *i.e.* $\eta \to 0^+$. This is introduced in the calculation by redefining the electric field as $E_\alpha(t) \to \lambda E_\alpha(t)e^{\eta t}$. Furthermore, we consider the external electric fields to be monochromatic plane waves[2], such that $E_\alpha(t)e^{\eta t} = \left[E^\alpha_\omega e^{-i(\omega+i\eta)t} + E^\alpha_{-\omega}e^{i(\omega-i\eta)t}\right]/2$. Given the initial condition and the power series in the electric field, we set to solve iteratively the differential equations, $\rho_{nn}(t)$ and $\rho_{mn}(t)$, equations 1.29a and 1.29b respectively. The iterative procedure starts at zeroth order in the electric field and each iteration increases one order. Hence, the iterative solution for the populations reads

$$\frac{\partial \rho^N_{nn}}{\partial t} = \frac{iq}{\hbar}E^\alpha(t)\left[\sum_l \bar{\delta}_{ln}\left(\mathcal{A}^\alpha_{nl}\rho^{N-1}_{ln} - \rho^{N-1}_{nl}\mathcal{A}^\alpha_{ln}\right) - i\frac{\partial \rho^{N-1}_{nn}}{\partial k_\alpha}\right] : N \geq 1\,, \tag{1.31a}$$

whereas the iterative solution for the coherences is defined by

$$\frac{\partial}{\partial t}\left(\rho^N_{mn}e^{i\omega_{mn}t}\right) = \frac{iq}{\hbar}E^\alpha(t)e^{i\omega_{mn}t}\bar{\delta}_{mn}\left(\sum_l \bar{\delta}_{lm}\bar{\delta}_{ln}\left(\mathcal{A}^\alpha_{ml}\rho^{N-1}_{ln} - \rho^{N-1}_{ml}\mathcal{A}^\alpha_{ln}\right) + \right.$$
$$\left. + \left(\mathcal{A}^\alpha_{mn}\rho^{N-1}_{nn} - \rho^{N-1}_{mm}\mathcal{A}^\alpha_{mn}\right) - i\left[\frac{\partial \rho^{N-1}_{mn}}{\partial k_\alpha} - i\rho^{N-1}_{mn}\left(\mathcal{A}^\alpha_{mm} - \mathcal{A}^\alpha_{nn}\right)\right]\right) : N \geq 1\,. \tag{1.31b}$$

[2]Since we limit the electric field to monochromatic plane waves we are limited to a narrow selection of wave-mixing processes, considering combinations $\pm\omega_i$. Beyond linear order complex phenomena can occur, such as the combination of two (or more) monochromatic electric fields with different frequency. This leads to processes such as the Sum Frequency Generation (SFG), and Difference Frequency Generation (DFG). For details on SFG and DFG and other wave-mixing processes, see [24, 25].

The zeroth order terms are determined by the initial conditions, $\rho_{mn}(\mathbf{E}=0) = f_m\delta_{mn}$, which read $\lambda^0: \ \rho^{(0)}_{mn} = 0 \ \ ; \ \rho^{(0)}_{nn} = f_n$. With respect to the iteration to first order, the coherence reads

$$\rho^{(1)}_{mn}(t) = -\bar{\delta}_{mn}\frac{q}{\hbar}\frac{\mathcal{A}^{\alpha}_{mn}f_{nm}}{2}\left[\frac{E^{\alpha}_{\omega}e^{-i(\omega+i\eta)t}}{\omega-\omega_{mn}+i\eta} - \frac{E^{\alpha}_{-\omega}e^{i(\omega-i\eta)t}}{\omega+\omega_{mn}-i\eta}\right], \tag{1.32a}$$

or, more condensely,

$$\rho^{(1)}_{mn}(t) = -\bar{\delta}_{mn}\frac{q}{\hbar}\sum_{\omega_1}\frac{\mathcal{A}^{\alpha}_{mn}f_{nm}}{2}\frac{E^{\alpha}_{\omega_1}e^{-i(\omega_1+i\eta)t}}{\omega_1-\omega_{mn}+i\eta}, \tag{1.32b}$$

where, we introduce $f_{nm} \equiv f_n - f_m$ and the frequency summation, $\sum_{\omega_1}$, should be interpreted as sum over the two possible Fourier components, *i.e.* $\sum_{\omega_1} g(\omega_1) \equiv g(-\omega_1) + g(\omega_1)$. Consequently, the respective Fourier components are trivially identified

$$\rho^{(1)}_{mn}(\omega_1) = -\bar{\delta}_{mn}\frac{q}{2\hbar}\frac{\mathcal{A}^{\alpha}_{mn}f_{nm}E^{\alpha}_{\omega_1}}{\omega_1-\omega_{mn}+i\eta} = -\bar{\delta}_{mn}\frac{iq}{2\hbar}\frac{v^{\alpha}_{mn}f_{nm}}{\omega_1-\omega_{mn}+i\eta}\frac{E^{\alpha}_{\omega_1}}{\omega_{mn}}, \tag{1.33}$$

where the inter-band matrix elements for the velocity and position operators are converted with the identity $\mathcal{A}^{\alpha}_{mn} = iv^{\alpha}_{mn}/\omega_{mn}$[3]. Regarding the first order correction to the equilibrium population, the integration reads

$$\rho^{(1)}_{nn}(\omega_1) = \frac{iq}{2\hbar}\frac{\partial f_n}{\partial k_{\alpha}}\frac{E^{\alpha}_{\omega_1}e^{-i(\omega_1+i\eta)t}}{\omega_1+i\eta}, \tag{1.34}$$

We can thus write the complete first order DM as

$$\rho^{(1)}_{mn}(t) = \frac{-q}{2\hbar}\sum_{\omega_1}\left[-i\delta_{mn}\frac{\partial f_n}{\partial k_{\alpha}} + \bar{\delta}_{mn}\mathcal{A}^{\alpha}_{mn}f_{nm}\right]\frac{E^{\alpha}_{\omega_1}e^{-i(\omega_1+i\eta)t}}{\omega_1-\omega_{mn}+i\eta}. \tag{1.35}$$

Proceeding to second order, the integration of the differential equations reads

$$\frac{\partial\rho^{(2)}_{mn}e^{i\omega_{mn}t}}{\partial t} = \bar{\delta}_{mn}\frac{-iq^2}{4\hbar^2}\sum_{\omega_2,\omega_1}E^{\beta}_{\omega_2}E^{\alpha}_{\omega_1}e^{-i(\omega_2+\omega_1-\omega_{mn}+i\eta)t}\Bigg[(-i)^2\mathcal{A}^{\alpha}_{mn}f_{nm}\frac{\mathcal{A}^{\beta}_{mm}-\mathcal{A}^{\beta}_{nn}}{\omega_1-\omega_{mn}+i\eta}$$
$$+\sum_l\bar{\delta}_{lm}\bar{\delta}_{ln}\left(\frac{\mathcal{A}^{\beta}_{ml}\mathcal{A}^{\alpha}_{ln}f_{nl}}{\omega_1-\omega_{ln}+i\eta} - \frac{f_{lm}\mathcal{A}^{\alpha}_{ml}\mathcal{A}^{\beta}_{ln}}{\omega_1-\omega_{ml}+i\eta}\right) - \frac{i\mathcal{A}^{\beta}_{mn}}{\omega_1+i\eta}\frac{\partial f_{nm}}{\partial k_{\alpha}} - \frac{\partial}{\partial k_{\beta}}\left[\frac{i\,\mathcal{A}^{\alpha}_{mn}f_{nm}}{\omega_1-\omega_{mn}+i\eta}\right]\Bigg), \tag{1.36a}$$

[3]The relation between inter-band matrix elements for position and velocity operators is easily verified from the time evolution of the position operator, *i.e.* compute the matrix elements of $i\hbar\partial\hat{x}/\partial t = i\hbar\hat{v} = [\hat{H}_0, \hat{x}]$.

where the derivative of the first order coherence with respect to k_β reduces to

$$\frac{\partial \rho^{(1)}_{mn}\bar{\delta}_{mn}}{\partial k_\beta} = -\bar{\delta}_{mn}\frac{q}{2\hbar}\sum_{\omega_1}\frac{\partial}{\partial k_\beta}\left[\frac{\mathcal{A}^\alpha_{mn}f_{nm}}{\omega_1-\omega_{mn}+i\eta}\right]E^\alpha_{\omega_1}e^{-i(\omega_1+i\eta)t}\,.$$

The time integration is a trivial operation and yields

$$\begin{aligned}\rho^{(2)}_{mn} = \bar{\delta}_{mn}\frac{q^2}{4\hbar^2}\sum_{\omega_2,\omega_1}\Bigg[\sum_l \bar{\delta}_{lm}\bar{\delta}_{ln}\left[\frac{\mathcal{A}^\beta_{ml}\mathcal{A}^\alpha_{ln}f_{nl}}{\omega_1-\omega_{ln}+i\eta}+-\frac{f_{ml}\mathcal{A}^\alpha_{ml}\mathcal{A}^\beta_{ln}}{\omega_1-\omega_{ml}+i\eta}\right]-i\frac{\partial f_{nm}}{\partial k_\alpha}\frac{\mathcal{A}^\beta_{mn}}{\omega_1+i\eta}\\ +(-i)\left(\frac{\mathcal{A}^\alpha_{mn}f_{nm}}{\omega_1-\omega_{mn}+i\eta}\right)_{;k_\beta}\Bigg]\frac{E^\beta_{\omega_2}E^\alpha_{\omega_1}e^{-i(\omega_2+\omega_1+2i\eta)t}}{\omega_2+\omega_1-\omega_{mn}+2i\eta},\end{aligned} \tag{1.36b}$$

where we used the definition of generalized derivative introduced in equation 1.28 to compactly write

$$\frac{\partial}{\partial k_\beta}\left[\frac{\mathcal{A}^\alpha_{mn}f_{nm}}{\omega_1-\omega_{mn}+i\eta}\right]-i\mathcal{A}^\alpha_{mn}f_{nm}\frac{\mathcal{A}^\beta_{mm}-\mathcal{A}^\beta_{nn}}{\omega_1-\omega_{mn}+i\eta}=\left(\frac{\mathcal{A}^\alpha_{mn}f_{nm}}{\omega_1-\omega_{mn}+i\eta}\right)_{;k_\beta}. \tag{1.37}$$

Proceeding to the diagonal elements, the time evolution of the respective elements of DM read

$$\frac{\partial \rho^{(2)}_{nn}e^{i\omega_{mn}t}}{\partial t} = \delta_{mn}\frac{iq}{\hbar}e^{i\omega_{mn}t}E^\beta(t)\left[\sum_l \bar{\delta}_{lm}\bar{\delta}_{ln}\left(\mathcal{A}^\beta_{ml}\rho^{(1)}_{ln}-\rho^{(1)}_{ml}\mathcal{A}^\beta_{ln}\right)-i\frac{\partial \rho^{(1)}_{nn}}{\partial k_\beta}\right]. \tag{1.38a}$$

Following the procedure used in the integration of the coherences and computing the derivative of the linear order population

$$\frac{\partial \rho^{(1)}_{nn}}{\partial k_\beta} = \frac{iq}{2\hbar}\sum_{\omega_1}\frac{\partial^2 f_n}{\partial k_\beta \partial k_\alpha}\frac{E^\alpha_{\omega_1}e^{-i(\omega_1+i\eta)t}}{\omega_1+i\eta}\,,$$

it can be shown that the second order correction to the population reads

$$\begin{aligned}\rho^{(2)}_{nn}(t) = \delta_{mn}\frac{q^2}{4\hbar^2}\sum_{\omega_2,\omega_1}\frac{E^\beta_{\omega_2}E^\alpha_{\omega_1}e^{-i(\omega_2+\omega_1+2i\eta)t}}{\omega_2+\omega_1-\omega_{mn}+i\eta}\Bigg[\frac{-1}{\omega_1+i\eta}\frac{\partial^2 f_n}{\partial k_\beta \partial k_\alpha}\\ +\sum_l \bar{\delta}_{ln}\left(\frac{\mathcal{A}^\beta_{nl}\mathcal{A}^\alpha_{ln}f_{nl}}{\omega_1-\omega_{ln}+i\eta}-\frac{f_{ln}\mathcal{A}^\alpha_{nl}\mathcal{A}^\beta_{ln}}{\omega_1-\omega_{nl}+i\eta}\right)\Bigg],\end{aligned} \tag{1.38b}$$

The total second order term of the DM reads

$$\rho^{(2)}_{mn}(t) = \frac{q^2}{4\hbar^2}\sum_{\omega_2,\omega_1}\frac{E^\beta_{\omega_2}E^\alpha_{\omega_2}e^{-i(\omega_2+\omega_1+2i\eta)t}}{\omega_2+\omega_1-\omega_{mn}+2i\eta}\left[\sum_l \bar{\delta}_{lm}\bar{\delta}_{ln}\left(\frac{\mathcal{A}^\beta_{ml}\mathcal{A}^\alpha_{ln}f_{nl}}{\omega_1-\omega_{ln}+i\eta}-\frac{f_{lm}\mathcal{A}^\alpha_{ml}\mathcal{A}^\beta_{ln}}{\omega_1-\omega_{ml}+i\eta}\right)\right.$$

$$- i\bar{\delta}_{mn}\left(\frac{\mathcal{A}^{\alpha}_{mn} f_{nm}}{\omega_1 - \omega_{mn} + i\eta}\right)_{;k_\beta} - i\bar{\delta}_{mn}\frac{\mathcal{A}_{mn}}{\omega_1 + i\eta}\frac{\partial f_{nm}}{\partial k_\alpha} - \frac{\delta_{mn}}{\omega_1 + i\eta}\frac{\partial^2 f_n}{\partial k_\beta \partial k_\alpha}\Bigg]. \tag{1.39}$$

This recursive integration of the DM is consistent with the "standard" calculation of the response function, equation 1.20. The apparent differences stem solely from the idiosyncrasies associated with the calculation of intraband elements for the position operator, particularly with the generalized derivative, equation 1.28.

1.3.2 Linear and quadratic response

The relation between an observable and the DM has been introduced earlier, see equation 1.30. Considering a plane wave monochromatic electric field, the current in linear response reads

$$J^{(1)}_{\lambda}(t) = \frac{iq^2 g}{2\hbar L^D}\sum_{\mathbf{k}}\sum_{mn}\sum_{\omega_1}\left[-\delta_{mn} v^{\lambda}_{nm}\frac{\partial f_n}{\partial k_\alpha} + \bar{\delta}_{mn}\frac{v^{\lambda}_{nm} v^{\alpha}_{mn} f_{nm}}{\omega_{mn}}\right]\frac{E^{\alpha}_{\omega_1} e^{-i(\omega_1 + i\eta)t}}{\omega_1 - \omega_{mn} + i\eta}, \tag{1.40a}$$

where we used the identity $\mathcal{A}^{\alpha}_{mn} = i v^{\alpha}_{mn}/\omega_{mn}$ and identify the intra (i) and inter-band (e) contribution with *Kronecker* deltas. Furthermore, by partial fraction decomposition[4] the linear response can be recast as

$$\begin{aligned} J^{(1)}_{\lambda}(t) = \frac{iq^2 g}{2\hbar L^D}\sum_{\mathbf{k}}\sum_{mn}\sum_{\omega_1}\Bigg[&\frac{1}{\omega_1 + i\eta}\left[-\delta_{mn} v^{\lambda}_{nn}\frac{\partial f_n}{\partial k_\alpha} + \bar{\delta}_{mn}\frac{v^{\lambda}_{nm} v^{\alpha}_{mn} f_{nm}}{\omega_{mn}}\right] \\ &+ \frac{\bar{\delta}_{mn}}{\omega_1 + i\eta}\frac{v^{\lambda}_{nm} v^{\alpha}_{mn} f_{nm}}{\omega_1 - \omega_{mn} + i\eta}\Bigg] E^{\alpha}_{\omega_1} e^{-i\omega_1 t}, \end{aligned} \tag{1.40b}$$

where the first term in *r.h.s.* contains the diamagnetic contributions to the total current and the second term is conventionally identified as the Optical Conductivity (OC) response. The former contains contributions from both intra and inter-band transitions, whereas the latter arises exclusively from inter-band transitions.

Moreover, the gradient of the Fermi distribution is proportional to the band velocity, *i.e.* $\partial f_n/\partial k_\alpha = -(1 - f_n) f_n v^{\alpha}_{nn}/k_B T$. Consequently, the integrand for the diamagnetic term reads

$$\sum_{mn}\frac{v^{\lambda}_{nm} v^{\alpha}_{mn}}{\omega_1 + i\eta}\left[-\delta_{mn}\frac{1 - f_n}{k_B T} + \bar{\delta}_{mn}\frac{f_{nm}}{\omega_{mn}}\right].$$

[4] For this particular case, the partial fraction decomposition reads $1/\bar{\omega}(\omega \pm \bar{\omega}) = 1/\omega\bar{\omega} \pm 1/\omega(\omega \mp \bar{\omega})$.

Furthermore, the respective conductivity tensor reads

$$\sigma^{(1)}_{\lambda\alpha} = \frac{2ig\,\sigma_1}{L^D}\sum_{\mathbf{k}}\sum_{mn}\frac{v^{\lambda}_{nm}}{\omega_1-\omega_{mn}+i\eta}\left[-\delta_{mn}\frac{\partial f_n}{\partial k_\alpha}+\bar{\delta}_{mn}\frac{v^{\alpha}_{mn}f_{nm}}{\omega_{mn}}\right], \tag{1.41}$$

where $\sigma_1 = \pi e^2/2h$ is the linear conductivity scale. Proceeding with the calculation of the current up to second order, the quadratic contributions read

$$\begin{aligned} J^{(2)}_{\lambda}(t) = \frac{-q^3}{4\hbar^2}\frac{g}{L^D}\sum_{\mathbf{k}}\sum_{lmn}\sum_{\omega_2,\omega_1}\frac{E^{\beta}_{\omega_2}E^{\alpha}_{\omega_2}e^{-i(\omega_2+\omega_1+2i\eta)t}v^{\lambda}_{nm}}{\omega_2+\omega_1-\omega_{mn}+2i\eta}\Bigg[&\frac{\delta_{lm}\delta_{mn}}{\omega_1+i\eta}\frac{\partial^2 f_n}{\partial k_\beta\partial k_\alpha}\\ -\,\delta_{lm}\bar{\delta}_{mn}\frac{v^{\beta}_{mn}/\omega_{mn}}{\omega_1+i\eta}\frac{\partial f_n}{\partial k_\alpha}&-\delta_{lm}\bar{\delta}_{mn}\left(\frac{v^{\alpha}_{mn}f_{nm}/\omega_{mn}}{\omega_1-\omega_{mn}+i\eta}\right)_{;k_\beta}\\ +\,\frac{\bar{\delta}_{lm}\bar{\delta}_{ln}}{\epsilon_{ml}\epsilon_{ln}}\left(\frac{v^{\beta}_{ml}v^{\alpha}_{ln}f_{nl}}{\omega_1-\omega_{ln}+i\eta}-\frac{f_{lm}v^{\alpha}_{ml}v^{\beta}}{\omega_1-\omega_{ml}+i\eta}\right)\Bigg]&. \end{aligned} \tag{1.42a}$$

Based on this result, we identify the respective second order conductivity tensor

$$\begin{aligned} \sigma^{(2)}_{\lambda\alpha\beta}(\omega_2+\omega_1) = \frac{g\,\sigma_2}{L^D}\frac{\hbar\gamma_0}{a}\sum_{\mathbf{k}}\sum_{lmn}\frac{v^{\lambda}_{nm}}{\hbar(\omega_2+\omega_1)-\epsilon_{mn}+2i\Gamma}\Bigg[&\frac{\delta_{lm}\delta_{mn}}{\hbar\omega_1+i\Gamma}\frac{\partial^2 f_n}{\partial k_\beta\partial k_\alpha}\\ -\,\hbar\frac{\delta_{lm}\bar{\delta}_{mn}v^{\beta}_{mn}}{\epsilon_{mn}(\hbar\omega_1+i\Gamma)}\frac{\partial f_n}{\partial k_\alpha}&-\hbar\,\delta_{lm}\bar{\delta}_{mn}\left(\frac{v^{\alpha}_{mn}f_{nm}/\epsilon_{mn}}{\hbar\omega_1-\epsilon_{mn}+i\Gamma}\right)_{;k_\beta}\\ +\,\hbar^2\frac{\bar{\delta}_{lm}\bar{\delta}_{ln}}{\epsilon_{ml}\epsilon_{ln}}\left(\frac{v^{\beta}_{ml}v^{\alpha}_{ln}f_{nl}}{\hbar\omega_1-\epsilon_{ln}+i\Gamma}-\frac{f_{lm}v^{\alpha}_{ml}v^{\beta}_{ln}}{\hbar\omega_1-\epsilon_{ml}+i\Gamma}\right)\Bigg]&, \end{aligned} \tag{1.42b}$$

where we introduce the second order conductivity scale

$$\sigma_2 = e^3 a/4\gamma_0\hbar\,, \tag{1.43}$$

a is the nearest neighbour distance, γ_0 the hopping integral.

The definition of the non-linear tensors does not follow a universal convention. For the sake of clarity and consistency, we follow throughout this thesis the convention introduced in §1.1, equation 1.7.

The previous result paves the way for the calculation of all second order sum or difference processes for any material at finite temperature and chemical potential. Moreover, we decompose the conductivity tensor, equation 1.42b, in contributions according to the type of transitions (intra or interband) associated with each term as $\sigma^{(2)}_{\lambda\alpha\beta} = \sigma^{(2,ii)}_{\lambda\alpha\beta} + \sigma^{(2,ei)}_{\lambda\alpha\beta} + \sigma^{(2,ie)}_{\lambda\alpha\beta} + \sigma^{(2,ee)}_{\lambda\alpha\beta}$, using the notation introduced in the definition of the matrix elements for the position operator, equation 1.26. The exclusively interband con-

tribution reads

$$\sigma^{(2,ee)}_{\lambda\alpha\beta}(\omega_2+\omega_1) = \frac{g\,\sigma_2}{L^D}\sum_{\mathbf{k}}\sum_{lmn}\frac{\hbar^3\gamma_0}{a}\frac{\bar{\delta}_{lm}\bar{\delta}_{ln}\,v^{\lambda}_{nm}\,/\,\epsilon_{ml}\epsilon_{ln}}{\hbar(\omega_2+\omega_1)-\epsilon_{mn}+2i\Gamma}\left(\frac{v^{\beta}_{ml}v^{\alpha}_{ln}f_{nl}}{\hbar\omega_1-\epsilon_{ln}+i\Gamma}\right.$$
$$\left.-\frac{f_{lm}v^{\alpha}_{ml}v^{\beta}_{ln}}{\hbar\omega_1-\epsilon_{ml}+i\Gamma}\right). \tag{1.44a}$$

With respect to the mixed intra and interband processes, there are two possibilities. Following Sipe's notation [10], one process reads

$$\sigma^{(2,ie)}_{\lambda\alpha\beta}(\omega_2+\omega_1) = -\frac{g\,\sigma_2}{L^D}\sum_{\mathbf{k}}\sum_{mn}\frac{\hbar^2\gamma_0\bar{\delta}_{mn}\,v^{\lambda}_{nm}/a}{\hbar(\omega_2+\omega_1)-\epsilon_{mn}+2i\Gamma}\left(\frac{v^{\alpha}_{mn}f_{nm}/\epsilon_{mn}}{\hbar\omega_1-\epsilon_{mn}+i\Gamma}\right)_{;k_\beta}, \tag{1.44b}$$

where we make use of the definition of generalized derivative, equation 1.28. The remaining mixed intra/interband process reads

$$\sigma^{(2,ei)}_{\lambda\alpha\beta}(\omega_2+\omega_1) = -\frac{g\,\sigma_2}{L^D}\sum_{\mathbf{k}}\sum_{mn}\frac{\hbar^2\gamma_0\,\bar{\delta}_{mn}/a}{\hbar(\omega_2+\omega_1)-\epsilon_{mn}+2i\Gamma}\frac{v^{\lambda}_{nm}v^{\beta}_{mn}}{\epsilon_{mn}(\hbar\omega_1+i\Gamma)}\frac{\partial f_{nm}}{\partial k_\alpha}. \tag{1.44c}$$

Finally, the purely intraband contribution reads

$$\sigma^{(2,ii)}_{\lambda\alpha\beta}(\omega_2+\omega_1) = \frac{g\,\sigma_2/L^D}{\hbar(\omega_2+\omega_1)+2i\Gamma}\frac{\hbar\gamma_0/a}{\hbar\omega_1+i\Gamma}\sum_{\mathbf{k}}\sum_{n}v^{\lambda}_{nn}\frac{\partial^2 f_n}{\partial k_\beta\partial k_\alpha}\,. \tag{1.44d}$$

The analysis of any response function can be greatly simplified by considering low temperature. Taking the low temperature limit, the Fermi function reduces to a sharp(er) step function at the chemical potential.

Cold insulator limit Before proceeding to analyse the general second order response, it is worth considering the so-called "cold insulator limit". In an undopped semiconductor, this limit does not require zero temperature, it solely requires the thermal energy to be much smaller than the insulator gap $k_{\mathrm{B}}T/E_g \ll 1$. In this limit all valence band states are fully occupied and all conduction band states are completely empty. Because of this, the gradient of the Fermi function vanishes in any band, $\partial f_n/\partial k_\alpha \to 0$. Consequently, the conductivity reduces to

$$\sigma^{(1)}_{\lambda\alpha}(\omega_1;\omega_1) = \frac{iq^2\hbar}{2L^D}\sum_{\mathbf{k}}\sum_{mn}\frac{\delta_{mn}\,f_{nm}}{\epsilon_{mn}}\frac{v^{\lambda}_{nm}v^{\alpha}_{mn}}{\hbar\omega_1-\epsilon_{mn}+i\Gamma}\,. \tag{1.45}$$

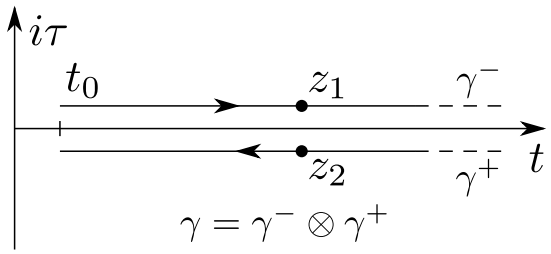

Figure 1.2: Contour for time evolution. The complete contour is the sum of two branches, the upper γ^- and the lower γ^+, such that $\gamma^- \oplus \gamma^+ = \gamma$. The apparently counter intuitive labelling of the branches becomes clear if one considers the contour starting at t_0^-, extending over γ^-, looping at $z = +\infty$ to γ^+, and returning to t_0^+. In this picture, any event associated with any time in the lower branch occurs at a time latter $(+)$ than any event associated with any time in γ^-.

By the same token, the second order conductivity tensor contains vanishing contributions and reduces to two components $\sigma^{(2)}_{\lambda\alpha\beta}(\omega_2+\omega_1) = \sigma^{(2,ee)}_{\lambda\alpha\beta}(\omega_2+\omega_1)+\sigma^{(2,ie)}_{\lambda\alpha\beta}(\omega_2+\omega_1)$[5]. This result has been identified both in the length [10] and velocity [9] gauges. It is rather straightforward to show that $\sigma^{(2,ie)}_{\lambda\alpha\beta}(\omega_2+\omega_1)$ is a "regular" quantity in the limit of zero frequency or OR, *i.e.* $\omega_2 = -\omega_1$. The $\bar{\delta}_{mn}$ forces the energy difference ω_{mn} to be finite at a non-degenerate k. This ensures that, even in the limit of zero frequency, the denominators are regular.

1.4 Non-equilibrium formalism

The purpose of this section is to review the NEF. It begins by evaluating the GF in complex time, more precisely along a contour. The complex time contour γ is represented in figure 1.2, where z_i are complex numbers and the real time is mapped to the real axis. Our review follows the notation and formalism presented in the textbook by Stefanucci and Leeuwen [20], and we limit ourselves to provide a review of the fundamental definitions and derivations required to analyse response functions using NEF The time (contour) evolution of GFs in NEF follows closely the "standard" time-evolution [14–19]. Indeed, the contour formalism is a generalization of the standard time evolution of GFs [20, 22, 23].

Let us consider a time-dependent quantum average for an operator $\hat{O}(t)$ when the

[5]To maintain the notation condensed, we define the following notation for the N^{th} order conductivity tensors: $\sigma^{(N)}_{\lambda\alpha\beta}(\omega_N+\cdots+\omega_1;\omega_1,\cdots,\omega_N) = \sigma^{(N)}_{\lambda\alpha\beta}(\omega_N+\cdots+\omega_1)$.

system has been prepared in a given initial state $|\Psi(t_0)\rangle = |\Psi_0\rangle$, *i.e.*

$$O(t) = \langle\Psi(t)|\hat{O}(t)|\Psi(t)\rangle = \langle\Psi_0|\hat{\mathcal{U}}(t_0,t)\hat{O}(t)\hat{\mathcal{U}}(t,t_0)|\Psi_0\rangle\,. \tag{1.46}$$

As mentioned before, in the NEF the time evolution takes place along a contour γ in a *complex time* variable z. We reserve the variables t and τ for purely real and imaginary times, respectively. Along such contour, the time evolution operator reads $\hat{\mathcal{U}}(t,t_0) = \mathcal{T}\{\exp[-i\int_{\gamma^-}\mathrm{d}\bar{z}\,\hat{H}(\bar{z})]\}$, where $\mathcal{T}$ is the contour ordering operator, defined as follows[6]

$$\mathcal{T}\big\{A(z_a)B(z_b)\big\} = \begin{cases} T\big\{A(z_a)B(z_b)\big\} & \text{if } z_a, z_b \in \gamma^- \\ A(z_a)B(z_b) & \text{if } z_b \in \gamma^- \wedge z_a \in \gamma^+ \\ B(z_b)A(z_a) & \text{if } z_a \in \gamma^- \wedge z_b \in \gamma^+ \\ \bar{T}\big\{A(z_a)B(z_b)\big\} & \text{if } z_a, z_b \in \gamma^+ \end{cases}. \tag{1.47}$$

Hence, the time-dependent quantum average reads

$$O(z) = \langle\Psi_0|\mathcal{T}\Big\{\exp\Big[-i\int_\gamma \mathrm{d}\bar{z}\,\hat{H}(\bar{z})\Big]\hat{O}(z)\Big\}|\Psi_0\rangle\,, \tag{1.48}$$

where $\hat{O}(t_\pm) = \hat{O}(t)$. Given a known initial eigenstate, the previous equation allows us to compute the expectation value of operator $\hat{O}(z)$ for isolated systems.

Within the context of quasi-independent particles, the behaviour of many-body systems can be mapped to ensemble averages of independent particles. In this context, a given operator is represented the by the ensemble average $\hat{O}(t) = \sum_n w_n\langle\chi_n|\hat{O}(t)|\chi_n\rangle$ in a basis of pure states $|\chi_n\rangle$, with the respective statistical weight w_n, which leads us to compute a time-dependent ensemble average, [20, eq. 4.21],

$$O(z) = \mathrm{Tr}\Big[\hat{\rho}\,\hat{O}(z)\Big] = \frac{\mathrm{Tr}\Big[\mathcal{T}\Big\{\exp\Big[-i\int_\gamma \mathrm{d}\bar{z}\,\hat{H}(\bar{z})\Big]\hat{O}(z)\Big\}\Big]}{\mathrm{Tr}\Big[\mathcal{T}\Big\{\exp\Big[-i\int_\gamma \mathrm{d}\bar{z}\,\hat{H}(\bar{z})\Big]\Big\}\Big]}\,, \tag{1.49}$$

where Tr indicates the trace over full Fock space and the contour γ is now extended along the vertical axis as depicted in figure 1.3a, with $\beta = 1/k_BT$.

[6] For details on the definition of the contour ordering operator, see ref. [20, §4].

The choice of contour In addition to the general definition for the calculation of the observable, it is important to consider the influence of alterations of the original contour γ. Below, we highlight the most relevant contours and identity the key characteristics of each. An in-depth analysis can be found in [20, §4.3].

In figure 1.3, we depict three distinct contours, representing three distinct protocols to compute an observable. Note that these contours differ not only by a deformation, but also by changing the definition of the Hamiltonian along the contour. For the sake of clarity, let us consider an Hamiltonian composed of two parts such as $\hat{H}(t) = \hat{H}_0(t) + \hat{U}(t)$. The respective Matsubara component used in the vertical track to compute the ensemble averages reads $\hat{H}^M = \hat{H}_0^M + \hat{U}$ where $\hat{H}_0^M = \hat{H}_0 - \mu\hat{N}$. Furthermore, contours 1.3b and 1.3c require an adiabatic *switch-on/off* of the interaction piece of the Hamiltonian. The adiabatic coupling reads $\hat{H}_\eta(z) = \hat{H}(z) + e^{-\eta|z-T|}\hat{U}$, where η is a positive infinitesimal that ensures convergence at $t \to \pm\infty$. To choose the most appropriate contour, we should keep in mind the most relevant details for each contour.

- The first contour, depicted in figure 1.3a, allows us to compute the exact time-dependent ensemble average and is associated with the Konstantinov-Perel' formalism, where the ensemble average is computed at the exact moment that the interaction is turned on, at t_0. Ideally, this is the best contour to use to compute any quantity. Yet, because the full Hamiltonian is used along the complete contour, evaluating even relatively simple interactions becomes impossible, in practice.

- The second contour, depicted in figure 1.3b, introduces the adiabatic approximation. Here, the interaction is switched on adiabatically along the upper branch of the contour from $-\infty^- \to t_0^-$[7]. Upon full switch on of the interaction, the system evolves in time from $T^- \to t_0^+$, followed by adiabatic decoupling of the interaction from $T^+ \to -\infty^+$. Finally, the vertical track is evaluated from $-\infty \to -\infty - i\beta$. As in the exact contour, the evaluation along the horizontal branches provides the time evolution with the interactions and the vertical track is associated with the ensemble average of the system after decoupling the interaction. The evaluation along this contour is equivalent to the standard Keldysh formalism [29].

[7] The notation $t_i^{\mp}$ defines the i^{th}-time variable in the upper $(-)$ or lower $(+)$ branch of the branch of the contour. The notation $\mp$ should be understood as $-$ for earlier and $+$ later times, as the contour starts in the upper branch and loops back at $z = +\infty$.

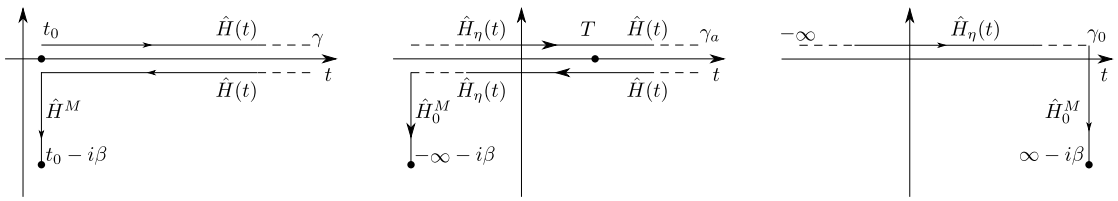

(a) Exact (b) Adiabatic approximation (c) Zero temperature

Figure 1.3: Contours to evaluate time-dependent ensemble averages. In all figures t_0, T and β are real. Furthermore, besides each segment of the contour we indicate the respective Hamiltonian. In the adiabatic contour, the interaction is switched on adiabatically from $t_0 \to -\infty$ to T. Moreover, at zero temperature the contour runs from $-\infty \to t = \infty$ and the statistical average, *i.e.* the vertical track, is computed at $t = +\infty$. Finally, the sections of the contours above and parallel to the real time axis define "earlier" and the sections below and parallel to the real time axis define "later" times. The respective notation for the contour and time variables reads $\gamma_x^{\mp}$ and $t^{\mp}$.

- Lastly, the third contour depicted in figure 1.3c, represents the zero temperature formalism. This protocol also makes use of the adiabatic coupling of the interaction, namely the interaction is adiabatically switched on from $-\infty \to t_0$ and adiabatically switched off from $t_0 \to \infty$.

The calculation of thermodynamic averages in the presence of most interactions is a daunting, if not impossible, task. This drastically reduces the practical usage of the exact contour to a few selected problems which lay outside the scope of non-linear response theory. Moreover, we are interested in a general formalism valid at room temperature and at finite chemical potential, two highly praised characteristics for realist devices. Hence, by making use of the adiabatic theorem to decouple the time dependent perturbation from the ensemble average, the adiabatic contour or the exact contour, limited to perturbations which have an intrinsic adiabatic time dependency, are the ideal contours to study response theory.

Green's functions The starting point to solve a non-equilibrium problem, as well as many problems in quantum mechanics is to compute the GF associated with this problem and then determine relevant quantities [14–20]. In the context of contour ordered functions, the $n-$particle GF operator is defined as the time ordered product of n annihilation and n creation field operators [20, eq. 4.58]

$$\hat{G}_n(1,\ldots,n;1',\ldots,n') = i^{-n}\,\mathcal{T}\left\{\,\hat{\psi}_H(1)\ldots\hat{\psi}_H(n)\,\hat{\psi}_H^{\dagger}(n')\ldots\hat{\psi}_H^{\dagger}(1')\,\right\}, \tag{1.50}$$

where the annihilation and creation field operators defined in HP read

$$\hat{O}_H(z) \equiv \hat{\mathcal{U}}(z_i, z)\, \hat{O}(z)\, \hat{\mathcal{U}}(z, z_i)\,. \tag{1.51}$$

Furthermore, we define the compact notation for the j^{th} time and position coordinate $j \equiv \mathbf{x}_j, z_j$ and the zeroth order reduces to the identity $\hat{G}_0 \equiv \hat{\mathbb{1}}$. The relation between a one-particle GF and observables [14, 20] allows us to compute the expected value of physical quantities from GFs. To extract this information, we must compute the trace of the operator associated with the observable with the respective contour-ordered GF evaluated at equal times [20, eq. 6.26]. This relation reads

$$O(t) = \pm i \sum\nolimits_{ij} O_{ij}\, G^{<}_{ji}(t, t^{+})\,, \tag{1.52}$$

where the contour order GF evaluated at equal times reduces to the lesser component of the respective GF [20, eq. 5.38] and indices i, j span all states.

The following subsections delve into the details of the evaluation of correlators (GFs) along the contour and the PE of GF.

1.4.1 Correlators on the contour and Langreth rules

Before proceeding to evaluate time-dependent ensemble averages using *contour formalism*, it will be necessary to present a brief review of some properties of *operator correlators* and the respective contour ordering. The analysis of the contour order components of general correlators is greatly simplified by considering the so-called Langreth's rules (LR) [20, 22, 23, 30–32], which allow a much easier and insightful calculation of contour order products or convolutions of correlators. The review of the general $n-$point operator correlator in Keldysh Space (KS) will follow closely [20, §5.5]. The $n-$point operator correlator can be written as a time ordered product of n operators [20, eq. 4.47]

$$\hat{k}(z_1, \ldots, z_n) = \mathcal{T}\{\hat{O}_1(z_1) \ldots \hat{O}_n(z_n)\}\,, \tag{1.53}$$

where $\hat{O}_i(z_1)$ are operators in the Heisenberg's Picture (HP), equation 1.51. A sub-class of operator correlators particular interest are the the n-particle Green's operator defined

previously in equation 1.50. Moreover, the expectation value for a general correlator follows the standard ensemble average calculation, *i.e.* evaluate the trace of the product with the density matrix

$$k(z_1, z_2) = \mathrm{Tr}\left[\hat{\rho}\,\hat{k}(z_1, z_2)\right] = \mathrm{Tr}\left[\hat{\rho}\,\mathcal{T}\{\,\hat{O}_1(z_1)\,\hat{O}_2(z_2)\,\}\right], \tag{1.54}$$

where the only difference resides in the more general "complex time" ordering along the contour. A general two point correlator in KS, *i.e.* $z_1, z_2 \in \gamma$, contains three distinct possible time orderings: the usual lesser, $k^<(z_1, z_2)$, and greater, $k^>(z_1, z_2)$, components and a *singular*, $k^\delta(z_1)$, component defined as follows

$$k(z_1, z_2) = k^\delta(z_1)\delta(z_1, z_2) + \theta(z_1, z_2)\,k^>(z_1, z_2) + \theta(z_2, z_1)\,k^<(z_1, z_2)\,, \tag{1.55}$$

where we introduce the generalized Dirac delta, $\delta(z; z')$ [20, eq. 4.49], and Heaviside theta, $\theta(z, z')$ [20, eq. 4.50], function

$$\delta(z_1, z_2) = \begin{cases} 0 & \text{if } z_1 = t_\pm \wedge z_2 = t_\mp \\ \delta(t_1 - t_2) & \text{if } z_1, z_2 \in \gamma^- \\ -\delta(t_1 - t_2) & \text{if } z_1, z_2 \in \gamma^+ \end{cases} \quad ; \quad \theta(z_1, z_2) = \begin{cases} 1 & \text{if } z_1 \text{ later than } z_2 \\ 0 & \text{if } z_2 \text{ later than } z_1 \end{cases}.$$

The singular part represents the correlator evaluated at equal times, with the following property $k^\delta(t_+) = k^\delta(t_-) \equiv k^\delta(t)$. Furthermore, the integration along γ of a generalized Dirac delta is analogous to the integration of a real time Dirac delta function, hence $\int_\gamma \mathrm{d}\bar{z}\,\delta(z, \bar{z}) f(\bar{z}) = f(z)$. The remaining terms are the usual lesser and greater components, defined by ensemble averages of the following correlators

$$k^>(z_1, z_2) = \mathrm{Tr}\left[\hat{\rho}\,\hat{O}_1(z_1)\,\hat{O}_2(z_2)\right] \quad ; \quad k^<(z_1, z_2) = \pm\,\mathrm{Tr}\left[\hat{\rho}\,\hat{O}_2(z_2)\,\hat{O}_1(z_!)\right], \tag{1.56}$$

such that $\pm$ indicates the statistics of the operators $\hat{O}_i$, namely bosonic $(+)$ or fermionic $(-)$. Even though the correlators are defined along the contour, the operators $\hat{O}_i(z_i)$ are functions of real time, hence $\hat{O}_i(t_+) = \hat{O}_i(t_-)$. Consequently, these correlators are independent of the contour branch and as result, the correlators must verify the following

relations [20, eq. 5.37]

$$k^{\lessgtr}(t_+, z') = k^{\lessgtr}(t_-, z') \quad ; \quad k^{\lessgtr}(z, t'_+) = k^{\lessgtr}(z, t'_-)\,. \tag{1.57}$$

From the previous discussion, several relations between real time and complex time (in the contour γ) correlators also emerge, such as [20, eq. 5.38]

$$k^{>}(t, t') = k(t_+, t'_-) \quad ; \quad k^{<}(t, t') = k(t_-, t'_+)\,; \tag{1.58}$$

$$k^{>}(t, t) = k(z^+, z) = k(z, z^-) \quad ; \quad k^{<}(t, t) = k(z, z^+) = k(z^-, z)\,. \tag{1.59}$$

Moreover, we can introduce the real time retarded and advanced components on the Keldysh correlator, which read [20, eq. 5.44 & 5.45]

$$k^R(t, t') \equiv k^\delta(t)\,\delta(t - t') + \theta(t - t')\big[k^{>}(t, t') + k^{<}(t, t')\big]\,, \tag{1.60}$$

$$k^A(t, t') \equiv k^\delta(t)\,\delta(t - t') - \theta(t' - t)\big[k^{>}(t, t') + k^{<}(t, t')\big]\,. \tag{1.61}$$

Note that, insofar we only took into consideration the horizontal branches of the contour and ignored the vertical branch. The correlators between a horizontal and the vertical branches are represented by the *left* ($\lceil$) and *right* ($\rceil$) correlators, defined as [20, eq. 5.39]

$$k^{\lceil}(\tau, t) \equiv k(t_0 - i\tau, t_\pm) \quad ; \quad k^{\rceil}(t, \tau) \equiv k(t_\pm, t_0 - i\tau)\,. \tag{1.62}$$

Finally, the correlators between points in the vertical branch, the *Matsubara* correlators,

$$\begin{aligned} k^M(\tau, \tau') \equiv k(t_0 - i\tau, t_0 - i\tau') &= \delta(t_0 - i\tau, t_0 - i\tau')k^\delta(t_0 - i\tau) + k_r^M(\tau, \tau') \\ &= \theta(\tau - \tau')k^{>}(t_0 - i\tau, t_0 - i\tau') + \theta(\tau' - \tau)k^{<}(t_0 - i\tau, t_0 - i\tau') \\ &+ \delta(t_0 - i\tau, t_0 - i\tau')k^\delta(t_0 - i\tau)\,, \end{aligned} \tag{1.63}$$

where $k_r^M(\tau, \tau')$ is defined as the regular part of the correlator [20, eq. 5.40].

Thus far this subsection has focussed on the formal definition of correlators and its basic properties. We now address two operations between different correlators, convolution integrals and products.

Convolution integrals along the contour The convolution integral in the KS follows the standard definition of a convolution integral in any contour. The standard notation for this section $c(z,z') = \int_\gamma \mathrm{d}\bar{z}\, a(z,\bar{z})\, b(\bar{z},z')$ [20, eq. 5.42]. Let us consider the lesser component of correlator $c(z,z')$, from equation 1.58, it reads $c^<(t,t') = c(t_-,t'_+) = \int_\gamma \mathrm{d}\bar{z}\, a(t_-,\bar{z})\, b(\bar{z},t'_+)$. The respective convolution integral reads

$$
\begin{aligned}
c^<(t,t') = c(t_-,t'_+) = \int_\gamma \mathrm{d}\bar{z} \Big[& a^\delta(t_-)\delta(t_-,\bar{z}) + \theta(t_-,\bar{z}) a^>(t_-,\bar{z}) + \theta(\bar{z},t_-) a^<(t_-,\bar{z}) \Big] \times \\
& \times \Big[b^\delta(\bar{z})\delta(\bar{z},t'_+)\theta(\bar{z},t'_+) b^>(\bar{z},t'_+) + \theta(t'_+,\bar{z}) b^<(\bar{z},t'_+) \Big] \\
= \int_\gamma \mathrm{d}\bar{z} \Bigg(& a^\delta(t_-)\delta(t_-,\bar{z})\; b^\delta(\bar{z})\delta(\bar{z},t'_+) + a^\delta(t_-)\delta(t_-,\bar{z}) \Big[\theta(\bar{z},t'_+) b^>(\bar{z},t'_+) \\
& + \theta(t'_+,\bar{z}) b^<(\bar{z},t'_+) \Big] \Big[\theta(t_-,\bar{z}) a^>(t_-,\bar{z}) + \theta(\bar{z},t_-) a^<(t,\bar{z}) \Big] b^\delta(\bar{z})\delta(\bar{z},t'_+) \\
& + \theta(t_-,\bar{z}) a^>(t_-,\bar{z})\; \theta(\bar{z},t'_+) b^>(\bar{z},t'_+) + \theta(t_-,\bar{z}) a^>(t_-,\bar{z})\; \theta(t'_+,\bar{z}) b^<(\bar{z},t'_+) \\
& + \theta(\bar{z},t_-) a^<(t_-,\bar{z})\; \theta(\bar{z},t'_+) b^>(\bar{z},t'_+) + \theta(\bar{z},t_-) a^<(t_-,\bar{z})\; \theta(t'_+,\bar{z}) b^<(\bar{z},t'_+) \Bigg).
\end{aligned}
\tag{1.64a}
$$

From the definitions of the Dirac delta and Heaviside step functions, we observe that $\delta(t_-,t'_+) = 0$, $\theta(t_-,t'_+) = 0$, $\theta(t'_+,t_-) = 1$ and $\theta(t_-,\bar{z})\theta(\bar{z},,t'_+) = 0$. The remaining Heaviside functions simply restrict the integration limits. Hence, the convolution integral reads

$$
\begin{aligned}
c^<(t,t') = {} & a^\delta(t_-)\; \delta(t_-,t'_+) b^\delta(t'_+) + a^\delta(t_-) \Big[\theta(t_-,t'_+) b^>(t_-,t'_+) + \theta(t'_+,t_-) b^<(t_-,t'_+) \Big] \\
& + \Big[\theta(t_-,t'_+) a^>(t_-,t'_+) + \theta(t'_+,t_-) a^<(t,t'_+) \Big] b^\delta(t'_+) \\
& + \int_\gamma \mathrm{d}\bar{z}\, \theta(t_-,t'_+)\; a^>(t_-,\bar{z}) b^>(\bar{z},t'_+) + \int_{t_0}^{t_-} \mathrm{d}\bar{z}\, a^>(t_-,\bar{z}) b^<(\bar{z},t'_+) \\
& + \int_{t'_+}^{t_0-i\beta} \mathrm{d}\bar{z}\, a^<(t_-,\bar{z}) b^>(\bar{z},t'_+) + \int_{t_-}^{t'_+} \mathrm{d}\bar{z}\, a^<(t_-,\bar{z}) b^<(\bar{z},t'_+)\,.
\end{aligned}
\tag{1.64b}
$$

Furthermore, the integration limits also provide useful information, for ease of reference we itemize this discussion by integration limit

- $\bar{z} \in [t_0,t_-]$ — the contour ordering imposes $a^>(t_-,\bar{z}) = a^>(t,\bar{t})$; $b^<(\bar{z},t'_+) = b^<(\bar{t},t')$ and consequently $\int_{t_0}^{t_-} \mathrm{d}\bar{z}\; a^>(t_-,\bar{z}) b^<(\bar{z},t'_+) = \int_{t_0}^{t} \mathrm{d}\bar{t}\; a^>(t,\bar{t}) b^<(\bar{t},t')$;
- $\bar{z} \in [t'_+,t_0-i\beta]$ — is split to match the contour segments γ^+ and γ^M, respectively $\bar{z} \in [t',t_0]$ and $\bar{z} \in [t_0,t_0-i\beta]$. The former imposes $\bar{z} \to \bar{t}$, hence $a^<(t,\bar{z}) = a^<(t,\bar{t})$ and $b^>(\bar{z},t'_+)$, whereas the latter $\bar{z} \to -i\bar{\tau}$ resulting in $a^<(t,\bar{z}) = a^<(t,t_0 - i\bar{t}) =$

$a^{\rceil}(t,\bar{\tau})$, $b^{>}(\bar{z},t') = b^{>}(t_0 - i\bar{\tau},t') = b^{\lceil}(\bar{\tau},t')$. Consequently, the integral containing the vertical branch is split as $\int_{t'_+}^{t_0-i\beta} \mathrm{d}\bar{z}\; a^{<}(t_-,\bar{z}) b^{>}(\bar{z},t'_+) = \int_{t'}^{t_0} \mathrm{d}\bar{t}\; a^{<}(t,\bar{t}) b^{>}(\bar{t},t') - i\int_0^{\beta} \mathrm{d}\bar{\tau}\; a^{\rceil}(t,\bar{\tau}) b^{\lceil}(\bar{\tau},t')$;

- $\bar{z} \in [t_-, t'_+]$ — is split into two integrals, one on the "later" (γ^+) and another in the "earlier" (γ^-) segments of the contour, *i.e.* $\int_{t_-}^{t'_+} \mathrm{d}\bar{z} \to \int_{t_0}^{t'_+} \mathrm{d}\bar{t} - \int_{t_0}^{t_-} \mathrm{d}\bar{t}$. The integration range in the former imposes $a^{<}(t_-,\bar{z}) = a^{<}(t,\bar{t})$ and $b^{<}(\bar{z},t'_+) = b^{<}(\bar{t},t')$. The latter imposes $a^{<}(t_-,\bar{z}) = a^{<}(t,\bar{t})$ and $b^{<}(\bar{z},t'_+) = b^{<}(\bar{t},t')$. Thus, we are able to separate the contour integral into two branches in real time $\int_{t_-}^{t'_+} \mathrm{d}\bar{z}\, a^{<}(t_-,\bar{z}) b^{<}(\bar{z},t'_+) = \left(\int_{t_0}^{t'} - \int_{t_0}^{t}\right) \mathrm{d}\bar{t}\; a^{<}(t,\bar{t}) b^{<}(\bar{t},t')$.

With these results in mind, the correlator reads

$$\begin{aligned} c^{<}(t,t') = a^{\delta}(t) b^{<}(t,t') + \int_{t_0}^{t} \mathrm{d}\bar{t}\, a^{>}(t,\bar{t}) b^{<}(\bar{t},t') - \int_{t_0}^{t} \mathrm{d}\bar{t}\, a^{<}(t,\bar{t}) b^{<}(\bar{t},t') + a^{<}(t,t') b^{\delta}(t') \\ + \int_{t'}^{t_0} \mathrm{d}\bar{t}\, a^{<}(t,\bar{t}) b^{>}(\bar{t},t') + \int_{t_0}^{t'} \mathrm{d}\bar{t}\, a^{<}(t,\bar{t}) b^{<}(\bar{t},t') - i\int_0^{\beta} \mathrm{d}\bar{\tau}\, a^{\rceil}(t,\bar{\tau}) b^{\lceil}(\bar{\tau},t')\,. \end{aligned} \tag{1.64c}$$

Using Dirac delta functions, the "singular" parts can be transformed into integrands over a region compatible with the remaining integrals. Furthermore, introducing Heaviside step functions allows the integration limits t and t' to be taken to $+\infty$. For the particular case of a correlation computed at times $t = T$ and $t' = T + \epsilon$, such that $\epsilon \to 0^{\pm}$, the contour can be shrunken by turning back at $z = T$ in opposition to the initial contour loop time at $z = +\infty$, see figure 1.4. In order to keep the analysis as general as possible, we continue the evaluation of the correlators along the complete exact contour. Hence, the lesser component of the correlator $c(z,z')$ reads

$$\begin{aligned} c^{<}(t,t') &= \int_{t_0}^{\infty} \mathrm{d}\bar{t} \Big(a^{\delta}(t)\delta(t-\bar{t}) + \theta(t-\bar{t}) \Big[a^{>}(t,\bar{t}) - a^{<}(t,\bar{t}) \Big] \Big) b^{<}(\bar{t},t') \\ &\quad + \int_{t_0}^{\infty} \mathrm{d}\bar{t}\, a^{<}(t,\bar{t}) \Big(b^{\delta}(\bar{t})\delta(\bar{t}-t') - \theta(t'-\bar{t}) \Big[b^{>}(\bar{t},t') - b^{<}(\bar{t},t') \Big] \Big) \\ &\quad - i\int_0^{\beta} \mathrm{d}\bar{\tau}\, a^{\rceil}(t,\bar{\tau}) b^{\lceil}(\bar{\tau},t') \\ &= \int_{t_0}^{\infty} \mathrm{d}\bar{t} \Big[a^{R}(t,\bar{t}) b^{<}(\bar{t},t') + a^{<}(t,\bar{t}) b^{A}(\bar{t},t') \Big] - i\int_0^{\beta} \mathrm{d}\bar{\tau}\, a^{\rceil}(t,\bar{\tau}) b^{\lceil}(\bar{\tau},t') \\ &= a^{<}(t) \cdot b^{A}(t') + a^{R}(t) \cdot b^{<}(t') + a^{\rceil}(t) \star b^{\lceil}(t')\,. \end{aligned} \tag{1.64d}$$

(a) Full exact contour (b) Shrunken exact contour

Figure 1.4: The complete and shrunken versions of the exact contour.

It should be noted that this result explicit demonstrates the causality of the lesser GF, as each integral in real time depends exclusively on times earlier than t. In the *l.h.s.* of the previous equation, we introduce the following $\cdot$ (dot) and $\star$ (star) notation for convolutions in the contour, *i.e.*

$$a(t)\cdot b(t') \equiv \int_{t_0}^{\infty} \mathrm{d}\bar{t}\, a(t,\bar{t})\, b(\bar{t},t') \quad ; \quad a(t)\star b(t') \equiv \int_{0}^{\beta} \mathrm{d}\bar{\tau}\, a(t,\bar{\tau})\, b(\bar{\tau},t')\,; \tag{1.65}$$

where the former $(\cdot)$ represents the convolution integral along the real time and latter $(\star)$ represents the convolution integral in the imaginary time. For the sake of clarity, the explicit dependency on non-integrated variables, *i.e.* either t, t' or τ, τ' may be suppressed. Equation 1.64 is one of several identities known as LR or *analytic continuations* for convolution integrals and products of correlators. Since we are interested in computing the lesser component of a GF, we only show the relevant LR for calculation of the desired correlator, see table 5.1 from ref. [20] for a complete and clear collection of the LR. The retarded correlator reads

$$\begin{aligned} c^R(t,t') = a^R\cdot b^R = \int_{t_0}^{\infty}\mathrm{d}\bar{t}\Big(a^\delta(t)\delta(t-\bar{t}) + \theta(t-\bar{t})\Big[a^>(t,\bar{t}) - a^<(t,\bar{t})\Big]\Big)\times \\ \times\Big(b^\delta(\bar{t})\delta(\bar{t}-t') + \theta(\bar{t}-t')\Big[b^>(\bar{t},t') - b^<(\bar{t},t')\Big]\Big)\,. \end{aligned} \tag{1.66}$$

The left and Matsubara components read

$$\begin{aligned} c^{\rceil}(t,t') &= a^R\cdot b^A + a^M\star b^{\rceil} = \\ &= \int_{t_0}^{\infty}\mathrm{d}\bar{t}\Big(a^\delta(t)\delta(t-\bar{t}) + \theta(t-\bar{t})\Big[k^>(t,\bar{t}) - k^<(t,\bar{t})\Big]\Big) b(\bar{t}, t_0 - i\tau') \\ &+ \int_0^{\beta}\mathrm{d}\bar{\tau}\, a(t, t_0 - i\bar{\tau})\Big[\delta(t_0 - i\bar{\tau}, t_0 - i\tau')b^\delta(t_0 - i\bar{\tau}) + b_r^M(\bar{\tau},\tau')\Big]\,, \\ c^M(\tau,\tau') &= a^M\star b^M = \int_0^{\beta}\mathrm{d}\bar{\tau}\Big[\delta(t_0 - i\tau, t_0 - i\bar{\tau})a^\delta(t_0 - i\tau) + a_r^M(\tau,\bar{\tau})\Big]\times \end{aligned} \tag{1.67}$$

$$\times \left[\delta(t_0 - i\bar{\tau}, t_0 - i\tau')b^{\delta}(t_0 - i\bar{\tau}) + b_r^M(\bar{\tau}, \tau')\right]. \tag{1.68}$$

Below we list the so-called LR for convolution integrals (in real and imaginary time) as defined at the beginning of this sub-subsection [20, table 5.1]

$$c^{\lessgtr}(t,t') = a^{\lessgtr}(t)\cdot b^{A}(t') + a^{R}(t)\cdot b^{\lessgtr}(t') + a^{\rceil}(t)\star b^{\lceil}(t')\,, \tag{1.69a}$$

$$c^{\mathrm{A/R}}(t,t') = a^{\mathrm{A/R}}(t)\cdot b^{\mathrm{A/R}}(t,t')\,, \tag{1.69b}$$

$$c^{\rceil}(t,\tau) = a^{R}(t)\cdot b^{\rceil}(t,\tau) + a^{\rceil}(t)\star b^{M}(t,\tau)\,, \tag{1.69c}$$

$$c^{\lceil}(\tau,t') = a^{\lceil}(t)\cdot b^{A}(t,\tau) + a^{M}(t)\star b^{\lceil}(t,\tau)\,, \tag{1.69d}$$

$$c^{M}(\tau,\tau') = a^{\delta}(\tau)\star b^{M}(\tau,\tau')\,. \tag{1.69e}$$

Convolutions with *singular* functions In addition to the evaluation of convolution between two complete functions in KS, it is important to compute the convolutions between *singular*, $a(z,z') = a^{\delta}(z)\delta(z,z')$, and *normal* $b(z,z')$ functions in KS. Consider once more the convolution integral for a lesser correlator

$$c^{<}(t,t') = c(t_-,t'_+) = \int_{\gamma} \mathrm{d}\bar{z}\, a(t_-,\bar{z})b(\bar{z},t'_+) \int_{\gamma} \mathrm{d}\bar{z}\, a^{\delta}(t_-)\delta(t_-,\bar{z})\Big[b^{\delta}(\bar{z})\delta(\bar{z},t'_+) + \\ + \theta(\bar{z},t'_+)b^{>}(\bar{z},t'_+) + \theta(t'_+,\bar{z})b^{<}(\bar{z},t'_+)\Big]\,. \tag{1.70a}$$

Following the procedure outlined in the derivation of equation 1.64, the evaluation is a straightforward problem and reads $c^{<}(t,t') = a^{\delta}(t)b^{<}(t,t')$. By the same token, convolution integrals with singular functions reduce to products in KS. The most relevant convolutions yield the following products [20, ex. 5.2]

$$c^{\lessgtr}(t,t') = a^{\delta}(t)b^{\lessgtr}(t,t')\,, \tag{1.71a}$$

$$c^{\mathrm{A/R}}(t,t') = a^{\delta}(t)b^{\mathrm{A/R}}(t,t')\,, \tag{1.71b}$$

$$c^{\rceil}(t,\tau) = a^{\delta}(t)b^{\rceil}(t,\tau)\,, \tag{1.71c}$$

$$c^{\lceil}(\tau,t') = a^{\delta}(\tau)b^{\lceil}(\tau,t')\,, \tag{1.71d}$$

$$c^{M}(\tau,\tau') = a^{\delta}(\tau)b^{M}(\tau,\tau')\,. \tag{1.71e}$$

In the subsections that follow, the tools defined here will be used to compute the system's GF and extract relevant information.

1.4.2 Perturbative expansion on the contour

So far this section has focussed on exact evaluation of $n-$particle GFs. Now, we will discuss the evaluation of the PE of GF within the NEF, following closely [20, §5.3] and adapting the PE to single particle interactions.

Consider a $n-$particle GF [20, eq. 5.1 & 4.58]

$$G_n \equiv \frac{1}{i^n} \frac{\mathrm{Tr}\left[\mathcal{T}\{\exp\left[-i\int_\gamma \mathrm{d}\bar{z}\,\hat{H}(\bar{z})\right]\hat{\psi}(1)\ldots\hat{\psi}(n)\hat{\psi}^\dagger(n')\ldots\hat{\psi}^\dagger(1')\}\right]}{\mathrm{Tr}\left[\mathcal{T}\{\exp\left[-i\int_\gamma \mathrm{d}\bar{z}\,\hat{H}(\bar{z})\right]\}\right]}\,, \tag{1.72}$$

where we introduce the shorthand notation $G_n(1,\ldots,n;1',\ldots,n') \equiv G_n$ and the field operators carry no time dependency [20, eq. 4.7]

$$\hat{\psi}(n) = \hat{\psi}(\mathbf{x}_n, z_n = t_\pm) \equiv \hat{\psi}(\mathbf{x}) \quad ; \quad \hat{\psi}^\dagger(n) = \hat{\psi}^\dagger(\mathbf{x}_n, z_n = t_\pm) \equiv \hat{\psi}^\dagger(\mathbf{x}_n)\,. \tag{1.73}$$

We keep the redundant time dependency, because it is useful to map the field operators between Schrödinger's Picture (SP) and HP for the evaluation of Green's operator along the contour. Recall that we define the Green operator with field operators in HP, equation 1.50. Assuming an Hamiltonian separable into a one body Hamiltonian $\hat{H}_0(z)$ and an interacting part $\hat{U}(z)$, the evaluation along the contour γ, see figure 1.3, of the $n-$particle GF reads

$$G_n = \frac{1}{i^n} \frac{\mathrm{Tr}\left[\mathcal{T}\{\exp\left[-i\int_\gamma \mathrm{d}\bar{z}\,\hat{H}_0(\bar{z})\right]\exp\left[-i\int_\gamma \mathrm{d}\bar{z}\,\hat{U}(\bar{z})\right]\hat{\psi}(1)\ldots\hat{\psi}^\dagger(1')\}\right]}{\mathrm{Tr}\left[\mathcal{T}\{\exp\left[-i\int_\gamma \mathrm{d}\bar{z}\,\hat{H}_0(\bar{z})\right]\exp\left[-i\int_\gamma \mathrm{d}\bar{z}\,\hat{U}(\bar{z})\right]\}\right]}\,, \tag{1.74}$$

where $\hat{H}_0^M = H_0(z)$, $\hat{H}(z) = \hat{H}_0(z) + \hat{U}(z)$ and the interaction Hamiltonian is defined as the coupling of an external time-dependent potential, $\hat{U}(\bar{\mathbf{x}}_k, z_k)$, with a single particle Hamiltonian from the unperturbed system

$$\hat{U}(z_i) = \int \mathrm{d}\bar{\mathbf{x}}_k\; \hat{U}(\bar{\mathbf{x}}_k, z_k)\; \hat{\psi}^\dagger(\bar{\mathbf{x}}_k, z_k^+)\hat{\psi}(\bar{\mathbf{x}}_k, z_k) = \int \mathrm{d}\bar{\mathbf{x}}_k\; \hat{U}(k)\; \hat{\psi}^\dagger(k^+)\hat{\psi}(k)\,. \tag{1.75}$$

Selecting any contour depicted in figure 1.3, allows the calculation of the ensemble average to be performed with the Matsubara component of the Hamiltonian $\hat{H}^M(z)$ and

the time evolution depends solely on the interacting part of the Hamiltonian. Hence, the ensemble average along the vertical track of the contour and interaction term read

$$\mathrm{Tr}\left[\mathcal{T}\Big\{\exp\Big[-i\int_\gamma \mathrm{d}\bar{z}\,\hat{H}_0(\bar{z})\Big](\cdots)\Big\}\right] = \langle\mathcal{T}\{(\cdots)\}\rangle_0\,, \tag{1.76}$$

$$\exp\Big[-i\int_\gamma \mathrm{d}\bar{z}\,\hat{U}(\bar{z})\Big] = \sum_{k=0}^{\infty}\frac{(-i)^k}{k!}\int_\gamma \mathrm{d}\bar{z}_1\ldots\mathrm{d}\bar{z}_k\;\hat{U}(\bar{z}_1)\ldots\hat{U}(\bar{z}_k)\,. \tag{1.77}$$

Therefore, we may define a PE for the $n-$particle GF as

$$G_n = \frac{1}{i^n}\frac{\sum_{k=0}^{\infty}\left[(-i)^k/k!\right]\int_\gamma \mathrm{d}\bar{z}_1\ldots\mathrm{d}\bar{z}_k\,\left\langle\mathcal{T}\{\hat{U}(\bar{z}_1)\ldots\hat{U}(\bar{z}_k)\;\hat{\psi}(1)\ldots\hat{\psi}^\dagger(1')\}\right\rangle_0}{\sum_{k=0}^{\infty}\left[(-i)^k/k!\right]\int_\gamma \mathrm{d}\bar{z}_1\ldots\mathrm{d}\bar{z}_k\,\left\langle\mathcal{T}\{\hat{U}(\bar{z}_1)\ldots\hat{U}(\bar{z}_k)\;\}\right\rangle_0}\,, \tag{1.78}$$

analogous to the two-body perturbation case [20, eq. 5.28]. Below, we consider the particular case of a single particle GF $G_1(1;1^+)\equiv G_1(b;a)$. The respective expansion reads

$$\begin{aligned} G_1(b;a) &= \frac{\sum_{k=0}^{\infty}\left[(-i)^{k+1}/k!\right]\int_\gamma \mathrm{d}\bar{z}_1\ldots\mathrm{d}\bar{z}_k\,\left\langle\mathcal{T}\{\hat{U}(\bar{z}_1)\ldots\hat{U}(\bar{z}_k)\;\hat{\psi}(b)\hat{\psi}^\dagger(a)\}\right\rangle_0}{\sum_{k=0}^{\infty}\left[(-i)^k/k!\right]\int_\gamma \mathrm{d}\bar{z}_1\ldots\mathrm{d}\bar{z}_k\,\left\langle\mathcal{T}\{\hat{U}(\bar{z}_1)\ldots\hat{U}(\bar{z}_k)\;\}\right\rangle_0} \\ &= \frac{\sum_{k=0}^{\infty}\left[(-i)^{k+1}/k!\right]\int_\gamma \mathrm{d}\bar{1}\ldots\mathrm{d}\bar{k}\;\hat{U}(\bar{1})\ldots\hat{U}(\bar{k})\,\left\langle\mathcal{T}\{\hat{\psi}^\dagger(1^+)\hat{\psi}(1)\ldots\hat{\psi}(k)\hat{\psi}(b)\hat{\psi}^\dagger(a)\}\right\rangle_0}{\sum_{k=0}^{\infty}\left[(-i)^k/k!\right]\int_\gamma \mathrm{d}1\ldots\mathrm{d}k\;\hat{U}(1)\ldots\hat{U}(k)\,\left\langle\mathcal{T}\{\hat{\psi}^\dagger(1^+)\hat{\psi}(1)\ldots\hat{\psi}^\dagger(k^+)\hat{\psi}(k)\}\right\rangle_0}. \end{aligned} \tag{1.79}$$

Note that in the second line we dropped the contour subscript in the integral, because integration variables $\{\bar{1},\bar{2},\ldots,\bar{k}\}$ represent time and position coordinates, as previously defined. Hence, these integrals span the whole real space and along the time path defined by the contour under consideration. The ensemble averages present in the last result are exclusively dependent on the "non-interacting" part of the Hamiltonian. Hence, taking the non-interacting Hamiltonian in equation 1.72, the respective $k+1=n$-order ensemble average with an $k+1=n$-particle non-interacting GF reads

$$\begin{aligned} \left\langle\mathcal{T}\{\hat{\psi}^\dagger(1^+)\hat{\psi}(1)\ldots\hat{\psi}(n)\}\right\rangle_0 &= \mathrm{Tr}\left[\mathcal{T}\Big\{e^{-i\int_\gamma \mathrm{d}\bar{z}\,\hat{H}_0(\bar{z})}\hat{\psi}^\dagger(1^+)\hat{\psi}(1)\ldots\hat{\psi}^\dagger(n^+)\hat{\psi}(n)\Big\}\right] \\ &= i^n Z_0\;\mathtt{G}_k(1\ldots n;\,1^+\ldots n^+)\,, \end{aligned} \tag{1.80}$$

in addition we introduce the non-interacting grand partition function, which reads $Z_0 = \mathrm{Tr}\left[\mathcal{T}\{\exp\left[-i\int_\gamma \mathrm{d}\bar{z}\,\hat{H}_0\right]\}\right]$. From Martin-Schwinger's hierarchy and Wick's Theorem (WT) [20, §5.1–5.2]a n-particle non-interacting GF is can be expressed as the permanent

(determinant) of single particle non-interacting bosonic (fermionic) GF [20, eq. 5.27]

$$\mathtt{G}_n(1\dots n;\, 1^+\dots n^+) = \begin{vmatrix} \mathtt{G}(1;1^+) & \mathtt{G}(1;2^+) & \cdots & \mathtt{G}(1;k^+) \\ \mathtt{G}(2;1^+) & \mathtt{G}(2;2^+) & \cdots & \mathtt{G}(2;k^+) \\ \vdots & \vdots & \ddots & \vdots \\ \mathtt{G}(k;1^+) & \mathtt{G}(k;2^+) & \cdots & \mathtt{G}(k;k^+) \end{vmatrix}_{\pm}, \tag{1.81}$$

where $\mathtt{G}(b;a)$ is a non-interacting GF, *i.e.* it depends on the Matsubara component of the Hamiltonian $\hat{H}_0^M = H_0(z)$. The object $|A|_\pm = \sum_P (\pm)^P \prod_{i=1}^n A_{iP(i)}$[8] represents a permanent (determinant) for bosons (fermions), *i.e.* $+(-)$, which computes all combinations of free bosonic (fermionic) propagators. Using equations 1.80 and 1.81, the ensemble averages present in the calculation of GFs can be cast into products of non-interacting propagators. First, we consider the ensemble average present in the numerator

$$\begin{aligned} \left\langle \mathcal{T}\{\hat{\psi}^\dagger(1^+)\hat{\psi}(1)\dots\hat{\psi}^\dagger(k^+)\hat{\psi}(k)\ \hat{\psi}(a)\hat{\psi}^\dagger(b)\ \}\right\rangle_0 &= i^{k+1} Z_0\ \mathtt{G}_{k+1}(b\dots k;\, a\dots k^+) \\ &= i^{k+1} Z_0 \begin{vmatrix} \mathtt{G}(b;a) & \mathtt{G}(b;1^+) & \cdots & \mathtt{G}(b;k^+) \\ \mathtt{G}(1;a) & \mathtt{G}(1;1^+) & \cdots & \mathtt{G}(1;k^+) \\ \vdots & \vdots & \ddots & \vdots \\ \mathtt{G}(k;a) & \mathtt{G}(k;1^+) & \cdots & \mathtt{G}(k;k^+) \end{vmatrix}_{\pm}. \end{aligned} \tag{1.82a}$$

Introducing this result in the numerator of equation 1.79, it can be shown that it factorizes into a product of two infinite set of diagrams product between two groups of connected diagrams. The numerator reads

$$\begin{aligned} N &= iZ_0 \sum_{k=0}^{\infty} \left[(-i)^k i^k/k!\right] \int \mathrm{d}1\dots\mathrm{d}k\ \hat{U}(1)\dots\hat{U}(k)\ G_{k+1}(b\dots k;\, a\dots k') \qquad (1.82b) \\ &= iZ_0 \Bigg[\mathtt{G}^<(b;a) + \int \mathrm{d}1\ \hat{U}(1)\,\mathtt{G}(b;1^+)\mathtt{G}(1;a) + \frac{2!}{2!}\int \mathrm{d}1\mathrm{d}2\ \hat{U}(1)\hat{U}(2)\,\mathtt{G}(b;1^+)\mathtt{G}(1;2^+)\mathtt{G}(2;a) \\ &+ \frac{3!}{3!}\int \mathrm{d}1\mathrm{d}2\mathrm{d}3\ \hat{U}(1)\hat{U}(2)\hat{U}(3)\ \mathtt{G}(b;1^+)\mathtt{G}(1;2^+)\mathtt{G}(2;3^+)\mathtt{G}(3;a) + \cdots \Bigg] \times \\ &\times \Bigg[\mathbb{1} + 1! \int \mathrm{d}1\ \hat{U}(1)\ \mathtt{G}(1;1^+) + 2! \int \mathrm{d}1\mathrm{d}2\ \hat{U}(1)\hat{U}(2)\ \mathtt{G}(t;1^+)\mathtt{G}(1;2^+)\mathtt{G}(2;1^+) \\ &+ 3! \int \mathrm{d}1\mathrm{d}2\mathrm{d}3 \hat{U}(1)\hat{U}(2)\hat{U}(3) \Big[\mathtt{G}(1;2^+)\mathtt{G}(2;3^+)\mathtt{G}(3;1^+) + \mathtt{G}(1;2^+)\mathtt{G}(2;1^+)\mathtt{G}(3;3^+) \Big] + \cdots \Bigg], \end{aligned}$$

where the pedantic usage of the canceling factorials has an important significance, it

[8] The notation $A_{iP(i)}$ represents any combination of the indices of matrix A, say $A_{1,1}, A_{1,2}, A_{2,1} \dots A_{n,n}$.

highlights the fact that Topologically Equivalent (TE) diagrams are equivalent [20]. The equivalence between different diagrams can be shown by recalling that the sets of variables and indices $\{1,\dots,k\}$ are internal variables integrated over its complete domain, hence we are free to interchange them. By carefully interchanging variables we can see that for, the class of perturbations under consideration (equation 1.75), there are $k!$ TE at order k in the perturbation. In addition, it is worth mentioning that the first group contains a set of GFs and perturbations propagating from the initial (a) to the final (b) times. In opposition, the second set contains the identity and closed loop diagrams involving internal times of the PEs.

With regards to the denominator, the respective ensemble average reads

$$\left\langle \mathcal{T}\{\hat{\psi}^\dagger(1^+)\hat{\psi}(1)\dots\hat{\psi}^\dagger(k^+)\hat{\psi}(k)\ \}\right\rangle_0 = i^k Z_0 \begin{vmatrix} \mathtt{G}(1;1^+) & \mathtt{G}(1;2^+) & \cdots & \mathtt{G}(1;k^+) \\ \mathtt{G}(2;1^+) & \mathtt{G}(2;2^+) & \cdots & \mathtt{G}(2;k^+) \\ \vdots & \vdots & \ddots & \vdots \\ \mathtt{G}(k;1^+) & \mathtt{G}(k;2^+) & \cdots & \mathtt{G}(k;k^+) \end{vmatrix}_{\pm} . \tag{1.83a}$$

In turn, the denominator can be cast as follows

$$\begin{aligned} D &= iZ_0 \sum_{k=0}^{\infty} \left[(-i)^k i^k/k!\right] \int \mathrm{d}1\dots\mathrm{d}k\ \hat{U}(1)\dots\hat{U}(k)\ G_k(1\dots k;\ 1\dots k') \\ &= iZ_0 \Bigg[1 + 1! \int \mathrm{d}1\ \hat{U}(1)\ \mathtt{G}(1;1^+) + 2! \int \mathrm{d}1\mathrm{d}2\ \hat{U}(1)\hat{U}(2)\ \mathtt{G}(t;1^+)\mathtt{G}(1;2^+)\mathtt{G}(2;1^+) \\ &\quad + 3! \int \mathrm{d}1\mathrm{d}2\mathrm{d}3 \left[\mathtt{G}(1;2^+)\mathtt{G}(2;3^+)\mathtt{G}(3;1^+) + \mathtt{G}(1;2^+)\mathtt{G}(2;1^+)\mathtt{G}(3;3^+)\right] + \cdots \Bigg] \end{aligned} \tag{1.83b}$$

This expansion generates the so-called *vacuum polarization*. Considering the ratio N/D the vacuum polarization cancel out [20, §10.3], simplifying extensively the evaluation of the PE

$$G(b;a) = \sum_{k=0}^{\infty} \int \mathrm{d}1\dots\mathrm{d}k\ \hat{U}(1)\dots\hat{U}(k)\ \bar{\mathtt{G}}_{k+1}(b,\dots,k;a,\dots,k^+), \tag{1.84}$$

where the Connected and Topologically Inequivalent (CTI) terms of non-interacting GF are represented by $\bar{\mathtt{G}}_{k+1}(b,\dots,k;a,\dots,k^+)$. Introducing an expansion of the field operators to one-particle states in the basis of creation/annihilation operators, $d_n^\dagger/\ d_n$, with

coefficients $\varphi_n(\mathbf{x}_k) = \langle \mathbf{x}_k | n \rangle$ and $\varphi_n^*(\mathbf{x}_k) = \langle n | \mathbf{x}_k \rangle$. The field operators read

$$\hat{\psi}(k) = \sum\nolimits_n \varphi_n(\mathbf{x}_k) d_n(z_k) \quad ; \quad \hat{\psi}^\dagger(k) = \sum\nolimits_n \varphi_n^*(\mathbf{x}_k) d_n^\dagger(z_k)\,, \tag{1.85a}$$

and the complementary expansions

$$d_n(z_k) = \int \mathrm{d}\mathbf{x}\; \varphi_n^*(\mathbf{x}_k) \hat{\psi}(k) \quad ; \quad d_n^\dagger(z_k) = \int \mathrm{d}\mathbf{x}\; \varphi_n(\mathbf{x}_k) \hat{\psi}^\dagger(k)\,, \tag{1.85b}$$

For the sake of clarity in the conversion between SP and HP, we keep the time dependency in the field operators, as discussed in 1.73. Taking the external one particle perturbation to be in the form $U(\mathbf{x}, \mathbf{x}'; z) = \langle \mathbf{x} | \hat{u}(z) | \mathbf{x}' \rangle$ and using the previously defined change of basis, it reads

$$\begin{aligned} \hat{U}(z) &= \int \mathrm{d}\mathbf{x}\mathrm{d}\mathbf{x}' \hat{\psi}^\dagger(\mathbf{x}, z^+) U(\mathbf{x}, \mathbf{x}'; z) \hat{\psi}(\mathbf{x}', z) = \int \mathrm{d}\mathbf{x}\mathrm{d}\mathbf{x}'\; \hat{\psi}^\dagger(\mathbf{x}, z^+)\; \langle \mathbf{x} | \hat{u}(z) | \mathbf{x}' \rangle\; \hat{\psi}(\mathbf{x}', z) \\ &= \sum_{\sigma\lambda} u_{\sigma\lambda} \int \mathrm{d}\mathbf{x}\; \varphi_\sigma(\mathbf{x}) \hat{\psi}^\dagger(\mathbf{x}, z^+) \int \mathrm{d}\mathbf{x}'\; \varphi_\lambda^*(\mathbf{x}') \hat{\psi}(\mathbf{x}', z) = \sum_{\sigma\lambda} u_{\sigma\lambda}\; d_\sigma^\dagger(z^+) d_\lambda(z). \end{aligned} \tag{1.86}$$

Representing the field operators in the k-particle GF, equation 1.72, by their representation in the new basis, the GF reads

$$\begin{aligned} G_k &= \sum_{\substack{\sigma_1 \ldots \sigma_k \\ \lambda_1 \ldots \lambda_k}} \frac{\varphi_{\sigma_1} \ldots \varphi_{\sigma_k} \varphi_{\lambda_1}^* \ldots \varphi_{\lambda_k}^*}{i^k} \frac{\mathrm{Tr}\left[\mathcal{T}\{ e^{-i \int_\gamma \mathrm{d}\bar{z}\, \hat{H}(\bar{z})} \hat{d}_{\sigma_1}(z_1) \ldots \hat{d}_{\sigma_k}(z_k) \hat{d}_{\lambda_1}^\dagger(z_k') \ldots \hat{d}_{\lambda_k}^\dagger(z_1') \}\right]}{\mathrm{Tr}\left[\mathcal{T}\{ \exp\left[-i \int_\gamma \mathrm{d}\bar{z}\, \hat{H}(\bar{z}) \right] \}\right]} \\ &= \sum_{\substack{\sigma_1 \ldots \sigma_k \\ \lambda_1 \ldots \lambda_k}} \varphi_{\sigma_1} \ldots \varphi_{\sigma_k} \varphi_{\lambda_1}^* \ldots \varphi_{\lambda_k}^* G^{\sigma_1 \ldots \sigma_k}_{\lambda_1 \ldots \lambda_k}(z_1, \ldots, z_k; z_1', \ldots, z_k')\,, \end{aligned} \tag{1.87}$$

where we used the shorthand notation $G_k \equiv G_k(1, \ldots, k; 1', \ldots, k')$. By the same token, the PE of the one particle GF, equation 1.84, and respective matrix elements read

$$G(b; a) = \sum_{\beta\alpha} \int \mathrm{d}\mathbf{x}_\beta \mathrm{d}\mathbf{x}_\alpha\; \varphi_\beta(\mathbf{x}_b) \varphi_\alpha^*(\mathbf{x}_a)\; G_{\beta\alpha}(z_b; z_a)\,. \tag{1.88}$$

$$\begin{aligned} G_{\beta\alpha}(z_b; z_a) = \sum_{k=0}^{\infty} \int_\gamma \mathrm{d}z_1 \ldots \mathrm{d}z_k \sum_{\substack{\sigma_1 \ldots \sigma_k \\ \lambda_1 \ldots \lambda_k}} u_{\sigma_1\lambda_1}(z_1) \ldots u_{\sigma_k\lambda_k}(z_k) \times \\ \times\; \bar{\mathtt{G}}^{\,\beta\,\sigma_1 \ldots \sigma_k}_{\alpha\,\lambda_1 \ldots \lambda_k}(z_b, z_1, \ldots, z_k; z_a, z_1^+, \ldots, z_k^+)\,. \end{aligned} \tag{1.89}$$

The matrix elements for a $k+1$-particle non-interacting Green's function also obeys

Martin-Schwinger's hierarchy and WT, hence

$$\bar{\mathtt{G}}_{\substack{\beta\,\sigma_1\ldots\sigma_k\\ \alpha\,\lambda_1\ldots\lambda_k}}(z_b,z_1,\ldots,z_k)=\begin{vmatrix} \mathtt{G}_{\beta\alpha}(z_b;z_a) & \mathtt{G}_{\beta\lambda_1}(z_b;z_1^+) & \cdots & \mathtt{G}_{\beta\lambda_k}(z_b;z_k^+)\\ \mathtt{G}_{\sigma_1\alpha}(z_1;z_a) & \mathtt{G}_{\sigma_1\lambda_1}(z_1;z_1^+) & \cdots & \mathtt{G}_{\sigma_1\lambda_k}(z_1;z_k^+)\\ \vdots & \vdots & \ddots & \vdots\\ \mathtt{G}_{\sigma_k\alpha}(z_k;z_a) & \mathtt{G}_{\sigma_k\lambda_1}(z_k;z_1^+) & \cdots & \mathtt{G}_{\sigma_k\lambda_k}(z_k;z_k^+) \end{vmatrix}_{\substack{\pm\,\mathrm{c.}\\ \mathrm{t.\,i.}}}, \tag{1.90}$$

with the notation $\bar{\mathtt{G}}_{\substack{\beta\,\sigma_1\ldots\sigma_k\\ \alpha\,\lambda_1\ldots\lambda_k}}(z_b,z_1,\ldots,z_k)\equiv\bar{\mathtt{G}}_{\substack{\beta\,\sigma_1\ldots\sigma_k\\ \alpha\,\lambda_1\ldots\lambda_k}}(z_b,z_1,\ldots,z_k;z_a,z_1^+,\ldots,z_k^+)$. Both equations 1.84 and 1.89 provide two different definitions for the PE. Each has its particular advantages and disadvantages with respect to the other and we are free to choose the most adequate for a given problem.

Below we compute the first four terms of the PE for the matrix elements of a GF, equation 1.89. The GF is evaluated along the shrunken exact contour, *i.e.* figure 1.4b. Finally, we extract the lesser component of the GF with the of LR, equations 1.69 and 1.71. Before proceeding, let us recall that we are considering an external perturbation with growing adiabatically from $t_0\to-\infty$, *i.e.* $\bar{u}_{\lambda\sigma}(z_1)\equiv u_{\lambda\sigma}(z_1)\exp[\eta z_1]$, where $\eta\to 0^+$.

At zeroth order, the expansion reduces to a single particle non-interacting GFs. The lesser component is extracted straightforwardly as a free particle GF.

$$G^{<,(0)}_{\beta\alpha}(b;a)=\mathtt{G}^{<}_{\beta\alpha}(b;a) \tag{1.91}$$

Proceeding to first order, the PE reads

$$G^{(1)}_{\beta\alpha}(z_b,z_a)=\sum_{\lambda\bar{\lambda}}\lim_{\eta\to0^+}\lim_{t_0\to-\infty}\int_\gamma \mathrm{d}z_1 e^{\eta z_1}u_{\lambda\bar{\lambda}}(z_1)\begin{vmatrix} \mathtt{G}_{\beta\alpha}(z_b;z_a) & \mathtt{G}_{\beta\lambda}(z_b;z_1)\\ \mathtt{G}_{\bar{\lambda}\alpha}(z_1;z_a) & \mathtt{G}_{\bar{\lambda}\lambda}(z_1;z_1^+)\end{vmatrix}_{\substack{\pm\,\mathrm{c.}\\ \mathrm{t.\,i.}}}. \tag{1.92a}$$

The determinant present in the previous equation generates only two terms. The first is a disconnected diagram (cancels out by the factorization of the vacuum polarization) and the second a connected diagram:

$$\begin{vmatrix} \mathtt{G}_{\beta\alpha}(z_b;z_a) & \mathtt{G}_{\beta\lambda}(z_b;z_1)\\ \mathtt{G}_{\bar{\lambda}\alpha}(z_1;z_a) & \mathtt{G}_{\bar{\lambda}\lambda}(z_1;z_1^+)\end{vmatrix}=\underbrace{\mathtt{G}_{\beta\alpha}(z_b;z_a)\mathtt{G}_{\bar{\lambda}\lambda}(z_1;z_1^+)}_{\text{disconnected}}-\mathtt{G}_{\beta\lambda}(z_b;z_1)\mathtt{G}_{\bar{\lambda}\alpha}(z_1;z_a)\,.$$

Therefore, the first order term contains only one contribution arising from the evaluation of the connected term over the exact contour γ (stretched along the real axis such that $t_0 \to -\infty$), $G^{<,(1)}_{\beta\alpha}(z_b; z_a) = \int_\gamma \mathrm{d}z_1\, e^{\eta z_1} \mathtt{G}_{\beta\lambda}(z_b; z_1) u_{\lambda\bar{\lambda}}(z_1) \mathtt{G}_{\bar{\lambda}\alpha}(z_1; z_a)$. The calculation of the lesser component follows the discussed in section §1.4.1, key results are displayed in equation 1.69 and 1.71. By extending the exact contour along the real axis to $t_0 \to -\infty$, the contributions arising from convolutions along the vertical track, γ_M, vanish.

This can be easily verified in the calculation of any LR. In particular, the lesser component of a correlator defined by the convolution of two complete correlators $(a,\ c)$ with a singular function in KS (b) reads

$$\begin{aligned} k^<(t, t^+) = k(z, z^+) &= \int_\gamma \mathrm{d}z_1\, a(z; z_1) \int_\gamma \mathrm{d}\bar{z}_1\, b(z_1, \bar{z}_1) c(\bar{z}_1; z^+) = \int_\gamma \mathrm{d}z_1\, a(z; z_1) g(z_1, z^+) \\ &= \int_{-\infty}^{\infty} \mathrm{d}t_1 \left[a^<(t, t_1) g^A(t_1, t) + a^R(t, t_1) g^<(t_1, t) \right] \\ &= \int_{-\infty}^{\infty} \mathrm{d}t_1 \left[a^<(t, t_1) b^\delta(t_1) c^A(t_1, t) + a^R(t, t_1) b^\delta(t_1) c^<(t_1, t) \right]. \end{aligned}$$

Using the previous result, we can easily evaluate the lesser component of the first order term in the PE

$$\begin{aligned} G^{<,(1)}_{\beta\alpha}(t, t^+) = \lim_{\eta \to 0^+} \sum_{\lambda\bar{\lambda}} \int_{-\infty}^{t} \mathrm{d}t_1\, e^{\eta t_1} \Big[&\mathtt{G}^<_{\beta\lambda}(t, t_1)\ u_{\lambda\bar{\lambda}}(t_1)\ \mathtt{G}^A_{\bar{\lambda}\alpha}(t_1, t^+) + \\ &+ \mathtt{G}^R_{\beta\lambda}(t, t_1)\ u_{\lambda\bar{\lambda}}(t_1)\ \mathtt{G}^<_{\bar{\lambda}\alpha}(t_1, t^+) \Big]. \end{aligned} \tag{1.92b}$$

Proceeding to higher orders, the quadratic term in the PE reads

$$\begin{aligned} G^{(2)}_{\beta\alpha}(z_b, z_a) = \lim_{\eta \to 0^+} \lim_{t_0 \to -\infty} \sum_{\lambda\bar{\lambda}} \sum_{\phi\bar{\phi}} \int_\gamma \mathrm{d}z_1 \mathrm{d}z_2\, e^{\eta(z_1 + z_2)}\ u_{\lambda\bar{\lambda}}(z_1) u_{\phi\bar{\phi}}(z_2) \times \\ \times \begin{vmatrix} \mathtt{G}_{\beta\alpha}(z_b; z_a) & \mathtt{G}_{\beta\lambda}(z_b; z_1) & \mathtt{G}_{\beta\phi}(z_b; z_2) \\ \mathtt{G}_{\bar{\lambda}\alpha}(z_1; z_a) & \mathtt{G}_{\bar{\lambda}\lambda}(z_1; z_1^+) & \mathtt{G}_{\bar{\lambda}\phi}(z_1; z_2^+) \\ \mathtt{G}_{\bar{\phi}\alpha}(z_2; z_a) & \mathtt{G}_{\bar{\phi}\lambda}(z_2; z_1^+) & \mathtt{G}_{\bar{\phi}\phi}(z_2; z_2^+) \end{vmatrix}^{\pm \text{c.}}_{\text{t. i.}}, \end{aligned} \tag{1.93a}$$

Due to the nature of the perturbation we are considering, there are only two connected and TE diagrams emerging from the determinant. Without loss of generality, one term reads $\mathtt{G}_{\beta\lambda}(t, t_1)\ \mathtt{G}_{\bar{\lambda}\phi}(t_1, t_2)\ \mathtt{G}_{\bar{\phi}\alpha}(t_2, t^+)$ and the other is computed by permutation of the internal times and indices. Having determined the second order term in PE of GF, we

computed the lesser component using LR. The respective lesser component reads

$$
\begin{aligned}
G^{<,(2)}_{\beta\alpha}(t,t^+) = \lim_{\eta\to 0^+} \sum_{\lambda\bar{\lambda}} \sum_{\phi\bar{\phi}} \int_{-\infty}^{t} \mathrm{d}t_1 \mathrm{d}t_2 \; e^{\eta(t_1+t_2)} \times \\
\Big[\; \mathtt{G}^{<}_{\beta\bar{\lambda}}(t,t_1)\, u_{\lambda\bar{\lambda}}(t_1)\, \mathtt{G}^{A}_{\bar{\lambda}\phi}(t_1,t_2)\, u_{\phi\bar{\phi}}(t_2)\, \mathtt{G}^{A}_{\bar{\phi}\alpha}(t_2,t^+) \\
+ \mathtt{G}^{R}_{\beta\bar{\lambda}}(t,t_1)\, u_{\lambda\bar{\lambda}}(t_1)\, \mathtt{G}^{<}_{\bar{\lambda}\phi}(t_1,t_2)\, u_{\phi\bar{\phi}}(t_2)\, \mathtt{G}^{A}_{\bar{\phi}\alpha}(t_2,t^+) \\
+ \mathtt{G}^{R}_{\beta\bar{\lambda}}(t,t_1)\, u_{\lambda\bar{\lambda}}(t_1)\, \mathtt{G}^{R}_{\bar{\lambda}\phi}(t_1,t_2)\, u_{\phi\bar{\phi}}(t_2)\, \mathtt{G}^{<}_{\bar{\phi}\alpha}(t_2,t^+) \Big] \, .
\end{aligned} \tag{1.93b}
$$

The generalization to third order is trivial and respective lesser component for the matrix elements of GF read

$$
\begin{aligned}
G^{<,(3)}_{\beta\alpha}(t,t^+) = \lim_{\eta\to 0^+} \sum_{\lambda\bar{\lambda}} \sum_{\phi\bar{\phi}} \sum_{\sigma\bar{\sigma}} \int_{-\infty}^{t} \mathrm{d}t_1 \mathrm{d}t_2 \mathrm{d}t_3 \; e^{\eta(t_1+t_2+t_3)} \times \\
\Big[\; \mathtt{G}^{<}_{\beta\bar{\lambda}}(t,t_1)\, u_{\lambda\bar{\lambda}}(t_1)\, \mathtt{G}^{A}_{\bar{\lambda}\phi}(t_1,t_2)\, u_{\phi\bar{\phi}}(t_2)\, \mathtt{G}^{A}_{\bar{\phi}\sigma}(t_2,t_3)\, u_{\sigma\bar{\sigma}}(t_3)\, \mathtt{G}^{A}_{\bar{\sigma}\alpha}(t_3,t^+) \\
+ \mathtt{G}^{R}_{\beta\bar{\lambda}}(t,t_1)\, u_{\lambda\bar{\lambda}}(t_1)\, \mathtt{G}^{<}_{\bar{\lambda}\phi}(t_1,t_2)\, u_{\phi\bar{\phi}}(t_2)\, \mathtt{G}^{A}_{\bar{\phi}\sigma}(t_2,t_3)\, u_{\sigma\bar{\sigma}}(t_3)\, \mathtt{G}^{A}_{\bar{\sigma}\alpha}(t_3,t^+) \\
+ \mathtt{G}^{R}_{\beta\bar{\lambda}}(t,t_1)\, u_{\lambda\bar{\lambda}}(t_1)\, \mathtt{G}^{R}_{\bar{\lambda}\phi}(t_1,t_2)\, u_{\phi\bar{\phi}}(t_2)\, \mathtt{G}^{<}_{\bar{\phi}\sigma}(t_2,t_3)\, u_{\sigma\bar{\sigma}}(t_3)\, \mathtt{G}^{A}_{\bar{\sigma}\alpha}(t_3,t^+) \\
+ \mathtt{G}^{R}_{\beta\bar{\lambda}}(t,t_1)\, u_{\lambda\bar{\lambda}}(t_1)\, \mathtt{G}^{R}_{\bar{\lambda}\phi}(t_1,t_2)\, u_{\phi\bar{\phi}}(t_2)\, \mathtt{G}^{R}_{\bar{\phi}\sigma}(t_2,t_3)\, u_{\sigma\bar{\sigma}}(t_3)\, \mathtt{G}^{<}_{\bar{\sigma}\alpha}(t_3,t^+) \Big] \, .
\end{aligned} \tag{1.94}
$$

Considering non-interacting particles, the lesser and greater components of the GF read

$$
\mathtt{G}^{<}_{\beta\alpha}(t_1,t_2) = \langle\beta|G^{<}(t_1,t_2)|\alpha\rangle = \mp i f_\alpha e^{-i\epsilon_\alpha(t_1-t_2)}\delta_{\beta\alpha} \, , \tag{1.95}
$$

$$
\mathtt{G}^{>}_{\beta\alpha}(t_1,t_2) = \langle\beta|G^{>}(t_1,t_2)|\alpha\rangle = -i \bar{f}_\alpha e^{-i\epsilon_\alpha(t_1-t_2)}\delta_{\beta\alpha} \, , \tag{1.96}
$$

where $\bar{f} = 1 \pm f_\alpha$ and $f_\alpha = f(\epsilon_\alpha) = 1/\big(\exp\big[\beta(\epsilon_\alpha-\mu)\big] \mp 1\big)$ is the equilibrium distribution function at chemical potential μ. Using the lesser and greater components, the retarded and advanced functions are computed from the respective definition for general correlators, *i.e.* equations 1.60 and 1.61, and read [20, eq. 6.50 & 6.51]

$$
\mathtt{G}^{R}_{\beta\alpha}(t_1,t_2) = \quad i\theta(t_1-t_2)e^{-i\epsilon_\alpha(t_1-t_2)}\delta_{\beta\alpha} \, , \tag{1.97}
$$

$$
\mathtt{G}^{A}_{\beta\alpha}(t_1,t_2) = -i\theta(t_2-t_1)e^{-i\epsilon_\alpha(t_1-t_2)}\delta_{\beta\alpha} \, . \tag{1.98}
$$

The Green correlators do not contain a singular component, as this would imply a creation/ annihilation and vice-versa at the exact same moment. Computing the expecta-

tion value for a single particle operator $\hat{O}$, equation 1.52, and introducing the definitions for lesser, retarded and advanced components of non-interacting GF in equations 1.91, 1.92b, 1.93b and 1.94 provides a point of comparison between the response functions obtained in the *standard* equilibrium formalism and in non-equilibrium[9].

The expectation value for operator $\hat{O}$ up to third order in the PE reads

$$\langle \hat{O}^{(0)}(t) \rangle = -i \sum_{\alpha\beta} O_{\alpha\beta} \bar{\mathtt{G}}_{\beta\alpha} = \sum_{\alpha} O_{\alpha\alpha} f_{\alpha} \,, \tag{1.99a}$$

$$\langle \hat{O}^{(1)}(t) \rangle = -i \sum_{\alpha\beta} O_{\alpha\beta}\, e^{-i\epsilon_{\beta\alpha}t}\, (f_{\alpha} - f_{\beta}) \int_{-\infty}^{t} \mathrm{d}t_1 e^{-i(\epsilon_{\alpha\beta}+i\eta)t_1} u_{\beta\alpha}(t_1)\theta[t-t_1] \,. \tag{1.99b}$$

$$\begin{aligned}\langle \hat{O}^{(2)}(t) \rangle = \sum_{\alpha\beta\phi} O_{\alpha\beta}\, e^{-i\epsilon_{\beta\alpha}t} \int_{-\infty}^{t} \mathrm{d}t_1 \mathrm{d}t_2\, e^{-i(\epsilon_{\phi\beta}+i\eta)t_1} e^{-i(\epsilon_{\alpha\phi}+i\eta)t_2} u_{\beta\phi}(t_1)\, u_{\phi\alpha}(t_2) \\ \times \Big[f_{\beta}\, \theta[t^{+}-t_2]\, \theta[t_2-t_1] - f_{\phi}\, \theta[t-t_1]\, \theta[t^{+}-t_2] + f_{\alpha}\, \theta[t-t_1]\, \theta[t_1-t_2] \Big],\end{aligned} \tag{1.99c}$$

$$\begin{aligned}\langle \hat{O}^{(3)}(t) \rangle = i \sum_{\alpha\beta\phi\lambda} O_{\alpha\beta}\, e^{-i\epsilon_{\beta\alpha}t} \int_{-\infty}^{t} \mathrm{d}t_1 \mathrm{d}t_2 \mathrm{d}t_3\, e^{-i(\epsilon_{\phi\beta}+i\eta)t_1} e^{-i(\epsilon_{\lambda\phi}+i\eta)t_2} e^{-i(\epsilon_{\alpha\lambda}+i\eta)t_3}\, u_{\beta\phi}(t_1) \\ \times u_{\phi\lambda}(t_2) u_{\lambda\alpha}(t_3) \Big[f_{\beta}\, \theta[t^{+}-t_3]\, \theta[t_3-t_2]\, \theta[t_2-t_1] - f_{\phi}\, \theta[t-t_1]\, \theta[t^{+}-t_3]\, \theta[t_3-t_2] \\ + f_{\lambda}\, \theta[t-t_1]\, \theta[t_1-t_2]\, \theta[t^{+}-t_3] - f_{\alpha}\, \theta[t-t_1]\, \theta[t_1-t_2]\, \theta[t_2-t_3] \Big] .\end{aligned} \tag{1.99d}$$

The previous result defines the general response of an observable to an external perturbation.

1.5 Alternative parametrizations of the coupling with radiation

In the previous section we presented the general result for the PE of a given observable, equations 1.99. Beyond the first order, the results computed in the NEF, equations 1.99, and the results from the "standard" response formalism, equation 1.20, may appear at first glance to be different. But a quick quick inspection of the integrals and respective limits shows that the integration can be converted from one to the other and vice-versa.

Since the general results from the NEF can be used to compute the desired response function with respect to an arbitrary perturbation, it can be used to compute the response considering the minimal coupling, $\mathbf{j} \cdot \mathbf{A}$ and compare it to the respective results

[9] Given the fact that in the NEF we consider an alternative approach to the time ordering of operators, it is paramount to verify the consistency this formalism with the *standard* recursive integration of the DM. The consistency can be checked by verifying that equations 1.20 and 1.99 define the same quantity

computed with the direct coupling, $\mathbf{r}\cdot\mathbf{E}$. Thus providing a comparison test between the so-called velocity and length gauges.

To compute the response in the velocity gauge, we consider a perturbation coupling the current density operator to the electromagnetic vector potential, *i.e.* $u_{\alpha\beta}(t) = -q\,\mathbf{v}_{\alpha\beta}\cdot\mathbf{A}(t) = -q\sum_{j,\omega_o} v^j_{\alpha\beta}A^j_{\omega_o}\exp[-i\omega_o t]/2$, where the details of the parametrization of the electromagnetic field have been discussed in §1.1, equation 1.2. Under the influence of such perturbation, the linear and quadratic contributions to the current read

$$\tilde{J}^{(1)}_\lambda(t) = \frac{igq^2}{2L^D}\sum_{\mathbf{k}}\sum_{mn}\frac{f_{mn}v^\lambda_{nm}v^\alpha_{mn}\,E^\alpha_{\omega_1}}{\hbar\omega_1+\epsilon_{mn}+i\Gamma}\,\frac{e^{-i\omega_1 t}}{\omega_1}\,, \tag{1.100a}$$

$$\tilde{J}^{(2)}_\lambda(t) = \frac{-gq^3\hbar}{4L^D}\sum_{\mathbf{k}}\sum_{lmn}\frac{v^\lambda_{nl}v^\beta_{lm}v^\alpha_{mn}\,E^\beta_{\omega_1}E^\alpha_{\omega_2}}{\hbar(\omega_1+\omega_2)+\epsilon_{mn}+2i\Gamma}\left[\frac{f_{nl}}{\hbar\omega_1+\epsilon_{ln}+i\Gamma}\right.$$
$$\left.-\frac{f_{lm}}{\hbar\omega_2+\epsilon_{ml}+i\Gamma}\right]\frac{e^{-i(\omega_1+\omega_2)t}}{\omega_1\omega_2}\,, \tag{1.100b}$$

where the $\tilde{J}$ is used to distinguish from the results computed in the length gauge, equation 1.42b.

The compatibility at linear order has been discussed in the literature [10] and has been identified in §1.3.1, equation 1.40b. Proceeding to second order and decomposing the previous result according to the type of transitions, we can identify four terms analogous to equations 1.42b.

Considering the exclusively interband term, $\beta\neq\lambda\neq\alpha$, we verify that this result is consistent with the respective component computed in the length gauge. The factor of $1/\omega_1\omega_2 \to 1/\epsilon_{ml}\epsilon_{ln}$ is expected and arises for two reasons. First, the calculation in length gauge requires the conversion of position to velocity matrix elements, $\mathcal{A}^\alpha_{mn} = iv^\alpha_{mn}/\omega_{mn}$. Second, the conversion of the components of the electromagnetic vector potential to electric field, $A^\alpha_{\omega_o} = iE^\alpha_{\omega_o}/\omega_o$, when computing the response in the velocity gauge. Regarding terms involving mixed transitions, *i.e.* $\beta=\lambda\neq\alpha$ and $\beta\neq\lambda=\alpha$, the direct comparison of the gauge is not trivial. This stems from the fact that the intraband matrix element in the length gauge contains a derivative (gradient in reciprocal space) in its definition. To circumvent the limitations associated with the direct comparison, we compare the symmetry properties of each element, particularly the parity of the integrands. Since all denominators are functions of the energy dispersion and external parameters, such as the frequency of the external field, it can be shown that these are

even functions in the reciprocal space. Hence, the parity is controlled by the matrix elements present in the numerator of the integrands. In the velocity gauge, the matrix elements read $v^i_{\alpha\beta}v^j_{\beta\alpha}v^k_{\alpha\alpha}$. For the sake of brevity, we consider the presence of a symmetry capable of reducing the independent tensor elements down to the diagonal elements $i = j = k$[10]. For instance, the three-fold symmetry present in honeycomb lattice satisfies this condition, by imposing $-t_{222} = t_{211} = t_{121} = t_{112}$. In such conditions, it is trivial to show that the integrand present in the mixed inter/intraband is an odd function in the reciprocal space, $|v^i_{\alpha\beta}|^2 v^i_{\alpha\alpha}$. Hence, the respective integral over the Brillouin zone (BZ) vanishes. Performing the equivalent analysis in the results computed in the length gauge, particularly in equation 1.44b, we verify that this term does not vanish due to parity symmetry. Hence, it can generate a finite contribution to the response. Finally, with respect to purely intraband terms, it can be shown that the results computed in both gauges lead to odd integrands, with vanishing integrals.

This brief analysis highlights a difference between the results computed in the velocity and length gauge. In the velocity gauge, only exclusively interband processes contribute for the second order response, whereas the response function computed in the length gauge can have finite contributions from mixed inter/ intraband processes. In §3.3 we compute the photocurrent response in monolayer hBN and "gapped" graphene. In both cases, the photocurrent is finite and arises entirely from one of the mixed inter/ intraband processes. Furthermore, in §3.4 we show that, even in a system with more than two bands, the mixed inter/ intraband process is dominant.

[10]The parity of the integrands is not a function of the underlying lattice symmetry. The lattice symmetry is introduced solely to reduce the complexity of the analysis and by no means determines this property.

Chapter 2

Optical dichroism in graphene nanoribbons

In this chapter, we calculate the OC in GNRs, particularly the dichroic absorption in the THz regime. Furthermore we propose a method to tune and enhance it. The calculation of the conductivity follows the standard Kubo formalism at finite temperature and the details of the calculation was published in [33].

2.1 Context

The different absorption of light as a function of the direction of the incident light, *i.e.* the polarization state of light, is known as dichroism. As a consequence of this effect, the plane of polarization of light, can be rotated simply be transmission through the material [34]. This effect is used in several optical instruments, such as wave retarders, polarisers, etc. Optical element such as this are essential for photonics and telecommunications. Also, dichroism is very important for several other fields, such as life sciences and chemistry, for substance characterization.

Among the several types of polarisers, the most common textbook example is a set of metallic wires aligned parellelly. This type of polariser is most effective if the wavelength of the impinging radiation (normal to plane of the wires and unpolarised) is much larger than the wire separation [35]. Furthermore, the polarization plane of the transmitted radiation is perpendicular to the wire direction. Such device is a good example of engineered geometrical anisotropy to induce dichroism. In section §2.2 we

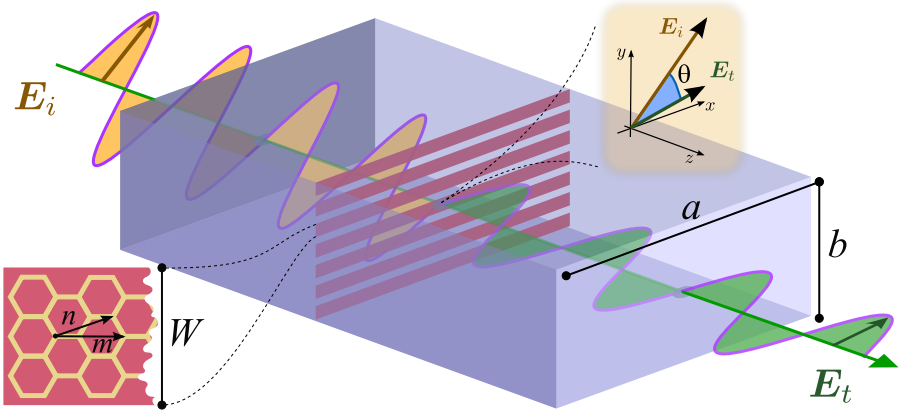

Figure 2.1: Illustration of the proposed device design. This device consists on a set of parallelly aligned GNRs in a plane normal to the incident wave. The array of ribbons can either be in vacuum, or in the interface of two different dielectric media. On top of all this, such device can be inside a waveguide of cross section $a \times b$. On the one hand, a plane linearly polarized incident wave, the plane of polarization is rotated upon transmission of the GNRs, by an angle θ. On the other hand, unpolarised incident wave will emerge partially polarized (linear polarization) upon transmission.

show that GNRs, the systems containing parallelly aligned GNRs can be used as polarizing elements. This property of GNRs is a consequence of several converging key properties. First, the nearly constant optical absorption of pristine graphene across a very large band of the spectrum [36, 37], ranging from the THz to the near ultraviolet. This uncommon property paves the way for exploration of optical response to engineer optical elements that can work consistently on such a broad frequency range. In telecommunications, particularly in photonic devices, elements with a large broadband, such as polarisers can be very important [38]. Second, in graphene optical absorption can be tuned with ease by simply varying the Fermi level, *i.e.* the charge carrier density [39]. Third, recent works have demonstrated that, thanks to the remarkable stiffness of the honeycomb lattice crystal lattice, gratings of the order of 10 nm can be produced in graphene [40]). In figure 2.1 we depict the design of such a system. Fourth, due to its atomic thickness, *i.e.* no bulk, and metallic characteristics graphene, Surface Plasmon-Polaritons (SPPs) are likely to add new features to the optical absorption of graphene, hence increasing the possibility of optical applications [41]. Finally, graphene despite having a very high transparency, $\sim 97.7\%$, due to its atomic thickness, is able to induce strong optical absorption along the confined direction (in ribbons). Yet, at the same time maintaining a rather large transmissivity and thus minimizing loss.

2.2 Anisotropic Optical Absorption

The study of optical devices starts with the analysis of intrinsic optical response of GNRs, to which this review is dedicated. The effect of confinement along the transverse direction of the ribbon, on the optical absorption at low energy is particularly interesting, since in the unconfined system is rather featureless [36]. In contrast, the GNRs present a much richer optical response. In this review we study the optical response of GNRs in a system depicted in figure 2.1. Despite the fact that, graphene ribbons can have two distinct types of edges, armchair or zigzag, the transverse confinement effects are independent of the edge type [33]. Therefore, the effects of confinement in the optical absorption can be analysed using either armchair (AC) or zigzag (ZZ) ribbons. With regards to the edges, another important aspect to take into consideration, is edge disorder, namely how significant this should be. This problem is addressed in two distinct steps. First, the frequency-dependent conductivity tensor $\sigma_{ij}(\omega)$ of a pristine AC GNRis computed analytically. Second, the effect of edge disorder is mimicked by performing an average over an ensemble of ribbons of different widths, to obtain the overall response of the system. This technique is based on the assumption that the main contribution to disorder in the optical response is caused by the broadening of quasi 1D electronic bands. Since the quasi 1D electronic bands are a direct consequence of finite width of the ribbon, the fluctuation of this parameter should reproduce the fluctuation due to edge disorder, *i.e.* variation of the width of the ribbon. Also, the current technological limitations prevents the fabrication of a set of ribbons with the exact same width [42] (which would require atomic precision at this scale) therefore the ensemble averaging should account for this variation.

2.2.1 Parametrization of the system

The ribbons can be characterized by either their absolute width W or the number N of dimer rows along the transverse direction. In the particular case of AC ribbons, the relation between these parameters reads $W = \sqrt{3}(N-1)a/2 \simeq 0.12\,N$ nm, where $a \simeq 1.42$ Å represents the C–C distance. Regarding the ensemble average[1], it is assumed that the ribbon widths follow a uniform distribution with a constant standard deviation, such

[1]Ensemble average refers to the calculation of an average optical response, of a ensemble of ribbons with different widths (typically the widths distribution follows a normal/ Gaussian distribution) [33].

that, $\langle N^2 - \langle N \rangle^2 \rangle^{1/2} = 10$. All the discussion presented below will focus in results obtained at room temperature $T = 300\,\mathrm{K}$ and the terms *intra-* or *inter*-band refer to absorption between subbands with the *same* or *opposite* sign of energy, respectively. Finally, the energy scale is defined by the hopping amplitude, so we put $t = 1$ throughout and the results of the OC are scaled to universal conductivity $\sigma_0 = \pi e^2/2h$ of pristine Two Dimensional (2D) graphene at low energies.

Lateral confinement and consequent breaking of translation invariance, reduces the energy spectrum of GNRs from a continuous 2D surface to a set of subbands, which represent an the dispersion of a set of effective 1D modes [33] ℓ ($\ell = 1, 2, \ldots, N$). These modes propagate longitudinally with momentum q: $E_{\ell,q,\lambda} = \lambda t\, \epsilon_{\ell,q}$, where $\lambda = \pm 1$, defines the valence and conduction subbands,

$$\epsilon_{\ell,q} = \sqrt{1 + 4\cos k_\ell \cos(q/2) + 4\cos^2 k_\ell}, \tag{2.1}$$

and $k_\ell = \pi\ell/(N+1)$. As result of the inverted curvature of the valence and conduction bands, the Density of States (DoS) is dominated by Van Hove singularities (VHss)[2] that develop at $q = 0$ in the longitudinal momentum for each subband [44–46]. This very intense and narrow features could yield a strong optical absorption for ideal GNRs, but due to disorder and thermal fluctuations, these are readily smoothed out in real systems.

The OC of GNRs was be calculated using the Kubo formula [33], *i.e.* the linear response computed in either the length or velocity gauges, equations 1.41 and 1.100a, respectively. The OC tensor is computed exactly for armchair GNRs [33] and the finite components read

$$\frac{\Re\,\sigma_{xx}}{\sigma_0} = \mathcal{N}_x \sum_{\ell_0} \delta f_{q_0^x,\ell_0} \frac{\left[\cos\left(\theta_{\ell_0,q_0^x}\right) - \cos\left(\theta_{\ell_0,q_0^x} - q_0^x/2\right)\cos\left(k_{\ell_0}\right)\right]^2}{\sin\left(q_0^x/2\right)\cos\left(k_{\ell_0}\right)}, \tag{2.2a}$$

$$\frac{\Re\,\sigma_{yy}}{\sigma_0} = \mathcal{N}_y \sum_{\ell_1,\ell_2} \sum_{\lambda,\lambda'} \frac{\mathcal{P}_{\ell_1,\ell_2}\, \delta f^{\lambda,\lambda'}_{q_0^y,\ell_1,\ell_2}\, \epsilon_{\ell_1,q_0^y} \epsilon_{\ell_2,q_0^y}}{\sin^2\left[\left(k_{\ell_1} + k_{\ell_2}\right)/2\right] \sin^2\left[\left(k_{\ell_1} - k_{\ell_2}\right)/2\right]} \frac{\sin^2\left(k_{\ell_1}\right)\sin^2\left(k_{\ell_2}\right)}{\left|\sin(q_0^y/2)\right|\hbar\omega}$$

[2] VHS are discontinuities in the energy dispersion, typically quasi divergent (*i.e.* it is always finite, but has a typical exponential decay in around the singularity point). VHss are common features to any perfect crystal, in the case of GNRs, there are two different types of VHss, the VHs of the high symmetry point of the honeycomb lattice and the VHss that appear due to the quantification of wavevector along the finite direction of the GNR. The former is locate at rather uninteresting high energy (at one third of the spectrum range) and is very resistant to any type of disorder, whereas the latter are dispersed over the whole spectrum range and can be easily washed out by disorder. A rigorous definition of VHs can be found in Ashcroft and Mermin[43].

$$\times \frac{1+\lambda\lambda'\cos\left(\theta_{\ell_1,q_0^y}+\theta_{\ell_2,q_0^y}-q_0^y\right)}{\left|\cos\left(k_{\ell_1}\right)\epsilon_{\ell_2,q_0^y}+\lambda\lambda'\cos\left(k_{\ell_2}\right)\epsilon_{\ell_1,q_0^y}\right|}\,, \tag{2.2b}$$

where $\delta f_{q_0^x,\ell_0} = f(E_{\ell_0,q_0^x,-}) - f(E_{\ell_0,q_0^x,+})$ is the difference between the Fermi functions of the valence and conduction bands, $\mathcal{N}_x = 4/3\sqrt{3}(N-1)$, ℓ_0 is set by solutions of $q_0^x = 2\arccos\left[\left(\Omega^2/4 - 1 - 4\cos^2 k_{\ell_0}\right)/4\cos k_{\ell_0}\right] \in \mathbb{R}$ and $\Omega = \hbar\omega/t$. Furthermore, $\mathcal{N}_y = 4/\sqrt{3}(N+1)(N^2-1)$, $\delta f^{\lambda,\lambda'}_{q_0^y,\ell_1,\ell_2} = n_F(E_{\ell_1,q_0^y,\lambda}) - n_F(E_{\ell_2,q_0^y,\lambda'})$, and $\mathcal{P}_{\ell_1,\ell_2} = 1-(-1)^{\ell_1+\ell_2}$ and $q_0^y = 2\arccos\left[(a_2-a_1)Q_b + \Omega^2(b_1+b_2) \pm Q_c\right]/(b_1-b_2)^2 \in \mathbb{R}$ with $Q_c = 2\sqrt{\Omega^4 b_1 b_2 + \Omega^2 Q_b Q_a}$, $Q_b = b_2 - b_1$, $Q_a = b_1 a_2 - b_2 a_1$, $a_i = 1 + 4\cos^2(k_{\ell_i})$ and $b_i = 4\cos(k_{\ell_i})$. The analytic calculation of conductivity tensor elements is reviewed in detail in appendix A.1. In figure 2.2 are shown the averages $\langle\sigma_{xx}\rangle$, equation 2.2a and $\langle\sigma_{yy}\rangle$ [33] for an ensemble with $\langle N\rangle = 150$, and finite chemical potential $\mu = 0.1t$. As a consequence of time reversal symmetry, only the diagonal components of σ_{ij} are non-zero. Translation invariance along the longitudinal direction means that only *inter*-band transitions contribute to $\sigma_{xx}(\omega)$. Consequently, on the one hand $\langle\sigma_{xx}(\omega)\rangle$ reproduces the bulk 2D behaviour, as is clearly seen in the Figure. On the other hand, the $\langle\sigma_{yy}(\omega)\rangle$ shows a intense peak at low energy arising from the *intra*-band contribution. Meanwhile, its *inter*-band contribution yields the bulk 2D behaviour.

2.3 Anisotropic optical properties

To determine the degree of polarization of graphene ribbons is required the knowledge of the transmission amplitudes, which relate the incident and transmitted fields: $t_\alpha(\omega) = E_\alpha^{(t)}/E_\alpha^{(i)}$, $(\alpha = x, y)$. For the system represented in figure 2.1, the transmission amplitude from medium 1 to 2 is defined by

$$t_\alpha(\omega) = \frac{2\,Z^{(2)}}{Z^{(1)} + Z^{(2)}[1 + Z^{(1)}\sigma_{\alpha\alpha}(\omega)]}, \quad (\alpha = x, y), \tag{2.3}$$

where $Z = \sqrt{\mu_0\mu/\epsilon_0\epsilon}$ is the impedance of each medium [34, 47]. Using the transmission amplitudes, one can determine the degree of polarization (for unpolarised light) or the rotation of the plane of polarization (for polarised light), using [47]:

$$\mathcal{P}(\omega) = \frac{|t_x|^2 - |t_y|^2}{|t_x|^2 + |t_y|^2}, \qquad \tan\theta_f = \frac{t_y(\omega)}{t_x(\omega)}\tan\theta_i, \tag{2.4}$$

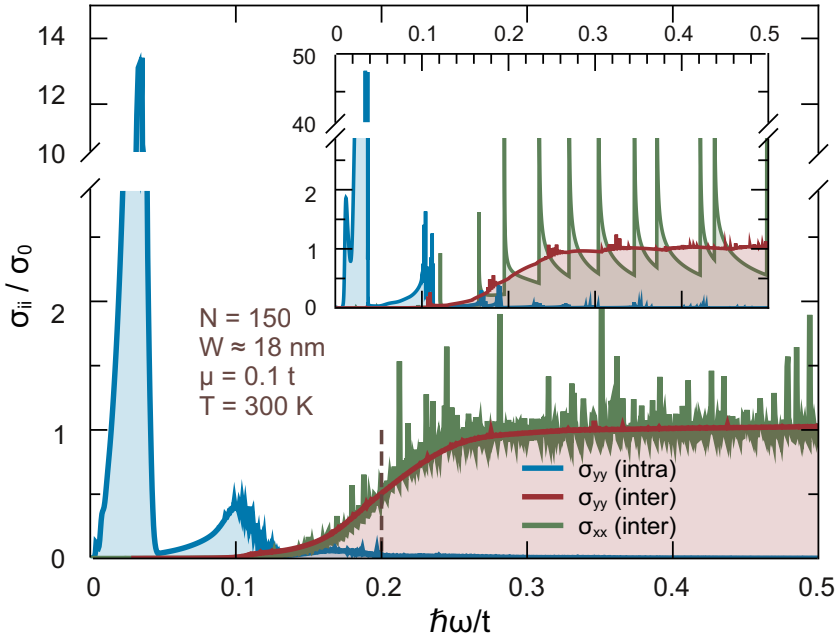

Figure 2.2: The OC of an ensemble of GNRs with average width of $\simeq 18.5\,\mathrm{nm}$, at $T = 300K$ and $\mu = 0.1t$. The "bulk" 2D behaviour is reproduced by the *inter*-band contributions and presents the expected step onset at $\hbar\omega = 2\mu$, broadened by temperature. The *intra*-band channel, opened due the broken translation invariance of the GNRs, presents a very strong response at very low energies. In the inset is show the conductivity of a single GNRof the same width.

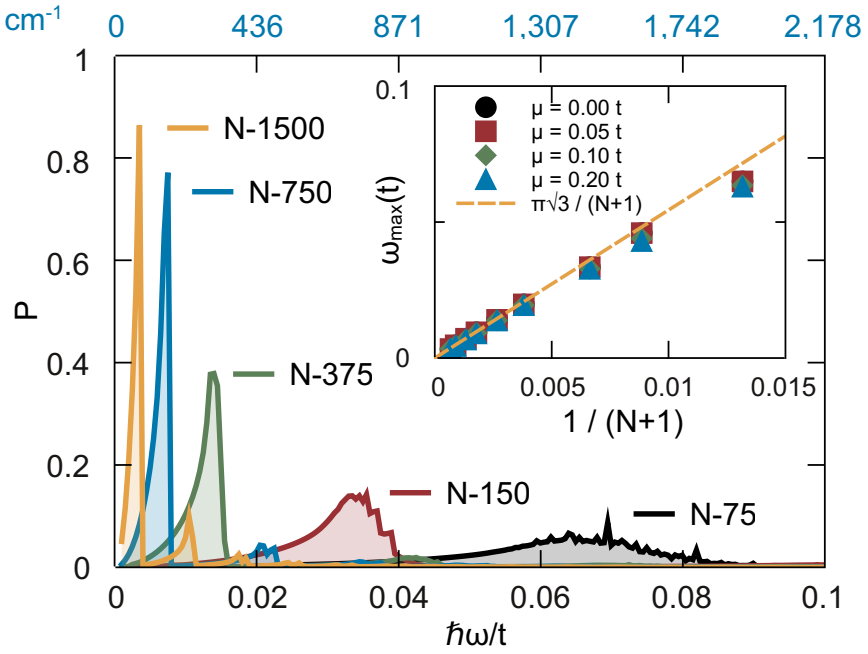

Figure 2.3: Degree of polarization $\mathcal{P}(\omega)$ at very low energies, for ribbons of different average width $\langle W\rangle = \{9, 18, 46, 92, 184\}\,\mathrm{nm}$). The inset shows the position of the most prominent peak in $\sigma^{\mathrm{intra}}_{yy}$ as a function of $\langle N\rangle$ and μ.

The result of $\mathcal{P}(\omega)$ allows one to identify the degree of dichroism, by comparing this value with the unit (perfect polarization). Analytical results for the degree of polarization $\mathcal{P}(\omega)$ are plotted in figure 2.3 under different conditions. These results forecast high polarizabilities for ribbons as narrow as 45 nm wide, which is a remarkable result for polarizability when the atomic thickness of graphene, *i.e.* Carbon atomic radius, is taken into account. Furthermore, the ribbon remains highly transparent along the longitudinal axis of the ribbons, despite near complete suppression of the electric field in the perpendicular direction.

Furthermore, the dichroic behaviour is enhanceable via a metallic waveguide, as depicted in figure 2.1, this effect manifests via the impedance. In metallic waveguides the impedance is renormalized and becomes frequency dependent $Z(\omega)$. Moreover, the propagation of waves in cavities have a low energy threshold, the TE_{mn}[3] characterized by an impedance $Z_{10}(\omega) = Z\,\omega/\sqrt{\omega^2 - \omega_{10}^2}$ [47]. The use of cavities has two useful and appealing characteristics, first, the adjustment of the cavities dimension determines the cut-off frequency for the propagating modes and as result allows one to clearly define a working band. Second, strong amplification of the impedance at frequencies greater and similar than the cut-off frequency $\left(Z_{10}(\omega \gtrsim \omega_{10}) \gg Z\right)$. For example, in figure 2.4 is illustrated the enhancement of the degree of polarization for two ensemble of ribbons. In the second ensemble, is shown that proper setting dimensions of the waveguide, can define a clear band filter for $\mathcal{P}(\omega)$, also one can observe a significant increase when compared with the free propagating wave.

2.3.1 Details and constraints of the anisotropic absorption

Manufacturing a grid of narrow GNRs with consistent and predictable width can be achieved by means of high precision patterning using a He-ion beam microscope in lithography mode [40], or more standard etch masks able to cut down to the 10 nm scale [48]. An alternative to cutting ribbons out of graphene sheets is the recently developed technique of unzipping Carbon NanoTubes (CNTs) [49–51]. Nowadays it is possible to produce batches of CNTs with similar radius [52], and so this would allow for the

[3] For a rectangular cavity, the modes TE_{10} and TE_{01} are linearly polarized along the two directions (a, b). For that reason, we need a linear superposition of the two to generate an arbitrary linear polarization state. The simplest situation is a square waveguide, where the two modes are degenerate, and have the same frequency-dependent impedance [47].

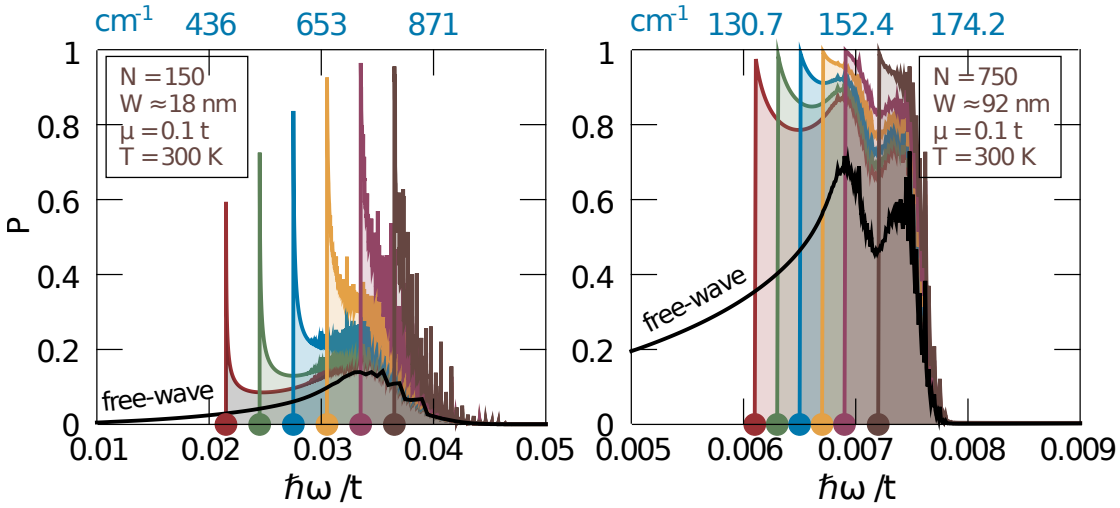

Figure 2.4: The effect of impedance amplification due to a metallic waveguide of square cross-section, in the degree of polarization $\mathcal{P}(\omega)$ for two ensembles of different average widths ($\langle N \rangle = 150, 750$). Both plots show $\mathcal{P}(\omega)$ for an incoming wave composed of a superposition of the degenerate modes of lower energy $\mathrm{TE}_{10,01}$, in vacuum (black) and in waveguides (colours) with different geometries, *i.e.* different cut-off frequency ω_{10}. All cut-off frequencies are represented by a coloured dot at the corresponding energy in the horizontal axis.

production of high quality ribbons without edge disorder. Another alternative, that completely bypasses patterning, consists in inducing effective GNRs by engineering a non-homogeneous distribution of strain in a graphene sheet [53].

The presence of a disorder-induced Drude peak at $\omega \approx 0$ is not expected to significantly change the effect the absorption peaks which occur at finite frequency $\omega = \omega_{\max}$. Normally the width associated with the Drude component is similar to 100 cm^{-1} [54], which when compared with the *intra*-band peaks in figure 2.3, show that these only have a significant overlap for ribbons with average width in excess of 184 nm ($\langle N \rangle \gtrsim 1500$). Moreover, it is expected that the *intra*-band peak magnitude to reach 10-20 times σ_0, which is significantly larger than the typical Drude peak, furthermore the *intra*-band peak magnitude increases with N and easily surpasses $100\sigma_0$. In the Direct Current (DC) regime, the electronic transport is characterized by the famous "universal" minimum-metallic conductivity, which is of the order of σ_0 itself, and sets the scale for the conductivity at moderate electron densities [37, 55]. As discussed before, the response of an array of GNRs with varying widths introduces a significant broadening, which leads one to assume that the dichroism of GNRs should remain strong in real systems with disorder.

One should draw some attention to the fact that, in GNRs the dichroic behaviour is a consequence of spectral properties. And, in graphene the scaling spectral properties

are independent of edge chirality. Therefore, the dichroic behaviour should be independent of the edge orientation and in the case of ensembles, this behaviour should not be affected by the presence of edges with different chirality.

Last, but not least, the dichroic behaviour of GNRs is an intrinsic property of each element in the ensemble, whereas in "normal" grating polarisers, the dichroism arises from the geometry and interference, not being affected by the isotropic metallic wires in the grating. As a result, the polarization of "normal" polariser is perpendicular to the slit or wire direction, whereas in GNRthe polarization is parallel to the ribbon length. The total polarization of an ensemble of GNRs should also have a contribution from the normal polarization, in which SPP physics can have a significant importance [56]. Moreover, one crucial reason for the existence frequency bands of strong SPP absorption (or transmission) in 3D metallic gratings arises from the coupling between those modes at the two opposing surfaces [56]. Being a strict 2D metallic system (in effect a metallic boundary condition for the propagation of electromagnetic waves), SPP cannot decay into the (non-existent) bulk of graphene. This points to the peculiarities of the SPP physics in this 2D Dirac metal [57].

This page was intentionally left blank.

Chapter 3

Photocurrent in 2D crystals

The purpose of this chapter is to review one class of higher order interaction between light and matter, namely the generation of photocurrents in two dimensional materials via Optical Rectification (OR). The focus on the OR stems from a collaboration with an experimental group, who are currently probing photocurrent in graphene based devices. The chapter is divided into four sections, the first contains a short literature review. In the second we provide a detailed phenomenological model for photocurrents, including both elastic and inelastic mechanism, such as photon drag. In addition, this section provides a bridge to connect the experimentally observable quantities and the relevant theoretical estimates. A a brief review of the semiclassical approach to the calculation of photocurrents can be found in the third section. Finally, the fourth section provides a microscopic calculation of the photocurrent, using a PE in the external potential.

Given the interest to a particular family of experiments, our analysis is based on a configuration compatible with these experiments. These experiments follow a relatively standard layout to probe non-linear interaction with light [1, 2, 4, 5, 58, 59]. In figure 3.1, we depict the design of an experimental setup to measure photocurrents, compatible with the experiments carried by our collaborators and the above-mentioned references.

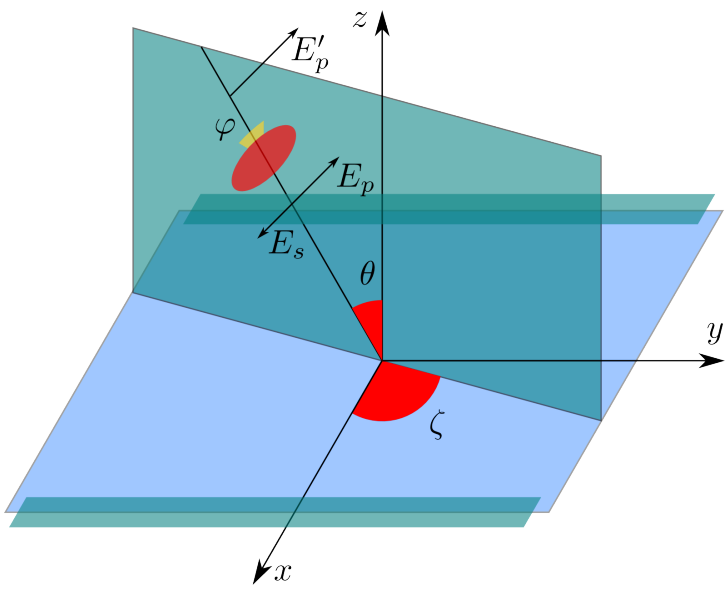

Figure 3.1: Representation of the incident transverse electromagnetic wave on graphene. The incident electromagnetic wave is considered to be p-polarised before reaching the quarter-wave plate, characterised its a wavevector $\mathbf{q}$ and the incidence polar (θ) and azimuthal (ζ) angles. The phase probing is determined by the angle between the "p" polarization plane and the fast axis of the quarter-wave plate, *i.e.* the φ angle. The quarter-wave plate polarises the light beam into a general elliptically polarised state, which can be tuned to linear or circular polarization by varying the angle φ. The light beam is linearly polarised light at $\varphi = n\pi/2 \forall n \in \mathbb{Z}$, *i.e.* $\varphi = \{0, \pm\pi/2, \pm\pi, \pm 3\pi/2, \pm 2\pi/, \ldots\}$ and circularly polarised at $\varphi = (2n+1)\pi/4 \forall n \in \mathbb{Z}$, *i.e.* $\varphi = \{\pm\pi/4, \pm 3\pi/4, \pm 5\pi/4, \pm 7\pi/4, \ldots\}$, see equation 3.4 for details.

3.1 Context

The past decade has seen the rapid development of photocurrents, initially in the 2D electron gas systems, such as GaAs [1, 58, 60–65]. More recently in graphene [2, 4, 59, 66] and topological insulators surface states [5, 67–69]. The phenomenological analysis of photocurrents has been address and discussed extensively in the reports on 2D electron gases and it is transversal to all materials, apart from symmetry details. With regards to a quantitative analysis of the photocurrent, reports published thus addressed this with semiclassical models or microscopic zero temperature formalism. Considering the semiclassical models, [63] considers a generalization of the standard semiclassical model, by means of the anomalous velocity, *i.e.* the Berry curvature term. Other works, for instance [2, 60, 62, 70, 71] solve classical Boltzmann equation to compute the current. In addition, the evaluation of the matrix elements for the relevant transitions is approximated by *Fermi Golden rule* like calculation. With respect to microscopic models for 2D systems, only a few reports have been published, analytic calculations are limited to zero-temperature formalism [72, 73], where as numerical implementations of

NEF probe more realistic system [74]. In addition, the susceptibility of cold semiconductors has been computed in the context of the recursive integration of the DM [10, 21]. Both the recursive integration of the DM and Perturbative Expansion (PE) of a GF, requires the interaction with an external perturbation potential, as discussed in the first chapter.

The following section concerns the qualitative/ phenomenological review of the properties of second order response in 2D crystals, with particular attention to crystals with threefold symmetry.

3.2 Phenomenological considerations

The lowest order non-linear current is proportional to the intensity of the light beam, *i.e.* quadratic in the electric field, which amounts to a second order response function. The photocurrent can be attributed to two distinct mechanisms, elastic interaction with photons (no photon momentum transfer, *i.e.* $\delta\mathbf{k} = 0$) and inelastic interaction commonly known as photon drag ($\delta\mathbf{k} \propto \boldsymbol{\kappa}$). In the non-linear regime several processes may occur in parallel, namely processes of the family of SFG and DFG. A large body of literature has been developed in the field of non-linear optics – references [24, 75] provide a comprehensive review of these phenomena. With respect to the photocurrent, it is a particular case of DFG in which the energy difference between the two photon vanishes. It is frequently identified as Optical Rectification (OR).

For the sake of brevity and clarity, we will restrict our analysis to non-linear response to monochromatic light. Hence, the SFG and DFG reduce to the following particular cases Second Harmonic Generation (SHG) and OR. Phenomenologically, these photocurrents can be represented by [60]

$$j_\alpha^{\mathtt{t}} = j_\alpha + j_\alpha(\boldsymbol{\kappa}) = \sum_{\{\omega_1,\omega_2\}} \left[\chi_{\alpha\beta\gamma} \frac{E^\beta_{\omega_1} E^\gamma_{\omega_2} e^{-i(\omega_1+\omega_2)t}}{4} + \xi_{\alpha\beta\gamma\nu}\, \hat{\kappa}_\beta \frac{E^\gamma_{\omega_1} E^\nu_{\omega_2} e^{-i(\omega_1+\omega_2)t}}{4} \right], \quad (3.1)$$

where the electric field follows the definition introduced in §1.1, equation 1.2. In addition, the vector $j_\alpha^{\mathtt{t}}$ represents the total current, j_α the current generated by the elastic absorption and emission of photons, $j_\alpha(\boldsymbol{\kappa})$ the current arising from the inelastic mechanism, the tensors $\chi_{\alpha\beta\gamma}$ and $\xi_{\alpha\beta\gamma\nu}$ are the non-linear conductivities for elastic and in-

elastic processes respectively. The vector $\hat{\kappa}_\beta = \boldsymbol{\kappa}/\kappa = \mathbf{e}_v$ is the unit vector of photon momentum, see equations (B.2). The above-mentioned definition accommodates a large range of distinct phenomena, including all SFG and DFG processes [24, 75]. The Second Harmonic Generation (SHG) and Optical Rectification (OR) processes are particular cases, defined by $\omega_2 = \omega_1$ and $\omega_2 = -\omega_1$, respectively. Due to the complex nature of the electric field, both tensors contain complex elements to ensure that the current is real. Therefore, one can separate these tensors into a combination of a symmetric (real) and an antisymmetric (purely imaginary) tensor. For the sake of brevity, we only show the separation for the elastic mechanism including the SHG and OR processes.

$$\begin{aligned} j_\alpha = \mathtt{S}_{\alpha\beta\gamma}\left(\frac{E^\beta_{\omega_1}E^\gamma_{\omega_1}e^{-2i\omega_t} + E^\beta_{-\omega_1}E^\gamma_{-\omega_1}e^{2i\omega_t}}{4} + \frac{E^\beta_{\omega_1}E^\gamma_{-\omega_1} + E^\beta_{-\omega_1}E^\gamma_{\omega_1}}{4}\right) \\ + \mathtt{A}_{\alpha\beta\gamma}\left(\frac{E^\beta_{\omega_1}E^\gamma_{\omega_1}e^{-2i\omega_t} - E^\beta_{-\omega_1}E^\gamma_{-\omega_1}e^{2i\omega_t}}{4} + \frac{E^\beta_{\omega_1}E^\gamma_{-\omega_1} - E^\beta_{-\omega_1}E^\gamma_{\omega_1}}{4}\right), \end{aligned} \tag{3.2}$$

where rank three tensors have the following properties $\mathtt{S}^*_{\alpha\beta\gamma} = \mathtt{S}_{\alpha\beta\gamma}$ and $\mathtt{A}^*_{\alpha\beta\gamma} = -\mathtt{A}_{\alpha\beta\gamma}$. Following the procedure outline before, the inelastic photocurrent reads

$$\begin{aligned} j_\alpha(\boldsymbol{\kappa}) = \mathtt{S}_{\alpha\beta\gamma\nu}\,\hat{\kappa}_\beta\left(\frac{E^\gamma_{\omega_1}E^\nu_{\omega_1}e^{-2i\omega_t} + E^\gamma_{-\omega_1}E^\nu_{-\omega_1}e^{2i\omega_t}}{4} + \frac{E^\gamma_{\omega_1}E^\nu_{-\omega_1} + E^\gamma_{-\omega_1}E^\nu_{\omega_1}}{4}\right) \\ + \mathtt{A}_{\alpha\beta\gamma\nu}\,\hat{\kappa}_\beta\left(\frac{E^\gamma_{\omega_1}E^\nu_{\omega_1}e^{-2i\omega_t} - E^\gamma_{-\omega_1}E^\nu_{-\omega_1}e^{2i\omega_t}}{4} + \frac{E^\gamma_{\omega_1}E^\nu_{-\omega_1} - E^\gamma_{-\omega_1}E^\nu_{\omega_1}}{4}\right), \end{aligned} \tag{3.3}$$

where the rank four tensors have the following properties $\mathtt{S}^*_{\alpha\beta\gamma\nu} = \mathtt{S}_{\alpha\beta\gamma\nu}$ and $\mathtt{A}^*_{\alpha\beta\gamma\nu} = -\mathtt{A}_{\alpha\beta\gamma\nu}$.

In order to probe the dependence on light polarization the radiation can transmit through a quarter-wave plate before interacting with the material. The calculation of a final polarization state (transmission through a quarter-wave plate) is most easily computed using Jones calculus [76], for details see §B.1. The standard experimental procedure probes the polarization state of the radiation by measuring the relative angle, φ, between the quarter-wave plate fast axis and polarization direction of initial linearly polarized light. Therefore, for initial p-polarized light, the electric field transmitted by

the quarter-wave plate reads (see equation B.6)[1]

$$\mathbf{E}' = E_0 \begin{pmatrix} s\sin(\zeta) + p\cos(\zeta)\cos(\theta) \\ -s\cos(\zeta) + p\sin(\zeta)\cos(\theta) \\ p\sin(\theta) \end{pmatrix} e^{i(\boldsymbol{\kappa}\cdot\mathbf{r}-\omega t)}\,, \tag{3.4}$$

where $s = \sin(2\varphi)/\sqrt{2}$ and $p = -[\cos(2\varphi) - i]/\sqrt{2}$. Immediately, we can verify that all $E_\beta E_\gamma$ and $E_\beta E_\gamma^*$ will be proportional to s^2, sp, p^2 (for OR process this involves the complex conjugate of one of the parameters s or p). Hence, the current is proportional to one of the following $\{constant,\ \cos(2\varphi),\ \cos(4\varphi),\ \sin(2\varphi),\ \sin(4\varphi)\}$. Yet, the terms linear in $\cos 2\varphi$ vanish for azimuthal angles $\zeta = n\pi/2, \forall\, n \in \mathbb{Z}$. This can be verified by explicitly computing the symmetric and antisymmetric combinations of the products of E_β and E_γ, for the sake of brevity, we display these in appendix §B.2, equations B.7 and B.8.

Replacing these terms in expressions 3.2 and 3.3 we obtain the different components of the current. For the sake of clarity we shall separate the calculation of the current into its several terms. We will start by addressing the the OR current, with particular emphasis in the circular polarization term.

3.2.1 DC current

The DC elastic ("galvanic") and inelastic ("drag") components of the total current, equation 3.1, are

$$j_\alpha = \mathtt{S}_{\alpha\beta\gamma}\frac{E^\beta_{\omega_1}E^\gamma_{-\omega_1} + E^\beta_{-\omega_1}E^\gamma_{\omega_1}}{4} + \mathtt{A}_{\alpha\beta\gamma}\frac{E^\beta_{\omega_1}E^\gamma_{-\omega_1} - E^\beta_{-\omega_1}E^\gamma_{\omega_1}}{4}\,, \tag{3.5a}$$

$$j_\alpha(\boldsymbol{\kappa}) = \mathtt{S}_{\alpha\beta\gamma\nu}\,\hat{\kappa}_\beta\frac{E^\gamma_{\omega_1}E^\nu_{-\omega_1} + E^\gamma_{-\omega_1}E^\nu_{\omega_1}}{4} + \mathtt{A}_{\alpha\beta\gamma\nu}\,\hat{\kappa}_\beta\frac{E^\gamma_{\omega_1}E^\nu_{-\omega_1} + E^\gamma_{-\omega_1}E^\nu_{\omega_1}}{4}\,, \tag{3.5b}$$

respectively. Without loss of generality, the light polarization dependency, φ, of photocurrent can be represented (for both elastic and inelastic processes) as

$$j_\alpha = A + C\sin(2\varphi) + L_1\cos(4\varphi) + L_2\sin(4\varphi)\,, \tag{3.6}$$

[1] Please note, that some of the results put forward in this manuscript were evaluated with the assistance of software. All calculations were performed with *Mathematica*, the source notebook for this calculation can be found in the following the *git* repository `graphenepccode.git`, in file `Rank3tensor.nb` at commit `#3f60cdaf`.

where $\{A, C, L_i\}$ are constant coefficients dependent on the geometric alignment, *i.e.* the incidence angles, polar (θ), and azimuthal (ζ), and on the microscopic properties of the system. The polarization dependency is the same for both elastic and inelastic processes, due to the fact that it arises solely from geometric properties of combination of the electric field components $\left(E^{\gamma}_{\omega}E^{\nu}_{\omega}\right)$ or $\left(E^{\gamma}_{\omega}E^{\nu}_{-\omega}\right)$. In both processes the electric field dependency is the same. Consequently, all geometric properties must have the same general form.

In the context of (quasi) 2D crystals, the coupling with the electric field is limited to the in-plane components of the electric field, *i.e.* (E^1_ω and E^2_ω in this setup). Moreover, these processes have distinct dependencies on the polarization state of the light (see the symmetric and antisymmetric combinations of $E_\beta E^*_\gamma$, equations B.7 and B.8 respectively). From this result, we may classify and group each contribution according to its dependency in polarization state. *First*, polarization-independent terms. *Second*, contribution that exhibit maximum amplitude for linearly polarized light and vanish for circularly polarized light, *i.e.* $j \propto \cos(4\varphi)$ or $j \propto \sin(4\varphi)$ or $j \propto \cos(2\varphi)$[2]. *Third*, contributions that exhibit maximum amplitude for circularly polarized light and vanish for linearly polarized light, *i.e.* $j \propto \sin(2\varphi)$.

To further extract information regarding the constants $\{A, C, L_i\}$, we must take into consideration some symmetry properties of the crystal under consideration. In (quasi) 2D crystals, the system is not capable of coupling along the out-of-plane direction. Taking into consideration this limitation and restricting the azimuthal angle to $\zeta = \pi/2$[3], *i.e.* propagation plane contained in the yOz plane, the current emerging from the elastic mechanism reads

$$j_1^{DC} = \frac{E_0^2}{8}\Big[2\mathtt{S}_{112}\sin(4\varphi)\cos(\theta) + \mathtt{S}_{111}\big[1-\cos 4\varphi\big] + \mathtt{S}_{122}\big[3+\cos(4\varphi)\big]\cos^2(\theta) - 4i\mathtt{A}_{112}\sin(2\varphi)\cos(\theta)\Big], \tag{3.7a}$$

$$j_2^{DC} = \frac{E_0^2}{8}\Big[\mathtt{S}_{222}\big[3+\cos(4\varphi)\big]\cos^2(\theta) - 2\mathtt{S}_{212}\sin(4\varphi)\cos(\theta) + \mathtt{S}_{211}\big[1-\cos(4\varphi)\big] - 4i\mathtt{A}_{212}\sin(2\varphi)\cos(\theta)\Big], \tag{3.7b}$$

[2]The latter vanishes for azimuthal angle $\zeta = n\pi/2, \forall\, n \in \mathbb{Z}$, *i.e.* current measured strictly along x or y directions.

[3]The choice a particular azimuthal angle causes no loss of relevant information, see appendices §B.2 and B.3 for the results at arbitrary incidence.

where the antisymmetric tensor elements $\mathtt{A}_{112} = \mathtt{A}_{212} = 0$, responsible for the response to circularly polarized light, vanishes in the presence of threefold symmetry. Hence, within the context of elastic interaction of light, crystals with threefold symmetry, do not generate OR in the presence of light with purely circular polarization.

Moreover, by considering inelastic mechanisms we observe that this limitations can, in principle, be lifted. For the sake of brevity, we display only the relevant terms for one component of the current response

$$j_1^{DC}(\boldsymbol{\kappa}) = -\frac{iE_0^2}{2}\sin(2\varphi)\Big(\mathtt{A}_{1212}\sin(\theta)\cos(\theta) - \mathtt{A}_{1312}\cos^2(\theta) + (\ldots)\Big)\,, \tag{3.7c}$$

where the elements $2\mathtt{A}_{1212} = \xi_{1212} - \xi_{1221}$ do not necessarily vanish in the presence of C_3 symmetry. Hence, the inelastic process may account for the response to circularly polarized light. Moreover, the tensor elements $\mathtt{A}_{1212}$ and $\mathtt{A}_{1312}$ account for different processes. The former is associated with momentum transfer in the lattice plane, whereas the latter requires momentum transfer along the normal of lattice plane.

Microscopic sources of circular photocurrents The results from the phenomenological analysis, equations 3.7, indicate that the elastic interaction in circularly polarized light cannot generate photocurrents in crystal with threefold symmetry. Notwithstanding this, experimental data [2, 4, 66] from graphene based devices indicates the existence photocurrents emerging from circularly polarized light. Hence, either the device breaks the threefold symmetry of the lattice of or another mechanism has to be present to account for this contribution.

Comparing the dependence on the incidence angle of the circular photocurrent elastic and inelastic processes, respectively $C_1 \propto \cos(\theta)$ and $C_2 \propto \sin(\theta)\cos(\theta)$, it possible to clearly identify the microscopic source of response.

3.2.2 Symmetry constraints for honeycomb lattices

Lattice symmetry plays a crucial role in physical properties associated with odd ranked tensors such as the second order conductivity tensor. Turning our attention to the symmetry of honeycomb lattices, we first consider the implication of the most basic symmetry common to all honeycomb lattice, the three fold symmetry, C_3, on a general rank

material	stacking	S.G.	P.G.	i	$t_{ijk} \neq 0$
graphene	SL	$P6/mmm$	$6/mmm \equiv D_{6h}$	yes	none
	AB	$P\bar{3}m1$	$\bar{3}m \equiv D_{3d}$	yes	none
(biased)	AB	$P3m1$	$3m \equiv C_{3v}$	no	t_{222}
hBN	SL	$P\bar{6}m2$	$\bar{6}m2 \equiv D_{3h}$	no	t_{222}
	AA	$P\bar{6}m2$	$\bar{6}m2 \equiv D_{3h}$	no	t_{222}
	AA′	$P\bar{3}m1$	$\bar{3}2/m \equiv D_{3d}$	yes	none
	AB	$P3m1$	$3m \equiv C_{3v}$	no	t_{222}
	A′B	$P\bar{3}m1$	$\bar{3}2/m \equiv D_{3d}$	yes	none
	AB′	$P\bar{3}m1$	$\bar{3}2/m \equiv D_{3d}$	yes	none

Table 3.1: In this table we condense information regarding symmetry properties for mono and bilayer of graphene and hBN. Regarding graphene, in addition to the mono and bilayer, we consider the effect of an external bias perpendicular to the bilayer plane. We include SG, PG, presence of inversion symmetry (i) and non-vanishing in-plane components for a general rank three tensor t_{ijk}. The labelling of stacking order in hBN follows ref. [79], were AA stackings indicate two pairs of vertically aligned atoms in the unit cell and AB indicates only one pair of vertically aligned atoms.

three tensor t_{ijk}. The presence of C_3 symmetry introduces several restrictions on the elements of rank three tensors. This symmetry reduces the in-plane independent tensor components to t_{111} and t_{222}. The non-vanishing linearly dependent components read $t_{211} = t_{121} = t_{112} = -t_{222}$ and $t_{122} = t_{212} = t_{221} = -t_{111}$. In table 3.1 we identify the symmetry and non-vanishing components of rank three tensors for mono and bilayers of graphene and hBN. This table contains the relevant Space Groups (SGs) and Point Groups (PGs) for the lattices under consideration and highlights the presence or absence of inversion symmetry [77, 78]. The restrictions imposed by lattice symmetry are most stringent in graphene, where both the free standing monolayer and AB bilayer have inversion symmetry. Nonetheless, under the presence of an external potential, the lattice symmetry can be reduced and create at least one finite in-plane component for rank three tensors. Due to the presence of two distinct elements in the unit cell, hBN monolayer does have inversion symmetry. The absence of inversion centre allows for the presence of non-vanishing rank three tensors in free standing monolayer hBN. Interestingly, the staking order order plays an important role in the bilayer. For AA', $A'B$ or AB' stacked bilayers, the lattice symmetry acquires an inversion and blocks the otherwise finite rank three tensors. From the analysis of lattice symmetry for pristine crystal, we can observe that, graphene (both mono and bilayer) always has an inversion centre. Whereas in hBN, monolayer, AA and AB bilayer, the inversion centre is not present. This indicates that second order light matter interaction processes in hBN should be observable without the necessity of symmetry breaking potentials. Moreover,

this analysis also shows that in graphene, the presence of an external potential perpendicular to the lattice plane, is sufficient to break inversion symmetry and thus open a channel for quadratic response.

3.2.3 Photocurrent as a manifestation of geometric phases

In this subsection we explore the effects of the so-called "anomalous" correction to the semiclassical equations of motion. It starts with a brief review of the standard semiclassical calculation of current density. Followed by the generalization of the semiclassical velocity and the propagation of this into the current density.

The starting point is the well known semiclassical result for currents emerging from intraband transitions, i.e the DC current [43]

$$\mathbf{j} = -g_s q \int \frac{d\mathbf{k}}{(2\pi)^2} \mathbf{v}(\mathbf{k}) \delta g \,, \tag{3.8}$$

where the wavepacket velocity and momentum read read

$$\dot{\mathbf{r}} = \mathbf{v}(\mathbf{k}) = \frac{1}{\hbar} \frac{\partial \epsilon(\mathbf{k})}{\partial \mathbf{k}} \,, \tag{3.9a}$$

$$\hbar \dot{\mathbf{k}} = -q\mathbf{E} - q\mathbf{v} \times \mathbf{B} \,, \tag{3.9b}$$

respectively. $\mathbf{E}$ and $\mathbf{B}$ are the electric and magnetic perturbations to the system, where the electric field reads $\mathbf{E} = \left(\mathbf{E}_0 e^{i(\boldsymbol{\kappa}\cdot\mathbf{r}-\omega t)} + \mathbf{E}_0^* e^{-i(\boldsymbol{\kappa}\cdot\mathbf{r}-\omega t)}\right)/4$ and $\mathbf{B}$ is defined analogously. In addition, the deviation from the equilibrium distribution reads $\delta g = g - g_0$, where g_0 is the equilibrium distribution functions. Finally, g_s is the spin degeneracy. Considering a time-dependent perturbation, such as an AC electric field, the deviation from the equilibrium distribution reads

$$\delta g = g(\mathbf{k}) - g^0(\mathbf{k}) = \frac{-q\mathbf{E}\cdot\mathbf{v}(\mathbf{k})\tau_{\mathbf{k}}}{1 - i\omega\tau_{\mathbf{k}}} \left(\frac{\partial f}{\partial \epsilon}\right)_{\epsilon=\epsilon(\mathbf{k})} + \text{c.c.}\,. \tag{3.10}$$

This approach is useful to compute some effects of an external electric field, yet it fails to account for the anomalous contributions arising from the Berry curvature. Several authors address this issue [61, 63, 70, 80] and the review by [28] and the textbooks [81, 82] provide a clear and detailed generalisation of the semiclassical results to include the contributions from the Berry curvature. In the general result the dispersion includes

the effect of an external magnetic field

$$\epsilon_M(\mathbf{k}) = \epsilon_0(\mathbf{k}) - \mathbf{B}\cdot\mathbf{L}(\mathbf{k})\,, \tag{3.11}$$

where $\mathbf{L}(\mathbf{k})$ is the orbital magnetic momentum. Since we are studying the effect of the Berry curvature in the absence of external magnetic field, the term proportional to the magnetic field is ignored. The semiclassical equations of motion are generalized and the wavepacket velocity now reads

$$\dot{\mathbf{r}} = \mathbf{v}(\mathbf{k}) = \frac{1}{\hbar}\frac{\partial\epsilon(\mathbf{k})}{\partial\mathbf{k}} - \dot{\mathbf{k}}\times\boldsymbol{\Omega}(\mathbf{k})\,, \tag{3.12}$$

and the momentum keeps the same form. The new term in the velocity is known as the anomalous velocity and $\boldsymbol{\Omega}(\mathbf{k})$ is the Berry curvature. In the absence of an external magnetic field ($\mathbf{B}=0$) the charge current is

$$\begin{aligned}\mathbf{j} = -g_s q\int\frac{\mathrm{d}\mathbf{k}}{(2\pi)^2}\left[\frac{1}{\hbar}\frac{\partial\epsilon(\mathbf{k})}{\partial\mathbf{k}} - \dot{\mathbf{k}}\times\boldsymbol{\Omega}(\mathbf{k})\right]\Bigg(\frac{q\tau_{\mathbf{k}}}{1-i\omega\tau_{\mathbf{k}}}\mathbf{E}\cdot\Big[\frac{1}{\hbar}\frac{\partial\epsilon(\mathbf{k})}{\partial\mathbf{k}}\\ - \dot{\mathbf{k}}\times\boldsymbol{\Omega}(\mathbf{k})\Big]\Big(-\frac{\partial f}{\partial\epsilon}\Big)_{\epsilon=\epsilon(\mathbf{k})} + \text{c.c.}\Bigg)\,.\end{aligned} \tag{3.13}$$

Focusing on the terms proportional Berry's curvature, which yield a 2^{nd} order response to the electric field, determines the so-called "anomalous" contributions to the current response [63]

$$\mathbf{j}_A = \frac{g_s q^3}{\hbar^2}\int\frac{\mathrm{d}\mathbf{k}\tau_{\mathbf{k}}}{(2\pi)^2}\Big[\mathbf{E}\times\boldsymbol{\Omega}(\mathbf{k})\Big]\frac{\mathbf{E}\cdot\boldsymbol{\nabla}\epsilon_{\mathbf{k}}\hbar}{1-i\omega\tau_{\mathbf{k}}}\Big(-\frac{\partial f}{\partial\epsilon}\Big)_{\epsilon=\epsilon(\mathbf{k})} + \text{c.c.}\,. \tag{3.14}$$

The semiclassical approximation falls short on several limitations, rendering little utility from this result for our purposes. Nonetheless, it clearly shows that the 2^{nd} response is intrinsically connected to the geometric phase.

3.3 Hexagonal monolayers

In this section we discuss the Optical Rectification (OR) in hexagonal monolayers, in the context of Tight-Binding (TB) models to characterize hBN and graphene and the response to elastic interaction with light via the direct coupling with the electric field.

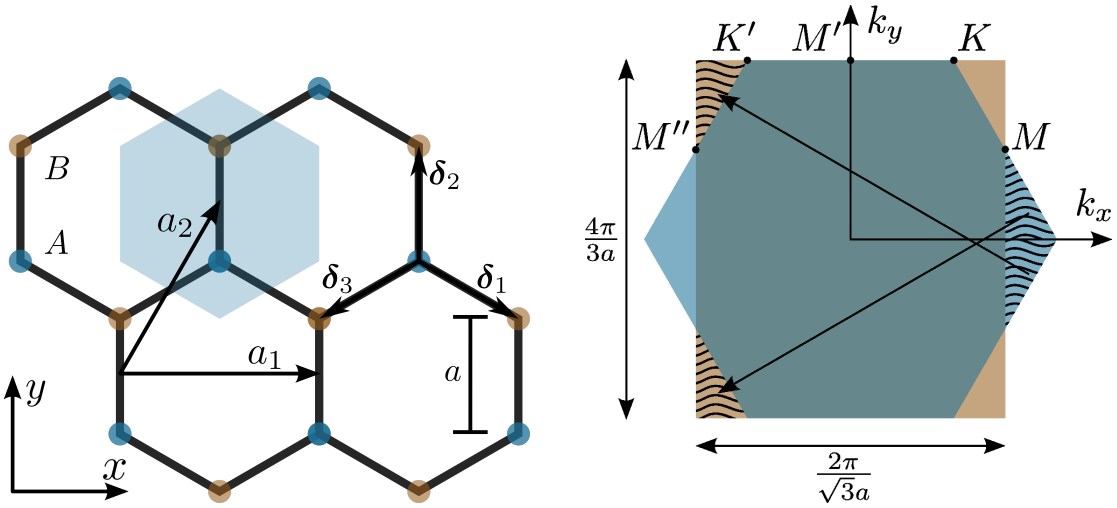

(a) Real space lattice. (b) Brillouin zone.

Figure 3.2: (a) 2D triangular lattice and respective (b) first BZ. The real lattice (a) contains two distinct elements (light and dark disks) and the respective WS cell is represented by a light hexagon. In (b) we identify conventional representation of the BZ for the triangular lattice, the light grey hexagon, and the construction scheme for an equivalent rectangular BZ.

All numerical results are evaluated according to the same procedure. The procedure starts by computing analytically the eigenvalues $\epsilon_m(\mathbf{k})$, and the respective eigenvectors, $|m, \mathbf{k}\rangle$ of system's Hamiltonian. For the sake of brevity and simplicity, we consider a generic two band TB Hamiltonian for the honeycomb lattice. The primitive and reciprocal vectors for the honeycomb lattice read

$$\mathbf{a}_1 = \frac{3a}{2}\left(\frac{2\sqrt{3}}{3}, 0\right);\ \mathbf{a}_2 = \frac{3a}{2}\left(\frac{\sqrt{3}}{3}, 1\right);\ \mathbf{b}_1 = \frac{4\pi}{3a}\left(\frac{\sqrt{3}}{2}, -\frac{1}{2}\right);\ \mathbf{b}_2 = \frac{4\pi}{3a}\left(0, -1\right) \quad (3.15)$$

respectively. In addition, the reciprocal vectors define the hexagonal BZ depicted in figure 3.2b, where the high-symmetry points read

$$\mathbf{K} = \frac{2\pi}{3a}\left(\frac{\sqrt{3}}{3}, 1\right),\ \mathbf{K}' = \frac{2\pi}{3a}\left(\frac{-\sqrt{3}}{3}, 1\right),\ \mathbf{M} = \frac{2\pi}{3a}\left(\frac{\sqrt{3}}{2}, \frac{1}{2}\right),\ \mathbf{M}' = \frac{2\pi}{3a}\left(0, 1\right). \quad (3.16)$$

The respective Hamiltonian reads

$$\mathcal{H} = \gamma_0 H = \gamma_0 \begin{pmatrix} \epsilon_1 & \phi(\mathbf{k}) \\ \phi(\mathbf{k})^* & \epsilon_2 \end{pmatrix}, \quad (3.17)$$

where $\phi(\mathbf{k}) = \exp\left[i(\sqrt{3}k_x - k_y)a/2\right] + \exp\left[ik_y a\right] + \exp\left[-i(\sqrt{3}k_x + k_y)a/2\right]$, with a being the nearest neighbour distance and $\mathrm{k}_\alpha = k_\alpha a$. The energy dispersion follows the

standard gapped dispersion for the honeycomb lattice $\varepsilon_\pm = \gamma_0\epsilon_\pm = \pm\gamma_0\sqrt{\Delta^2/4 + |\phi|^2}$, with $\Delta = \epsilon_2 - \epsilon_1$ and $|\phi|^2 = 3 + 2\cos(\sqrt{3}\mathrm{k}_x) + 4\cos(\sqrt{3}\mathrm{k}_x/2)\cos(3\mathrm{k}_y/2)$. We express quantities dependent on the crystal momentum, $p_\alpha = \hbar k_\alpha$, as functions of the dimensionless quantity $\mathrm{k}_\alpha \equiv k_\alpha a$. This is extended to the derivatives of any quantity with respect to k_α. Therefore, the velocity operator and respective matrix element read

$$\hat{v}^\alpha(\mathbf{k}) = \frac{\partial\hat{\mathcal{H}}}{\partial p_\alpha} = \frac{\gamma_0}{\hbar}\frac{\partial\hat{H}}{\partial k_\alpha} = \frac{\gamma_0 a}{\hbar}\frac{\partial\hat{H}}{\partial \mathrm{k}_\alpha} \equiv \frac{\gamma_0 a\,\hat{\mathrm{v}}^\alpha}{\hbar} \quad , \quad v^\alpha_{mn} = \frac{\gamma_0 a \mathrm{v}^\alpha_{mn}}{\hbar} \, , \tag{3.18}$$

where we introduce the dimensionless velocity operator $\hat{\mathrm{v}}^\alpha$. The derivatives with respect to k_β are computed also with respect to the dimensionless k_β. The gradients of the velocity and energy read

$$\frac{\partial v^\alpha_{mn}}{\partial k_\beta} = \frac{\gamma_0 a^2}{\hbar}\frac{\partial \mathrm{v}^\alpha_{mn}}{\partial \mathrm{k}_\beta} \quad ; \quad \frac{\partial\gamma_0\epsilon_{mn}}{\partial k_\beta} = \gamma_0 a\frac{\partial\epsilon_{mn}}{\partial \mathrm{k}_\beta} \, . \tag{3.19}$$

By the same token, we evaluate the Berry connections as

$$\mathcal{A}^\beta_{mn}(\mathrm{k}_\alpha) = i\langle m,\mathrm{k}_\alpha|\frac{\partial|n,\mathrm{k}_\alpha\rangle}{\partial k_\beta} = ia\langle m,\mathrm{k}_\alpha|\frac{\partial|n,\mathrm{k}_\alpha\rangle}{\partial \mathrm{k}_\beta} \equiv a\bar{\mathcal{A}}^\beta_{mn}(\mathrm{k}_\alpha) \, . \tag{3.20}$$

Making use of these dimensionless definitions and writing both the photon energy and the broadening parameter in units of γ_0, we recast the OC tensor, equation 1.41, as

$$\sigma^{(1,i)}_{\lambda\alpha}(\omega_1) = \frac{\sigma_1}{\bar{A}}\frac{2ig}{N}\sum_{\mathbf{k}}\sum_n \frac{\mathrm{v}^\lambda_{nn}}{\hbar\omega_1 + i\Gamma}\frac{\partial f_n}{\partial \mathrm{k}_\alpha} \tag{3.21a}$$

$$\sigma^{(1,e)}_{\lambda\alpha}(\omega_1) = \frac{\sigma_1}{\bar{A}}\frac{2ig}{N}\sum_{\mathbf{k}}\sum_{mn}\frac{\bar{\delta}_{mn}}{\epsilon_{mn}}\frac{f_{nm}\mathrm{v}^\lambda_{nm}\mathrm{v}^\alpha_{mn}}{\hbar\omega_1 - \epsilon_{mn} + i\Gamma} \, , \tag{3.21b}$$

where, $L^2 = A_{WS}N = \bar{A}a^2N$. Likewise, the OR tensor, equations 1.44, read

$$\sigma^{(2,ee)}_{\lambda\alpha\beta}(\omega_2+\omega_1) = \frac{g\,\sigma_2}{\bar{A}N}\sum_{\mathbf{k}}\sum_{lmn}\frac{\bar{\delta}_{lm}\bar{\delta}_{ln}\,\mathrm{v}^\lambda_{nm}/(\epsilon_{ml}\epsilon_{ln})}{\hbar(\omega_2+\omega_1) - \epsilon_{mn} + 2i\Gamma}\left(\frac{\mathrm{v}^\beta_{ml}\mathrm{v}^\alpha_{ln}f_{nl}}{\hbar\omega_1 - \epsilon_{ln} + i\Gamma}\right.$$
$$\left. - \frac{f_{lm}\mathrm{v}^\alpha_{ml}\mathrm{v}^\beta_{ln}}{\hbar\omega_1 - \epsilon_{ml} + i\Gamma}\right) \, , \tag{3.22a}$$

$$\sigma^{(2,ie)}_{\lambda\alpha\beta}(\omega_2+\omega_1) = \frac{-g\,\sigma_2}{\bar{A}N}\sum_{\mathbf{k}}\sum_{mn}\frac{\bar{\delta}_{mn}\,\mathrm{v}^\lambda_{nm}}{\hbar(\omega_2+\omega_1) - \epsilon_{mn} + 2i\Gamma}\left(\frac{\mathrm{v}^\alpha_{mn}f_{nm}/\epsilon_{mn}}{\hbar\omega_1 - \epsilon_{mn} + i\Gamma}\right)_{;\mathrm{k}_\beta} \, , \tag{3.22b}$$

$$\sigma^{(2,ei)}_{\lambda\alpha\beta}(\omega_2+\omega_1) = \frac{g\,\sigma_2}{\bar{A}N}\sum_{\mathbf{k}}\sum_{mn}\frac{\bar{\delta}_{mn}\,\mathrm{v}^\lambda_{nm}}{\hbar(\omega_2+\omega_1) - \epsilon_{mn} + 2i\Gamma}\frac{\mathrm{v}^\beta_{mn}/\epsilon_{mn}}{\hbar\omega_1 + i\Gamma}\frac{\partial f_{nm}}{\partial \mathrm{k}_\alpha} \, , \tag{3.22c}$$

$$\sigma^{(2,ii)}_{\lambda\alpha\beta}(\omega_2+\omega_1) = \frac{g\,\sigma_2/(\bar{A}N)}{\hbar(\omega_2+\omega_1)+2i\Gamma}\frac{1}{\hbar\omega_1+i\Gamma}\sum_{\mathbf{k}}\sum_{n}\mathrm{v}^{\lambda}_{nn}\frac{\partial^2 f_n}{\partial \mathrm{k}_\beta \partial \mathrm{k}_\alpha}\,. \tag{3.22d}$$

The dimensionality of the previous results, equations 3.21 and 3.22, are entirely defined by $\left[\sigma_1\right] = \mathrm{S}$ and $\left[\sigma_2\right] = \mathrm{S\,m/V}$, respectively. A brief review of the dimensionality of conductivity tensor can be found in appendix B.5. The previous result indicates all second order processes including inter and intra-band transitions.

Parity symmetry Thus far our analysis has been completely agnostic with respect to the parity of the integrands present in equations 3.22. For the sake of simplicity, we address the parity of the integrands with the restrictions associated with C_3 rotation, *i.e.* $\lambda = \alpha = \beta$. Considering the exclusively intraband term, equation 3.22d, the diagonal velocity matrix element is clearly an odd function in $\mathbf{k}$, where as the second derivative of the Fermi function is an even function. The resulting integrand is an odd function of $\mathbf{k}$ and vanishes under integration/ summation. Proceeding with the mixed inter/ intraband term, equation 3.22c, the product of matrix elements yields $|v_{mn}|^2$, which is an even function. The remaining elements in the integrand are the energy dispersion, an even function, and the first derivative of the Fermi function, an odd function. Once more, we obtain an odd integration resulting in a vanishing integral/ summation. To address the remaining mixed intra/ interband term, equation 3.22b, we must consider the expansion of the generalized derivative as defined in equation 1.28 [10]

$$\begin{aligned}\left(\frac{\mathcal{A}^{\alpha}_{mn}f_{nm}}{\omega_1-\omega_{mn}+i\eta}\right)_{;k_\beta} = \frac{\hbar^2\epsilon^{-1}_{mn}}{\hbar\omega_1-\epsilon_{mn}+i\Gamma}\Bigg[&\frac{\partial v^{\alpha}_{mn}}{\partial k_\beta}f_{nm}+v^{\alpha}_{mn}\frac{\partial f_{nm}}{\partial k_\beta}-i\,v^{\alpha}_{mn}f_{nm}\left(\mathcal{A}^{\beta}_{mm}-\mathcal{A}^{\beta}_{nn}\right)\\ &-\frac{v^{\alpha}_{mn}}{\epsilon_{mn}}\frac{\partial\epsilon_{mn}}{\partial k_\beta}\frac{\hbar\omega_1-2\epsilon_{mn}+i\Gamma}{\hbar\omega_1-\epsilon_{mn}+i\Gamma}f_{nm}\Bigg]\,.\end{aligned} \tag{3.23}$$

On the one hand, the terms involving the gradient of the dispersion or the gradient of the Fermi function yield odd integrands. On the other hand, the remaining two terms yield finite contributions. Last but not least, the exclusively interband term, equation 3.22a, yields only an odd integrand if and if only $m = n$.

The above-mentioned restrictions can also be shown without invoking C_3 symmetry. The formal proof is lengthy and cumbersome, it can be found by separating each complex quantity into a real and imaginary contribution and considering the parity of each combination. Notwithstanding this, the numerical evaluation of the integrand verifies

this for arbitrary $\lambda \neq \alpha \neq \beta$.

3.3.1 Numerical implementation

The size and complexity of the full expressions associated with the second order response render analytic evaluation impossible for most systems. Nonetheless, we proceed with the analytic calculation up to the integration of the response functions. The discrete summation over all wavevectors is converted to an integral over the first BZ as $N^{-1}\sum_{\mathbf{k}} \to \bar{A}(2\pi)^{-2}\int \mathrm{d}\mathbf{k}^2$.

All numerical implementations require basic benchmarking test to verify the accuracy of the method and also the physical significance of the results. At the purely numerical domain, the testing reduced to convergence testing and numerical verification of robust principles such as symmetry and conservation laws. Having verified the numerical consistency of the method, we address the physical relevance of the output. To test this, we compare our results with relevant and experimentally verified results. In light of this, we address the calculation of the OC in graphene, a perfect candidate for this task. During the the past decade a vast amount of literature has addressed the linear interactions of light and graphene, particularly the OC. Theory not only reproduces experimental data accurately, it also shows that, in the low photon energy regime, the OC reduces to a constant dependent only on fundamental physical constants [33, 37]. Therefore, the calculation of the OC of graphene can be used as a benchmark for our numerical implementation, particularly for the inter-band transitions. In figure 3.3 we plot the real and imaginary parts of the total OC in graphene, equations 3.21a and 3.21b. A quick inspection shows that the low photon energy regime reduces to $\sigma_1 = \pi e^2/2h$ and the expected features at the VHs. Having used the calculation of the OC in graphene as a benchmark for our numerical implementation, we proceed with the calculation of the second order conductivity tensor in bilayer graphene and in the mono and bilayers of hBN.

3.3.2 Hexagonal Boron Nitride

Here we address the second order response monolayer hBN. The presence of two distinct elements in hBN allows the formation of several distinct lattices, just by interchanging the elements in one layer. Symmetry restrictions narrow the study the of second or-

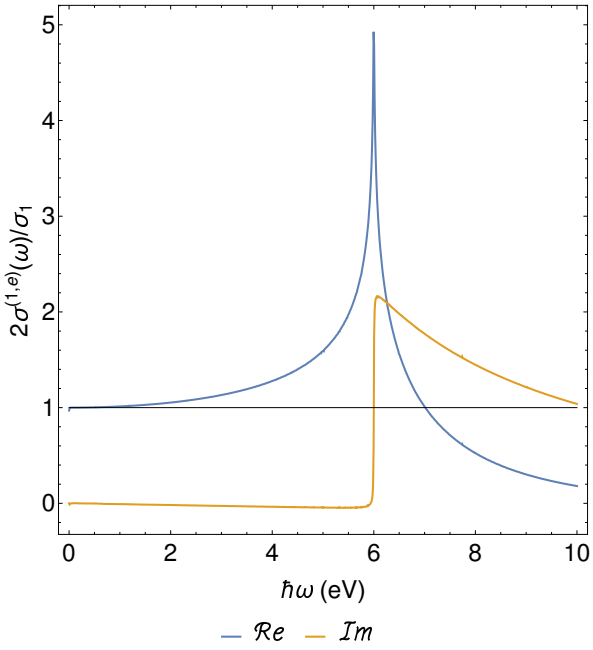

Figure 3.3: Optical conductivity in graphene. In this figure we plot the longitudinal components of the OC tensor for graphene. We consider a nearest-neighbour TB model with hopping integral set to $\gamma_0 = 3\text{eV}$ and used a broadening energy $\Gamma\gamma_0 = 0.005\text{eV}$. The factor 2 stems from the definition of the response functions and conductivity tensor, equations 1.4 and 1.7 respectively.

der processes to lattices without inversion symmetry, such as the hBN monolayer (see table 3.1 for additional information regarding lattice symmetry).

The relevant TB Hamiltonian was introduced in equation 3.17, where the in-plane hopping integral and gap follow the estimate by [83], namely $\gamma_0 = 2.31\,\text{eV}$, $\gamma_0\Delta = 7.80\,\text{eV}$ and nearest neighbour distance $a = 1.45 \times 10^{-10}\,\text{m}$. The parametrization of hopping integrals and gap estimate in hBN remains an unsettled discussion, with particularly dissonant estimates for the band gap [83–87]. Finally, the second order conductivity scale, equation 1.43, reads $\sigma_2 = 3.79 \times 10^{-15}\,\text{S m/V}$. In figure 3.4a we plot the energy dispersion for monolayer hBN. As expected, the monolayer dispersion follows the standard dispersion for the honeycomb lattice with a very large gap. Monolayer h-BN belongs to space group $\text{P}\bar{6}m2 \equiv D^1_{3h}$. Hence, all rank three tensors associated with this lattice contain only one independent in-plane tensor element, t_{222} [78]. The presence of C_3 symmetry enforces the following relation for in-plane tensor elements $t_{211} = t_{121} = t_{112} = -t_{222}$. In figure 3.4b, we plot the four non-vanishing tensor components. As expected these are linearly dependent and verify the above-mentioned relation down to the precision of the numerical integration, *i.e.* $\delta = 10^{-4}$. The results clearly indicate that the OR occurs only for photon energies greater, or equal, to the

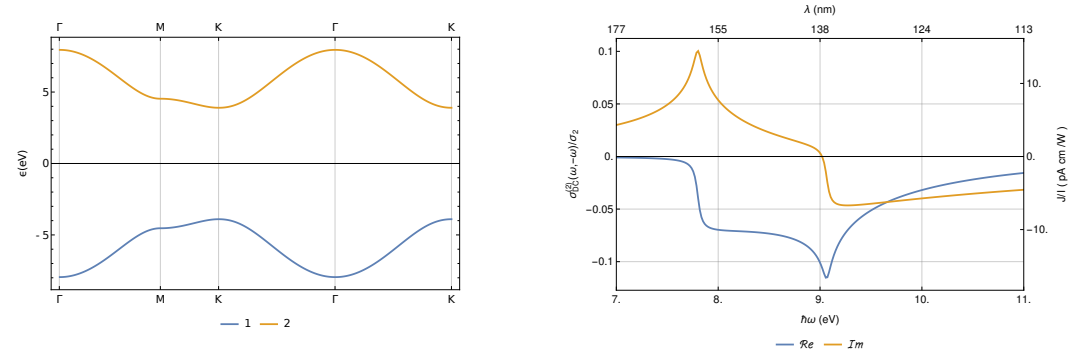

(a) (b)

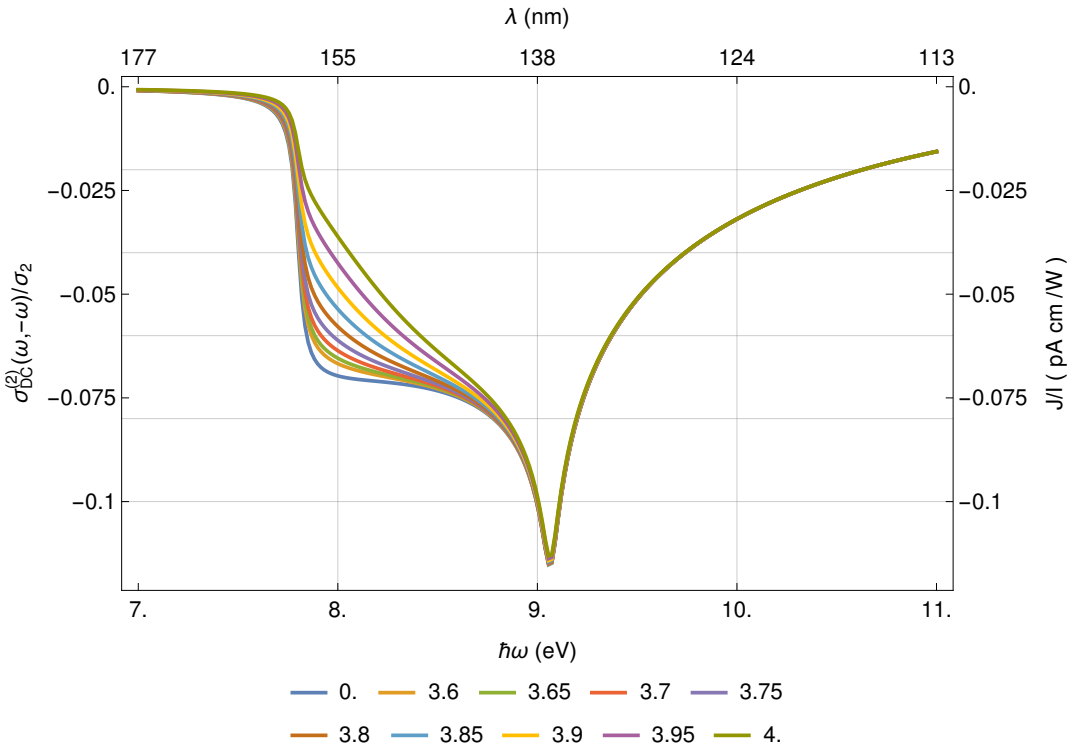

(c)

Figure 3.4: Energy dispersion and non-vanishing elements of the second order conductivity for OR, $\sigma^{(2)}_{\lambda\alpha\beta}/\sigma_2$, for monolayer hBN. The monolayer h-BN Hamiltonian is parametrized as follows $\gamma_0 = 2.33\,\mathrm{eV}$, $\Delta\gamma_0 = 7.8\,\mathrm{eV}$, $\mu\gamma_0 = 0.0\,\mathrm{eV}$ at room temperature and $\Gamma\gamma_0 = 0.03\mathrm{eV}$. (a) Energy dispersion along the high symmetry path. Inset: zoom in the vicinity of $\mathbf{K}$ (b) Real and imaginary parts of $\sigma^{(2)}_{222}$, $-\sigma^{(2)}_{211}$, $-\sigma^{(2)}_{121}$ and $-\sigma^{(2)}_{112}$. In (c), we analyse the effect of finite doping by plot several curves for $\sigma^{(2)}_{yyy}$ with $\mu = \{0.0, 3.8, 3.85, 3.9, 3.95, 4.0\}$ eV at high temperature $T = 1500\,\mathrm{K}$. In plots (b) and (c), the scale on the right measures the photocurrent in units of current density per laser intensity (J/I), *e.g.* ref. [4].

band gap. Furthermore, results show a clear peak at the VHs and a monotonic decrease of the response for energies above the VHs.

From the definition of the second order response tensor, we can easily verify that matching Fourier components for this process are conjugate of each other, $\sigma^{(2)}(-\omega,\omega) = \sigma^{(2)}(\omega,-\omega)^*$, resulting in a purely real OR conductivity tensor. Hence, the imaginary part of the tensor can only be analysed for each frequency component. In figure 3.4b, we plot the real and imaginary parts of a single frequency component. In this plot we can verify that each feature in the real part has its reciprocal in the imaginary part, as expected from the Krammers-Kronig relations. In addition, our results show that the full response arises exclusively from the mixed intra/inter-band term in equation 1.42b, as all other contributions present in equation 1.42b vanish in the entire bandwidth.

In spite of the lack of consensus regarding the correct gap for monolayer hBN, even the smallest estimates propose a gap much larger than any change to chemical potential that can be generated in an electrostatically gated device. Hence, it seems unrealistic to study the dependence in the chemical potential by analysing either the OC or OR tensor. Nonetheless, in figure 3.4c we plot the expected change of the conductivity tensor when the chemical potential is in the vicinity of the bottom of the conduction band at high temperature [88–90]. In the context of non-linear experiments, the laser intensities required to measure non-linear phenomena can cause significant local heating of the system. Moreover, recent reports have shown that the interaction with such intense laser beams can generate *hot carries* in graphene with temperatures $T \sim 1500$K [88–90] In extreme cases, the maximum temperature estimates for *"hot charged carriers"* in graphene exceed $T = 4000$K in time scales smaller than 1ps [88].

The effect of a large chemical potential should resemble the traditional Pauli blocking associated with the Fermi distribution function. By quick inspection of the mixed intra/inter-band, equation 3.22b, including the expansion of the generalized derivative, equation 3.23, it can be shown that the term involving the gradient of the Fermi function is an odd function in the BZ. As a result, all non-vanishing contributions to $\sigma^{(2.ie)}_{\lambda\alpha\beta}$ are proportional to a Fermi function, hence the traditional Pauli blocking.

3.3.3 Gapped graphene

Second order interaction of light with graphene is not expected due to the presence of an inversion centre. The presence of inversion centres is observed in free standing graphene, and all even numbered Bernal stacked multi-layers [91]. Odd number Bernal stacked multi-layers break inversion symmetry and could in principle support second order response. Notwithstanding the presence of inversion, higher order processes can circumvent this restriction, for instance processes involving exchange of photon momentum or circular AC Hall effect [2, 4, 60, 70]. In addition to higher order processes, photocurrent can be generated by interactions with external fields or strain, which effectively break inversion symmetry by blocking one or more symmetries present in the pristine form of the crystal. Several device designs with graphene (or its multilayers) can apply external electric fields which, at least in principle, should break the horizontal mirror symmetry, thus breaking the inversion symmetry. Such devices have been extensively studied [55, 92–97] and a combination of back and top gates in bilayer graphene devices can generate large external fields capable of opening considerable gaps and effectively doping the system. Furthermore, strain is another tool to reduce the symmetries present in the system [53, 98–106]. Achieving the desired effects with strain is not a trivial process, particularly if we wish to preserve the threefold symmetry present in the pristine lattice.

Thus far, the microscopic modelling of both second or higher order processes is limited. The analysis of most higher order processes involves either a phenomenological description of the effect or a model based on semiclassical dynamics. Our focus aims at the development of a reliable method to determine non-linear response functions, starting from a given microscopic model. We analyse the intrinsic OR in graphene by computing the second order current response function in the length gauge, equations 3.22. Below, we consider the generation of photocurrents in a "gapped" graphene monolayer. The source of this gap a simple imbalance, Δ, in the on-site potentials at sublattices A and B. While this has not been observed in pristine crystals of graphene, it has been predicted on layered structures of graphene and hBN [102]. The respective Hamiltonian was introduced in equation 3.17, where the hopping integral $\gamma_0 = 3.00\,\mathrm{eV}$, the gap, unless otherwise stated, is $\Delta = 0.20\,\mathrm{eV}$ and the lattice parameter $a = 1.45 \times 10^{-10}\,\mathrm{m}$. Fi-

nally, the second order conductivity scale, equation 1.43, reads $\sigma_2 = 2.88 \times 10^{-15}\,\mathrm{S\,m/V}$. In figure 3.5a, we plot the energy dispersion for a "gapped" monolayer. From this energy dispersion, we expect to observe features associated with regions of the BZ where the dispersion is flat, *i.e.* regions associated with large DoS. Hence, we expect at least two features in the photocurrent associated with vertical transitions at the high symmetry points $\mathbf{K}$ and $\mathbf{M}$. The low energy response is dominated by vertical transitions in the vicinity of the the gap, which lays at the $\mathbf{K}$ point. The $\mathbf{M}$ point is associated with photon energies near $\hbar\omega \sim 2\gamma_0 = 6\,\mathrm{eV}$, in the near-UV region. In figure 3.5b, we plot the non-vanishing elements of the second order conductivity tensor for OR, considering a gap of $100\,\mathrm{meV}$. The second order conductivity exhibits a prominent feature at the band gap, but nearly negligible response at the $\mathbf{M}$ point, *i.e.* $\hbar\omega \sim 6\,\mathrm{eV}$. In addition, the finite tensor elements obey relations imposed by the trigonal symmetry, namely $-t_{211} = -t_{121} = -t_{112} = t_{222}$. The OR in monolayer hBN exhibits two distinct bands at photon energies associated with vertical transition at the $\mathbf{K}$ and $\mathbf{M}$ points. In spite the fact that both hBN and "gapped" graphene share the same Hamiltonian, apart from the parametrization of the hopping integral and gap, the photocurrent response is significantly different. First, at the $\mathbf{K}$ point we observe a quasi step-like feature in hBN and an asymmetric peak in gapped graphene. Second, the VHs dominant in hBN, is negligible in gapped graphene. Third, the dominant feature in hBN is the peak at the VHs, whereas in the gapped graphene is the peak at the gap. Although both materials share the same Hamiltonian and have similar in-plane hopping integrals, the respective gap differ significantly. This difference can be highlighted by the ratio between the two parameters, we read $3.0/0.1 = 30$ and $2.33/7.80 \sim 0.3$. In graphene, the gap under consideration is much smaller than the hopping integral, in opposition to hBN where the gap is nearly four times larger. In figure 3.6a we plot the variation of the OR with respect to the gap parameter. It clearly shows that, for small gap to hopping integral ratio, the dominant feature is the very low energy response. Increasing this ratio to unity or larger leads the response to contain two features with comparable magnitude and significant overlap. Despite the fact that we are considering a very simple two band TB Hamiltonian, even the integrands in equations 3.22 are very complex functions. To shed some light in the dependence of the response of the gap, we compute the effective mass tensor at high symmetry points. Given the energy dispersion for the gapped monolayer,

$\epsilon(\mathbf{k}) = \pm\sqrt{\Delta^2/4 + |\phi|^2}$, the effective mass tensor reads

$$M^{-1}_{\alpha\beta} = \frac{1}{\hbar^2}\frac{\partial\epsilon(\mathbf{k})}{\partial k_\alpha \partial k_\beta} = \frac{1}{m^*}\frac{\partial\epsilon(\mathbf{k})}{\partial \mathrm{k}_\alpha \partial \mathrm{k}_\beta}$$
$$= \frac{1}{m^*}\frac{1}{2\,\epsilon(\mathbf{k})}\left(\frac{\partial^2|\phi|^2}{\partial \mathrm{k}_\beta \partial \mathrm{k}_\alpha} - \frac{1}{2\epsilon^2(\mathbf{k})}\frac{\partial|\phi|^2}{\partial \mathrm{k}_\beta}\frac{\partial|\phi|^2}{\partial \mathrm{k}_\alpha}\right), \tag{3.24}$$

where we introduce the effective mass scale $m^* = \hbar^2/(\gamma_0 a^2) \sim 1.26\, m_e$ and the electron rest mass $m_e \sim 9.11 \times 10^{-31}$ kg. At the high symmetry points, the non-vanishing components of the effective mass tensor read $M_{yy}(\mathbf{K}) = M_{xx}(\mathbf{K}) = 2m^*\Delta/9$ and $M_{yy}(\mathbf{M}) = M_{xx}(\mathbf{M})/3 = m^*\sqrt{4+\Delta^4}/9$. Taking the vanishing gap limit, the effective mass of the electrons at the $\mathbf{K}$ point vanishes, whereas the effective mass at the $\mathbf{M}$ point remains finite at similar to the electron rest mass $M_{yy}(\mathbf{M}) \sim 0.28 m_e$. In the opposite limit, the ratios between the effective masses at $\mathbf{K}$ and $\mathbf{M}$ points are $M_{yy}(\mathbf{K})/M_{yy}(\mathbf{M}) = 2$ and $M_{xx}(\mathbf{K})/M_{xx}(\mathbf{M}) = 6$. Despite the fact that effective mass is not present in the calculation of the second order response, we can take it as a proxy for the DoS in the vicinity of a given point in reciprocal space. Within the semiclassical model, we can interpret that smaller effective mass leads to a larger response. Hence, a plausible explanation for the origin of the dominant nature of the response at low energy in the small gap regime. In figure 3.6a we plot the dependence of the second order conductivity tensor on the gap parameter.

In addition, such a simple system provides an excellent opportunity to clearly observe Pauli blocking in a second order process. In figure 3.6b we plot the dependence of the second order conductivity tensor on the chemical potential. Results clearly reproduce the Pauli blocking for photon energy $\hbar\omega < 2|\mu|$. The smoothen step between blocked and unblocked transitions stems from two factors. First, finite temperature broadening of the Fermi function. The broadening of the Fermi function is significant in an energy range $k_B T = k_B 1 \sim 10^{-4}$eV around the chemical potential. Second, the finite broadening parameter, Γ, introduced by the adiabatic assumption. This introduces a broadening $2\Gamma \sim 0.002$eV on the calculation of the otherwise divergent propagators. The final broadening is a combination of both contributions, but at low temperatures, the second is the dominant factor.

As explained earlier, the physical realization of the Hamiltonian under consideration suffers from several limitations. Nonetheless, the analysis of this simple and highly

symmetric system provides the fundamental understanding of the basic mechanisms involved in the interaction of light with Bloch electrons.

3.4 Hexagonal bilayers

In this section we discuss the Optical Rectification (OR) in hexagonal bilayers, in the context of TB models to characterize hBN and graphene and the response to elastic interaction with light via the direct coupling with the electric field. The TB Hamiltonians for both systems are defined is a similar fashion to the monolayer Hamiltonians. For bilayer hBN, the relevant Hamiltonians read

$$\mathcal{H}_{\mathtt{AA}} = -\gamma_0 \begin{pmatrix} E_1 & \phi & \gamma_1 & 0 \\ \phi^* & E_2 & 0 & \gamma_1 \\ \gamma_1 & 0 & E_3 & \phi \\ 0 & \gamma_1 & \phi^* & E_4 \end{pmatrix} \quad ; \qquad \mathcal{H}_{\mathtt{AB}} = -\gamma_0 \begin{pmatrix} E_1 & \phi & \gamma_1 & 0 \\ \phi^* & E_2 & 0 & 0 \\ \gamma_1 & 0 & E_3 & \phi^* \\ 0 & 0 & \phi & E_4 \end{pmatrix} , \tag{3.25}$$

where $E_i = \pm\Delta/2$ is the gap parameter and γ_1 the interlayer hopping. In addition, the stacking order is fully determined by the sign of the on-site energies. For both AA and AB stacking orders, the vertical alignments of atoms is selected by the relation between the on-site potentials. On the one hand, setting $E_1 = E_3 = -E_2 = -E_4 = \Delta/2$ selects equal atoms vertically aligned for AA, AB' and $A'B$. On the other hand, setting $E_1 = E_4 = -E_2 = -E_3 = \Delta/2$ selects different atoms vertically aligned. For the sake of simplicity, take the same parametrization of monolayer hBN layers, where the in-plane hopping integral and gap follow the estimate by [83], namely $\gamma_0 = 2.31\,\mathrm{eV}$, $\gamma_0\Delta = 7.80\,\mathrm{eV}$ and nearest neighbour distance $a = 1.45 \times 10^{-10}\,\mathrm{m}$. The out-of-plane hopping integrals follow the estimate by [79] for the AB stacking order, namely $\gamma_1\gamma_0 = 0.60\,\mathrm{eV}$, respectively. Finally, the second order conductivity scale, equation 1.43, reads $\sigma_2 = 3.79 \times 10^{-15}\,\mathrm{S\,m/V}$.

Regarding the Bernal stacked graphene bilayer in the presence of an external static

and uniform field perpendicular to the lattice plane, the respective Hamiltonian reads

$$\mathcal{H}_{\mathtt{AB}} = -\gamma_0 \begin{pmatrix} -\Delta/2 & 0 & 0 & \phi \\ 0 & \Delta/2 & \phi* & 0 \\ 0 & \phi & \Delta/2 & \gamma_1 \\ \phi* & 0 & \gamma_1 & -\Delta/2 \end{pmatrix}, \tag{3.26}$$

where $\gamma_1 = 0.40\,\mathrm{eV}$ the interlayer hopping, the effective external potential gap reads $\Delta = 0.20\,\mathrm{eV}$ (unless otherwise mentioned), lattice parameter reads $a = 1.42 \times 10^{-10}\,\mathrm{m}$ and the second order conductivity scale, equation 1.43, reads $\sigma_2 = 2.88 \times 10^{-15}\,\mathrm{S\,m/V}$. The generation of external potential in bilayer graphene is a relatively common practice in the so-called BBGs devices [92–97].

The following subsections address the details of the photocurrent generation in each system, starting with bilayer hBN and then proceed to BBG.

3.4.1 Bilayer Boron Nitride

Due to symmetry restrictions and lattice stability we consider only the AB staked bilayer. In figure 3.7 we plot the energy dispersion and OR tensor for AB bilayer hBN. The dispersion is particle hole symmetric and has no band crossings or degeneracies (apart from spin degeneracy). The band gap is located at the high symmetry point K and the saddle points are located at the symmetry point M in the first BZ. The separation between the two valence (and conduction) bands is minimum at the K point, where we also find the band gap between the top valence and bottom conduction bands. The separation at K reads $\delta\epsilon \sim \gamma_1^2\Delta \sim 46\,\mathrm{meV}$, which leads to a rather small difference, $\sim 90\,\mathrm{meV}$, between the two direct gaps, $\sim 7.8\,\mathrm{eV}$ at the K point.

From the monolayer result, we expect to observe step like features at photon frequencies associated with minimum energy difference for each vertical transition. These features are present in our results, figure3.7b, yet at this energy scale these features appear superimposed[4]. The VHss in the honeycomb lattice can be found at the saddle points, the high symmetry M points. At the saddle point the separation between both valence (and conduction) bands is large, $\sim 307\,\mathrm{meV}$, leading to a considerable separa-

[4]Results computed at low temperature 1K, with a smaller broadening parameter, $\Gamma = 5\,\mathrm{meV}$, show the two step like features.

tion, $\sim 614\,\mathrm{meV}$, between the two allowed vertical transitions. The latter is $\sim 20\mathrm{x}$ larger than the energy resolution of these results. Hence, the respective features are easily identified in figure 3.7b.

In addition to the above-mentioned properties, the bilayer can support second order response between the valence or conduction bands, *i.e.* transitions between bands $\epsilon_3 \to \epsilon_1$ or $\epsilon_2 \to \epsilon_4$. Due to the large gap between the valence and conduction bands, this transitions are forbidden by Pauli blocking, as both valence bands are fully occupied and both conduction bands are effectively empty. Considering a system with finite doping, circumvents Pauli blocking opening a response channel at very low frequency. In figure 3.8 we plot the variation of the second order response with the increase of the chemical potential. The large gap and narrow separation between bands $1, 3$ and $2, 4$, generate responses at frequency ranges significantly apart. Hence, we separate the plots for the high and low energy regimes and present results at different temperatures. In the high energy regime, *i.e.* transitions from valence to conduction bands, the effect of the chemical potential reduces to Pauli blocking. Due to the energy scale, we choose to plot the effect at high-temperature [88–90]. With regards to the response arising from transition between the conduction bands, results show that the response not only occurs at a completely distinct energy range, but has an opposite sign and can be an order of magnitude larger. In this regime we consider the effect of doping at lower temperature for several reasons. First, it highlights Pauli blocking by an increasing (absolute value) response for $\mu \lesssim 3.9\,\mathrm{eV}$. Second, the thermal energy $k_B 1500$ is comparable to the energy range under consideration, which introduces a significant broadening in the response. Third, at this temperature Pauli blocking remains strong enough to limit the response to transitions in vicinity of the chemical potential. For instance, at $\mu = 4.5\,\mathrm{eV}$, the chemical potential lies in the middle of bands 4 and 2 at saddle point, $\mathbf{M}$. The energy separation between the bands at this point is $\epsilon_{43}(\mathbf{M}) \sim 0.3\,\mathrm{eV}$, consistent with the response for the yellow curve in figure 3.8b.

3.4.2 Biased Bilayer Graphene

Here, we address the photocurrent generation in the BBG. The physics of BBG has been extensively studied and characterized, particularly its transport properties. The largest gaps obtained by field effect on top and bottom gated devices reach at most half an

electron volt [92–97]. As discussed earlier, our effort is focused on calculating the response function rather than on the construction of the TB Hamiltonian. Hence, unless otherwise mentioned, we set the gap to $200\,\mathrm{meV}$. Once more, the analysis of the band structure provides useful insight. In figure 3.9a we plot the energy dispersion for the respective four band TB Hamiltonian. In contrast with the monolayer, the gap in the bilayer is not located at the high symmetry K point. Instead, it lays in the vicinity of the high symmetry point and the magnitude of gap is no longer equal to the external potential [92]. In addition to the transitions in the vicinity of the $\mathbf{K}$ point, bilayer graphene also supports low energy transitions between the valence or conduction bands, *i.e.* transitions between bands $\epsilon_3 \to \epsilon_1$ or $\epsilon_2 \to \epsilon_4$. The separation between theses bands is controlled by the interlayer hopping which, in the case of graphene can be comparable to the band gap. Furthermore, the minimum separation between the valence and second conduction band, $\epsilon_1 \to \epsilon_4$ is of the order of $\gamma_1 + \Delta$, which also lies in the low energy regime. In a pristine system, the chemical potential should lay in the gap, blocking the transitions $3 \to 1$ and $2 \to 4$. Nonetheless, a key feature of gated devices is not only the control of the external field, but also the control of Fermi level of the system via doping. The band structure can accommodate a significantly large number of vertical transitions in the low energy regime, thus potentially increasing the richness of interaction with light. The number of tunable parameters is large, therefore I will address each individually. We start by analysing the OR in BBG at the charge neutrality point, low temperature and with a reasonable $100\mathrm{meV}$ gap. In figure 3.9b, we plot the non-vanishing elements of the second order conductivity tensor for OR. The response at charge neutrality and low temperature exhibits two key features at minimum energy for transitions $1 \to 2$ and $1 \to 4$. As expected no feature can be observed between bands $3 \to 1$ or $2 \to 4$. Moreover, the results are consistent with the restrictions imposed by the lattice symmetry. Considering low temperatures can facilitate significantly the analysis of transport properties. For several reasons, several experiments are performed at very low temperatures. Yet, this is not always possible or feasible. In figure 3.10a, we consider three different regimes, low temperature $T = 1\,\mathrm{K}$, room temperature $T = 300\,\mathrm{K}$ and high temperature $T = 1500\,\mathrm{K}$. The last temperature follows the order of magnitude of several estimates presented in recent experimental reports [88–90]. For the sake of clarity, we consider the chemical at the middle of the gap. In

addition to the expected effects of smoothening of the Fermi function, increasing the temperature to $T = 1500\,\mathrm{K}$ introduces new features in the response at an energy range compatible with transitions from the bands $\epsilon_3 \to \epsilon_1$ and $\epsilon_2 \to \epsilon_4$. This clearly shows that even a system set at the charge neutrality point can accommodate more complex transitions, given a high enough temperature. In the case of the BBG, local temperatures of the order of $1000\mathrm{K}$ are capable of "opening" these transitions. In figure 3.10b, we take the chemical potential into consideration. For the sake of clarity, we present only results at room temperature. These results show that the variation of chemical potential drastically changes the photocurrent, particularly in the region $\hbar\omega \sim [0.3 - 0.45]\,\mathrm{eV}$. In this region, the photocurrent can be continuously tuned from a positive quantity to a negative by controlling the doping level.

This chapter began by describing the photocurrent in 2D crystal on the basis of phenomenological considerations It went on to show how to compute and analyse the photocurrent in selected 2D mono and bilayers. The calculation was based in a Perturbative Expansion (PE), considering the direct coupling between the position operator and the electric field, the so-called length gauge. In addition, it analysed the dependence of the photocurrent on several external and tunable parameters, namely the temperature, chemical potential and static external potential (in the BBG only). Results show interesting properties, particularly in the BBG, were the sign of the response can be changed by controlling the doping level.

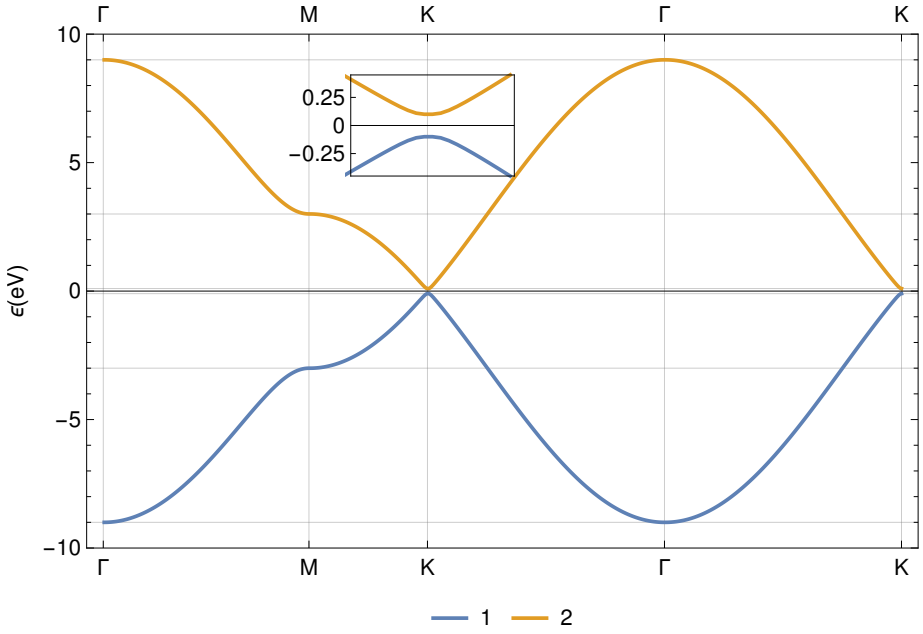

(a)

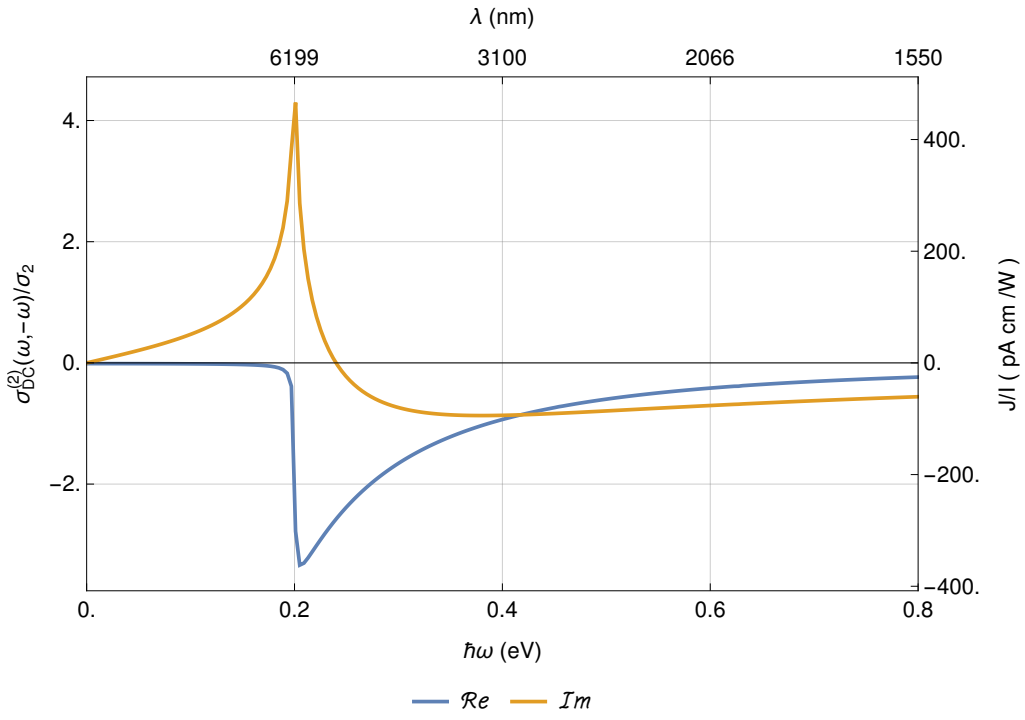

(b)

Figure 3.5: Energy dispersion and second order OR, for "gapped" graphene. In (a) we show the energy dispersion of graphene, the inset zooms in the vicinity of the high symmetry **K** point, confirming that the dispersion is not degenerate in any region of BZ. In (b) we plot the the real and imaginary parts of the non-vanishing components of the optical rectification tensor according to $\sigma^{(2)}_{222}$, $-\sigma^{(2)}_{211}$, $-\sigma^{(2)}_{121}$ and $-\sigma^{(2)}_{112}$. The scale on the right measures the photocurrent in units of current density (J) per laser intensity (I), *e.g.* ref. [4].

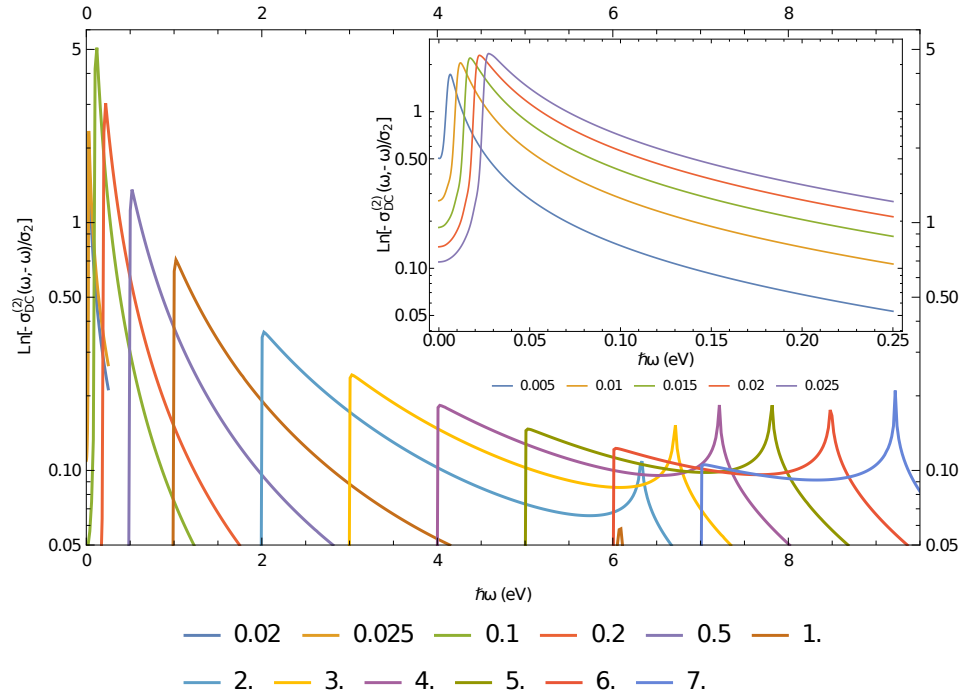

(a)

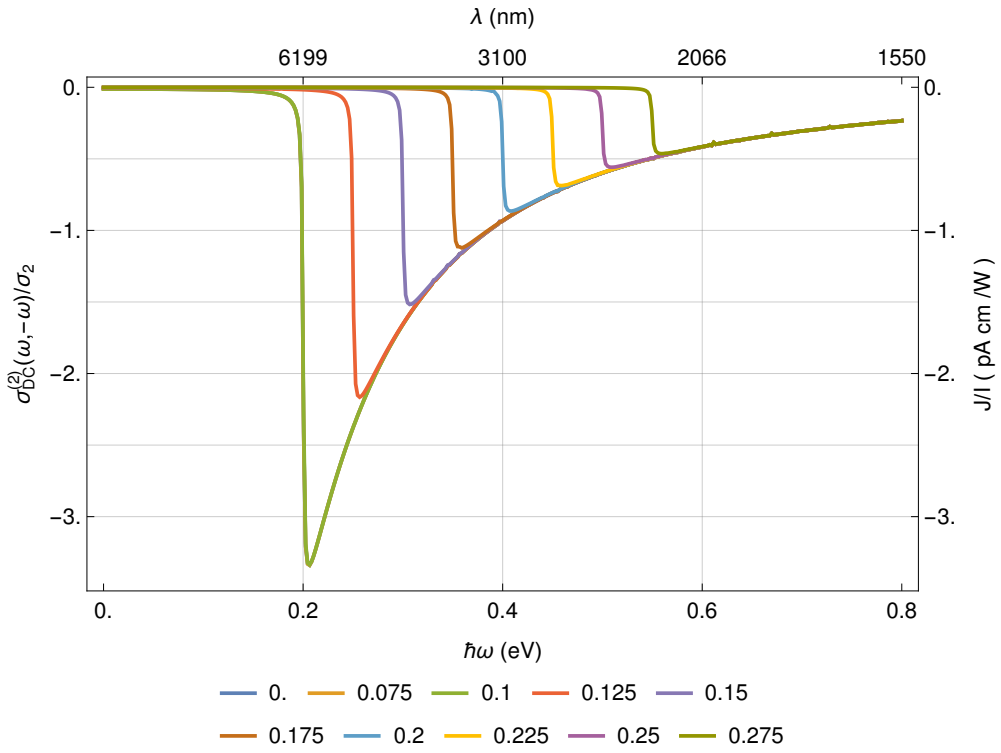

(b)

Figure 3.6: Photocurrent dependence on chemical potential and gap. The Hamiltonian is parametrized as follows $\gamma_0 = 3.00\,\mathrm{eV}$, $\Delta\gamma_0 = 0.2\,\mathrm{eV}$, at $T = 1\,\mathrm{K}$ and $\Gamma\gamma_0 = 0.001\mathrm{eV}$. In (a) we analyse the dependence of the optical rectification tensor on the gap. Due to the large variation, we use a logarithmic scale. In (b) we consider the effect of the chemical potential on the OR by varying the chemical potential in the range $\mu = \{0.0, 0.275\}\,\mathrm{eV}$. The scale on the right measures the photocurrent in units of current density (J) per laser intensity (I), *e.g.* ref. [4].

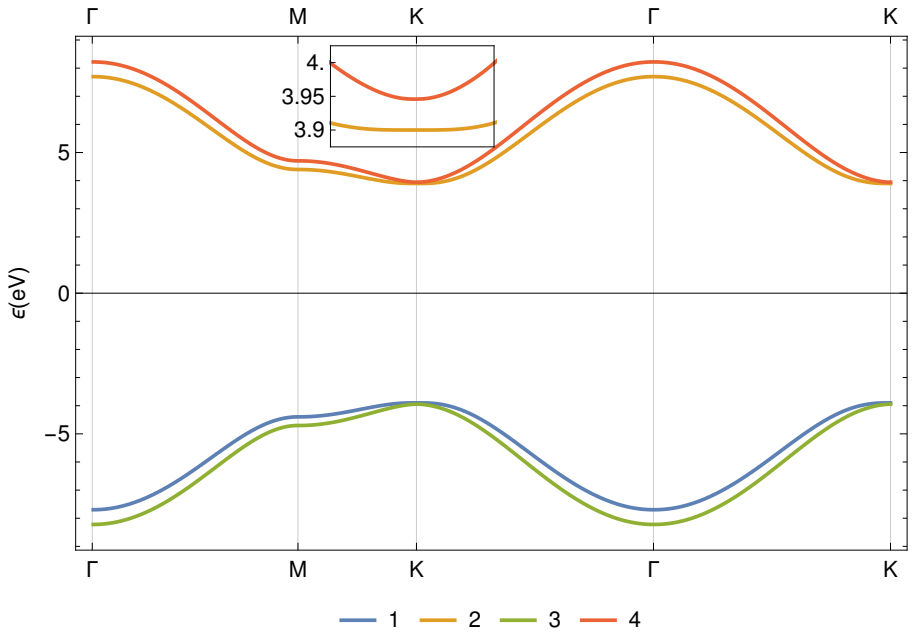

(a)

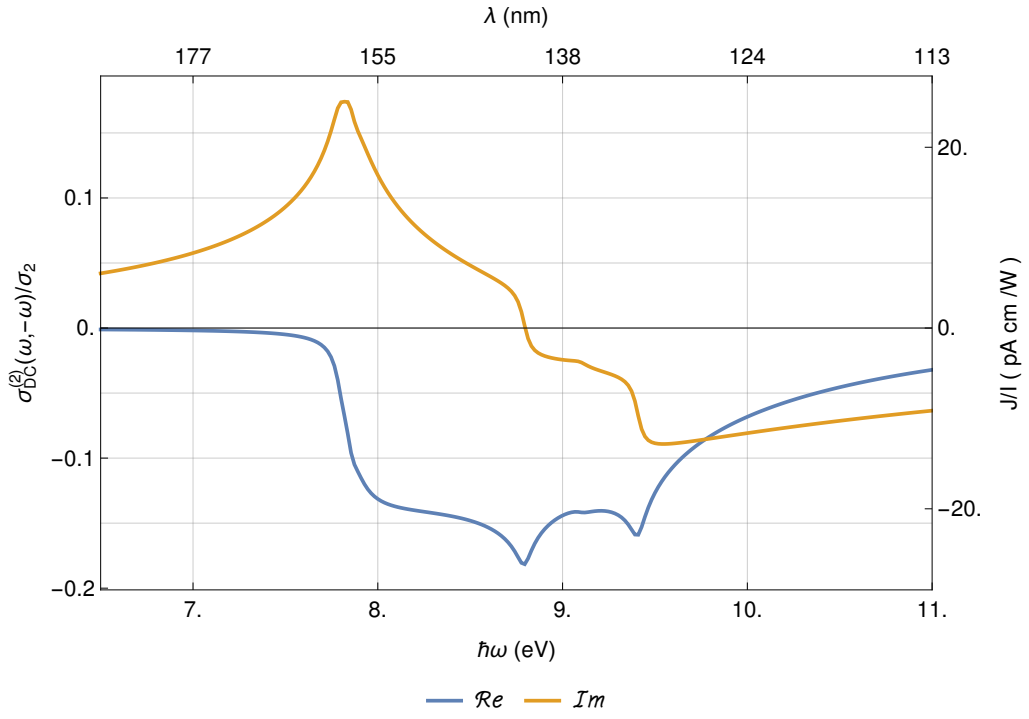

(b)

Figure 3.7: Energy dispersion and second order OR for non-centrosymmetric hBN AB bilayer. In (a) we show the energy dispersion of AB bilayer hBN, the inset zooms in the vicinity of the high symmetry $\mathbf{K}$ point. The latter confirms that the dispersion is not degenerate in any region of BZ. In (b) we plot the the real and imaginary parts of the non-vanishing components of the optical rectification tensor according to $\sigma^{(2)}_{222}$, $-\sigma^{(2)}_{211}$, $-\sigma^{(2)}_{121}$ and $-\sigma^{(2)}_{112}$. Due to the very large bandwidth for hBN, $\sim 16\,\mathrm{eV}$, we limit the plot to energies slightly higher than the features associated with the VHs, $\lesssim 12\,\mathrm{eV}$. The scale on the right measures the photocurrent in units of current density per laser intensity (J/I), *e.g.* ref. [4].

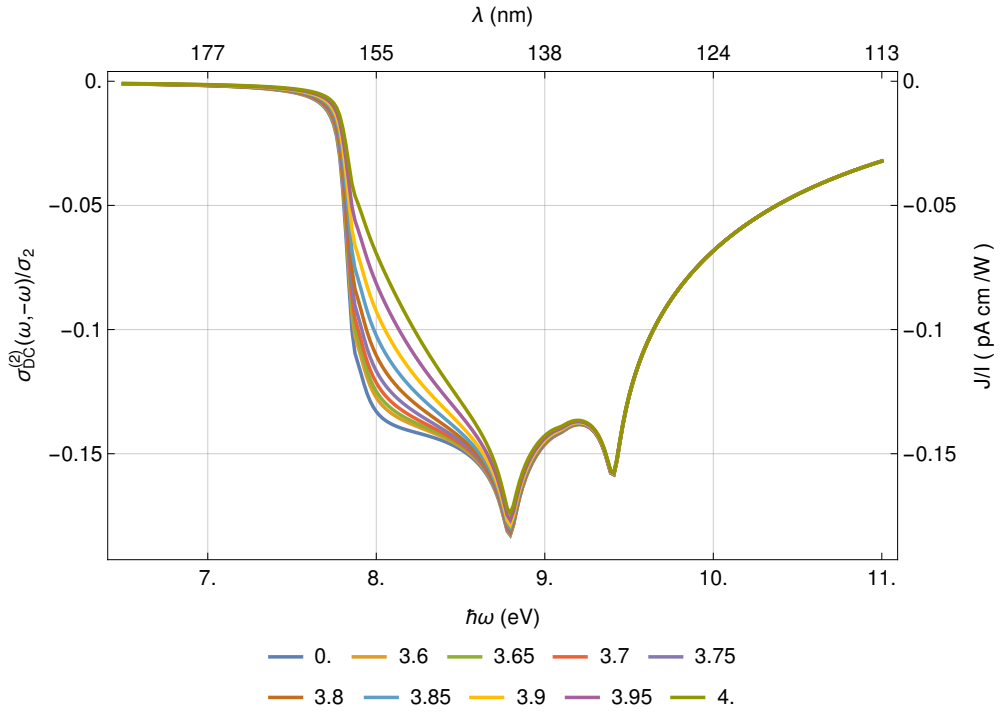

(a)

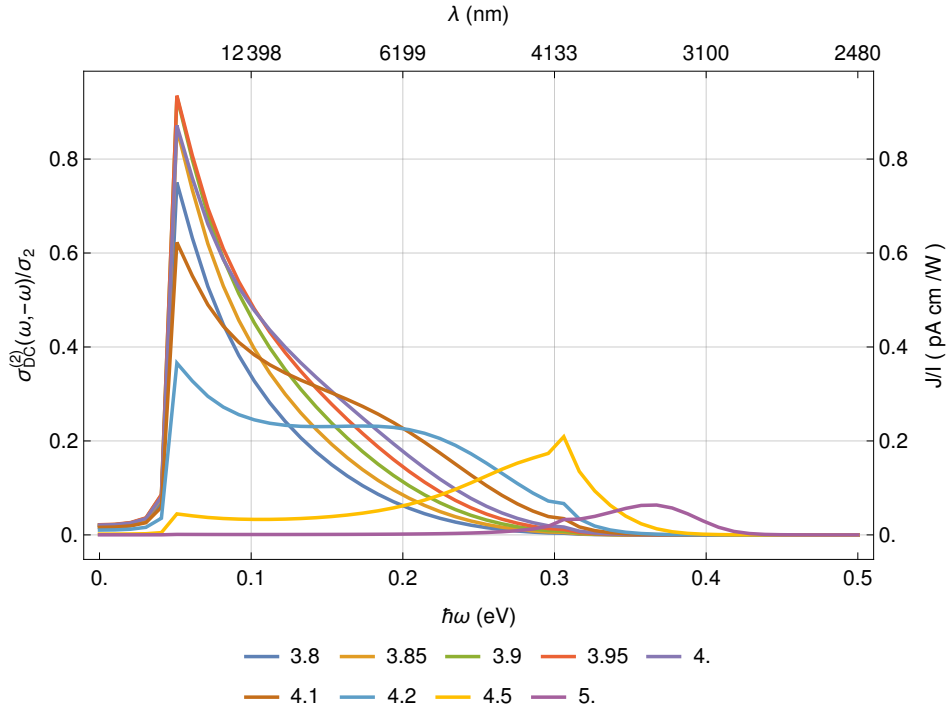

(b)

Figure 3.8: Effect of chemical potential on photocurrent for bilayer hBN at high and low energy. In (a) we observe the effect of the chemical potential at high photon energy. It plots the OR for bilayer hBN as function of the chemical potential at high temperature $T = 1500\,\mathrm{K}$. Due to the very large bandwidth for hBN, $\sim 16\,\mathrm{eV}$, we limit the plot in (b) to energies slightly higher than the features associated with the VHss, $\lesssim 11\,\mathrm{eV}$. In (b) we probe the effects of high chemical potential at a photon energy range comparable to the separation between the valence (conduction) bands $\epsilon_{13} = \epsilon_{42} \in [46,\ 522]\,\mathrm{meV}$. In both plots, the scale on the right measures the photocurrent in units of current density per laser intensity (J/I), *e.g.* ref. [4].

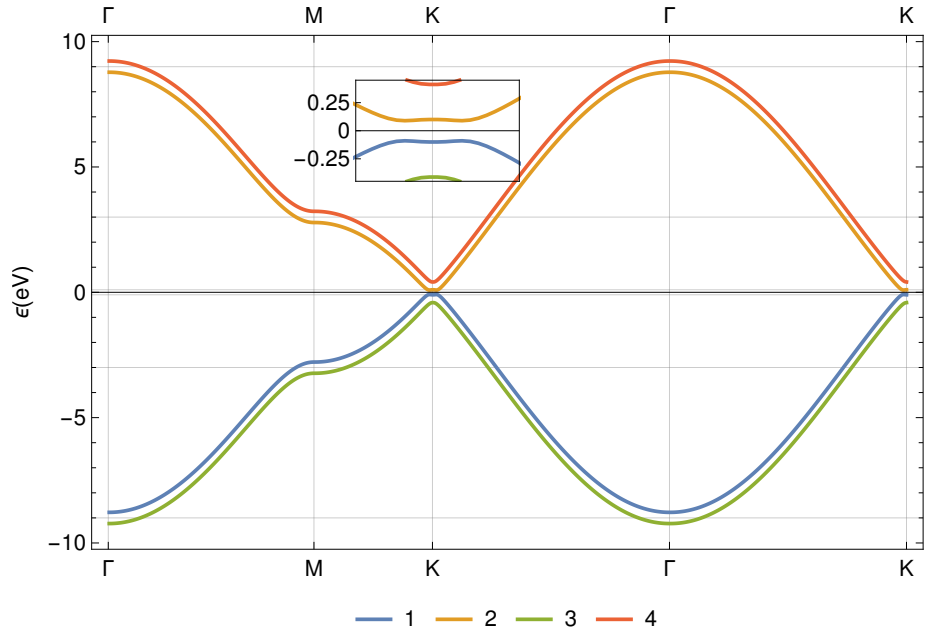

(a)

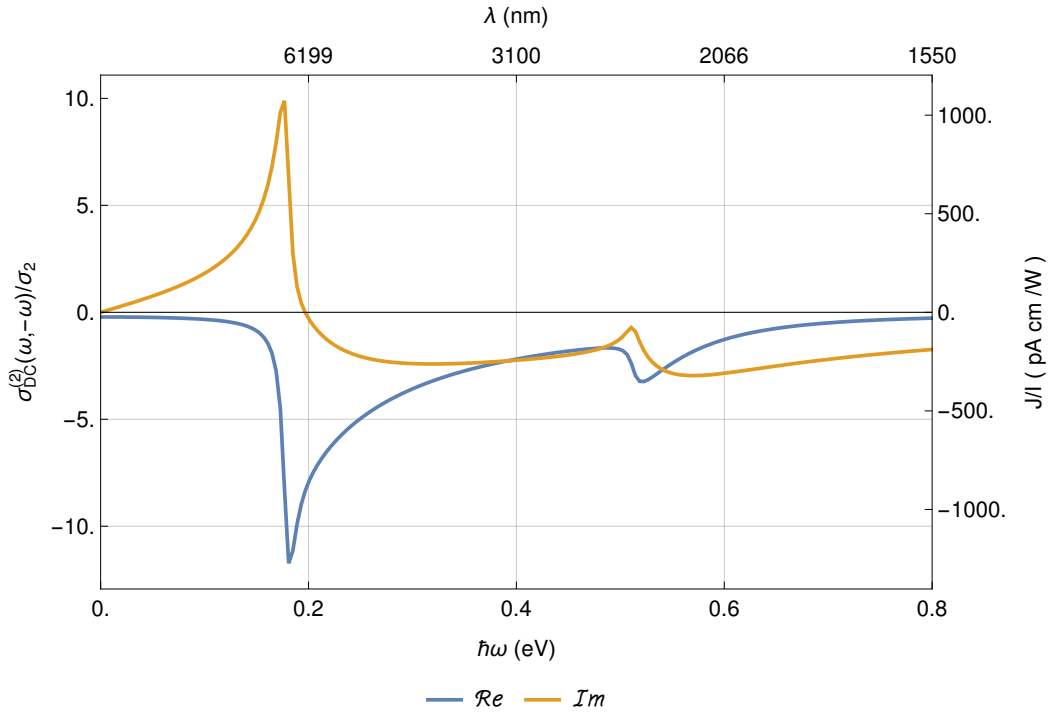

(b)

Figure 3.9: Energy dispersion and second order OR for non-centrosymmetric AB BBG. The Hamiltonian is parametrized as follows $\gamma_0 = 3.00\,\mathrm{eV}$, $\Delta\gamma_0 = 0.2\,\mathrm{eV}$, at $T = 1\,\mathrm{K}$ and $\Gamma\gamma_0 = 0.001\mathrm{eV}$. In (a) we show the energy dispersion of BBG, the inset zooms in the vicinity of the high symmetry **K** point. The latter confirms that the dispersion is not degenerate in any region of BZ. In addition, we overlay dashed vertical lines indicating $\mu + nk_BT$ for $T = \{300, 1500\}\,\mathrm{K}$ to serve as guide lines to map the region were the Fermi functions is depleted (populated) beyond the low temperature threshold. In (b) we plot the the real and imaginary parts of the non-vanishing components of the optical rectification tensor according to $\sigma^{(2)}_{222}$, $-\sigma^{(2)}_{211}$, $-\sigma^{(2)}_{121}$ and $-\sigma^{(2)}_{112}$. The scale on the right measures the photocurrent in units of current density per laser intensity (J/I), *e.g.* ref. [4].

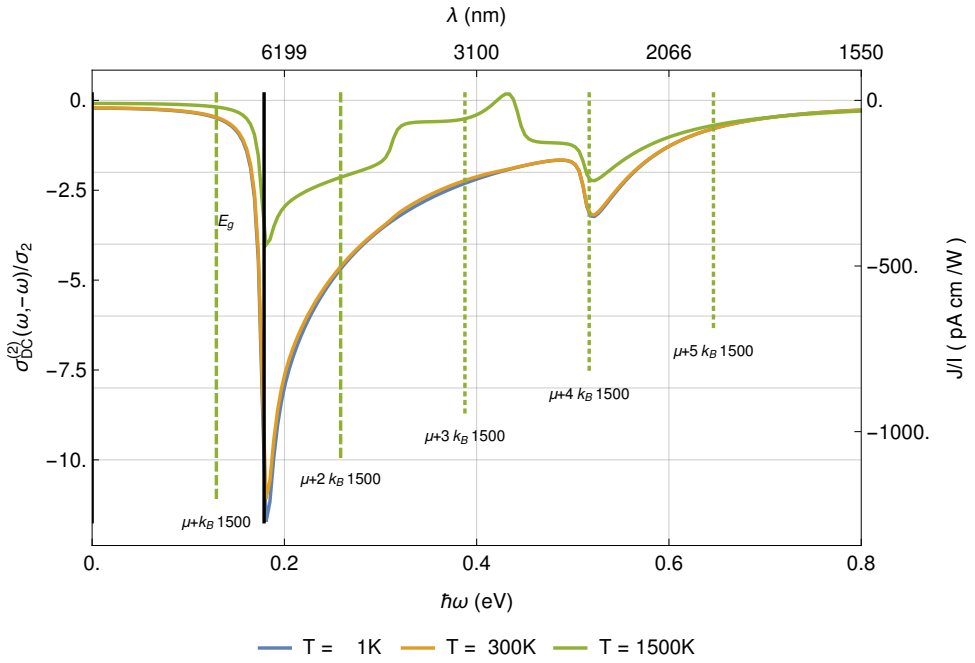

(a)

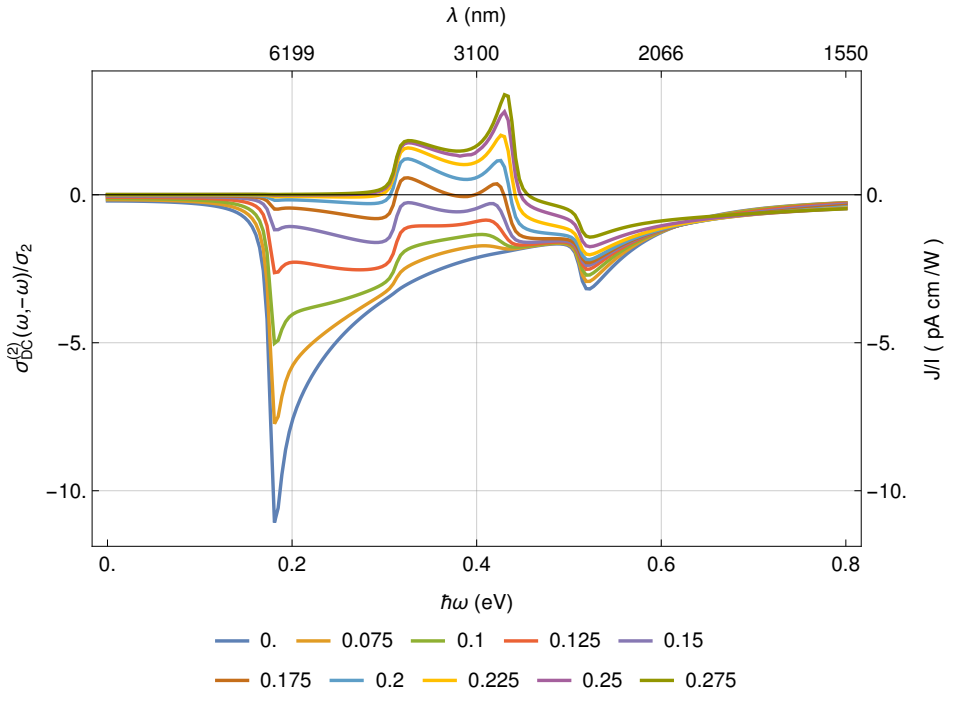

(b)

Figure 3.10: Dependence of photocurrent on temperature and chemical potential for BBG. The Hamiltonian is parametrized as follows $\gamma_0 = 3.00\,\mathrm{eV}$, $\Delta\gamma_0 = 0.2\,\mathrm{eV}$ and $\Gamma\gamma_0 = 0.001\,\mathrm{eV}$. In (a) we study the dependence of the photocurrent on temperature in BBG at the charge neutrality point. The plot contains three curves at selected temperatures $T = \{1, 300, 1500\}\,\mathrm{K}$, *i.e.* low, room and an estimate for the effective temperature in the presence of an intense laser [88–90]. The vertical dashed lines indicate the energy difference to the chemical potential, serving as an indicator of the region where the Fermi function varies significantly. In (b) we study the effect of chemical potential in BBG at room temperature. The plot contains several curves at different chemical potential in the range $\mu = \{0.01, 0.275\}\,\mathrm{eV}$. In both plots, the scale on the right measures the photocurrent in units of current density per laser intensity (J/I), *e.g.* ref. [4].

This page was intentionally left blank.

Chapter 4

Spin Orbit Coupling in 2D materials

4.1 Context

This chapter describes and discusses a method to determine effective Hamiltonians, within the framework of the Tight-Binding (TB) model. TB model has been used extensively in condensed matter physics to compute electronic properties of many materials. Despite the large success of TB, it frequently generates Hamiltonians that are not practical for analytic calculations. A good example of the quality and limitations of the TB Hamiltonian can be seen in graphene. On the one hand, the simple one band, p_z, Hamiltonian in graphene has proven immensely useful and accurate to characterize a wide range of physical properties, from the electronic properties, to transport and light-matter interaction. On the other hand, Although the shortcomings of the simple model can be easily solved, this is at the expense of a significant increase in complexity due to the growth of the basis.

Alternatively, effective mass models or $\mathbf{k}\cdot\mathbf{p}$ methods can be used to determine an effective Hamiltonian, capable of capturing properties such as Spin–Orbit Coupling (SOC) in graphene [107]. Another set of limitations are introduced by this method. For instance, these methods rely on approximations valid in the vicinity of high-symmetry points, which in turn introduces a new set of limitations.

In 1950 Löwdin [108] proposed a partitioning technique that allows the calculation of an effective Hamiltonian requiring only a subset of the initial Hamiltonian basis. Recent works [109, 110] used this technique with success to study SOC, mainly for numerical studies. In addition, refs. [111, 112] use similar methods to compute effective

Hamiltonians and analyse electronic properties of silicene.

The following section is dedicated to a review of LPT, which will serve as reference for the remainder of this chapter.

4.2 Löwdin's partitioning technique

In this section we review Löwdin's Partitioning Technique (LPT). The starting point is the definition of unitary transformation, $A' = UAU^{-1}$, which projects a block Hamiltonian, H, into a new basis where the Hamiltonian has a block diagonal form, H', *i.e.*

$$H = \begin{pmatrix} H_0 & T \\ T^\dagger & \Delta \end{pmatrix} \quad \rightarrow \quad H' = \begin{pmatrix} H_{\text{eff}} & 0 \\ 0 & \Delta' \end{pmatrix} .$$

The final blocks are ideally decoupled and characterize completely the physics associated with their respective basis. Now, let us define unitary transformation matrix $U = e^{-S}$, where S is anti-hermitian. This transformation is known as the Schrieffer–Wolf transformation [113, 114]

$$\begin{aligned}
\hat{H}' &= e^{-\hat{S}}\hat{H}e^{\hat{S}} = \left(\sum_{n=0}^{\infty}\frac{(-\hat{S})^n}{n!}\right)\hat{H}\left(\sum_{n=0}^{\infty}\frac{\hat{S}^n}{n!}\right) \\
&= \left(1-\hat{S}+\hat{S}^2/2-\hat{S}^3/6+\mathcal{O}(\hat{S}^4)\right)\hat{H}\left(1+\hat{S}+\hat{S}^2/2+\hat{S}^3/6+\mathcal{O}(\hat{S}^4)\right) \\
&= \hat{H}+\hat{H}\hat{S}-\hat{S}\hat{H}+\hat{H}\hat{S}^2/2-\hat{S}\hat{H}\hat{S}+\hat{H}\hat{S}^2/2+\hat{H}\hat{S}^3/6-\hat{S}\hat{H}\hat{S}^2/2 \\
&+ \hat{S}^2\hat{H}\hat{S}/2-\hat{S}^3\hat{H}/6+\mathcal{O}(\hat{S}^4) \\
&= \hat{H}+\left[\hat{H},\hat{S}\right]+\left[\left[\hat{H},\hat{S}\right],\hat{S}\right]/2+\left[\left[\left[\hat{H},\hat{S}\right],\hat{S}\right],\hat{S}\right]/6+\mathcal{O}(\hat{S}^4) \\
&= \sum_{n=0}^{\infty}\frac{(-1)^n}{n!}\mathbb{S}^n\hat{H} \;: \quad \mathbb{S}\hat{A} = \left[\hat{S},\hat{A}\right] .
\end{aligned} \tag{4.1}$$

Defining S as an anti-hermitian matrix with structure [109]

$$S = \begin{pmatrix} 0 & M \\ -M^\dagger & 0 \end{pmatrix} , \tag{4.2}$$

the terms up to $\mathcal{O}\left(S^4\right)$ can be written as

$$[H,S] = \begin{pmatrix} -TM^\dagger - MT^\dagger & H_0M - M\Delta \\ -\Delta M^\dagger + M^\dagger H_0 & T^\dagger M + M^\dagger T \end{pmatrix} = \begin{pmatrix} a & b \\ c & d \end{pmatrix} \tag{4.3a}$$

$$[[H,S],S] = \begin{pmatrix} -bM^\dagger & aM \\ -DM^\dagger & cM \end{pmatrix} - \begin{pmatrix} Mc & Md \\ -M^\dagger a & -M^\dagger b \end{pmatrix} = \begin{pmatrix} e & f \\ g & h \end{pmatrix} \tag{4.3b}$$

$$[[[H,S],S],S] = \begin{pmatrix} -fM^\dagger & eM \\ -hM^\dagger & gM \end{pmatrix} - \begin{pmatrix} Mg & Mh \\ -M^\dagger e & -M^\dagger f \end{pmatrix} \tag{4.3c}$$

Since we are only interested in computing one final decoupled block, we are free to choose either H_{eff} or Δ' in equation 4.1. Collecting the relevant terms from equations 4.3, the "effective" Hamiltonian reads

$$H_{\text{eff}} = A^{(0)} + A^{(1)} + A^{(2)} + A^{(3)} + \mathcal{O}\left(S^4\right), \tag{4.4}$$

such that:

$$A^{(0)} = H_0\,; \quad A^{(1)} = -\left(TM^\dagger + MT^\dagger\right)\,; \quad A^{(2)} = -\frac{bM^\dagger - Mc}{2}\,;$$
$$A^{(3)} = \frac{-fM^\dagger - Mg}{6} = \frac{-\left\{a, MM^\dagger\right\} + 2MdM^\dagger}{6}\,.$$

Löwdin set the condition that the choice of the transformation matrix S, must return a block diagonal Hamiltonian to $\mathcal{O}\left(S^2\right)$, *i.e.* the Hamiltonian in the new basis must be block diagonal

$$H' \simeq H + [H,S] = \begin{pmatrix} A' & 0 \\ 0 & D' \end{pmatrix}. \tag{4.6}$$

The previous conditions yield the following relations:

$$H_0 + TM^\dagger - M^\dagger T = A'\,; \tag{4.7a}$$
$$T + H_0M - M\Delta = 0\,; \tag{4.7b}$$
$$T^\dagger - \Delta M^\dagger + M^\dagger H_0 = 0\,; \tag{4.7c}$$
$$\Delta + T^\dagger M + M^\dagger T = D'\,. \tag{4.7d}$$

The relations determined from the diagonal elements establish the leading order contribution for the effective Hamiltonians, namely A' and D'. Whereas the relations from the off-diagonal elements, set the conditions for matrices M $(M^\dagger)$ and T $(T^\dagger)$

$$M = T\Delta^{-1} + H_0 M\Delta^{-1}\,, \tag{4.8a}$$
$$M^\dagger = \Delta^{-1}T^\dagger + \Delta^{-1}M^\dagger H_0\,, \tag{4.8b}$$
$$T = -H_0 M + M\Delta = -b\,, \tag{4.8c}$$
$$T^\dagger = \Delta M^\dagger - M^\dagger H_0 = -c\,. \tag{4.8d}$$

Equations 4.8a and 4.8b do not have a closed-form solution, but can be solved recursively

$$M = T\Delta^{-1} + H_0 T\Delta^{-2} + H_0^2 T^2\Delta^{-3} + \left(\Delta^{-4}\right), \tag{4.9a}$$
$$M^\dagger = \Delta^{-1}T^\dagger + \Delta^{-2}T^\dagger H_0 + \Delta^{-3}{T^\dagger}^2 H_0^2 + \left(\Delta^{-4}\right). \tag{4.9b}$$

The solution for matrices T $(T^\dagger)$ stems from the recursive solutions of M $(M^\dagger)$,

$$TM^\dagger + MT^\dagger = 2T\Delta^{-1}T^\dagger + \left\{T\Delta^{-2}T^\dagger, H_0\right\} + \left\{T\Delta^{-3}T^\dagger, H_0^2\right\} + \mathcal{O}\left(\Delta^{-4}\right), \tag{4.10a}$$
$$T^\dagger M + M^\dagger T = \left\{T^\dagger T, \Delta^{-1}\right\} + \left\{T^\dagger H_0 T, \Delta^{-2}\right\} + \left\{T\,\dagger\, H_0 T, \Delta^{-3}\right\} + \mathcal{O}\left(\Delta^{-4}\right), \tag{4.10b}$$
$$MM^\dagger = T\Delta^{-2}T^\dagger + \left\{T\Delta^{-3}T^\dagger, H_0\right\} + \mathcal{O}\left(\Delta^{-4}\right). \tag{4.10c}$$

Combining the above-mentioned results, the series expansion for the effective Hamiltonian, equation 4.4, can be computed explicitly. Hence, the effective Hamiltonian, up to $\mathcal{O}\left(\Delta^{-4}\right)$, reads

$$H_{\text{eff}} = H_0 - T\Delta^{-1}T^\dagger - \frac{\left\{T\Delta^{-2}T^\dagger, H_0\right\}}{2} - \frac{\left\{T\Delta^{-3}T^\dagger, H_0^2\right\}}{2} + 2\frac{\left\{T\Delta^{-1}T^\dagger, T\Delta^{-2}T^\dagger\right\}}{3}. \tag{4.11}$$

This solution can be expanded to an arbitrarily large order, yet for all purposes and intentions the most relevant information stems from low order expansions. In addition, each iteration in this series requires the calculation of a higher power of the inverse matrix Δ^{-1}. Due to the nature of the calculation of the inverse matrix, this imposes a practical limit to second or third order in all but a few simplistic calculations.

In the following sections, we apply LPT to compute effective Hamiltonians for graphene and silicene including SOC.

4.3 Slater–Koster parameters

The basis for all calculations in this chapter is a TB Hamiltonian, constructed from Slater–Koster (SK) parameters [115]. The typical textbook TB is a single band Hamiltonian for a linear chain of atoms, where the one electron can hop from an atom's orbital to its nearest neighbour orbital reads

$$H = \sum_i \left(\epsilon_i a_i^\dagger a_i + t\, a_i^\dagger a_{i+1} + H.c. \right) \tag{4.12}$$

where t is the hopping integral, ϵ_i the on-site energy. Due to its simplicity, this model has been extensively used for systems such as graphene [55], charge density wave metals [17, 116] and many others.

Despite the impressive analytic results obtained with this simple Hamiltonian, there are clear limitations of a model with a single electron hopping from one atom to another and to the same orbital. Fortunately, this model can be easily generalized to account for hopping to other neighbours and orbitals. Such Hamiltonian can be written as

$$H = \sum_{i=1}^{N_a} \sum_{n=1}^{N_n} \sum_{\alpha,\beta} \left[\epsilon^{(\alpha)}_{\mathbf{R}_i} a^\dagger_{\mathbf{R}_i,\alpha} a_{\mathbf{R}_i,\alpha} + \left(t_n^{(\alpha\beta)} a^\dagger_{\mathbf{R}_i,\alpha} a_{\mathbf{R}_i+\boldsymbol{\delta}_n,\beta} + H.c. \right) \right] , \tag{4.13}$$

where i, ϵ_i, $\mathbf{R}_i$ and N_a are the atom index, on-site energy, respective position vector and total number of atoms, n, $\boldsymbol{\delta}_n$ and N_n are the neighbour index, respective distance vector and total number of neighbours with non-zero hopping, α and β are the orbital indices and finally $t_n^{(\alpha\beta)}$ is the respective hopping integral.

The calculation of the hopping integrals is a non trivial problem and a significant numerical challenge. In addition, this falls beyond the scope of this project, and we choose to fit these hopping integrals from experimental data or from *ab-initio* calculations. Nonetheless, it is important to review to some extent the results by Slater and Koster [115], particularly the symmetry properties of such integrals. Using the two-centre approximation [115], it is possible to define all hopping integrals, $E_{\alpha\beta}$, between two bands, α and β, as a function of a minimal set of parameters, $V_{\alpha\beta\gamma}$ (where γ indicates the type of bond, *i.e.* σ, π, etc…) and the bond direction, *i.e.* $(l, m, n) = \boldsymbol{\delta}_n/|\boldsymbol{\delta}_n|$. Most of two-centre integrals for s, p and d can be found in table C.1, those not present in this table can be computed by interchanging the band indices, such that $E_{\beta,\alpha} = (-1)^{\ell_\alpha+\ell_\beta} E_{\alpha,\beta}$

(where ℓ_α is the angular quantum number of atomic orbital α) and/ or changing the direction of the orbitals and the respective directions, *i.e.* $E_{x,y} = lm(V_{pp\sigma} - V_{pp\pi}) \rightarrow E_{x,z} = ln(V_{pp\sigma} - V_{pp\pi})$. Furthermore, the two centre integrals parity is a function of the nearest-neighbour vectors and their respective angular quantum numbers $E_{\alpha,\beta}(\boldsymbol{\delta}) = (-1)^{\ell_\alpha+\ell_\beta} E_{\alpha,\beta}(-\boldsymbol{\delta})$. Due to the long and tedious nature of the evaluation of the SK hopping terms, we present all the relevant terms in appendix §C.2.

In the following subsections we review the calculation of Hamiltonian for systems with honeycomb lattice.

4.3.1 Graphene, the two π bands

We shall use graphene's simple two p_z band Hamiltonian to lay the basics of our procedure to study SOC in 2D materials. The primitive (and reciprocal) vectors for the honeycomb lattice are defined in equations 3.15 and depicted in figure 3.2a. In addition, the nearest neighbour vectors read

$$\delta_1 = a\big(\sqrt{3}/2, -1/2, 0\big) \ , \quad \delta_2 = a\big(0, 1, 0\big) \ , \quad \delta_3 = -a\big(\sqrt{3}/2, 1/2, 0\big) \ . \tag{4.14}$$

In this frame work the Hamiltonian reads

$$H = -t \sum_{\mathbf{R}_i, \boldsymbol{\delta}} a^\dagger_{\mathbf{R}_i} b_{\mathbf{R}_i + \boldsymbol{\delta}} + H.c. \ , \tag{4.15}$$

where $a_{\mathbf{R}_i}$ and $b_{\mathbf{R}_i}$ are fermionic operators for sublattice A and B respectively, $\mathbf{R}_i$ is the position vector for the i^{th} unit cell[1]and $t = V_{pp\pi}$ is the hopping energy for the $\mathrm{p_z}$ band (see table C.1 for details) and $\boldsymbol{\delta}$ are the vectors connecting nearest neighbours[2]. Introducing the Fourier transform of the fermionic operators as

$$a_{\mathbf{R}_i} = \frac{1}{\sqrt{N}} \sum_{\mathbf{k}} e^{-i\mathbf{k}\cdot\mathbf{R}_i} a_{\mathbf{k}} \quad ; \qquad b_{\mathbf{R}_i} = \frac{1}{\sqrt{N}} \sum_{\mathbf{k}} e^{-i\mathbf{k}\cdot\mathbf{R}_i} b_{\mathbf{k}} \ , \tag{4.16}$$

[1]Note that the sum over $\mathbf{R}_i$, runs over the unit cells, which contain two atoms (sublattices) labelled A and B and that A and B are separated by $\boldsymbol{\delta}_2$.

[2]Since we are computing the Hamiltonian with only one band, the on-site energy of the $\mathrm{p_z}$ band only introduces a shift in energy, so for sake of simplicity we ignore it.

the Hamiltonian reads in momentum space as

$$H_{\mathbf{k}} = -t \sum_{\mathbf{k}} \sum_{\boldsymbol{\delta}} e^{-i\mathbf{k}\cdot\boldsymbol{\delta}} a^{\dagger}_{\mathbf{k}} b_{\mathbf{k}} + H.c.\,. \tag{4.17}$$

Taking into account solely nearest neighbour hopping, the Hamiltonian can be simplified to

$$H_{\mathbf{k}} = t \sum_{\mathbf{k}} \left(e^{-i\mathbf{k}\cdot\boldsymbol{\delta}_1} + e^{-i\mathbf{k}\cdot\boldsymbol{\delta}_2} + e^{-i\mathbf{k}\cdot\boldsymbol{\delta}_3} \right) a^{\dagger}_{\mathbf{k}} b_{\mathbf{k}} + H.c. = \sum_{\mathbf{k}} \phi(\mathbf{k}) a^{\dagger}_{\mathbf{k}} b_{\mathbf{k}} + H.c.\,, \tag{4.18}$$

where $\phi(\mathbf{k})$ contains the contribution of each hopping to the nearest neighbour. The previous Hamiltonian can be written compactly as

$$H_{\mathbf{k}} = \left(a^{\dagger}_{\mathbf{k}},\, b^{\dagger}_{\mathbf{k}} \right) \begin{pmatrix} 0 & \phi(\mathbf{k}) \\ \phi^{*}(\mathbf{k}) & 0 \end{pmatrix} \begin{pmatrix} a_{\mathbf{k}} \\ b_{\mathbf{k}} \end{pmatrix} . \tag{4.19}$$

The diagonalization of this Hamiltonian returns the well known energy dispersion of graphene [55].

4.3.2 Honeycomb lattice multi-band Hamiltonian

The work by Kane and Mele [107] introduces the SOC in the simple two $\mathrm{p_z}$ bands Hamiltonian as a perturbation. Since SOC requires interaction with states with non-zero angular momentum, we must add such states to the Hamiltonian. In the case of graphene, common sense would lead us to consider the most likely candidates the other two $2\mathrm{p}$ orbitals, *i.e.* $2\mathrm{p_x}$ and $2\mathrm{p_y}$. Yet, a careful analysis of table C.1 shows that the hopping integral between $2\mathrm{p_z}$ and $2\mathrm{p_x}$ or $2\mathrm{p_z}$ and $2\mathrm{p_y}$ is zero for pristine graphene, a flat monolayer with $n = 0$, therefore the direct interaction between these bands is very small. A detailed discussion of the relevant bands and interaction mechanisms will be addressed in the following subsections. In the case of pristine and homogeneous graphene, the form of the Hamiltonian is a simplification of equation 4.13, in which the hopping amplitudes and on-site energies taken to be independent of the position

$$H = \sum_{\mathbf{R}_i, \boldsymbol{\delta}} \sum_{\alpha \neq \beta} \left[\epsilon^{(\alpha)} \left(a^{\dagger}_{\mathbf{R}_i,\alpha} a_{\mathbf{R}_i,\alpha} + b^{\dagger}_{\mathbf{R}_i,\alpha} b_{\mathbf{R}_i,\alpha} \right) + \left(t^{(\alpha\beta)}_{\boldsymbol{\delta}} a^{\dagger}_{\mathbf{R}_i,\alpha} b_{\mathbf{R}_i+\boldsymbol{\delta},\beta} + H.c. \right) \right] . \tag{4.20}$$

Generalizing the Fourier transformations of the fermionic operators to accommodate an orbital index

$$a_{\mathbf{R}_i,\alpha} = \frac{1}{\sqrt{N}} \sum_{\mathbf{k}} e^{-i\mathbf{k}\cdot\mathbf{R}_i} a_{\mathbf{k},\alpha} \quad ; \qquad b_{\mathbf{R}_i,\alpha} = \frac{1}{\sqrt{N}} \sum_{\mathbf{k}} e^{-i\mathbf{k}\cdot\mathbf{R}_i} b_{\mathbf{k},\alpha} \,, \tag{4.21}$$

and proceeding as in §4.3.1, we obtain the Hamiltonian in the reciprocal space as

$$H_{\mathbf{k}} = \sum_{\mathbf{k},\boldsymbol{\delta}} \sum_{\alpha,\beta} \left[\epsilon^{(\alpha)} \left(a^{\dagger}_{\mathbf{k},\alpha} a_{\mathbf{k},\alpha} + b^{\dagger}_{\mathbf{k},\alpha} b_{\mathbf{k},\alpha} \right) + \left(\phi^{\alpha\beta}_{\boldsymbol{\delta}}(\mathbf{k}) a^{\dagger}_{\mathbf{k},\alpha} b_{\mathbf{k},\beta} + H.c. \right) \right] \tag{4.22}$$

where the elements $\phi^{\alpha\beta}_{\boldsymbol{\delta}}(\mathbf{k}) = t^{(\alpha\beta)}_{\boldsymbol{\delta}} e^{i\mathbf{k}\cdot\boldsymbol{\delta}}$ will be specified latter. Throughout this notes, we shall refer to these elements as SK hopping terms. Following the same procedure, one can write the multi-band Hamiltonian in a matrix form by projecting the Hamiltonian in the basis of the fermionic operators $H_{\mathbf{k}} = \sum_{\mathbf{k},\boldsymbol{\delta}} \Psi^{\dagger}_{\mathbf{k}} \, \mathcal{H} \, \Psi_{\mathbf{k}}$ where

$$\mathcal{H} = \begin{pmatrix} \epsilon_{\alpha_1} & \phi^{\alpha_1\alpha_1}_{\boldsymbol{\delta}}(\mathbf{k}) & 0 & \phi^{\alpha_1\alpha_2}_{\boldsymbol{\delta}}(\mathbf{k}) & \cdots & \phi^{\alpha_1\alpha_n}_{\boldsymbol{\delta}}(\mathbf{k}) \\ \phi^{\alpha_1\alpha_1}_{-\boldsymbol{\delta}}(\mathbf{k}) & \epsilon_{\alpha_1} & \phi^{\alpha_1\alpha_2}_{-\boldsymbol{\delta}}(\mathbf{k}) & 0 & \cdots & 0 \\ 0 & \phi^{\alpha_2\alpha_1}_{\boldsymbol{\delta}}(\mathbf{k}) & \epsilon_{\alpha_2} & \phi^{\alpha_2\alpha_2}_{\boldsymbol{\delta}}(\mathbf{k}) & \cdots & \phi^{\alpha_2\alpha_n}_{\boldsymbol{\delta}}(\mathbf{k}) \\ \phi^{\alpha_2\alpha_1}_{-\boldsymbol{\delta}}(\mathbf{k}) & 0 & \phi^{\alpha_2\alpha_2}_{-\boldsymbol{\delta}}(\mathbf{k}) & \epsilon_{\alpha_2} & \cdots & 0 \\ \vdots & \vdots & \vdots & \vdots & \ddots & \vdots \\ \phi^{\alpha_n\alpha_1}_{-\boldsymbol{\delta}}(\mathbf{k}) & 0 & \phi^{\alpha_n\alpha_2}_{-\boldsymbol{\delta}}(\mathbf{k}) & 0 & \cdots & \epsilon_{\alpha_n} \end{pmatrix}. \tag{4.23}$$

In this notation, the basis vector $\Psi^{\dagger}_{\mathbf{k}}$ is a row vector with the $2n$ elements (n elements for each sub-lattice), *i.e.* two times as many different orbitals used, $\Psi^{\dagger}_{\mathbf{k}} = (a^{\dagger}_{\mathbf{k},\alpha_1}, b^{\dagger}_{\mathbf{k},\alpha_1}, a^{\dagger}_{\mathbf{k},\alpha_2}, b^{\dagger}_{\mathbf{k},\alpha_2}, \ldots, b^{\dagger}_{\mathbf{k},\alpha_n})$.

4.3.3 Multi-band Hamiltonian for pristine graphene

In the case of pristine graphene all nearest neighbours are in plane and equally spaced, therefore all hopping integrals proportional to the z component of nearest neighbour vectors, are zero. From the SK two centre integrals, see table C.1, one can shown that the only orbitals that have a non-zero overlap with the $2\mathrm{p_z}$ orbital are $3\mathrm{d_{zx}}$ and $3\mathrm{d_{yz}}$[3].

[3]Note that we are only interested in bands that lay in a energy range sufficiently closed to the $2\mathrm{p_z}$, therefore the we neglect bands with energy greater or equal to the $4\mathrm{s}$ bands. A hand waiving argument to justify this, can be extracted from perturbation theory, in which all correction are at least inversely proportional to the energy difference between the initial and final state. Therefore, states separated by a large energy difference, should yield a small or insignificant contribution.

To specify the Hamiltonian in equation 4.22, we must determine the hopping terms between all bands with finite overlap. For the sake of brevity, we list all relevant hopping terms, $\phi_{\boldsymbol{\delta}}^{\alpha,\beta}(\mathbf{k})$, in appendix §C.2.1, equations C.2. In addition, the Hamiltonian contains all on-site energies for each band. Therefore, the Hamiltonian matrix reads

$$H_{\mathbf{k}} = \begin{pmatrix} \epsilon_p & \phi_{\boldsymbol{\delta}}^{z,z}(\mathbf{k}) & 0 & \phi_{\boldsymbol{\delta}}^{z,zx}(\mathbf{k}) & 0 & \phi_{\boldsymbol{\delta}}^{z,yz}(\mathbf{k}) \\ \phi_{-\boldsymbol{\delta}}^{z,z}(\mathbf{k}) & \epsilon_p & \phi_{-\boldsymbol{\delta}}^{z,zx}(\mathbf{k}) & 0 & \phi_{-\boldsymbol{\delta}}^{z,yz}(\mathbf{k}) & 0 \\ 0 & \phi_{\boldsymbol{\delta}}^{zx,z}(\mathbf{k}) & \epsilon_d & \phi_{\boldsymbol{\delta}}^{zx,zx}(\mathbf{k}) & 0 & \phi_{\boldsymbol{\delta}}^{zx,yz}(\mathbf{k}) \\ \phi_{-\boldsymbol{\delta}}^{zx,z}(\mathbf{k}) & 0 & \phi_{-\boldsymbol{\delta}}^{zx,zx}(\mathbf{k}) & \epsilon_d & \phi_{-\boldsymbol{\delta}}^{zx,yz}(\mathbf{k}) & 0 \\ 0 & \phi_{\boldsymbol{\delta}}^{yz,z}(\mathbf{k}) & 0 & \phi_{\boldsymbol{\delta}}^{yz,zx}(\mathbf{k}) & \epsilon_d & \phi_{\boldsymbol{\delta}}^{yz,yz}(\mathbf{k}) \\ \phi_{-\boldsymbol{\delta}}^{yz,z}(\mathbf{k}) & 0 & \phi_{-\boldsymbol{\delta}}^{yz,zx}(\mathbf{k}) & 0 & \phi_{-\boldsymbol{\delta}}^{yz,yz}(\mathbf{k}) & \epsilon_d \end{pmatrix}, \tag{4.24}$$

Since the interactions between $3d$ bands, lay at a much higher energy level, we discard these by eliminating the respective hopping integral $V_{dd\sigma} = V_{dd\pi} = V_{dd\delta} = 0$. In addition, we redefine $V_{pp\pi} = t$ and $V_{pd\pi} = t'$. The eigenvalues for this matrix are

$$\lambda_1 = \lambda_2 = \epsilon_d \,, \tag{4.25a}$$

$$\lambda_{3,4} = \frac{\epsilon_d + \epsilon_p}{2} \mp \frac{|\phi_{\boldsymbol{\delta}}^{z,z}|}{2} \pm \sqrt{\left[|\phi_{\boldsymbol{\delta}}^{z,z}(\mathbf{k})| \pm \epsilon_{dp}\right]^2/4 + |\phi_{\boldsymbol{\delta}}^{z,zx}(\mathbf{k})|^2 + |\phi_{\boldsymbol{\delta}}^{z,zy}(\mathbf{k})|^2} \,. \tag{4.25b}$$

$$\lambda_{5,6} = \frac{\epsilon_d + \epsilon_p}{2} \pm \frac{|\phi_{\boldsymbol{\delta}}^{z,z}|}{2} \pm \sqrt{\left[|\phi_{\boldsymbol{\delta}}^{z,z}(\mathbf{k})| \mp \epsilon_{dp}\right]^2/4 + |\phi_{\boldsymbol{\delta}}^{z,zx}(\mathbf{k})|^2 + |\phi_{\boldsymbol{\delta}}^{z,zy}(\mathbf{k})|^2} \,, \tag{4.25c}$$

where $\epsilon_{dp} = \epsilon_d - \epsilon_p$. Note that bands $\lambda_{3,4}$ exhibit a minor dispersion due to the presence of finite finite t' hopping integral, akin to the correction of dispersion of the p bands, $\lambda_{5,6}$. Thus far, the calculation is exact and the hopping terms are defined in the full BZ. Making a series expansion around the high symmetry point $\mathbf{K}$ determines the low energy approximation for the dispersion

$$\lambda_{1,2} = \epsilon_d \,, \tag{4.26a}$$

$$\lambda_{3,4} = \epsilon_d - 2\gamma^2\epsilon_{dp} \mp 2\gamma^2 v_F \hbar|\mathbf{k}| \,, \tag{4.26b}$$

$$\lambda_{5,6} = \epsilon_p \mp (1 - 2\gamma^2) v_F \hbar|\mathbf{k}| - 2\gamma^2\epsilon_{dp} \,, \tag{4.26c}$$

where $2\gamma^2 = 9t'^2/2\epsilon_{dp}^2$ and $v_F = 3at/2\hbar$. This result indicates that the contributions arising from the $p - d$ coupling simply introduce a small renormalization of the Fermi velocity. Therefore, the leading order effect of the direct interaction with the $3d$ bands

can be incorporated into the simple two p_z band model via the renormalization of the Fermi velocity. In addition, the same renormalization factor can be identified in the DoS

$$\rho(\epsilon) = \frac{3\sqrt{3}a^2\hbar^2}{2v_F^2}\frac{\epsilon}{1 - 9V_{pd\pi}^2/2\epsilon_{dp}^2} \simeq \rho_0(\epsilon)\left(1 + \frac{9V_{pd\pi}^2}{2\epsilon_{dp}^2}\right). \tag{4.27}$$

where the renormalized DoS increases slightly compared with the initial model. The common trait here, is that all this renormalization can be accommodated in a single parameter, *i.e.* redefining the hopping integral $V_{pp\pi}$ to fit the data.

This section has reviewed the construction of an Hamiltonian in graphene with multiple bands that will serve as a benchmark test for the calculation of effective Hamiltonians using LPT. The section that follows moves on to consider the calculation of effective Hamiltonians, starting with the calculation of an effective two band Hamiltonian for graphene with corrections from the $p - d$ orbital coupling.

4.4 Effective Hamiltonian for graphene

In §4.3.3 we obtained the TB Hamiltonian for the honeycomb lattice considering the p_z, d_{zx} and d_{yz} orbitals. In spite of the fact that the increase in complexity of the Hamiltonian provides little extra information regarding the low energy physics near ϵ_p, when compared with the simpler p_z orbital Hamiltonian. These results, in particular the eigenvalues for the low energy bands in the vicinity of ϵ_p, provide a good benchmark for the calculation of effective Hamiltonians. Therefore, the first application of our implementation of LPT is to map the Hamiltonian in the $p-d$ basis to an effective Hamiltonian in the p_z basis. Since we are interested in computing the effective Hamiltonian in the p_z orbital basis, the basis defined in equation C.12 is perfectly suitable. In this basis the full Hamiltonian can be divided into the following block matrices

$$H_0 = \begin{pmatrix} \epsilon_p & \phi_{\boldsymbol{\delta}}^{z,z}(\mathbf{q}) \\ \phi_{-\boldsymbol{\delta}}^{z,z}(\mathbf{q}) & \epsilon_p \end{pmatrix}, \; T = \begin{pmatrix} 0 & \phi_{\boldsymbol{\delta}}^{z,zx}(\mathbf{q}) & 0 & \phi_{\boldsymbol{\delta}}^{z,yz}(\mathbf{q}) \\ \phi_{-\boldsymbol{\delta}}^{z,zx}(\mathbf{q}) & 0 & \phi_{-\boldsymbol{\delta}}^{z,yz}(\mathbf{q}) & 0 \end{pmatrix}, \; \Delta = \epsilon_d \mathbb{1}_4 \,, \tag{4.28}$$

according to equation 4.1. Having defined the relevant block matrices, the respective effective Hamiltonian computed by LPT, equation 4.4, reads

$$H_{\text{eff}} = \begin{pmatrix} \epsilon_p - \frac{1+a^2|\mathbf{k}|^2}{8/9}\frac{\epsilon_{dp}t'^2}{\epsilon_d^2} & \frac{3at(k_x-ik_y)}{2}\left[1-\left(1+\frac{a^2|\mathbf{k}|^2}{4}\right)\frac{9t'^2}{2\epsilon_d^2}\right] \\ \frac{3at(k_x+ik_y)}{2}\left[1-\left(1+\frac{a^2|\mathbf{k}|^2}{4}\right)\frac{9t'^2}{2\epsilon_d^2}\right] & \epsilon_p - \frac{1+a^2|\mathbf{k}|^2}{8/9}\frac{\epsilon_{dp}t'^2}{\epsilon_d^2} \end{pmatrix} . \quad (4.29)$$

where, we already made the small $\mathbf{k}$ expansion around the $\mathbf{K}$ point. Taking the limit $a|\mathbf{k}| \ll 1$ the effective Hamiltonian reads

$$H_{\text{eff}} = \begin{pmatrix} \epsilon_p - 2\gamma'^2\epsilon_{dp} & (1-2\gamma'^2)v_F\hbar(k_x - ik_y) \\ (1-2\gamma'^2)v_F\hbar(k_x + ik_y) & \epsilon_p - 2\gamma'^2\epsilon_{dp} \end{pmatrix} , \quad (4.30)$$

where $2\gamma'^2 = 9t'^2/2\epsilon_d^2$. Setting the on-site potential for the p-bands to zero, $\epsilon_p = 0$, recovers the result obtained in equation 4.26c with the exact diagonalization of the Hamiltonian.

In the following sections, we approximate our ultimate goal of handling the spin-orbit coupling.

It starts with coupling between p and d orbitals and proceeds to coupling between σ bands and, finally, lattice deformations are introduced.

4.5 Atomic Spin-Orbit effects

The previous discussion regarding the electronic properties deliberately neglected the spin of electrons. In systems such as graphene, the SOC is most frequently ignored. As a result, spin only accounts for a degeneracy constant. This stems from the fact that, the SOC constant increases with the increase of the atomic number. Due to carbon's small atomic number, barely any SOC effects are expected in graphene. Nonetheless, it was shown that, in spite of its small magnitude, SOC must open a gap at the Dirac points in graphene, Kane and Mele [107]. This seminal work by Kane and Mele paved the way for a large expansion of research on the field of spintronics not only in graphene based devices [117–121] and more generally spintronics in 2D materials [112, 122–127].

The SOC connects the spin and angular momentum degree's of freedom in each orbital and can be defined simply by the dot product of the angular momentum operator

L with the spin operator **s** and reads

$$H_{\mathrm{SOC}} = \sum_{\ell} \xi_{\alpha,\beta} \langle \mathbf{L} \cdot \mathbf{s} \rangle_{\alpha,\beta} \,, \tag{4.31}$$

where $\xi_{\alpha,\beta}$ is the SOC strength for the orbitals α, β and $\langle \mathbf{L} \cdot \mathbf{s} \rangle_{\alpha,\beta}$ is the expectation value of the $\mathbf{L} \cdot \mathbf{s}$ operator in the basis of the atomic orbitals, namely p_z, s, p_x and p_y. The calculation and results for the matrix elements $\langle \mathbf{L} \cdot \mathbf{s} \rangle_{\alpha,\beta}$ is discussed in §C.3. Therefore, the SOC Hamiltonian reads

$$H_{\mathbf{k}}^{SO} = \sum_{\mathbf{k}} \sum_{\alpha,\beta} \sum_{\sigma,\sigma'} \xi_{\alpha,\beta} \langle \mathbf{L} \cdot \mathbf{s} \rangle_{\alpha,\beta} \left(a^{\dagger}_{\mathbf{k},\alpha,\sigma} a_{\mathbf{k},\beta,\sigma'} + b^{\dagger}_{\mathbf{k},\alpha,\sigma} b_{\mathbf{k},\beta\sigma'} \right) , \tag{4.32}$$

where σ, σ' are the spin indices. Since electrons have spin $s = 1/2$, the size of the Hamiltonian matrix doubles. The full Hamiltonian becomes

$$H = H_{\mathbf{k}}^{(0)} + H_{\mathbf{k}}^{SO} \,. \tag{4.33}$$

The evaluation of the $\langle \mathbf{L} \cdot \mathbf{s} \rangle$ matrix elements, discussed in appendix C.3, shows that diagonal terms in the dot product are null, *i.e.* $\langle \mathbf{L} \cdot \mathbf{s} \rangle_{\alpha,\alpha} = 0, \forall\, \alpha = \{s, p_x, \ldots\}$. Hence, it is impossible (within the context of the TB model) to obtain SOC effects using only one type orbitals, such as $\mathrm{p_z}$. In the following subsection, SOC is considered within the framework of the π band Hamiltonian.

4.5.1 Effective Hamiltonian for π bands

In the context of the π bands for graphene, *i.e.* $\mathrm{p_z}$, $\mathrm{d_{xz}}$ and $\mathrm{d_{yz}}$ orbitals, one expects to observe a small but finite SOC between the d orbitals. The presence of SOC lifts the spin degeneracy of the Hamiltonian and doubles the basis. For the system under consideration a good basis is

$$\begin{aligned} \Psi^{\dagger}_{\mathbf{k}} = \Big\{ & a^{\dagger}_{\mathbf{k},p_z,+} \,,\; b^{\dagger}_{\mathbf{k},p_z,+} \,,\; a^{\dagger}_{\mathbf{k},d_{zx},+} \,,\; b^{\dagger}_{\mathbf{k},d_{zx},+} \,,\; a^{\dagger}_{\mathbf{k},d_{yz},+} \,,\; b^{\dagger}_{\mathbf{k},d_{yz},+} \,, \\ & a^{\dagger}_{\mathbf{k},p_z,-} \,,\; b^{\dagger}_{\mathbf{k},p_z,-} \,,\; a^{\dagger}_{\mathbf{k},d_{zx},-} \,,\; b^{\dagger}_{\mathbf{k},d_{zx},-} \,,\; a^{\dagger}_{\mathbf{k},d_{yz},-} \,,\; b^{\dagger}_{\mathbf{k},d_{yz},-} \Big\} \,. \end{aligned} \tag{4.34}$$

The respective TB Hamiltonian reads

$$\mathcal{H}_\pi = \begin{pmatrix} H_+ & 0 \\ 0 & H_- \end{pmatrix}, \tag{4.35}$$

where the block matrices are

$$H_\pm = \begin{pmatrix} \epsilon_p & \phi_{\boldsymbol{\delta}}^{z,z} & 0 & \phi_{\boldsymbol{\delta}}^{z,zx} & 0 & \phi_{\boldsymbol{\delta}}^{z,yz} \\ \phi_{-\boldsymbol{\delta}}^{z,z} & \epsilon_p & \phi_{-\boldsymbol{\delta}}^{z,zx} & 0 & \phi_{-\boldsymbol{\delta}}^{z,yz} & 0 \\ 0 & \phi_{\boldsymbol{\delta}}^{zx,z} & \epsilon_d & \phi_{\boldsymbol{\delta}}^{zx,zx} & \mp i\xi_d/2 & \phi_{\boldsymbol{\delta}}^{zx,yz} \\ \phi_{-\boldsymbol{\delta}}^{zx,z} & 0 & \phi_{-\boldsymbol{\delta}}^{zx,zx} & \epsilon_d & \phi_{-\boldsymbol{\delta}}^{zx,yz} & \mp i\xi_d/2 \\ 0 & \phi_{\boldsymbol{\delta}}^{yz,z} & \pm i\xi_d/2 & \phi_{\boldsymbol{\delta}}^{yz,zx} & \epsilon_d & \phi_{\boldsymbol{\delta}}^{yz,yz} \\ \phi_{-\boldsymbol{\delta}}^{yz,z} & 0 & \phi_{-\boldsymbol{\delta}}^{yz,zx} & \pm i\xi_d/2 & \phi_{-\boldsymbol{\delta}}^{yz,yz} & \epsilon_d \end{pmatrix}. \tag{4.36}$$

The nature of this Hamiltonian stems from several properties. First, the SOC between d_{zx} and d_{yz} orbitals is diagonal in spin, *i.e.* $\propto \sigma_z$ (see appendix C.3 table C.4 for details). Consequently, no spin flip terms are present and the TB Hamiltonian can be cast in a block diagonal form. Hence, the two independent matrices present in equation 4.35. Second, the SOC is present only between the d_{zx} and d_{yz}. Hence, it is completely confined to the Δ matrix (see notation in §4.2) as defined in appendix §C.4, equations C.14. Hence, the leading order term of ξ_d in Δ^{-1} sets the leading order contribution to the effective Hamiltonian.

Following the procedure outlined previously, the effective Hamiltonians (up to second order in the parameter) are spin independent $H_+^{\text{eff}} = H_-^{\text{eff}}$. Hence, the effective Hamiltonian reduces to a two band spin degenerate Hamiltonian. Considering the small $\mathbf{k}$ expansion around the $\mathbf{K}$ point it reads

$$H_\pi^{\text{eff}} = \begin{pmatrix} \epsilon_p - \frac{9t'^2}{2\epsilon_{dp}-\xi_d} & \frac{t(q_x-iq_y)}{\xi_d^2-4\epsilon_{dp}^2}\frac{18t'^2(4\epsilon_{dp}^2+\xi_d^2)-(\xi_d^2-4\epsilon_{dp}^2)^2}{\xi_d^2-4\epsilon_{dp}^2} \\ \frac{t(q_x+iq_y)}{\xi_d^2-4\epsilon_{dp}^2}\frac{18t'^2(4\epsilon_{dp}^2+\xi_d^2)-(\xi_d^2-4\epsilon_{dp}^2)^2}{\xi_d^2-4\epsilon_{dp}^2} & \epsilon_p - \frac{9t'^2}{2\epsilon_{dp}+\xi_d} \end{pmatrix}, \tag{4.37}$$

where, to keep consistent with the linear approximation of the elements $\phi_{\boldsymbol{\delta}}^{\alpha,\beta}$, we retain only linear terms in q_x or q_y. The diagonalization is straight-forward and the (spin

degenerate) respective eigenvalues read

$$\lambda_{\pm} = \frac{18t'^2\epsilon_{dp}}{|\xi_d^2 - 4\epsilon_{dp}^2|} \pm \sqrt{\left(\frac{9t'^2\xi_d}{\xi_d^2 - 4\epsilon_{dp}^2}\right)^2 + v_F^2\hbar^2|\mathbf{k}|^2\left[1 - 18t'^2\frac{\xi_d^2 + 4\epsilon_{dp}^2}{(\xi_d^2 - 4\epsilon_{dp}^2)^2}\right]^2}. \tag{4.38}$$

This result is consistent with the result in the absence of SOC, *i.e.* $\xi_d \to 0$. The first term corresponds to the vertical shift of both bands and the constant term inside the square root, the gap term, only exists for finite SOC.

Moreover, taking into consideration the magnitude of the SOC with respect to the energy level separation, *i.e.* $\xi_d^2/2\epsilon_{dp}^2 \ll 1$, the Hamiltonian reduces to

$$H_{\text{eff}} \simeq \begin{pmatrix} -\frac{9t'^2}{2\epsilon_d}\left(1 - \frac{\xi_d}{2\epsilon_d}\right) & v'_F\hbar(k_x - ik_y) \\ v'_F\hbar(k_x + ik_y) & -\frac{9t'^2}{2\epsilon_d}\left(1 + \frac{\xi_d}{2\epsilon_d}\right) \end{pmatrix} \simeq v'_F\hbar\,\mathbf{k}\cdot\boldsymbol{\sigma} + \gamma^2\epsilon_d\mathbb{1} - \xi_d\,\gamma^2\sigma_z\,, \tag{4.39}$$

where $\sigma_i : i = \{x, y, z\}$ are Pauli pseudo-spin matrices for the honeycomb lattice basis and ξ_d is the SOC constant for d orbitals. This Hamiltonian can be easily diagonalized and yields the eigenvalues consistent with equation 4.38, with gap $E_g = \gamma^2\xi_d$. Taking typical values for the respective parameters, the spin–orbit gap due to $\mathrm{d_{zx}}$ and $\mathrm{d_{yz}}$ interaction is very small, $E_{\text{gap}}^{\text{SOC}} \sim 24\,\mu\text{eV}$, following in line with other theoretical and DFT and/or *ab-initio* estimates [109] for SOC between p and d orbitals. Temperatures associated with this energy are impressively small, $T = E_g/k_B \sim 24\times10^{-6}/8.617\times10^{-5} \sim 12\,\text{mK}$. Hence, for all intents and purposes, SOC between π bands in pristine graphene is negligible.

The following subsection considers the coupling between the orbitals present in the so-called σ bands.

4.5.2 Spin–orbit coupling with sigma bands

In §4.4 we focused our attention solely in bands composed of orbitals that have a finite overlap with the $\mathrm{p_z}$ orbital, while neglecting interactions with other bands. Below, we address the effects arising between SOC with the otherwise orthogonal σ bands (with respect to p_z basis). The so-called σ-orbitals comprise the s, p_x and p_y orbitals responsible for the $\mathrm{sp_2}$ hybridization in the honeycomb lattice. Most frequently, these bands are associated with the mechanical properties of system, for instance the carbon–carbon

interaction in graphene. Whereas, the π-bands, associated with the *dangling* $\mathrm{p_z}$ orbitals, are mapped to the electronic properties of the system.

Following the procedure outlined in the previous sections, we compute an effective low energy Hamiltonian in the p_z basis using LPT. In this case, the SOC is confined to the p orbitals and contains spin-flipping terms, see table C.2. Consequently, the TB Hamiltonian cannot be cast into a block diagonal form in the spin degree of freedom, as was the case in the previous section. Furthermore, for the sake of simplicity, we keep the TB Hamiltonian as simple as possible, setting zero energy at ϵ_p and restrict the hopping terms. The following calculations consider hopping between p_z orbitals and hopping between s, p_x and p_y. Finally, basis and respective Hamiltonian read

$$\begin{aligned}\Psi^\dagger_{\mathbf{k}} = \Big\{ & a^\dagger_{\mathbf{k},p_z,+}\,,\ b^\dagger_{\mathbf{k},p_z,+}\,,\ a^\dagger_{\mathbf{k},p_z,-}\,,\ b^\dagger_{\mathbf{k},p_z,-}\,,\ a^\dagger_{\mathbf{k},s,+}\,,\ b^\dagger_{\mathbf{k},s,+}\,,\ a^\dagger_{\mathbf{k},s,-}\,,\ b^\dagger_{\mathbf{k},s,-}\,, \\ & a^\dagger_{\mathbf{k},p_x,+}\,,\ b^\dagger_{\mathbf{k},p_x,+}\,,\ a^\dagger_{\mathbf{k},p_x,-}\,,\ b^\dagger_{\mathbf{k},p_x,-}\,,\ a^\dagger_{\mathbf{k},p_y,+}\,,\ b^\dagger_{\mathbf{k},p_y,+}\,,\ a^\dagger_{\mathbf{k},p_y,-}\,,\ b^\dagger_{\mathbf{k},p_y,-}\Big\}\,, \end{aligned} \tag{4.40}$$

$$\mathcal{H} = \begin{pmatrix} H_\pi & H_{\pi\sigma} \\ H^\dagger_{\pi\sigma} & H_\sigma \end{pmatrix}. \tag{4.41}$$

Before proceeding with the projection, we compute numerically the spectrum of the Hamiltonian by means of a full numerical diagonalization. In figure 4.1 we plot the numerical evaluation of the spectrum along the $\mathbf{\Gamma}, \mathbf{M}, \mathbf{K}, \mathbf{\Gamma}, \mathbf{K}$ path. Given the small magnitude of the SOC, it is impossible to distinguish the effects in the band structure at energy scales comparable with the band width of the system. Therefore, to visualize the effect of SOC, we artificially increase the coupling constant by a factor of 300, where $\xi_p^{(0)} = 2.8\,\mathrm{meV}$. In addition to breaking the spin degeneracy, a qualitative analysis shows significant deformation of energy dispersion in the vicinity of the $\mathbf{\Gamma}$ point and the opening of a small gap at $\mathbf{K}$. Yet, apart from this significant change, the separation between the respective bands remains large (several eV) for any reasonable SOC constant. Therefore, the low energy physics remains dominated by the properties of the Hamiltonian in the vicinity of the $\mathbf{K}$ point. In figure 4.2, we focus in the vicinity of the $\mathbf{K}$ point. Due to the small magnitude of the SOC, the effect reduces to a very small gap and a vertical shift of the bands, such that the bottom of the conduction band lies at the energy for p bands (zero energy due to the fact that we set $\epsilon_p = 0$). Moreover, the linear dispersion is quickly recovered in the vicinity of the high symmetry point.

Regarding the calculation of the effective Hamiltonian, the calculation of the inverse of H_σ for $\mathbf{q} \neq 0$ for a generic point in the BZ returns an exceptionally complex matrix. As a result, we are forced to consider particular solutions of the inverse matrix. From the numerical diagonalization, we identify that the SOC gap emerges at the high symmetry **K** point. To study this particular case, we compute the effective Hamiltonian at the high symmetry point

$$H_{\text{eff}}(\mathbf{K}) = \begin{pmatrix} 0 & 0 & 0 & 0 \\ 0 & 4\epsilon_{ps}\xi_p^2/9V_{sp\sigma}^2 & 0 & 0 \\ 0 & 0 & 4\epsilon_{ps}\xi_p^2/9V_{sp\sigma}^2 & 0 \\ 0 & 0 & 0 & 0 \end{pmatrix}. \tag{4.42}$$

This result reproduces the expected gap $E_{\text{gap}} = 4\epsilon_{ps}\,\xi_p^2/9V_{sp\sigma}^2 = \xi_p^2/\epsilon_{ps}\gamma_s^2$, where $\epsilon_{ps} = \epsilon_s - \epsilon_p$ and $\gamma_s^2 = 9V_{sp\sigma}^2/4\epsilon_{ps}^2$ [109, 117] and fits the results from the full numerical diagonalization.

Although it was not possible to analytically obtain an effective Hamiltonian at finite $\mathbf{k}$, even in the vicinity of the K point, is possible to write down the effective Hamiltonian based on these results. By considering the results from the full numerical diagonalization and the previous result, we can write the effective low energy Hamiltonian around **K** as

$$H = v_F\hbar\,\mathbf{k}\cdot\boldsymbol{\sigma} + \frac{\mathbb{1} - \sigma_z s_z}{2}\frac{\xi_p^2}{\epsilon_{ps}\gamma_s^2} \tag{4.43}$$

where v_F is not determined explicitly but, from the numerical diagonalization, it can be shown to reduce to the Fermi velocity in the absence of SOC by a comparison of the slope of the blue and red curves in figure 4.2.

Thus far, results, particularly the gap, indicate that the effect of SOC between p bands is significantly smaller than the effect arising from the d bands. This indicates that pristine graphene is not a good candidate for applications or devices requiring a large band gap. Notwithstanding these results, numerical results indicate that the degenerate σ bands experience strong SOC effects. Hence, any physical quantity dependent on these bands should be subject to the effect of SOC. In a perfectly flat crystal, the SK integrals between p_z and the σ bands are identically zero, see table C.1 in appendix §C.1.

In the following section we take into consideration a particular type of lattice de-

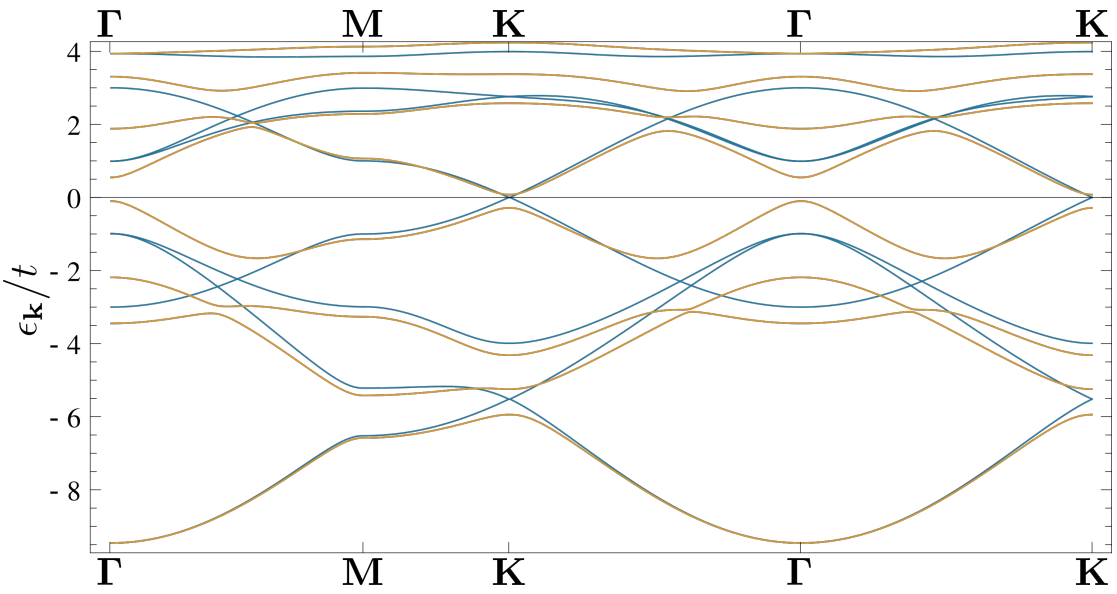

Figure 4.1: Spectrum with and without SOC along the high symmetry path $\mathbf{\Gamma}$, $\mathbf{M}$, $\mathbf{K}$, $\mathbf{\Gamma}$, $\mathbf{K}$ considering p_z, s, p_x and p_y bands. The solid blue lines represent the dispersion without SOC and the brown lines represent the energy dispersion with an increased coupling constant, such that $\xi_p = 300\xi_p^{(0)}$, where $\xi_p^{(0)} = 2.8\,\mathrm{meV}$. [109]. The coupling was artificially increased to allow the visualization of the SOC, which would otherwise be invisible in this energy scale. The energy dispersions were computed by numerical diagonalization of the full TB Hamiltonian with s and p bands.

formation and compute the dependence of the gap as a function of lattice deformation.

4.5.3 The buckled honeycomb

Insofar, we have considered corrections to the system Hamiltonian which arise solely from interactions with additional bands and the respective SOC. In this section, we address the effects of lattice deformation on the system. Among the plethora of possible lattice deformations, we consider a simple vertical displacement of one sub-lattice with respect to the translation plane, in figure 4.3, we depict the buckling distortion of the honeycomb lattice, 3.2a, by projecting it in the plane yOz. This deformation preserves the fundamental symmetry of the honeycomb lattice, the three-fold rotation symmetry, while breaking other lattice symmetries such as the horizontal mirror symmetry.

This small deformation leaves the primitive (and reciprocal) vectors unchanged up to a constant factor determined by the buckling angle, equations C.4, but changes significantly the nearest neighbour vectors with the inclusion of a finite component along the z direction. Below, we address the calculation of the Hamiltonian at the high symmetry point $\mathbf{K}$ as a function of a small deformation of the lattice.

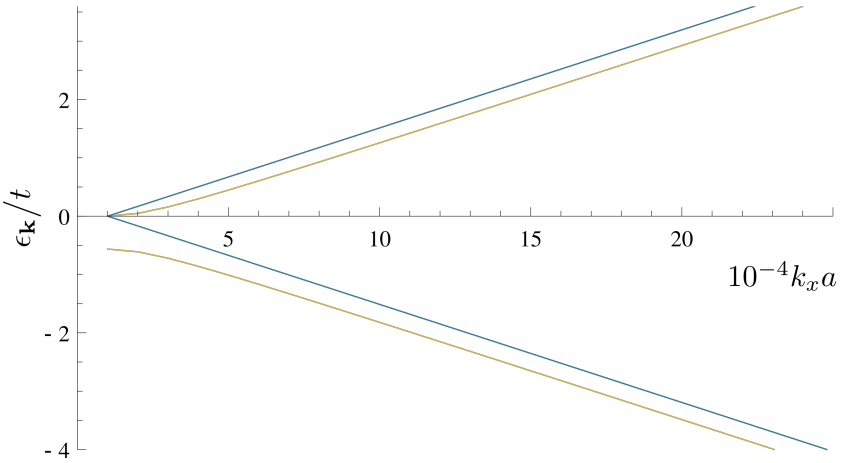

Figure 4.2: Spectrum with and without SOC from the **K** point towards the **Γ**, considering p_z, s, p_x and p_y bands. The blue line shows the dispersion without gap and brown line shows the dispersion with SOC from the p bands. The energy dispersions were computed from by numerical diagonalization of the full TB Hamiltonian with s and p bands.

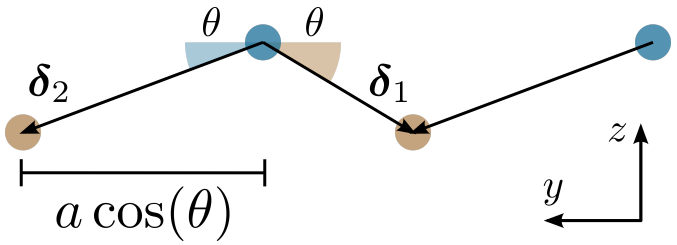

Figure 4.3: Projection on yOz plane of the buckled honeycomb lattice. The buckling distortion consists in the uniform vertical (along the z-direction) displacement of sublattice A with respect to sublattice B (or vice-versa). The projection on the lattice plane, xOy, is a normal honeycomb lattice, as depicted in figure 3.2a, with a redefined lattice parameter $a' = a\cos(\theta)$, where θ measures the distortion angle with respect to the flat, undeformed, lattice. Note that the difference between the blue and brown representations of the buckling angle, θ, are a consequence of distortion cause by the yOz projection.

From the qualitative analysis of the full numerical diagonalization, it appears that the degenerate σ bands experience the most significant change under the presence of SOC. Hence, we consider once more the p_z and σ orbital basis used in the previous section, equation 4.40. The lattice deformation changes significantly the calculation of the SK hopping terms, but the procedure follows as outlined above. For the sake of brevity, we present all finite contributions to the SK hopping terms in appendix §C.2.2, equations C.6

Having defined the Hamiltonian, we proceed with the calculation of the effective Hamiltonian, including terms up to $\mathcal{O}(\Delta^{-4})$. As discussed in §4.5, the calculation of an effective Hamiltonian for $\mathbf{q} \neq 0$ is non-trivial due to the necessity to invert a 12×12 matrix and could not be completed to this date. Below, we show the results obtain at K

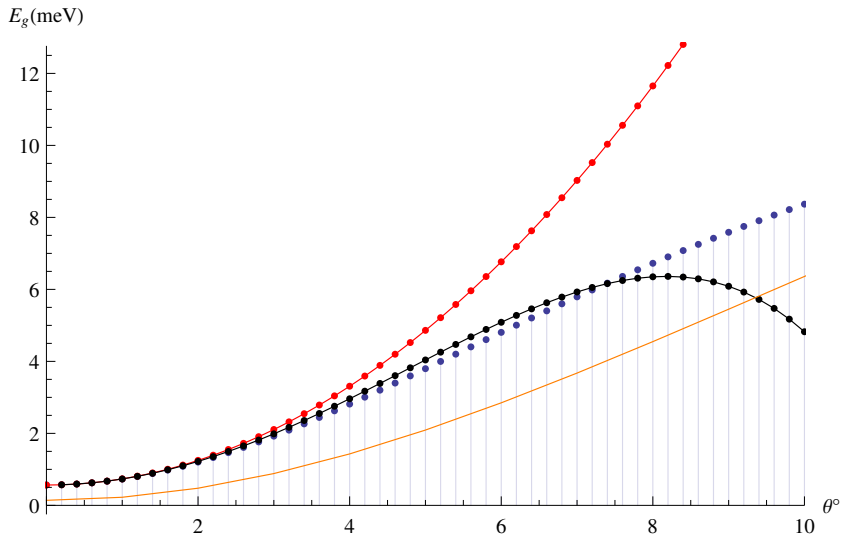

Figure 4.4: Energy gap at the K point. The blue dots were computed by full numerical diagonalization of the Hamiltonian, red solid line with dots was computed from the effective Hamiltonian using all terms up to $\mathcal{O}\left(\Delta^{-3}\right)$ in LPT, black solid line with dots was computed from the effective Hamiltonian using all terms up to $\mathcal{O}\left(\Delta^{-4}\right)$ and the solid orange line is the result from [128].

point.

We begin with the consistency test of computing the effective Hamiltonian and take the particular solution for $\theta = 0$. In this case the effective Hamiltonian at the **K** point reads

$$H = v_f \hbar \mathbf{k} \cdot \boldsymbol{\sigma} + \frac{\mathbb{1} - \sigma_z s_z}{2} \frac{\xi_p^2}{\epsilon_{ps} \gamma_s^2} \left(1 - \frac{2\xi_p}{\epsilon_{ps} \gamma_s^2}\right) + \frac{\mathbb{1} + \sigma_z s_z}{2} \gamma_p \xi_p^3 \,, \tag{4.44}$$

where $\gamma_p = 9\left(V_{pp\pi} - V_{pp\sigma}\right)^2/8$. The differences to the previous result, equation 4.43, stem solely from the third order terms in ξ_p, as expected with the generalization up to $\mathcal{O}\left(\xi_p^4\right)$ in the Löwdin partitioning scheme.

At a finite buckling angle θ, both the effective Hamiltonian matrix and the respective eigenvalues are composed of extensive and complex trigonometric functions dependent on the buckling angle, rendering the analytic result useless for analytic calculations. Nonetheless, good estimates can be computed by Taylor series in the buckling angle. In figure 4.4, we plot the energy gap for silicene at the high symmetry **K** point as a function of deformation angle for comparison. The numerical values for SK integrals and Spin–Orbit (SO) coupling follow ref. [128]. The gap is computed in three different ways: by full numerical diagonalization of the Hamiltonian, by evaluation of the eigenvalues for the effective Hamiltonian and the evaluation of the solution proposed by [128], see

equation 4.46. The Taylor series for the gap reads

$$E_g/t = 5.04 \times 10^{-4} + 5.00\,\theta^2 - 12.8\,\theta^4\,. \tag{4.45a}$$

As highlighted by both the red and black curves, the Taylor expansion quickly diverges for buckling angles greater than $8°$. A previous work by [128] proposes a simple analytic solution for the gap as a function of the deformation angle, which reads

$$\lambda_1 = \frac{\xi_p \epsilon_{ps}^2 \left(V_{pp\pi} - V_{pp\sigma}\right)^2 \cot^2\theta}{9V_{sp\sigma}^4 \left(1 + \frac{\left(V_{pp\pi}-V_{pp\sigma}\right)^2 \cos^2\theta}{V_{sp\sigma}^2}\left(1 + \frac{2\epsilon_{ps}^2}{V_{sp\sigma}^2 \sin^2\theta}\right)\right)}\;; \quad \lambda_2 = -\frac{\xi_p^2 \epsilon_{ps}}{18V_{sp\sigma}^2 \sin^2\theta}\,. \tag{4.46}$$

This solution provides a beautiful closed-form. Nonetheless, the result significantly under estimates the exact result. The underestimate in the full range, because it is based in a blunt approximation, namely in equations 19 of [128], which are only valid at $\theta = 0$.

The method discussed throughout this chapter is general and can be quickly applied to other materials. Moreover, the above-mention results can be applied to other crystals with an underlying honeycomb lattice, such as silicene, germanene and stanene [128–131]. Germanene and stanene exhibit a large gap, estimates $E_g^{Ge} \sim 23.9 - 93\,\mathrm{meV}$, $E_g^{Sn} \sim 73.5 - 129\,\mathrm{meV}$, respectively [128]. In addition to the large gap, these materials exhibit topological insulator phases [129–134]. Combining both properties with the (quasi) two dimensionality, these materials stand as good platforms to develop new and exciting knowledge and applications, expanding significantly the already vast domain of (quasi) two dimensional physics.

Conclusion

The main goal of this thesis was to determine linear and non-linear interactions of light with two dimensional crystals. Current methods to compute the response function for solids relies exclusively on the interaction between light and matter, within the framework of independent particles. Given the importance of interactions with phonons, plasmons and the frequently pivotal role of disorder in condensed matter, we aimed at development of a more generic method, capable of handling (at least to some extent) the natural interactions of system. To meet this goal, we review the calculation of the response function to an external arbitrary perturbation within the framework of non-equilibrium formalism and diagrammatic analysis. Moreover, our results show that, by considering an adiabatic coupling for the interaction the general response reduces to the response determined by the standard methods. Furthermore, our results indicate that different choices of coupling to radiation, can lead to different results for second and higher order processes, §1.5. In the case of second order current response, our results show significant differences between the results computed when considering the minimal coupling, *i.e.* the so-called velocity gauge, and the direct coupling, *i.e.* the length gauge. The former neglects all contributions arising from mixed inter/intraband processes. In the particular case of a two band systems, the current response computed in minimal coupling is identically zero by parity symmetry. Whereas, the latter generates a finite response for systems such as monolayer hBN.

Regarding the linear response in GNRs, our results show that strong and tunable anisotropic optical absorption can be obtained with GNRs, by proper choice of ribbon's width and amplification of medium impedance. Quantitative analysis of GNR dichroism forecasts a very high degree of polarization, $\sim 85\%$, taking into account the effects disorder, which altogether make this an impressive result given the atomic thickness of graphene. Given the current state of the art of techniques in precision patterning and

growth of narrow GNRs, should be possible to build test devices operating in the THz and infra-red bands, paving the way for working optical elements in the low energy bands.

With respect to studies on the photocurrent generation in hexagonal lattices, our studies show several interesting results. First, for all systems under consideration, the dominant process involved in the generation of photocurrent involves both inter and intraband transitions. Moreover, our results allow for a detailed characterization the effects caused by manipulation of several external and internal parameters, such as temperature, chemical potential and magnitude of the gap. Regarding doping, the effect on monolayers is essentially Pauli blocking at photon energy $\hbar\omega = 2|\mu|$, with the temperature defining the sharpness of the effect. In bilayers, chemical doping opens secondary channels for the photocurrent at the photon energies comparable to energy separation between the two conduction (or valence) bands. In the case of BBG, results show that the photocurrent is highly sensitive to the chemical potential. Furthermore, for photon energies comparable to separation between the two conduction bands, the photocurrent can be continuously tuned from a positive maximum at the charge neutrality, down to zero inverting the current and for specific frequencies reaching an absolute value comparable to the undoped system. This particular case might prove interesting for applications in opto-electronics and other fields.

An important limitation, common to the studies on the linear response of GNRs and on the photocurrent in honeycomb lattices, is the fact that both rely exclusively on the intrinsic response of system without the presence of sources of scattering or other interactions with the system. This deserves further attention and we plan to address it in the near future. In the case of BBG, it is known that electrons in graphene couple phonons in the substrate, introducing a mechanism capable of supporting momentum transfer[135]. As regards hBN, ab-initio results indicate strong interactions with excitons. On top of this, it is known that the effect of excitons changes significantly the linear response and second harmonic generation on hBN and two dimensional materials [136, 137].

The above-mentioned limitations highlight the importance of generalizing the method of calculating the response to an external perturbation in the context of condensed matter. Notwithstanding these limitations, these our results shed light on the intrinsic

mechanisms responsible for the generation of linear and quadratic response.

With regards to the studies on the SOC, our results show that LPT provides and alternative technique to determine the effective Hamiltonian for several systems, by means of a projection in the an subspace of the original basis. The calculation of the Hamiltonian buckled honeycomb highlights the potential of this technique to extract information from an Hamiltonian that would otherwise only be useful for numerical calculations. In spite of the interesting results obtained with this technique, it suffers from several shortcomings. Particularly, the calculation of the inverse matrix Δ^{-1} and respective powers. This introduces a daunting problem that cannot be easily solved.

On a final note, it is worth mentioning this thesis is accompanied by large body of numerical and analytic calculations computed entirely or partially with support from computational utilities. The challenges associated with these tasks provided the author with an opportunity to acquire an important set of skills in several programming languages and software utilities.

This page was intentionally left blank.

Bibliography

[1] P. Olbrich et al. "Observation of the orbital circular photogalvanic effect". In: *Physical Review B* 79.12 (2009), p. 1302. DOI: 10.1103/PhysRevB.79.121302 (cit. on pp. 1, 53, 54).

[2] J. Karch et al. "Dynamic Hall Effect Driven by Circularly Polarized Light in a Graphene Layer". In: *Physical Review Letters* 105.22 (2010), p. 227402. DOI: 10.1103/PhysRevLett.105.227402 (cit. on pp. 1, 53, 54, 59, 70).

[3] Vl. a. Margulis, E. E. Muryumin, and E. a. Gaiduk. "Second-order nonlinear optical response of zigzag BN single-walled nanotubes". In: *Physical Review B* 82.23 (2010), p. 235426. DOI: 10.1103/PhysRevB.82.235426 (cit. on p. 1).

[4] Chongyun Jiang et al. "Helicity-dependent photocurrents in graphene layers excited by midinfrared radiation of a CO_2 laser". In: *Physical Review B* 84.12 (2011), p. 125429. DOI: 10.1103/PhysRevB.84.125429 (cit. on pp. 1, 53, 54, 59, 68, 70, 78–83).

[5] J. W. McIver et al. "Control over topological insulator photocurrents with light polarization." In: *Nature Nanotechnology* 7.2 (2012), pp. 96–100. DOI: 10.1038/nnano.2011.214 (cit. on pp. 1, 53, 54, 123).

[6] Vl. a. Margulis, E. E. Muryumin, and E. a. Gaiduk. "Large nonlinear optical rectification in atomic hexagonal layers with broken space inversion symmetry". In: *Journal of Optics* 15.10 (2013), p. 105204. DOI: 10.1088/2040-8978/15/10/105204 (cit. on p. 1).

[7] Vl. a. Margulis, E E Muryumin, and E. a. Gaiduk. "Optical second-harmonic generation from two dimensional hexagonal crystals with broken space inversion symmetry". In: *Journal of Physics: Condensed Matter* 25.19 (2013), p. 195302. DOI: 10.1088/0953-8984/25/19/195302 (cit. on p. 1).

[8] D. J. Moss et al. "Band-structure calculation of dispersion and anisotropy in $\chi \rightarrow^{(3)}$ for third-harmonic generation in Si, Ge, and GaAs". In: *Physical Review B* 41.3 (1990), pp. 1542–1560. DOI: 10.1103/PhysRevB.41.1542 (cit. on p. 1).

[9] J. E. Sipe and Ed Ghahramani. "Nonlinear optical response of semiconductors in the independent-particle approximation". In: *Physical Review B* 48.16 (1993), pp. 11705–11722. DOI: 10.1103/PhysRevB.48.11705 (cit. on pp. 1, 21).

[10] Claudio Aversa and J. E. Sipe. "Nonlinear optical susceptibilities of semiconductors: Results with a length-gauge analysis". In: *Physical Review B* 52.20 (1995), pp. 14636–14645. DOI: 10.1103/PhysRevB.52.14636 (cit. on pp. 1, 5, 12–14, 20, 21, 41, 55, 65).

[11] James R. Chelikowsky and Marvin L. Cohen. "Nonlocal pseudopotential calculations for the electronic structure of eleven diamond and zinc-blende semiconductors". In: *Physical Review B* 14.2 (1976), pp. 556–582. DOI: 10.1103/PhysRevB.14.556 (cit. on p. 1).

[12] Donald H. Kobe. "Gauge-invariant resolution of the controversy over length versus velocity forms of the interaction with electric dipole radiation". In: *Physical Review A* 19.1 (1979), pp. 205–214. DOI: 10.1103/PhysRevA.19.205 (cit. on p. 1).

[13] K. Rzążewski and Robert W. Boyd. "Equivalence of interaction hamiltonians in the electric dipole approximation". In: *Journal of Modern Optics* 51.8 (2004), pp. 1137–1147. DOI: 10.1080/09500340408230412 (cit. on pp. 1, 8).

[14] Alexander L. Fetter and John Dirk Walecka. *Quantum Theory of Many-Particle Systems*. Dover. Mineola, New York: Dover Publication, Inc., 1971 (cit. on pp. 5, 9, 10, 21, 24, 25).

[15] Eleftherios N. Economou. *Green's Functions in Quantum Physics*. Third. Vol. 7. Springer Series in Solid-State Sciences. Berlin, Heidelberg: Springer Berlin Heidelberg, 2006. DOI: 10.1007/3-540-28841-4 (cit. on pp. 5, 10, 21, 24).

[16] Gerald D. Mahan. *Many-Particle Physics*. 3rd. Boston, MA: Springer US, 2000. DOI: 10.1007/978-1-4757-5714-9 (cit. on pp. 5, 10, 21, 24).

[17] Alexander Altland and Ben Simons. *Condensed Matter Field Theory*. 2nd. Cambridge: Cambridge University Press, 2010 (cit. on pp. 5, 10, 21, 24, 89).

[18] Gabriele F Giuliani and Giovanni Vignale. *Quantum Theory of the Electron Liquid*. Cambridge: Cambridge University Press, 2005. DOI: 10.1017/CBO9780511619915 (cit. on pp. 5, 10, 21, 24).

[19] Philip Phillips. *Advanced Solid State Physics*. 2nd. Cambridge: CAMBRIDGE UNIVERSITY PRESS, 2012 (cit. on pp. 5, 10, 21, 24).

[20] Gianluca Stefanucci and Robert van Leeuwen. *Nonequilibrium Many-Body Theory of Quantum Systems*. 1st. Cambridge: Cambridge University Press, 2013. DOI: 10.1017/CBO9781139023979 (cit. on pp. 5, 10, 21–28, 30–35, 39).

[21] James L. P. Hughes and J. E. Sipe. "Calculation of second-order optical response in semiconductors". In: *Physical Review B* 53.16 (1996), pp. 10751–10763. DOI: 10.1103/PhysRevB.53.10751 (cit. on pp. 5, 55).

[22] Jørgen Rammer and H Smith. "Quantum field-theoretical methods in transport theory of metals". In: *Reviews of Modern Physics* 58.2 (1986), pp. 323–359. DOI: 10.1103/RevModPhys.58.323 (cit. on pp. 5, 21, 25).

[23] Jørgen Rammer. *Quantum Transport Theory*. Reading, Massachusetts: Perseus Publishing, 1998 (cit. on pp. 5, 21, 25).

[24] Robert W. Boyd. *Nonlinear Optics*. 3rd. Elsevier Science Publishing Co Inc, 2008 (cit. on pp. 7, 15, 55, 56).

[25] Y Ron Shen. *The Principles of Nonlinear Optics*. 2002 (cit. on pp. 7, 15).

[26] E.I. Blount. "Formalisms of Band Theory". In: *Solid State Physics - Advances in Research and Applications*. Vol. 13. C. 1962, pp. 305–373. DOI: 10.1016/S0081-1947(08)60459-2 (cit. on p. 12).

[27] M. V. Berry. "Quantal Phase Factors Accompanying Adiabatic Changes". In: *Proceedings of the Royal Society A: Mathematical, Physical and Engineering Sciences* 392.1802 (1984), pp. 45–57. DOI: 10.1098/rspa.1984.0023 (cit. on p. 13).

[28] Di Xiao, Ming-Che Chang, and Qian Niu. "Berry phase effects on electronic properties". In: *Reviews of Modern Physics* 82.3 (2010), pp. 1959–2007. DOI: 10.1103/RevModPhys.82.1959 (cit. on pp. 13, 61).

[29] L. V. Keldysh. "DIAGRAM TECHNIQUE FOR NONEQUILIBRIUM PROCESSES". In: *Soviet Physics JETP* 20.4 (1965), pp. 1018–1026. DOI: 10.1007/BF02724324 (cit. on p. 23).

[30] David C. Langreth et al. *Linear and Nonlinear Electron Transport in Solids*. Ed. by J. T. Devreese and V. E. Doren. NATO ASI series. Series B : Physics. Boston, MA: Springer US, 1976. DOI: 10.1007/978-1-4757-0875-2 (cit. on p. 25).

[31] Karsten Balzer and Michael Bonitz. *Nonequilibrium Green's Functions Approach to Inhomogeneous Systems*. Vol. 867. Lecture Notes in Physics. Berlin, Heidelberg: Springer Berlin Heidelberg, 2013. DOI: 10.1007/978-3-642-35082-5 (cit. on p. 25).

[32] Hartmut J. W. Haug and Antti-pekka Jauho. *Quantum Kinetics in Transport and Optics of Semiconductors*. Second. Vol. 123. Solid-State Sciences. Berlin, Heidelberg: Springer Berlin Heidelberg, 2008. DOI: 10.1007/978-3-540-73564-9 (cit. on p. 25).

[33] F. Hipolito et al. "Enhanced Optical Dichroism of Graphene Nanoribbons". In: *Physical Review B* 86.11 (2011), p. 115430. DOI: 10.1103/PhysRevB.86.115430. arXiv: 1107.1509v2 (cit. on pp. 43, 45–47, 66).

[34] Max Born and Emil Wolf. *Principles of optics*. 6th. Oxford: Pergamon Press Ltd., 1986 (cit. on pp. 43, 47).

[35] M. H. Fizeau. "Recherches sur plusieurs phenomenes relatifs a la polarisation de la lumiere". In: *Ann. Chim. (Phys.)* 63 (1861), p. 385 (cit. on p. 43).

[36] R. R. Nair et al. "Fine Structure Constant Defines Visual Transparency of Graphene". In: *Science* 320.5881 (2008), p. 1308. DOI: 10.1126/science.1156965. arXiv: 0803.3718v1 (cit. on pp. 44, 45).

[37] N. M. R. Peres. "Colloquium: The transport properties of graphene: An introduction". In: *Reviews of Modern Physics* 82.3 (2010), pp. 2673–2700. DOI: 10.1103/RevModPhys.82.2673. arXiv: arXiv:1007.2849v2 (cit. on pp. 44, 50, 66, 128).

[38] Qiaoliang Bao et al. "Broadband graphene polarizer". In: *Nature Photonics* 5.July (2011), pp. 411–415. DOI: 10.1038/NPHOTON.2011.102 (cit. on p. 44).

[39] Z. Q. Li et al. "Dirac charge dynamics in graphene by infrared spectroscopy". In: *Nature Physics* 4 (2008), pp. 532–535. DOI: 10.1038/nphys989 (cit. on p. 44).

[40] Max C. Lemme et al. "Etching of Graphene Devices with a Helium Ion Beam". In: *ACS Nano* 3.9 (2009), pp. 2674–2676. DOI: 10.1021/nn900744z (cit. on pp. 44, 49).

[41] T. J. Echtermeyer et al. "Strong plasmonic enhancement of photovoltage in graphene". In: *Nature Communications* 2.aug (2011), p. 458. DOI: 10.1038/ncomms1464 (cit. on p. 44).

[42] Guangyu Xu et al. "Linewidth roughness in nanowire-mask-based graphene nanoribbons". In: *Applied Physics Letters* 98.24 (2011), p. 243118. DOI: 10.1063/1.3599596 (cit. on p. 45).

[43] Neil W. Ashcroft and N. David Mermin. *Solid state physics*. London: Thomson Learning, Inc., 1976 (cit. on pp. 46, 61).

[44] Mitsutaka Fujita et al. "Peculiar Localized State at Zigzag Graphite Edge". In: *J. Phys. Soc. Jpn.* 65 (1996), pp. 1920–1923. DOI: 10.1143/JPSJ.65.1920 (cit. on p. 46).

[45] Katsunori Wakabayashi et al. "Electronic states of graphene nanoribbons and analytical solutions". In: *Sci. Technol. Adv. Mater.* 11.5 (2010), p. 4504. DOI: 10.1088/1468-6996/11/5/054504 (cit. on p. 46).

[46] Katsunori Wakabayashi et al. "Electronic and magnetic properties of nanographite ribbons". In: *Physical Review B* 59.12 (1999), pp. 8271–8282. DOI: 10.1103/PhysRevB.59.8271 (cit. on p. 46).

[47] John David Jackson. *Classical electrodynamics*. 3rd. John Wiley & Sons, Inc., 1999 (cit. on pp. 47, 49, 123, 124).

[48] Jingwei Bai, Xiangfeng Duan, and Yu Huang. "Rational Fabrication of Graphene Nanoribbons Using a Nanowire Etch Mask". In: *Nano Lett.* 9.5 (2009), pp. 2083–2087. DOI: 10.1021/nl900531n (cit. on p. 49).

[49] Dmitry V. Kosynkin et al. "Longitudinal unzipping of carbon nanotubes to form graphene nanoribbons". In: *Nature* 458 (2009), pp. 872–876. DOI: 10.1038/nature07872 (cit. on p. 49).

[50] Liying Jiao et al. "Facile synthesis of high-quality graphene nanoribbons." In: *Nature Nanotechnology* 5.5 (2010), pp. 321–5. DOI: 10.1038/nnano.2010.54 (cit. on p. 49).

[51] Chenggang Tao et al. "Spatially Resolving Edge States of Chiral Graphene Nanoribbons". In: *Nature Physics* 7 (2011), pp. 616–620. DOI: 10.1038/nphys1991 (cit. on p. 49).

[52] Tianshu Li and Giulia Galli. "Electronic Properties of MoS2 Nanoparticles". In: *Journal of Physical Chemistry C* 111.44 (2007), pp. 16192–16196. DOI: 10.1021/jp075424v (cit. on p. 49).

[53] Vitor M. Pereira and A. H. Castro Neto. "All-graphene integrated circuits via strain engineering". In: *Physical Review Letters* 103.4 (2009), p. 046801. DOI: 10.1103/PhysRevLett.103.046801 (cit. on pp. 50, 70).

[54] Jason Horng et al. "Drude conductivity of Dirac fermions in graphene". In: *Physical Review B* 83.16 (2011), pp. 1–5. DOI: 10.1103/PhysRevB.83.165113 (cit. on p. 50).

[55] A. H. Castro Neto et al. "The electronic properties of graphene". In: *Reviews of Modern Physics* 81.1 (2009), pp. 109–162. DOI: 10.1103/RevModPhys.81.109. arXiv: 0709.1163 (cit. on pp. 50, 70, 89, 91).

[56] J. A. Porto, F. J. García-Vidal, and J. B. Pendry. "Transmission Resonances on Metallic Gratings with Very Narrow Slits". In: *Physical Review Letters* 83.14 (1999), pp. 2845–2848. DOI: 10.1103/PhysRevLett.83.2845 (cit. on p. 51).

[57] Yu. V. Bludov, M. I. Vasilevskiy, and N. M. R. Peres. "Mechanism for graphene-based optoelectronic switches by tuning surface plasmon-polaritons in monolayer graphene". In: *EPL (Europhysics Letters)* 92.68001 (2010), pp. 1–6. DOI: 10.1209/0295-5075/92/68001. arXiv: 1009.1739v2 (cit. on p. 51).

[58] S. D. Ganichev and W. Prettl. "Spin Photocurrents in Quantum Wells review part I". In: *Journal of Physics: Condensed Matter* 15.20 (2003), R935–R983. DOI: 10.1088/0953-8984/15/20/204. arXiv: 0304266 [cond-mat] (cit. on pp. 53, 54, 123).

[59] M. M. Glazov and S. D. Ganichev. "High frequency electric field induced nonlinear effects in graphene". In: *Physics Reports* 535.3 (2014), pp. 101–138. DOI: 10.1016/j.physrep.2013.10.003 (cit. on pp. 53, 54).

[60] Eougenious L. Ivchenko. *Optical Spectroscopy of Semiconductor Nanostructures*. Alpha Science International, Ltd, 2005, p. 350 (cit. on pp. 54, 55, 70, 123).

[61] H. Diehl et al. "Spin photocurrents in (110)-grown quantum well structures". In: *New Journal of Physics* 9.349 (2007), pp. 1–14. DOI: 10.1088/1367-2630/9/9/349 (cit. on pp. 54, 61).

[62] S. A. Tarasenko. "Orbital mechanism of the circular photogalvanic effect in quantum wells". In: *JETP Letters* 85.3 (2007), pp. 182–186. DOI: 10.1134/S0021364007030113 (cit. on p. 54).

[63] Joel E Moore and J. Orenstein. "Confinement-Induced Berry Phase and Helicity-Dependent Photocurrents". In: *Physical Review Letters* 105.2 (2010), p. 6805. DOI: 10.1103/PhysRevLett.105.026805 (cit. on pp. 54, 61, 62).

[64] Kai-He Ding and Guanghui Zhou. "Time-dependent electron transport in HgTe/CdTe quantum wells". In: *Physics Letters A* 378.13 (2014), pp. 966–969. DOI: 10.1016/j.physleta.2014.01.046 (cit. on p. 54).

[65] Junxi Duan et al. "Identification of Helicity-Dependent Photocurrents from Topological Surface States in Bi2Se3 Gated by Ionic Liquid". In: *Scientific Reports* 4 (2014), p. 4889. DOI: 10.1038/srep04889 (cit. on p. 54).

[66] J. Karch et al. "Photon helicity driven electric currents in graphene". In: *arXiv preprint* 1002.1047 (2010), pp. 1–13. arXiv: 1002.1047 (cit. on pp. 54, 59).

[67] D. Hsieh et al. "Nonlinear Optical Probe of Tunable Surface Electrons on a Topological Insulator". In: *Physical Review Letters* 106.5 (2011), p. 057401. DOI: 10.1103/PhysRevLett.106.057401 (cit. on p. 54).

[68] J. W. McIver et al. "Theoretical and experimental study of second harmonic generation from the surface of the topological insulator Bi_2Se_3". In: *Physical Review B* 86.3 (2012), p. 035327. DOI: 10.1103/PhysRevB.86.035327 (cit. on p. 54).

[69] Rodrigo a. Muniz and J. E. Sipe. "Coherent control of optical injection of spin and currents in topological insulators". In: *Physical Review B* 89.20 (2014), p. 205113. DOI: 10.1103/PhysRevB.89.205113. arXiv: 1401.1241 (cit. on p. 54).

[70] E Deyo et al. "Semiclassical theory of the photogalvanic effect in non-centrosymmetric systems". In: *arXiv preprint* 0904.1917 (2009), pp. 1–7. arXiv: 0904.1917 (cit. on pp. 54, 61, 70).

[71] S. A. Tarasenko. "Direct current driven by ac electric field in quantum wells". In: *Physical Review B* 83.3 (2011), p. 035313. DOI: 10.1103/PhysRevB.83.035313 (cit. on p. 54).

[72] Pavan Hosur. "Circular photogalvanic effect on topological insulator surfaces: Berry-curvature-dependent response". In: *Physical Review B* 83.03 (2011), p. 5309. DOI: 10.1103/PhysRevB.83.035309 (cit. on p. 54).

[73] Alexandra Junck, Gil Refael, and Felix von Oppen. "Photocurrent response of topological insulator surface states". In: *Physical Review B* 88.7 (2013), p. 075144. DOI: 10.1103/PhysRevB.88.075144 (cit. on p. 54).

[74] U. Aeberhard and R. H. Morf. "Microscopic non-equilibrium theory of quantum well solar cells". In: *Physical Review B* 77.12 (2007), p. 125343. DOI: 10.1103/PhysRevB.77.125343. arXiv: 0709.4131 (cit. on p. 55).

[75] Shun-Qing Shen. *Topological Insulators*. Vol. 174. Springer Series in Solid-State Sciences. Berlin, Heidelberg: Springer Berlin Heidelberg, 2012, pp. 15–18. DOI: 10.1007/978-3-642-32858-9 (cit. on pp. 55, 56).

[76] R. Clarck Jones. "A New Calculus for the Treatment of Optical Systems". In: *Journal of the Optical Society of America* 31.7 (1941), p. 488. DOI: 10.1364/JOSA.31.000488 (cit. on pp. 56, 123, 124).

[77] Mildred S. Dresselhaus, Gene Dresselhaus, and Ado Jorio. *Group Theory*. Berlin, Heidelberg: Springer Berlin Heidelberg, 2008. DOI: 10.1007/978-3-540-32899-5 (cit. on p. 60).

[78] Siegfried Haussühl. *Physical Properties of Crystals*. Ed. by Siegfried Hausshl. Weinheim, Germany: Wiley-VCH Verlag GmbH, 2007. DOI: 10.1002/9783527621156 (cit. on pp. 60, 67).

[79] R. M. Ribeiro and N. M. R. Peres. "Stability of boron nitride bilayers: Ground-state energies, interlayer distances, and tight-binding description". In: *Physical Review B* 83.23 (2011), p. 235312. DOI: 10.1103/PhysRevB.83.235312. arXiv: 1101.3950 (cit. on pp. 60, 73).

[80] Eric Suárez Morell and Luis E. F. Foa Torres. "Radiation effects on the electronic properties of bilayer graphene". In: *Physical Review B* 86.125449 (2012), pp. 1–5. DOI: 10.1103/PhysRevB.86.125449 (cit. on p. 61).

[81] Michael P. Marder. *Condensed Matter Physics*. 2nd Editio. Hoboken, NJ, USA: John Wiley & Sons, Inc., 2010. DOI: 10.1002/9780470949955 (cit. on pp. 61, 119).

[82] Arno Bohm et al. *The Geometric Phase in Quantum Systems*. 1st. New York: Springer-Verlag Berlin Heidelberg GmbH, 2003. DOI: 10.1007/978-3-662-10333-3 (cit. on p. 61).

[83] Ludger Wirtz, Andrea Marini, and Angel Rubio. "Excitons in Boron Nitride Nanotubes: Dimensionality Effects". In: *Physical Review Letters* 96.12 (2006), p. 126104. DOI: 10.1103/PhysRevLett.96.126104 (cit. on pp. 67, 73).

[84] X. Blase et al. "Quasiparticle band structure of bulk hexagonal boron nitride and related systems". In: *Physical Review B* 51.11 (1995), pp. 6868–6875. DOI: 10.1103/PhysRevB.51.6868 (cit. on p. 67).

[85] Kenji Watanabe, Takashi Taniguchi, and Hisao Kanda. "Direct-bandgap properties and evidence for ultraviolet lasing of hexagonal boron nitride single crystal". In: *Nature Materials* 3.6 (2004), pp. 404–409. DOI: 10.1038/nmat1134 (cit. on p. 67).

[86] Kikuo Harigaya. "Exciton Effects in Optical Absorption of Boron-Nitride Nanotubes". In: *Physical Review Letters* 96.12 (2007), p. 126104. DOI: 10.1143/JJAP.48.065007. arXiv: 0708.1203 (cit. on p. 67).

[87] Cheol-Hwan Park and Steven G Louie. "Energy gaps and stark effect in boron nitride nanoribbons." In: *Nano letters* 8.8 (2008), pp. 2200–2203. DOI: 10.1021/nl080695i. arXiv: arXiv:0808.1833v1 (cit. on p. 67).

[88] Brian A. Ruzicka et al. "Hot carrier diffusion in graphene". In: *Physical Review B* 82.19 (2010), p. 195414. DOI: 10.1103/PhysRevB.82.195414 (cit. on pp. 69, 75, 76, 83).

[89] Dong Sun et al. "Ultrafast hot-carrier-dominated photocurrent in graphene". In: *Nature Nanotechnology* 7.2 (2012), pp. 114–118. DOI: 10.1038/nnano.2011.243 (cit. on pp. 69, 75, 76, 83).

[90] K. J. Tielrooij et al. "Photoexcitation cascade and multiple hot-carrier generation in graphene". In: *Nature Physics* 9.4 (2013), pp. 248–252. DOI: 10.1038/nphys2564 (cit. on pp. 69, 75, 76, 83).

[91] Ado Jorio et al. *Raman Spectroscopy in Graphene Related Systems*. Weinheim, Germany: Wiley-VCH Verlag GmbH & Co. KGaA, 2011. DOI: 10.1002/9783527632695 (cit. on p. 70).

[92] Eduardo V. Castro et al. "Biased bilayer graphene: semiconductor with a gap tunable by the electric field effect". In: *Physical Review Letters* 99.21 (2007), p. 6802. DOI: 10.1103/PhysRevLett.99.216802. arXiv: 0611342v2 (cit. on pp. 70, 74, 76).

[93] B. N. Szafranek et al. "High on/off ratios in bilayer graphene field effect transistors realized by surface dopants". In: *Nano Letters* 11 (2011), pp. 2640–2643. DOI: 10.1021/nl200631m. arXiv: 1102.4927 (cit. on pp. 70, 74, 76).

[94] J. Velasco et al. "Transport spectroscopy of symmetry-broken insulating states in bilayer graphene". In: *Nature Nanotechnology* 7.3 (2012), pp. 156–160. DOI: 10.1038/nnano.2011.251 (cit. on pp. 70, 74, 76).

[95] A. Pachoud et al. "Graphene transport at high carrier densities using a polymer electrolyte gate". In: *EPL (Europhysics Letters)* 92.27001 (2010), p. 27001. DOI: 10.1209/0295-5075/92/27001 (cit. on pp. 70, 74, 76).

[96] L. Britnell et al. "Field-Effect Tunneling Transistor Based on Vertical Graphene Heterostructures". In: *Science* 335.6071 (2012), pp. 947–950. DOI: 10.1126/science.1218461 (cit. on pp. 70, 74, 76).

[97] Adam A. Stabile et al. "Electrically tunable resonant scattering in fluorinated bilayer graphene". In: *Physical Review B* 92.12 (2015), p. 121411. DOI: 10.1103/PhysRevB.92.121411 (cit. on pp. 70, 74, 76).

[98] Vitor M. Pereira, A. H. Castro Neto, and N. M. R. Peres. "Tight-binding approach to uniaxial strain in graphene". In: *Physical Review B* 80.4 (2009), p. 045401. DOI: 10.1103/PhysRevB.80.045401 (cit. on p. 70).

[99] Francisco Guinea, M. I. Katsnelson, and A. K. Geim. "Energy gaps and a zero-field quantum Hall effect in graphene by strain engineering". In: *Nature Physics* 6.1 (2010), pp. 30–33. DOI: 10.1038/nphys1420 (cit. on p. 70).

[100] Francisco Guinea et al. "Generating quantizing pseudomagnetic fields by bending graphene ribbons". In: *Physical Review B* 81.3 (2010), p. 035408. DOI: 10.1103/PhysRevB.81.035408 (cit. on p. 70).

[101] N. Levy et al. "Strain-Induced Pseudo-Magnetic Fields Greater Than 300 Tesla in Graphene Nanobubbles". In: *Science* 329.5991 (2010), pp. 544–547. DOI: 10.1126/science.1191700 (cit. on p. 70).

[102] Gianluca Giovannetti et al. "Substrate-induced band gap in graphene on hexagonal boron nitride: Ab initio density functional calculations". In: *Physical Review B* 76.7 (2007), p. 073103. DOI: 10.1103/PhysRevB.76.073103 (cit. on p. 70).

[103] Zhen Hua Ni et al. "Uniaxial Strain on Graphene: Raman Spectroscopy Study and Band-Gap Opening". In: *ACS Nano* 2.11 (2008), pp. 2301–2305. DOI: 10.1021/nn800459e. arXiv: 0810.3476 (cit. on p. 70).

[104] J. Hicks et al. "A wide-bandgap metal–semiconductor–metal nanostructure made entirely from graphene". In: *Nature Physics* 9.1 (2012), pp. 49–54. DOI: 10.1038/nphys2487 (cit. on p. 70).

[105] Jeil Jung et al. "Origin of band gaps in graphene on hexagonal boron nitride". In: *Nature Communications* 6 (2014), p. 6308. DOI: 10.1038/ncomms7308. arXiv: 1403.0496 (cit. on p. 70).

[106] Ashwin Ramasubramaniam, Doron Naveh, and Elias Towe. "Tunable band gaps in bilayer graphene bn heterostructures". In: *Nano Letters* 11.3 (2011), pp. 1070–1075. DOI: 10.1021/nl1039499. arXiv: 1011.2489 (cit. on p. 70).

[107] C. L. Kane and E. J. Mele. "Quantum Spin Hall Effect in Graphene". In: *Physical Review Letters* 95.22 (2005), p. 226801. DOI: 10.1103/PhysRevLett.95.226801 (cit. on pp. 85, 91, 95).

[108] Per-Olov Löwdin. "On the Non-Orthogonality Problem Connected with the Use of Atomic Wave Functions in the Theory of Molecules and Crystals". In: *The Journal of Chemical Physics* 18.3 (1950), pp. 365–375. DOI: 10.1063/1.1747632 (cit. on p. 85).

[109] Sergej Konschuh, Martin Gmitra, and Jaroslav Fabian. "Tight-binding theory of the spin-orbit coupling in graphene". In: *Physical Review B* 74.245412 (2010), p. 10. DOI: 10.1103/PhysRevB.82.245412 (cit. on pp. 85, 86, 98, 100, 101).

[110] Sergej Konschuh et al. "Theory of spin-orbit coupling in bilayer graphene". In: *Physical Review B* 85.11 (2012), p. 115423. DOI: 10.1103/PhysRevB.85.115423 (cit. on p. 85).

[111] Han Liu, Adam T Neal, and Peide D Ye. "Channel length scaling of MoS 2 MOSFETs". In: *ACS Nano* 6.10 (2012), pp. 8563–8569. DOI: 10.1021/nn303513c (cit. on p. 85).

[112] Christian R. Ast and Isabella Gierz. "Sp-band tight-binding model for the Bychkov-Rashba effect in a two-dimensional electron system including nearest-neighbor contributions from an electric field". In: *Physical Review B* 86.8 (2012), pp. 1–8. DOI: 10.1103/PhysRevB.86.085105 (cit. on pp. 85, 95).

[113] Diego Mastrogiuseppe et al. "Quantum phase transitions into Kondo states in bilayer graphene". In: *Physical Review B* 89.8 (2014), p. 081101. DOI: 10.1103/PhysRevB.89.081101. arXiv: 1310.0502 (cit. on p. 86).

[114] Sergey Bravyi, David DiVincenzo, and Daniel Loss. "Schrieffer-Wolff transformation for quantum many-body systems". In: *Annals of Physics* 326.10 (2011), pp. 2793–2826. DOI: 10.1016/j.aop.2011.06.004. arXiv: 1105.0675 (cit. on p. 86).

[115] J. C. Slater and G. F. Koster. "Simplified LCAO Method for the Periodic Potential Problem". In: *Physical Review* 94.6 (1954), pp. 1498–1524. DOI: 10.1103/PhysRev.94.1498 (cit. on pp. 89, 131).

[116] George Grüner. *Density Waves in Solids*. Paperback. Cambridge, Massachusetts: Perseus Publishing, 1994, p. 259 (cit. on p. 89).

[117] Daniel Huertas-Hernando, Francisco Guinea, and Arne Brataas. "Spin-orbit coupling in curved graphene, fullerenes, nanotubes, and nanotube caps". In: *Physical Review B* 74.15 (2006), p. 155426. DOI: 10.1103/PhysRevB.74.155426 (cit. on pp. 95, 100, 134).

[118] Jayakumar Balakrishnan et al. "Giant spin Hall effect in graphene grown by chemical vapour deposition". In: *Nature Communications* 5 (2014), p. 4748. DOI: 10.1038/ncomms5748 (cit. on p. 95).

[119] Aires Ferreira et al. "Extrinsic spin hall effect induced by resonant skew scattering in Graphene". In: *Physical Review Letters* 112.6 (2014), pp. 1–5. DOI: 10.1103/PhysRevLett.112.066601. arXiv: 1304.7511v3 (cit. on p. 95).

[120] Alexandre Pachoud et al. "Scattering theory of spin-orbit active adatoms on graphene". In: *Physical Review B* 90.3 (2014), p. 035444. DOI: 10.1103/PhysRevB.90.035444. arXiv: 1403.1251 (cit. on p. 95).

[121] Matthias Droth and Guido Burkard. "Spintronics with graphene quantum dots". In: 16 (2015), pp. 1–16. DOI: 10.1002/pssr.201510182. arXiv: 1506.03991 (cit. on p. 95).

[122] Y. K. Kato. "Observation of the Spin Hall Effect in Semiconductors". In: *Science* 306.5703 (2004), pp. 1910–1913. DOI: 10.1126/science.1105514 (cit. on p. 95).

[123] V. Sih et al. "Spatial imaging of the spin Hall effect and current-induced polarization in two-dimensional electron gases". In: *Nature Physics* 1.1 (2005), pp. 31–35. DOI: 10.1038/nphys009. arXiv: 0506704 [cond-mat] (cit. on p. 95).

[124] S. O. Valenzuela and M. Tinkham. "Direct electronic measurement of the spin Hall effect". In: *Nature* 442.7099 (2006), pp. 176–179. DOI: 10.1038/nature04937 (cit. on p. 95).

[125] Ming-Hao Liu, Son-Hsien Chen, and Ching-Ray Chang. "Nonequilibrium spin transport on Au(111) surfaces". In: *Physical Review B* 78.19 (2008), p. 195413. DOI: 10.1103/PhysRevB.78.195413 (cit. on p. 95).

[126] Takeshi Seki et al. "Giant spin Hall effect in perpendicularly spin-polarized FePt/Au devices". In: *Nature Materials* 7.2 (2008), pp. 125–129. DOI: 10.1038/nmat2098 (cit. on p. 95).

[127] Kazuya Ando and Eiji Saitoh. "Observation of the inverse spin Hall effect in silicon". In: *Nature Communications* 3 (2012), p. 629. DOI: 10.1038/ncomms1640. arXiv: 1107.2585v1 (cit. on p. 95).

[128] Cheng-Cheng Liu, Hua Jiang, and Yugui Yao. "Low-energy effective Hamiltonian involving spin-orbit coupling in silicene and two-dimensional germanium and tin". In: *Physical Review B* 84.19 (2011), p. 195430. DOI: 10.1103/PhysRevB.84.195430 (cit. on pp. 103, 104).

[129] Feng-feng Zhu et al. "Epitaxial growth of two-dimensional stanene". In: *Nature Materials* 14.10 (2015), pp. 1020–1025. DOI: 10.1038/nmat4384 (cit. on p. 104).

[130] Stephan Rachel and Motohiko Ezawa. "Giant magnetoresistance and perfect spin filter in silicene, germanene, and stanene". In: *Physical Review B* 89.19 (2014), p. 195303. DOI: 10.1103/PhysRevB.89.195303 (cit. on p. 104).

[131] Peizhe Tang et al. "Stable two-dimensional dumbbell stanene: A quantum spin Hall insulator". In: *Physical Review B* 90.12 (2014), p. 121408. DOI: 10.1103/PhysRevB.90.121408 (cit. on p. 104).

[132] Motohiko Ezawa. "A topological insulator and helical zero mode in silicene under an inhomogeneous electric field". In: *New Journal of Physics* 14.3 (2012), p. 033003. DOI: 10.1088/1367-2630/14/3/033003. arXiv: 1201.3687 (cit. on p. 104).

[133] Yong Xu et al. "Large-Gap Quantum Spin Hall Insulators in Tin Films". In: *Physical Review Letters* 111.13 (2013), p. 136804. DOI: 10.1103/PhysRevLett.111.136804 (cit. on p. 104).

[134] M Tahir et al. "Quantum spin/valley Hall effect and topological insulator phase transitions in silicene". In: *Applied Physics Letters* 102.16 (2013), p. 162412. DOI: 10.1063/1.4803084 (cit. on p. 104).

[135] S. Fratini and Francisco Guinea. "Substrate-limited electron dynamics in graphene". In: *Physical Review B* 77.19 (2008), p. 195415. DOI: 10.1103/PhysRevB.77.195415 (cit. on p. 106).

[136] Mads Lund Trolle, Gotthard Seifert, and Thomas Garm Pedersen. "Theory of excitonic second-harmonic generation in monolayer MoS_2". In: *Physical Review B* 89.23 (2014), p. 235410. DOI: 10.1103/PhysRevB.89.235410. arXiv: 1310.0674 (cit. on p. 106).

[137] Thomas Garm Pedersen. "Intraband effects in excitonic second-harmonic generation". In: *Physical Review B* 92.23 (2015), p. 235432. DOI: 10.1103/PhysRevB.92.235432 (cit. on p. 106).

[138] David Jefferey Griffiths. *Introduction to Quantum Mechanics – Solutions*. New Jersey: Pearson Education International, 2005, p. 303 (cit. on p. 119).

[139] Eugene Hecht. *Optics*. 4th. Addison-Wesley, 2002 (cit. on pp. 123, 124).

[140] Colin D. H. Chisholm. *Group Theoretical Techniques in Quantum Chemistry*. 1st. Academic Press, Inc, 1976 (cit. on p. 134).

[141] George B. Arfken, Hans J. Weber, and Frank E. Harris. *Mathematical Methods for Physicists*. 7th. Singapore: Academic Press, 2013, p. 120 (cit. on p. 135).

This page was intentionally left blank.

Appendix A

Auxiliary calculations for GNRs

A.1 Exact calculation of the optical conductivity tensor

The purpose of this appendix is to review the calculation of the optical conductivity of GNRs. It begins with the evaluation of the energy dispersion of armchair nanoribbons, based on a plane wave basis expansion. It the proceeds with the calculation of the velocity operator and terminates with the evaluation of the conductivity tensor matrix elements.

A.1.1 Electronic properties of armchair GNRs

To study the effect of electronic confinement in graphene, we consider a system where translation invariance is broken along a single direction. For the sake of clarity and simplicity, we address confinement along one direction by considering a rectangular ribbon of infinite length along the x-direction and finite width along the y-direction, in figure A.1 we depict the real lattice representation for such system. The lattice is characterized by the primitive and translation vectors

$$\mathbf{a}_1 = \frac{3a_0}{2}\left(1, \frac{\sqrt{3}}{3}\right) ; \quad \mathbf{a}_2 = \frac{3a_0}{2}\left(1, -\frac{\sqrt{3}}{3}\right) , \tag{A.1a}$$

$$\hat{\mathbf{m}} = \frac{\mathbf{a}_1 + \mathbf{a}_2}{|\mathbf{a}_1 + \mathbf{a}_2|} = \big(1, 0\big) ; \quad \hat{\mathbf{n}} = \frac{\mathbf{a}_1}{|\mathbf{a}_1|} = \left(\frac{1}{2}, \frac{\sqrt{3}}{2}\right) \tag{A.1b}$$

respectively. Where the ribbon width reads $W = \sqrt{3}a_0(N_c - 1)/2$. In the non-orthogonal basis defined by $\hat{\mathbf{m}}$ and $\hat{\mathbf{n}}$ vectors, the nearest neighbour Hamiltonian for graphene

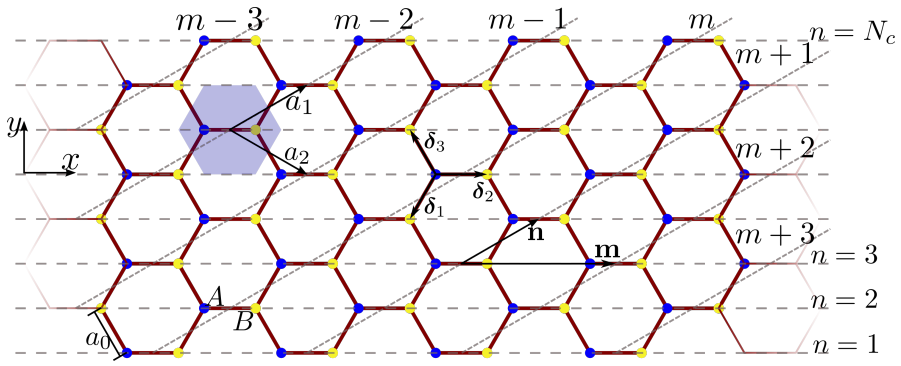

Figure A.1: Depiction of an idealized armchair nanoribbon of finite width, *i.e.* finite number of unit cells along the y-direction and infinite length along x-direction. The lattice primitive vectors are $\mathbf{a}_1$ and $\mathbf{a}_2$, the lattice parameter a_0 is the carbon-carbon distance and $\mathbf{m}$ and n are the translation vectors along the infinite and quantized direction of the ribbon.

reads

$$\mathcal{H} = -t \sum_{n,m} \big(|A,n,m\rangle\langle B,n,m| + |A,n,m\rangle\langle B,n-1,m| + |A,n,m\rangle\langle B,n+1,m-1| + \text{H.c.} \big) , \tag{A.2}$$

where we consider a wave function defined in a plane wave expansion over the two sublattice sites A and B, such

$$|\psi\rangle = \sum_{m,n} e^{iqm} e^{ikn} \Big[A_{m,n} |A,m,n\rangle + B_{m,n} |B,m,n\rangle \Big] . \tag{A.3}$$

Using this trial wave function, the Hamiltonian is cast into matrix form

$$H \equiv \begin{pmatrix} E/t & \phi(q,k) \\ \phi^*(q,k) & E/t \end{pmatrix} \tag{A.4}$$

with $\phi(q,k) = 1 + \exp[-ik] + \exp[i(k-q)]$. The respective eigenvalues read

$$\big[E(q,k)/t\big]^2 = \phi(q,k)\phi^*(q,k) = 1 + 4\cos(k-q/2)\cos(q/2) + 4\cos^2(k-q/2) . \tag{A.5}$$

To address the particular case of GNRs, we consider a particular solution for the wave function, where we consider the propagation of two waves with opposite wavectors

$$|\psi\rangle = \sum_{m,n} e^{iqm} \Big[A_n(k) |A,m,n\rangle + B_n(k) |B,m,n\rangle \Big] , \tag{A.6}$$

with the finite boundary conditions

$$A_0(k) = A_{Nc+1}(k) = B_0(k) = B_{Nc+1}(k) = 0\,. \tag{A.7}$$

The above-mentioned boundary conditions quantize the wavevector along the n-direction as $k_\ell \equiv \pi\ell/(N_c+1) + q/2$, where $\ell = 0, 1, \ldots N_c$. In turn, the wave function for GNRs can be cast in the form

$$|\psi_{\ell,\lambda}\rangle = \frac{1}{\sqrt{N_c}} \sum_{m,n} e^{iq(m+n/2)} \sin(k_\ell n) \Big[|A,m,n\rangle + \lambda e^{-i\theta_\ell(q)} |B,m,n\rangle \Big]\,, \tag{A.8}$$

where the $\lambda = \pm 1$ encodes the band index and the phase difference between the two sublattice arises from hopping elements reads

$$\theta_\ell(q) = \arctan\left(\frac{\mathrm{Im}[\phi_\ell(q)]}{\mathrm{Re}[\phi_\ell(q)]} \right) = \frac{2\cos\left[k_\ell\right] \sin\left(q/2\right)}{1 + 2\cos\left[k_\ell\right] \cos\left(q/2\right)}\,. \tag{A.9}$$

Based on this results, we can proceed with the calculation of linear response.

A.1.2 The velocity operator

The evaluation of the Kubo-Greenwood formula [81] requires the explicit evaluation of the velocity matrix elements. We compute the Hamiltonian by considering Heisemberg's equation of motion [138]

$$\mathbf{v}(\mathrm{R}) \equiv \frac{\mathrm{d}\mathbf{R}}{\mathrm{d}t} = \frac{i}{\hbar}\big[\mathcal{H}, \mathbf{R}\big]\,. \tag{A.10}$$

In the context of the honeycomb lattice, we represent the position operator as the sum of the position operators for each sub-lattice $\mathbf{R} = \mathbf{R}_A + \mathbf{R}_B$, with

$$\mathbf{R}_A = \mathbf{R}_n |A, \mathbf{R}_n\rangle\langle A, \mathbf{R}n| \quad ; \quad \mathbf{R}_B = \big(\mathbf{R}_n + \boldsymbol{\delta}_n\big)|B, \mathbf{R}_n + \boldsymbol{\delta}_i\rangle\langle B, \mathbf{R}n + \boldsymbol{\delta}_i|\,, \tag{A.11}$$

where $\mathbf{R}_n$ represent the position of the n^{th} unit cell and $\boldsymbol{\delta}_i$ is a translation vector between nearest neighbours. Evaluating the commutator, we determine the velocity operator

$$\mathbf{v} = \frac{-ia_0\gamma_0}{2\hbar} \sum_{m,n} \Big[(\boldsymbol{\delta}_2 - \mathbf{n}) |A,m,n\rangle\langle B,m,n-1| + \boldsymbol{\delta}_2 |A,m,n\rangle\langle B,m,n|$$

$$+ (\boldsymbol{\delta}_2 + \mathbf{n} - \mathbf{m})|A, m, n\rangle\langle B, m-1, n+1| - \text{H.c.}\Big] \,. \tag{A.12}$$

We evaluate the matrix elements for the velocity operator using the eigenvalues and wave-functions computed in the previous section. The velocity matrix element along the x-direction, the velocity reads

$$\langle \psi_{\ell,\lambda}|v_x|\psi_{\ell',\lambda'}\rangle = \frac{a_o\gamma_0\lambda}{i\hbar}\left[\cos\left(k_\ell\right)\cos\left[\theta_\ell(q)+\frac{q}{2}\right] - \cos\left[\theta_\ell(q)\right]\right]\delta_{\ell,\ell'} \,, \tag{A.13}$$

whereas the velocity matrix element along the y-direction reads

$$\begin{aligned}\langle \psi_{\ell,\lambda}|v_y|\psi_{\ell',\lambda'}\rangle = \frac{i\sqrt{3}a_0 t}{2\hbar N_c}\frac{S_{\ell,\ell'}\ \sin(k_\ell)\sin(k'_\ell)}{\sin\left[(k_\ell+k_{\ell'})/2\right]\sin\left[(k_\ell-k_{\ell'})/2\right]}\Big[\lambda\sin(k_\ell)e^{i(\theta_\ell+q/2)} \\ + \lambda'\sin(k_{\ell'})e^{-i(\theta_{\ell'}+q/2)}\Big] \quad : \quad S_{\ell,\ell'} = \frac{1-(-1)^{\ell+\ell'}}{2} \,.\end{aligned} \tag{A.14}$$

A.1.3 The optical conductivity tensor

In the context of GNRs, the calculation of the Kubo formula reduces to

$$\sigma_{\alpha\beta} = \frac{2ie^2}{\omega A_r}\sum_{\ell,\ell',q}\sum_{\lambda,\lambda'}\left[f_{\ell,\lambda}(q) - f_{\ell',\lambda'}(q)\right]\frac{\langle\psi_{\ell,\lambda}|v_\alpha|\psi_{\ell',\lambda'}\rangle\langle\psi_{\ell',\lambda'}|v_\beta|\psi_{\ell,\lambda}\rangle}{\hbar\omega - \left[\epsilon_{\ell,\lambda}(q) - \epsilon_{\ell',\lambda'}(q)\right] + i0^+} \,, \tag{A.15}$$

where $A_r = A_{WS}(N_c - 1)$ is the ribbon area, $f_{\ell,\lambda}(q)$ is the Fermi distribution and $\epsilon_{\ell,\lambda}(q)$ is the energy dispersion. Note that the matrix elements for the velocity operator have incompatible selection rules, namely $\delta_{\ell,\ell'}$ and $1-(-1)^{\ell+\ell'}$. Therefore, the off diagonal matrix elements for the conductivity tensor are identically zero, *i.e.* $\sigma_{xy} = \sigma_{yx} = 0$. In addition, we consider the limit of and infinitely long ribbon, hence the summation over the discrete momentum q is replace by an integral as follows $N^{-1}\sum_q \to \int_{-\pi}^{\pi}\mathrm{d}q$. Therefore, the diagonal elements of conductivity tensor read

$$\sigma_{\alpha\alpha} = \frac{2ie^2}{\omega A_r}\sum_{\ell,\ell'}\sum_{\lambda,\lambda'}\int_{-\pi}^{\pi}\mathrm{d}q\left[f_{\ell,\lambda}(q) - f_{\ell',\lambda'}(q)\right]\frac{\left|\langle\psi_{\ell,\lambda}|v_\alpha|\psi_{\ell',\lambda'}\rangle\right|^2}{\hbar\omega - \left[\epsilon_{\ell,\lambda}(q) - \epsilon_{\ell',\lambda'}(q)\right] + i0^+} \,. \tag{A.16}$$

Given the nature of the integrand, we can compute the real of diagonal elements of the conductivity tensor by means of the Plemelj theorem, *i.e.* $\lim_{\eta\to 0^+} f(x)/(x \pm i\eta) =$

$f(x)/x \mp i\pi f(x)\delta(x)$. Hence, the real part of the conductivity tensor reads

$$\sigma_{\alpha\alpha} = \frac{2\pi e^2}{\omega A_r}\sum_{\ell,\ell'}\sum_{\lambda,\lambda'}\int_{-\pi}^{\pi} \mathrm{d}q\big[f_{\ell,\lambda}(q) - f_{\ell',\lambda'}(q)\big]\big|\langle\psi_{\ell,\lambda}|v_\alpha|\psi_{\ell',\lambda'}\rangle\big|^2 \times \delta\big[\hbar\omega - \big[\epsilon_{\ell,\lambda}(q) - \epsilon_{\ell',\lambda'}\big]\,. \tag{A.17}$$

To proceed with the integration over q, we consider the properties of the Dirac delta function, namely the composition with a function $\delta\big[g(x)\big] = \sum_{x_0}\delta(x-x_0)/|g'(x_0)|$, where $g(x_0)=0$ and then evaluate explicitly the velocity matrix elements.

The longitudinal component along the x-direction

Given the particle hole symmetry and the above mentioned properties, the real part of σ_{xx} reads

$$\frac{\mathrm{Re}\,\sigma_{xx}}{\sigma_0} = \mathcal{N}_x\sum_{\ell_0}\delta f_{q_0^x,\ell_0}\frac{\big[\cos\left(\theta_{\ell_0,q_0^x}\right) - \cos\left(\theta_{\ell_0,q_0^x} - q_0^x/2\right)\cos\left(k_{\ell_0}\right)\big]^2}{\sin\left(q_0^x/2\right)\cos\left(k_{\ell_0}\right)}\,, \tag{A.18}$$

where $\sigma_0 = \pi e^2/2h$, $\mathcal{N}_x = 4/3\sqrt{3}(N_c-1)$, $\delta f_{q_0^x,\ell_0} = f_{\ell_0,-}(q_0^x) - f_{\ell_0,+}(q_0^x)$ and l_0 is such that $q_0^x = 2\arccos\big[(\Omega/2)^2 - 1 - 4\cos^2\left(k_{\ell_0}\right)\big]/4\cos\left(k_{\ell_0}\right) \in \mathbb{R}$.

The longitudinal component along the y-direction

The derivation of $\mathrm{Re}\sigma_{yy}$ follows the same procedure, but the results are cumbersome due to the more rich nature of the selection rules involved in this process.

$$\frac{\Re\,\sigma_{yy}}{\sigma_0} = \mathcal{N}_y\sum_{\ell_1,\ell_2}\sum_{\lambda,\lambda'}\frac{\mathcal{P}_{\ell_1,\ell_2}\,\delta f^{\lambda,\lambda'}_{q_0^y,\ell_1,\ell_2}\,\epsilon_{\ell_1,q_0^y}\epsilon_{\ell_2,q_0^y}}{\sin^2\left[\left(k_{\ell_1}+k_{\ell_2}\right)/2\right]\sin^2\left[\left(k_{\ell_1}-k_{\ell_2}\right)/2\right]}\frac{\sin^2\left(k_{\ell_1}\right)\sin^2\left(k_{\ell_2}\right)}{|\sin(q_0^y/2)|\,\hbar\omega} \times \frac{1+\lambda\lambda'\cos\left(\theta_{\ell_1,q_0^y}+\theta_{\ell_2,q_0^y}-q_0^y\right)}{\left|\cos\left(k_{\ell_1}\right)\epsilon_{\ell_2,q_0^y}+\lambda\lambda'\cos\left(k_{\ell_2}\right)\epsilon_{\ell_1,q_0^y}\right|}\,, \tag{A.19}$$

where $\mathcal{N}_y = 4/\sqrt{3}N_c(N_c+1)^2$, $\delta f^{\lambda,\lambda'}_{q_0^y,\ell_1,\ell_2} = n_F(E_{\ell_1,q_0^y,\lambda}) - n_F(E_{\ell_2,q_0^y,\lambda'})$, and $\mathcal{P}_{\ell_1,\ell_2} = 1-(-1)^{\ell_1+\ell_2}$ and $q_0^y = 2\arccos\big[(a_2-a_1)Q_b + \Omega^2(b_1+b_2) \pm Q_c\big]/(b_1-b_2)^2 \in \mathbb{R}$ with $Q_c = 2\sqrt{\Omega^4 b_1 b_2 + \Omega^2 Q_b Q_a}$, $Q_b = b_2 - b_1$, $Q_a = b_1a_2 - b_2a_1$, $a_i = 1+4\cos^2(k_{\ell_i})$ and $b_i = 4\cos(k_{\ell_i})$.

This page was intentionally left blank.

Appendix B

Auxiliary calculations for photocurrent

B.1 Jones' calculus – quarter-wave plates

In this appendix we review the propagation of light in devices relevant for photocurrent experiments. The final goal is to clearly define the state of polarization of light incident on the sample, by means of Jones' calculus [47, 76, 139].

A standard experimental setup designed to generate monochromatic light use a quarter-wave plates (retarder) to tune the state of polarization. In such setups, it is possible to precisely define and tune the polarization of light. Photocurrent measurements typically rely on such setups to control the state of polarization of light [5, 58, 60]. The basis configuration of this setup is depicted in figure 3.1, where the polarization state of the light is controlled by the relative angle between the fast axis of the quarter-wave plate and the polarization plane of the incident linearly In order to analyse the interaction of light with a sample, it is paramount to properly characterize the propagation of light through the device. Considering an ideal linear polariser, the light beam incident at the quarter-wave plate is defined by

$$\mathbf{E} = E_s(t)\mathbf{e}_s + E_p(t)\mathbf{e}_p = \frac{E_0}{\sqrt{1+r^2}}\left(e^{i\phi_s}\ ,\ re^{i\phi_p}\right)^T e^{i(\boldsymbol{\kappa}\cdot\mathbf{r}-\omega t)}\,, \tag{B.1}$$

where the basis reads $\{\mathbf{e}_s,\, \mathbf{e}_p,\, \mathbf{e}_v\}$, such that: $\mathbf{e}_v$ defines the propagation direction, *i.e.* $\boldsymbol{\kappa} = \kappa\mathbf{e}_v$, $\mathbf{e}_p$ is chosen such that $\mathbf{e}_p \times \mathbf{e}_v = \mathbf{e}_s$, and $\mathbf{e}_s$ defines the normal vector of the

propagation plane. In addition, ϕ_i is the phase of each polarization and r the quotient between E_p and E_s. This defines the basis for the matrix representation used in "Jones' calculus" [47, 76, 139]. Moreover, this basis is mapped to the Cartesian basis by the following relations

$$\mathbf{e}_s = \sin(\zeta)\mathbf{e}_x - \cos(\zeta)\mathbf{e}_y \,, \tag{B.2a}$$

$$\mathbf{e}_p = \cos(\theta)\cos(\zeta)\mathbf{e}_x + \cos(\theta)\sin(\zeta)\mathbf{e}_y + \sin(\theta)\mathbf{e}_z \,, \tag{B.2b}$$

$$\mathbf{e}_v = \sin(\theta)\cos(\zeta)\mathbf{e}_x + \sin(\theta)\sin(\zeta)\mathbf{e}_y - \cos(\theta)\mathbf{e}_z \,, \tag{B.2c}$$

where θ and ζ are the polar and azimuthal angles. Using Jones' calculus it can be shown that effects of anisotropic materials can be mathematically represented by a matrices, the so-called Jones matrices. Hence, the effect of a material on the polarization state of light, is computed by simple matrix products, such as $M|J_i\rangle = |J_f\rangle$. Quarter-wave plates have simple representations as Jones' matrices. For instance, a quarter-wave plate aligned such that its fast axis is parallel to the horizontal reads [47, 76, 139]

$$M = e^{i\pi/4}\begin{pmatrix} 1 & 0 \\ 0 & i \end{pmatrix} . \tag{B.3}$$

Rotating the the quarter-wave plate by an angle φ around the propagation direction $\mathbf{e}_v$

$$M(\varphi) = R(\varphi)MR^{-1}(\varphi) = \begin{pmatrix} \cos(\varphi) & -\sin(\varphi) \\ \sin(\varphi) & \cos(\varphi) \end{pmatrix} MR^{-1}(\varphi) = \begin{pmatrix} -p^* & s \\ s & p \end{pmatrix} , \tag{B.4}$$

where $s = \sin(2\varphi)/\sqrt{2}$ and $p = -[\cos(2\varphi) - i]/\sqrt{2}$. Considering the purely "p" polarized initial electric field, $|J_i\rangle = (0, 1)^T$, the respective outgoing electric field reads

$$\mathbf{E}' = E_0\Big(0\,,\ 1\Big)^T e^{i(\boldsymbol{\kappa}\cdot\mathbf{r}-\omega t)} \,, \tag{B.5}$$

which projects in Cartesian coordinates as

$$\mathbf{E}' = E_0\Big(s\sin(\zeta) + p\cos(\zeta)\cos(\theta)\,,\ -s\cos(\zeta) + p\sin(\zeta)\cos(\theta)\,,\ p\sin(\theta)\Big)^T e^{i(\boldsymbol{\kappa}\cdot\mathbf{r}-\omega t)} \,. \tag{B.6}$$

This defines the electric field incident on the sample, as a function of the geometric alignment and as a function of the polarization state of light.

B.2 Quadratic combinations of the electric field

In this appendix we show the relevant quadratic combinations of the electric for the analysis of the photocurrent in 2D materials. The electric field follows the definition introduced in §3.2, equation 3.4. Hence, the symmetric combinations read

$$E^x_\omega E^x_{-\omega} + E^x_{-\omega} E^x_\omega = E_0^2 \Big(\cos^2(\zeta)\, \cos^2(\theta) \big[\cos(4\varphi) + 3\big] - \sin(2\zeta)\cos(\theta)\sin(4\varphi) + 2\sin^2(\zeta)\sin^2(2\varphi)\Big)/4\,, \tag{B.7a}$$

$$E^x_\omega E^y_{-\omega} + E^x_{-\omega} E^y_\omega = E_0^2 \Big[\frac{\sin(2\zeta)}{2}\Big(\cos^2(\theta)\big[\cos(4\varphi) + 3\big] + \cos(4\varphi) - 1\Big) + \cos(2\zeta)\cos(\theta)\sin(4\varphi)\Big]/4\,, \tag{B.7b}$$

$$E^x_\omega E^z_{-\omega} + E^x_{-\omega} E^z_\omega = E_0^2\, \sin(\theta) \Big(\cos(\zeta)\cos(\theta)\big[\cos(4\varphi) + 3\big] - \sin(\zeta)\sin(4\varphi)\Big)/4\,, \tag{B.7c}$$

$$E^y_\omega E^y_{-\omega} + E^y_{-\omega} E^y_\omega = E_0^2 \Big(\sin^2(\zeta)\cos^2(\theta)\big[\cos(4\varphi) + 3\big] + \sin(2\zeta)\cos(\theta)\sin(4\varphi)/4 + 8\cos^2(\zeta)\sin^2(\varphi)\cos^2(\varphi)\Big)/4\,, \tag{B.7d}$$

$$E^y_\omega E^z_{-\omega} + E^y_{-\omega} E^z_\omega = E_0^2\, \sin(\theta) \Big(\sin(\zeta)\cos(\theta)\big[\cos(4\varphi) + 3\big] + \cos(\zeta)\sin(4\varphi)\Big)/4\,, \tag{B.7e}$$

$$E^z_\omega E^z_{-\omega} + E^z_{-\omega} E^z_\omega = E_0^2\, \sin^2(\theta) \big[\cos(4\varphi) + 3\big]/4\,, \tag{B.7f}$$

and the non-vanishing antisymmetric terms are

$$E^x_\omega E^y_{-\omega} - E^x_{-\omega} E^y_\omega = -iE_0^2\, \sin(2\varphi)\, \cos(\theta)/2\,, \tag{B.8a}$$

$$E^x_\omega E^z_{-\omega} - E^x_{-\omega} E^z_\omega = -iE_0^2\, \sin(2\varphi)\, \sin(\zeta)\, \sin(\theta)/2\,, \tag{B.8b}$$

$$E^y_\omega E^z_{-\omega} - E^y_{-\omega} E^z_\omega = \;\; iE_0^2\, \sin(2\varphi)\, \cos(\zeta)\, \sin(\theta)/2\,. \tag{B.8c}$$

B.3 Quadratic response at arbitrary incidence

In this section we show the dependence of the photocurrent on an arbitrary incidence configuration. The electric field is parametrized as a function of the polar (θ) and azimuthal (ζ) angles. In addition, we consider separately the symmetric and antisymmet-

ric combinations of the electric fields. The symmetry contribution reads

$$\begin{aligned}\frac{8j_1^{\mathtt{S}}}{\mathrm{E}_0^2} &= \mathtt{S}_{111}\Big(\cos^2(\zeta)\cos^2(\theta)[\cos(4\varphi)+3]-\sin(2\zeta)\cos(\theta)\sin(4\varphi)+2\sin^2(\zeta)\sin^2(2\varphi)\Big)+\\ &+2\mathtt{S}_{122}\sin^2(\zeta)\cos^2(\theta)\cos^2(2\varphi)-2\mathtt{S}_{113}\sin(\zeta)\sin(\theta)\sin(4\varphi)+2\mathtt{S}_{123}\sin(\zeta)\sin(2\theta)\times\\ &\times\cos^2(2\varphi)+\mathtt{S}_{113}\cos(\zeta)\sin(2\theta)[\cos(4\varphi)+3]+\mathtt{S}_{122}\sin(2\zeta)\cos(\theta)\sin(4\varphi)\\ &+\mathtt{S}_{112}\Big(\sin(2\zeta)\big(\cos^2(\theta)[\cos(4\varphi)+3]+\cos(4\varphi)-1\big)+2\cos(2\zeta)\cos(\theta)\sin(4\varphi)\Big)+\\ &+2\mathtt{S}_{123}\cos(\zeta)\sin(\theta)\sin(4\varphi)+2\mathtt{S}_{123}\sin(\zeta)\sin(2\theta)+2\mathtt{S}_{122}\sin^2(\zeta)\cos^2(\theta)\\ &+8\mathtt{S}_{122}\cos^2(\zeta)\sin^2(\varphi)\cos^2(\varphi)+\mathtt{S}_{133}\sin^2(\theta)[\cos(4\varphi)+3]\,,\end{aligned}\tag{B.9a}$$

$$\begin{aligned}\frac{8j_2^{\mathtt{S}}}{\mathrm{E}_0^2} &= \mathtt{S}_{211}\Big(\cos^2(\zeta)\cos^2(\theta)[\cos(4\varphi)+3]-\sin(2\zeta)\cos(\theta)\sin(4\varphi)+2\sin^2(\zeta)\sin^2(2\varphi)\Big)\\ &+2\mathtt{S}_{223}\sin(\zeta)\sin(2\theta)\cos^2(2\varphi)+2\mathtt{S}_{222}\sin^2(\zeta)\cos^2(\theta)\cos^2(2\varphi)-2\mathtt{S}_{213}\sin(\zeta)\sin(\theta)\times\\ &\times\sin(4\varphi)+2\mathtt{S}_{223}\sin(\zeta)\sin(2\theta)\cos^2(2\varphi)+\mathtt{S}_{213}\cos(\zeta)\sin(2\theta)[\cos(4\varphi)+3]\\ &+\mathtt{S}_{211}\Big(\cos^2(\zeta)\cos^2(\theta)[\cos(4\varphi)+3]-\sin(2\zeta)\cos(\theta)\sin(4\varphi)+2\sin^2(\zeta)\sin^2(2\varphi)\Big)\\ &+\mathtt{S}_{212}\Big[\sin(2\zeta)\big(\cos^2(\theta)[\cos(4\varphi)+3]+\cos(4\varphi)-1\big)+2\cos(2\zeta)\cos(\theta)\sin(4\varphi)\Big]+\\ &+\mathtt{S}_{222}\sin(2\zeta)\cos(\theta)\sin(4\varphi)+2\mathtt{S}_{223}\cos(\zeta)\sin(\theta)\sin(4\varphi)+2\mathtt{S}_{223}\sin(\zeta)\sin(2\theta)+\\ &+2\mathtt{S}_{222}\sin^2(\zeta)\cos^2(\theta)+8\mathtt{S}_{222}\cos^2(\zeta)\sin^2(\varphi)\cos^2(\varphi)+\mathtt{S}_{233}\sin^2(\theta)[\cos(4\varphi)+3]\,,\end{aligned}\tag{B.9b}$$

$$\begin{aligned}\frac{8j_3^{\mathtt{S}}}{\mathrm{E}_0^2} &= \mathtt{S}_{311}\Big(\cos^2(\zeta)\cos^2(\theta)[\cos(4\varphi)+3]-\sin(2\zeta)\cos(\theta)\sin(4\varphi)+2\sin^2(\zeta)\sin^2(2\varphi)\Big)\\ &+2\mathtt{S}_{322}\sin^2(\zeta)\cos^2(\theta)\cos^2(2\varphi)-2\mathtt{S}_{313}\sin(\zeta)\sin(\theta)\sin(4\varphi)+2\mathtt{S}_{323}\sin(\zeta)\sin(2\theta)\times\\ &\times\cos^2(2\varphi)+\mathtt{S}_{313}\cos(\zeta)\sin(2\theta)[\cos(4\varphi)+3]+\mathtt{S}_{322}\sin(2\zeta)\cos(\theta)\sin(4\varphi)\\ &\mathtt{S}_{312}\big[\sin(2\zeta)\Big(\cos^2(\theta)[\cos(4\varphi)+3]+\cos(4\varphi)-1\Big)+2\cos(2\zeta)\cos(\theta)\sin(4\varphi)\big]\\ &+2\mathtt{S}_{323}\cos(\zeta)\sin(\theta)\sin(4\varphi)+2\mathtt{S}_{323}\sin(\zeta)\sin(2\theta)+2\mathtt{S}_{322}\sin^2(\zeta)\cos^2(\theta)\\ &+8\mathtt{S}_{322}\cos^2(\zeta)\sin^2(\varphi)\cos^2(\varphi)+\mathtt{S}_{333}\sin^2(\theta)[\cos(4\varphi)+3]\,,\end{aligned}\tag{B.9c}$$

and the antisymmetric reads

$$-2j_1^{\mathtt{A}}/i\mathrm{E}_0^2=\sin(2\varphi)\Big(\sin(\theta)\big[\mathtt{A}_{113}\sin(\zeta)-\mathtt{A}_{123}\cos(\zeta)\big]+\mathtt{A}_{112}\cos(\theta)\Big)\,,\tag{B.10a}$$

$$-2j_2^{\mathtt{A}}/i\mathrm{E}_0^2=\sin(2\varphi)\Big(\sin(\theta)\big[\mathtt{A}_{213}\sin(\zeta)-\mathtt{A}_{223}\cos(\zeta)\big]+\mathtt{A}_{212}\cos(\theta)\Big)\,,\tag{B.10b}$$

$$-2j_3^{\mathtt{A}}/i\mathrm{E}_0^2=\sin(2\varphi)\Big(\sin(\theta)\big[\mathtt{A}_{313}\sin(\zeta)-\mathtt{A}_{323}\cos(\zeta)\big]+\mathtt{A}_{312}\cos(\theta)\Big)\,.\tag{B.10c}$$

In addition to the elastic photocurrent generation, we also consider inelastic processes such as photon drag. Due to the large number of independent elements on fourth-rank tensor, $3^{4-2}3^{2-1} = 27$, the complete symmetric contribution is too extensive for any practical use. Hence, we choose not to omit this and display only the antisymmetric part

$$\frac{2j_1^{\mathtt{A}}(\boldsymbol{\kappa})}{-i\,\mathrm{E}_0^2} = \sin(2\varphi)\Big(\sin(\zeta)\sin(\theta)\big[\hat{\kappa}_1 A_{1113} + \hat{\kappa}_2 A_{1213} + \hat{\kappa}_3 A_{1313}\big] - \cos(\zeta)\sin(\theta)\big[\hat{\kappa}_1 A_{1123} + \hat{\kappa}_2 A_{1223} + \hat{\kappa}_3 A_{1323}\big] + \cos(\theta)\big[\hat{\kappa}_1 A_{1112} + \hat{\kappa}_2 A_{1212} + \hat{\kappa}_3 A_{1312}\big]\Big)\,, \tag{B.11a}$$

$$\frac{2j_2^{\mathtt{A}}(\boldsymbol{\kappa})}{-i\,\mathrm{E}_0^2} = \sin(2\varphi)\Big(\sin(\zeta)\sin(\theta)\big[\hat{\kappa}_1 A_{2113} + \hat{\kappa}_2 A_{2213} + \hat{\kappa}_3 A_{2313}\big] - \cos(\zeta)\sin(\theta)\big[\hat{\kappa}_1 A_{2123} + \hat{\kappa}_2 A_{2223} + \hat{\kappa}_3 A_{2323}\big] + \cos(\theta)\big[\hat{\kappa}_1 A_{2112} + \hat{\kappa}_2 A_{2212} + \hat{\kappa}_3 A_{2312}\big]\Big)\,, \tag{B.11b}$$

$$\frac{2j_3^{\mathtt{A}}(\boldsymbol{\kappa})}{-i\,\mathrm{E}_0^2} = \sin(2\varphi)\Big(\sin(\zeta)\sin(\theta)\big[\hat{\kappa}_1 A_{3113} + \hat{\kappa}_2 A_{3213} + \hat{\kappa}_3 A_{3313}\big] - \cos(\zeta)\sin(\theta)\big[\hat{\kappa}_1 A_{3123} + \hat{\kappa}_2 A_{3223} + \hat{\kappa}_3 A_{3323}\big] + \cos(\theta)\big[\hat{\kappa}_1 A_{3112} + \hat{\kappa}_2 A_{3212} + \hat{\kappa}_3 A_{3312}\big]\Big)\,. \tag{B.11c}$$

The above-mentioned results were not computed by hand, instead we wrote a *Mathematica* notebooks to computed all elements. The respective notebooks, *Rank3tensor.nb* and *Rank4tensor.nb*, can be found in the `git` repository `graphenepccode`, under commits `#8fa05fc6` and `#3f60cdaf`, respectively.

B.4 Details on the numerical calculation

Regarding the numerical integration, we use *Mathematica*'s internal *NIntegrate* function with the *Local Adaptive* method and require the integrals to converge to a relative variation $\delta = [10^{-5}, 10^{-3}]$. The convergence test simply compares the relative difference between two consecutive iterations. Hence, this can be prone an incorrect convergence. By inspection it can be verified that the integrands are continuous complex functions in the BZ, but exhibit very large variations in very small regions. These variations are particularly strong in the vicinity of the K-point and at the propagator resonances. Due the nature of the integrands, different initial samplings of the integration domain can lead to different results. The selected method performs an automatic sampling, which can be tuned by increasing minimum and maximum number of recursions. Higher setting generate a more refined sampling and more accurate estimate for the integral. All

abrupt variation changes in the final result were tested with refined sampling to ensure convergence of the integral.

In addition to tackling the problems associated with the numerical functions for the product of matrix elements and the propagators, the integrand contains the Fermi function (or its derivatives). A straightforward evaluation of the derivatives (particularly the second order at low temperatures) can be challenging due to numerical under/overflow problems. Fortunately, these can be sorted by converting exponential functions to trigonometric functions in the derivatives, namely

$$\frac{\partial f_n}{\partial k_\alpha} = -\frac{\beta a}{4}\mathrm{sech}^2\left(\beta\frac{\mu-\epsilon_n}{2}\right)\frac{\partial \epsilon_n}{\partial \mathrm{k}_\alpha}\,, \tag{B.12}$$

$$\frac{\partial^2 f_n}{\partial k_\beta \partial k_\alpha} = -\frac{\beta a^2}{4}\mathrm{sech}^2\left(\beta\frac{\mu-\epsilon_n}{2}\right)\left[\beta a \tanh\left(\beta\frac{\mu-\epsilon_n}{2}\right)\frac{\partial \epsilon_n}{\partial \mathrm{k}_\beta}\frac{\partial \epsilon_n}{\partial \mathrm{k}_\alpha} + \frac{\partial^2 \epsilon_n}{\partial \mathrm{k}_\beta \partial \mathrm{k}_\alpha}\right], \tag{B.13}$$

where inverse of the thermal energy $\beta = k_B T$.

B.5 Dimensional analysis

In order to avoid confusion with the multiple definitions of non-linear tensors and respective units, we identify systematically the dimension and units of the conductivity tensors below. At linear order the dimension and units of the conductivity tensor read

$$\left[\sigma^{(1)}\right] \equiv \frac{\left[j^{(1)}\right]}{\left[E\right]} = \frac{\mathrm{QLT}^{-1}/\mathrm{L}^3}{\mathrm{MLT}^{-2}\mathrm{Q}^{-1}} = \frac{1}{\mathrm{L}^3}\frac{\mathrm{I}^2}{\mathrm{MT}^{-3}} \to \frac{1}{\mathrm{m}^3}\frac{\mathrm{A}^2}{\mathrm{kg\,s}^{-3}} = \mathrm{S/m}\,. \tag{B.14}$$

In the particular case of a 2D system, the current density is defined as current per area, instead of current per volume. Hence, the linear conductivity for 2D systems has dimensions of conductance

$$\left[\sigma^{(1)}\right] = \frac{\mathrm{QLT}^{-1}/\mathrm{L}^2}{\mathrm{MLT}^{-2}\mathrm{Q}^{-1}} = \frac{1}{\mathrm{L}^2}\frac{\mathrm{I}^2}{\mathrm{MT}^{-3}} \to \frac{1}{\mathrm{m}^2}\frac{\mathrm{A}^2}{\mathrm{kg\,s}^{-3}} = \mathrm{S}\,. \tag{B.15}$$

The so-called universal OC of graphene, $\sigma_1 = \pi e^2/(2h)$ [37], has dimensions of conductance and can be used as a "scale" for the 2D conductivity tensor. Proceeding to second order, the dimensions of the conductivity tensor read

$$\left[\sigma^{(2)}\right] \equiv \frac{\left[j^{(2)}\right]}{\left[E^2\right]} = \frac{\mathrm{QLT}^{-1}/\mathrm{L}^3}{(\mathrm{MLT}^{-2}\mathrm{Q}^{-1})^2} = \frac{1}{\mathrm{L}^3}\frac{\mathrm{I}^3}{\mathrm{M}^2\mathrm{LT}^{-6}} \to \frac{1}{\mathrm{m}^3}\frac{\mathrm{A}^3}{\mathrm{kg}^2\,\mathrm{m\,s}^{-6}} = \frac{\mathrm{S}}{\mathrm{V}}\,. \tag{B.16}$$

By the same token, the dimensions of the second order conductivity tensor change in 2D system

$$\left[\sigma^{(2)}\right] = \frac{\mathrm{QLT}^{-1}/\mathrm{L}^2}{(\mathrm{MLT}^{-2}\mathrm{Q}^{-1})^2} = \frac{1}{\mathrm{L}^2}\frac{\mathrm{I}^3}{\mathrm{M}^2\mathrm{LT}^{-6}} \to \frac{1}{\mathrm{m}^2}\frac{\mathrm{A}^3}{\mathrm{kg}^2\,\mathrm{m}\,\mathrm{s}^{-6}} = \frac{\mathrm{S\,m}}{\mathrm{V}}\,. \tag{B.17}$$

The latter is compatible with the dimensionality of the constant σ_2 introduced earlier in this section, equation 1.42b,

$$\left[\sigma_2\right] = \left[\frac{e^3 a}{4\gamma_0\hbar}\right] = \frac{\mathrm{Q}^3\mathrm{L}}{((\mathrm{ML}^2\mathrm{T}^{-2})^2\mathrm{T}} = \frac{1}{\mathrm{L}^2}\frac{\mathrm{I}^3}{\mathrm{M}^2\mathrm{LT}^{-6}} \to \frac{\mathrm{S\,m}}{\mathrm{V}}\,. \tag{B.18}$$

From the previous results, we identify the dimension and our choice of units for the linear and quadratic conductivity tensors in 2D systems, $\sigma_1 = \pi e^2/(2h)$ and $\sigma_2 = e^3 a/(4\gamma_0\hbar)$. The second order scale, unlike the first order, is not a universal quantity as it depends on the nearest neighbour hopping integral and distance.

This page was intentionally left blank.

Appendix C

Tight-Binding parametrization

This appendix provides auxiliary data and results for the calculation of Hamiltonians using TB method. The first and second section contain all relevant information for the construction of the TB Hamiltonians. The first section includes all relevant Slater–Koster two centre integrals [115], whereas the second contains all hopping terms for the above-mentioned Hamiltonians. The third section contains the relevant SOC for p and d orbitals. In the last section we present in details the some Hamiltonians, omitted from the main text due to their large size.

C.1 Slater–Koster two centre integrals

Table C.1: SK two centre hopping integrals for *s*, *p* and *d* orbitals, adapted from [115]. To compute the integrals not shown in the table follow the rules depicted in §4.3. The notation used is this table is defined as follows: the hopping integrals between orbitals α and β are $E_{\alpha\beta}$; $V_{\alpha\beta\gamma}$ represents the minimal set of two-centre integrals, γ indicates the type of bond, *i.e.* σ, π etc …; and finally the direction of the bond is defined by $(l, m, n) = \boldsymbol{\delta}_n/|\boldsymbol{\delta}_n|$

$E_{\alpha,\beta}$	SK hopping integrals
$E_{s,s}$	$V_{ss\sigma}$
$E_{s,x}$	$l\,V_{sp\sigma}$
$E_{s,xy}$	$\sqrt{3}\,l\,m\,V_{sp\sigma}$
E_{s,x^2-y^2}	$\sqrt{3}\left(l^2-m^2\right)V_{sp\sigma}/2$
E_{s,z^2}	$\left[n^2-\left(l^2+m^2\right)/2\right]V_{sp\sigma}$
$E_{x,x}$	$l^2V_{pp\sigma}+\left(1-l^2\right)V_{pp\pi}$
$E_{x,y}$	$l\,m\,\left(V_{pp\sigma}-V_{pp\pi}\right)$
$E_{x,xy}$	$\sqrt{3}\,l^2m\,V_{pd\sigma}+m\left(1-2l^2\right)V_{pd\pi}$
$E_{x,yz}$	$\sqrt{3}\,l\,m\,n\,V_{pd\sigma}-2\,l\,m\,n\,V_{pd\pi}$
E_{x,x^2-y^2}	$\sqrt{3}\,l\,\left(l^2-m^2\right)V_{pd\sigma}/2+l\,\left(1-l^2+m^2\right)V_{pd\pi}$
E_{y,x^2-y^2}	$\sqrt{3}\,l\,\left(l^2-m^2\right)V_{pd\sigma}/2-m\,\left(1+l^2-m^2\right)V_{pd\pi}$

Continued on next page

Table C.1 – continued from previous page

$E_{\alpha,\beta}$	SK hopping integrals
E_{z,x^2-y^2}	$\sqrt{3}\,n\,\left(l^2-m^2\right)V_{pd\sigma}/2 - n\,\left(l^2-m^2\right)V_{pd\pi}$
E_{x,z^2}	$l\,\left[n^2-\left(l^2+m^2\right)/2\right]V_{pd\sigma} - \sqrt{3}\,l\,n^2 V_{pd\pi}$
E_{y,z^2}	$m\,\left[n^2-\left(l^2+m^2\right)/2\right]V_{pd\sigma} - \sqrt{3}\,m\,n^2 V_{pd\pi}$
E_{z,z^2}	$n\,\left[n^2-\left(l^2+m^2\right)/2\right]V_{pd\sigma} + \sqrt{3}\,n\,\left(l^2+m^2\right)V_{pd\pi}$
$E_{xy,xy}$	$3\,l^2m^2V_{dd\sigma} + \left(l^2+m^2-4\,l^2m^2\right) + \left(n^2+l^2m^2\right)V_{dd\pi}V_{dd\delta}$
$E_{xy,yz}$	$3\,l\,m^2n\,V_{dd\sigma} + l\,n\,\left(1-4\,m^2\right)V_{dd\pi} + l\,n\,\left(m^2-1\right)V_{dd\delta}$
$E_{xy,zx}$	$3\,l^2m\,n\,V_{dd\sigma} + m\,n\,\left(1-4\,l^2\right)V_{dd\pi} + m\,n\,\left(l^2-1\right)V_{dd\delta}$
E_{xy,x^2-y^2}	$l\,m\,\left(l^2-m^2\right)\left(3V_{dd\sigma}/2 - 2V_{dd\pi} + V_{dd\delta}/2\right)$
E_{yz,x^2-y^2}	$3\,m\,n\,\left(l^2-m^2\right)V_{dd\sigma}/2 - m\,n\,\left[1+2\left(l^2-m^2\right)\right]V_{dd\pi}$ $+m\,n\,\left[1+\left(l^2-m^2\right)/2\right]V_{dd\delta}$
E_{zx,x^2-y^2}	$3\,n\,l\,\left(l^2-m^2\right)V_{dd\sigma}/2 + n\,l\,v\,\left[1-2\left(l^2-m^2\right)\right]V_{dd\pi}$ $+n\,l\,\left[1-\left(l^2-m^2\right)/2\right]V_{dd\delta}$
E_{xy,z^2}	$\sqrt{3}\,l\,m\,\left[n^2-\left(l^2+m^2\right)/2\right]V_{dd\sigma} - 2\sqrt{3}\,l\,m\,n^2V_{dd\pi}$ $+\sqrt{3}\,l\,m\,\left(1+n^2\right)/2V_{dd\delta}$
E_{yz,z^2}	$\sqrt{3}\,m\,n\,\left[n^2-\left(l^2+m^2\right)/2\right]V_{dd\sigma} + \sqrt{3}\,m\,n\,\left(l^2+m^2-n^2\right)V_{dd\pi}$ $-\sqrt{3}\,m\,n\,\left(l^2+m^2\right)V_{dd\delta}/2$
E_{zx,z^2}	$\sqrt{3}\,l\,n\,\left[n^2-\left(l^2+m^2\right)/2\right]V_{dd\sigma} + \sqrt{3}\,m\,n\,\left(l^2+m^2-n^2\right)V_{dd\pi}$ $-\sqrt{3}\,m\,n\,\left(l^2+m^2\right)V_{dd\delta}/2$
$E_{x^2-y^2,x^2-y^2}$	$3\left(l^2-m^2\right)^2V_{dd\sigma}/4 + \left(l^2+m^2-\left(l^2-m^2\right)\right]V_{dd\pi}$ $+\left[n^2+\left(l^2-m^2\right)/4\right]V_{dd\delta}$
$E_{x^2-y^2,z^2}$	$+\sqrt{3}\,n^2\left(m^2-l^2\right)V_{dd\pi} + \sqrt{3}\left(1+n^2\right)\left(l^2-m^2\right)V_{dd\delta}/4$ $\sqrt{3}\left(l^2-m^2\right)\left[n^2-\left(l^2+m^2\right)/2\right]V_{dd\sigma}/2$
E_{z^2,z^2}	$\left[n^2-\left(l^2+m^2\right)/2\right]^2V_{dd\sigma} + 3\,n^2\left(l^2+m^2\right)V_{dd\pi}$ $+3\left(l^2+m^2\right)V_{dd\delta}$

C.2 Slater–Koster hopping terms

C.2.1 SK hopping terms for the honeycomb

Below we compute the Slater–hopping terms for the π bands for the honeycomb lattice with primitive (and reciprocal) lattice vectors defined in equations 3.15 and depicted in figure 3.2a. In addition the nearest neighbour vectors read

$$\delta_1 = a\big(\sqrt{3}/2, -1/2, 0\big)\,, \quad \delta_2 = a\big(0, 1, 0\big)\,, \quad \delta_3 = -a\big(\sqrt{3}/2, 1/2, 0\big)\,. \tag{C.1}$$

Therefore, the hopping terms read

$$\phi^{z,z}_{\boldsymbol{\delta}}(\mathbf{k}) = V_{pp\pi}\left[e^{ik_y a} + 2e^{-ik_y a/2}\cos\left(\sqrt{3}k_x a/2\right)\right]\,, \tag{C.2a}$$

$$\phi^{z,zx}_{\boldsymbol{\delta}}(\mathbf{k}) = \sqrt{3}i\,V_{pd\pi}e^{-ik_y a/2}\sin\left(\sqrt{3}k_x a/2\right)\,, \tag{C.2b}$$

$$\phi^{z,yz}_{\boldsymbol{\delta}}(\mathbf{k}) = V_{pd\pi}\left[e^{ik_y a} - e^{ik_y a/2}\cos\left(\sqrt{3}k_x a/2\right)\right]\,, \tag{C.2c}$$

$$\phi_{\boldsymbol{\delta}}^{zx,zx}(\mathbf{k}) = V_{dd\delta}e^{ik_y a} + \frac{3V_{dd\pi}+V_{dd\delta}}{2}e^{-ik_y a/2}\cos\left(\sqrt{3}k_x a/2\right), \tag{C.2d}$$

$$\phi_{\boldsymbol{\delta}}^{zx,zy}(\mathbf{k}) = \sqrt{3}i\,\frac{V_{dd\delta}-V_{dd\pi}}{2}e^{-ik_y a/2}\sin\left(\sqrt{3}k_x a/2\right), \tag{C.2e}$$

$$\phi_{\boldsymbol{\delta}}^{zy,zy}(\mathbf{k}) = V_{dd\pi}e^{ik_y a} + \frac{V_{dd\pi}+3V_{dd\delta}}{2}e^{-ik_y a/2}\cos\left(\sqrt{3}k_x a/2\right). \tag{C.2f}$$

Power series expansion up to linear order around the high symmetry point $\mathbf{K}$

$$\phi_{\boldsymbol{\delta}}^{z,z}(\mathbf{q}) = V_{pp\pi}\left(\tau q_x + iq_y\right), \tag{C.3a}$$

$$\phi_{\boldsymbol{\delta}}^{z,zx}(\mathbf{q}) = V_{pd\pi}\left(-3\tau i - iq_x - \tau q_y\right), \tag{C.3b}$$

$$\phi_{\boldsymbol{\delta}}^{z,yz}(\mathbf{q}) = V_{pd\pi}\left(3 - \tau q_x + iq_y\right), \tag{C.3c}$$

$$\phi_{\boldsymbol{\delta}}^{zx,zx}(\mathbf{q}) = V_{dd\pi}\left(\frac{-3+3\tau q_x+iq_y}{4}\right) + V_{pp\delta}\left(\frac{3+3\tau q_x+iq_y}{4}\right), \tag{C.3d}$$

$$\phi_{\boldsymbol{\delta}}^{zx,zy}(\mathbf{q}) = \frac{V_{dd\pi}-V_{dd\delta}}{4}\left(3\tau i + iq_x + \tau q_y\right), \tag{C.3e}$$

$$\phi_{\boldsymbol{\delta}}^{zy,zy}(\mathbf{q}) = V_{dd\pi}\left(\frac{3+3\tau q_x+iq_y}{4}\right) + V_{pp\delta}\left(\frac{-3+3\tau q_x+iq_y}{4}\right), \tag{C.3f}$$

where $\tau = \pm 1$ distinguishes the Dirac cones and $\mathbf{q} = 3a\,\mathbf{k}/2$, such that $|\mathbf{q}| \in [-\pi, \pi]$.

C.2.2 SK hopping terms for the buckled honeycomb

Below, we show the set Slater-Koster hopping terms between atomic orbitals following set $\{\mathrm{p_z}\,,\ \mathrm{s}\,,\ \mathrm{p_x}\,,\ \mathrm{p_y}\}$ for the buckled honeycomb lattice. The buckled honeycomb lattice is defined by opposite vertical displacements of the A and B sublattices, with respect to the pristine honeycomb lattice. Due to the particular nature of this deformation, the in-plane projections of the lattice remain unchanged, apart from the redefinition of the lattice constant, which becomes dependent on the buckling angle. Hence, the primitive (and reciprocal) lattice vectors remain as defined in equations 3.15

$$\mathbf{a}_1 = \frac{3a'}{2}\left(\frac{2\sqrt{3}}{3}, 0\right);\ \mathbf{a}_2 = \frac{3a'}{2}\left(\frac{\sqrt{3}}{3}, 1\right);\ \mathbf{b}_1 = \frac{4\pi}{3a'}\left(\frac{\sqrt{3}}{2}, -\frac{1}{2}\right);\ \mathbf{b}_2 = \frac{4\pi}{3a'}\left(0, -1\right), \tag{C.4}$$

where $a' = a\cos(\theta)$ and θ is the buckling angle, *i.e.* $\theta = 0$ flat honeycomb. In addition, the nearest neighbour vectors read

$$\delta_1 = a'\Big(\sqrt{3}/2, -1/2, \tan(\theta)\Big), \delta_2 = a'\Big(0, 1, \tan(\theta)\Big), \delta_3 = -a'\Big(\sqrt{3}/2, 1/2, \tan(\theta)\Big). \tag{C.5}$$

Therefore, the respective hopping terms read

$$\phi_{\boldsymbol{\delta}_j}^{z,z} = \sum_{j=1}^{3} E_{z,z}^{(j)} e^{ia\mathbf{k}\cdot\boldsymbol{\delta}_j} = \left[n^2\,V_{pp\sigma} + (1-n^2\,V_{pp\pi})\right]\sum_{j=1}^{3} e^{ia(l_j\,k_x + m_j\,k_y + n_j\,k_z)}$$

$$= \left[n^2\, V_{pp\sigma} + (1 - n^2\, V_{pp\pi})\right] \sum_{j=1}^{3} e^{ia(l_j k_x + m_j k_y + n_j k_z)}\,, \tag{C.6a}$$

$$\phi_{\boldsymbol{\delta}}^{z,s} = V_{sp\sigma} \sum_{j=1}^{3} n_j\, e^{ia(l_j k_x + m_j k_y + n_j k_z)}\,, \tag{C.6b}$$

$$\phi_{\boldsymbol{\delta}}^{z,x} = \left(V_{pp\pi} - V_{pp\sigma}\right) \sum_{j=1}^{3} l_j\, n_j\, e^{ia(l_j k_x + m_j k_y + n_j k_z)}\,, \tag{C.6c}$$

$$\phi_{\boldsymbol{\delta}}^{z,y} = \left(V_{pp\pi} - V_{pp\sigma}\right) \sum_{j=1}^{3} n_j\, m_j\, e^{ia(l_j k_x + m_j k_y + n_j k_z)}\,, \tag{C.6d}$$

$$\phi_{\boldsymbol{\delta}}^{s,s} = V_{ss\sigma} \sum_{j=1}^{3} e^{ia(l_j k_x + m_j k_y + n_j k_z)}\,, \tag{C.6e}$$

$$\phi_{\boldsymbol{\delta}}^{s,x} = V_{sp\sigma} \sum_{j=1}^{3} l_j\, e^{ia(l_j k_x + m_j k_y + n_j k_z)}\,, \tag{C.6f}$$

$$\phi_{\boldsymbol{\delta}}^{s,y} = V_{sp\sigma} \sum_{j=1}^{3} m_j\, e^{ia(l_j k_x + m_j k_y + n_j k_z)}\,, \tag{C.6g}$$

$$\phi_{\boldsymbol{\delta}}^{x,x} = \left[n^2\, V_{pp\sigma} + (1 - n^2\, V_{pp\pi})\right] \sum_{j=1}^{3} e^{ia(l_j k_x + m_j k_y + n_j k_z)}\,, \tag{C.6h}$$

$$\phi_{\boldsymbol{\delta}}^{x,y} = \left(V_{pp\sigma} - V_{pp\pi}\right) \sum_{j=1}^{3} l_j\, m_j\, e^{ia(l_j k_x + m_j k_y + n_j k_z)}\,, \tag{C.6i}$$

$$\phi_{\boldsymbol{\delta}}^{y,y} = \sum_{j=1}^{3} \left[m_j^2\, V_{pp\sigma} + (1 - m_j^2\, V_{pp\pi})\right] e^{ia(l_j k_x + m_j k_y + n_j k_z)}\,, \tag{C.6j}$$

where $E_{\alpha,\beta}^{(j)}$ is the two centre SK integral between orbitals α and β with centres separated by distance $\boldsymbol{\delta}_j/\left|\boldsymbol{\delta}_j\right| = \left(l_j, m_j, n_j\right)$.

C.3 Calculation of $\langle \mathbf{L}\cdot\mathbf{s}\rangle_{\alpha,\beta}$

In this section we present the detailed calculation of the matrix elements $\langle \mathbf{L}\cdot\mathbf{s}\rangle$, evaluated in a basis of atomic orbitals to be used in the TB calculations. We only compute the matrix elements relevant for graphene, nevertheless the same procedure can be applied to any other atomic orbital. To compute these matrix elements, we must first define our eigenstates, which must take into account the angular momentum and spin degrees of freedom. Since, these are independent, we can write the basis as the direct product of the angular and spin components $|\psi\rangle = |L_\alpha\rangle \otimes |s_\alpha\rangle$. The natural basis for the angular momentum state is $|n, \ell, m_\ell\}$, where n, ℓ and m_ℓ are the principal, angular and magnetic quantum, respectively. Indeed we only need ℓ and m_ℓ quantum numbers, therefore the basis can be written as [117, 140]

$$|s\rangle = |0, 0\rangle\,, \tag{C.7a}$$

$$|p_z\rangle = |1,0\rangle\,, \quad |p_x\rangle = \frac{|1,-1\rangle - |1,1\rangle}{\sqrt{2}}\,, \quad |p_y\rangle = i\frac{|1,-1\rangle + |1,1\rangle}{\sqrt{2}}\,, \tag{C.7b}$$

$$|d_{z^2}\rangle = |2,0\rangle\,, \tag{C.7c}$$

$$|d_{zx}\rangle = \frac{|2,-1\rangle - |2,1\rangle}{\sqrt{2}}\,, \quad |d_{yz}\rangle = i\frac{|2,-1\rangle + |2,1\rangle}{\sqrt{2}}\,, \tag{C.7d}$$

$$|d_{xy}\rangle = i\frac{|2,-2\rangle - |2,2\rangle}{\sqrt{2}}\,, \quad |d_{x^2-y^2}\rangle = \frac{|2,-2\rangle + |2,2\rangle}{\sqrt{2}}\,, \tag{C.7e}$$

The dot product $\mathbf{L}\cdot\mathbf{s}$ can expressed as function of angular momentum operators $L_\pm$ and L_z, by simply inverting the definition of angular momentum ladder operators $L_\pm = L_x + iL_y$. In this representation, the matrix elements of the dot product can be trivially calculated using [141]

$$\mathbf{L}^2|\ell, m_\ell\rangle = \hbar\,\ell(\ell+1)|\ell, m_\ell\rangle\,, \tag{C.8a}$$

$$L_z|\ell, m_\ell\rangle = \hbar\, m_\ell|\ell, m_\ell\rangle\,, \tag{C.8b}$$

$$L_\pm|\ell, m_\ell\rangle = \hbar\sqrt{\ell(\ell+1) - m_\ell(m_\ell \pm 1)}|\ell, m_\ell \pm 1\rangle\,. \tag{C.8c}$$

Regarding the spin, the spin operator reads as

$$\mathbf{s} = s_x\mathbf{x} + s_y\mathbf{y} + s_z\mathbf{z}\,, \tag{C.9}$$

and just as the angular momentum, the spin operator can be expressed by s_z and $s_\pm$, where s_i is the *i-th* Pauli matrix and $s_\pm = s_x \pm is_y$. The matrix elements of the spin operators can be easily evaluated by recalling

$$\mathbf{s}^2|s, m_s\rangle = \hbar s(s+1)|s, m_s\rangle\,, \tag{C.10a}$$

$$s_z|s, m_s\rangle = \hbar m_s|s, m_s\rangle\,, \tag{C.10b}$$

$$s_\pm|s, m_s\rangle = \hbar\sqrt{s(s+1) - m_s(m_s \pm 1)}|s, m_s \pm 1\rangle\,. \tag{C.10c}$$

Therefore, the expectation value of the dot product reads

$$\langle \mathbf{L}\cdot\mathbf{s}\rangle_{\alpha,\beta} = \langle L_\alpha| \otimes \langle s_\alpha|\Big(\sum_{i=x,y,z} L_i s_i\Big)|L_\beta\rangle \otimes |s_\beta\rangle = \sum_{i=x,y,z} \langle L_\alpha|L_i|L_\beta\rangle\langle s_\alpha|s_i|s_\beta\rangle\,. \tag{C.11}$$

The expectation values for relevant matrix elements for graphene can be found in tables C.2 and C.4 (in both the spin degree of freedom is hidden in the Pauli matrices). In table C.3, the matrix elements have been computed explicitly.

Table C.2: Expectation values for the $\mathbf{L}\cdot\mathbf{s}_{\alpha,\beta}$ operator in the basis of $2p$ atomic orbitals. α,β are the atomic orbital indices and s_x, s_y and s_z are the spin operator projections.

α,β	p_x	p_y	p_z
p_x	0	is_z	s_x
p_y	$-is_z$	0	$-s_y$
p_z	s_x	$-s_y$	0

Table C.3: Expectation values for the $\mathbf{L}\cdot\mathbf{s}_{\alpha,\beta}$ operator in the basis of $2p$ atomic orbitals and spin up/down. α,β are the atomic orbital indices.

α,β	p_x	p_y	p_z
p_x	$\begin{pmatrix}0&0\\0&0\end{pmatrix}$	$\begin{pmatrix}i&0\\0&-i\end{pmatrix}$	$\begin{pmatrix}0&1\\1&0\end{pmatrix}$
p_y	$\begin{pmatrix}-i&0\\0&i\end{pmatrix}$	$\begin{pmatrix}0&0\\0&0\end{pmatrix}$	$\begin{pmatrix}0&i\\-i&0\end{pmatrix}$
p_z	$\begin{pmatrix}0&1\\1&0\end{pmatrix}$	$\begin{pmatrix}0&i\\-i&0\end{pmatrix}$	$\begin{pmatrix}0&0\\0&0\end{pmatrix}$

C.4 Hamiltonians with spin component

This section contains large size Hamiltonians discussed in §4.5.1 to 4.5.3.

C.4.1 π-bands

Below we introduce in detail the Hamiltonian under consideration in §4.5.1. The basis reads

$$\Psi^\dagger_{\mathbf{k}} = \Big\{a^\dagger_{\mathbf{k},p_z,+},\ b^\dagger_{\mathbf{k},p_z,+},\ a^\dagger_{\mathbf{k},d_{zx},+},\ b^\dagger_{\mathbf{k},d_{zx},+},\ a^\dagger_{\mathbf{k},d_{yz},+},\ b^\dagger_{\mathbf{k},d_{yz},+},\\ a^\dagger_{\mathbf{k},p_z,-},\ b^\dagger_{\mathbf{k},p_z,-},\ a^\dagger_{\mathbf{k},d_{zx},-},\ b^\dagger_{\mathbf{k},d_{zx},-},\ a^\dagger_{\mathbf{k},d_{yz},-},\ b^\dagger_{\mathbf{k},d_{yz},-}\Big\}, \tag{C.12}$$

and the respective Hamiltonian can be written in the block diagonal form

$$\mathcal{H}_\pm = \begin{pmatrix}H_+ & 0\\ 0 & H_-\end{pmatrix} \quad : \quad \mathcal{H}_\pm = \begin{pmatrix}H_p & H_{pd}\\ H^\dagger_{pd} & H^\pm_d\end{pmatrix} \tag{C.13}$$

Table C.4: Expectation values for the $\mathbf{L}\cdot\mathbf{s}_{\alpha,\beta}$ operator in the basis $3d$ of atomic orbitals. α,β are the atomic orbital indices and s_x, s_y and s_z are the spin operator projections.

α,β	d_{z^2}	d_{zx}	d_{yz}	d_{xy}	$d_{x^2-y^2}$
d_{z^2}	0	$-\sqrt{3}is_y$	$\sqrt{3}is_y$	0	0
d_{zx}	$\sqrt{3}is_y$	0	$-is_z$	is_x	$-is_y$
d_{yz}	$-\sqrt{3}is_y$	is_z	0	$-is_y$	$-is_x$
d_{xy}	0	$-is_x$	is_y	0	$2is_z$
$d_{x^2-y^2}$	0	is_y	is_x	$-2is_z$	0

where the block matrices read

$$H_p = \begin{pmatrix} \epsilon_p & \phi^{z,z}_{\boldsymbol{\delta}} \\ \phi^{z,z}_{-\boldsymbol{\delta}} & \epsilon_p \end{pmatrix}, \tag{C.14a}$$

$$H_{pd} = \begin{pmatrix} 0 & \phi^{z,zx}_{\boldsymbol{\delta}} & 0 & \phi^{z,yz}_{\boldsymbol{\delta}} \\ \phi^{z,zx}_{-\boldsymbol{\delta}} & 0 & \phi^{z,yz}_{-\boldsymbol{\delta}} & 0 \end{pmatrix}, \tag{C.14b}$$

$$H_d^{\pm} = \begin{pmatrix} \epsilon_d & \phi^{zx,zx}_{\boldsymbol{\delta}} & \mp i\xi_d/2 & \phi^{zx,yz}_{\boldsymbol{\delta}} \\ \phi^{zx,zx}_{-\boldsymbol{\delta}} & \epsilon_d & \phi^{zx,yz}_{-\boldsymbol{\delta}} & \mp i\xi_d/2 \\ \pm i\xi_d/2 & \phi^{yz,zx}_{\boldsymbol{\delta}} & \epsilon_d & \phi^{yz,yz}_{\boldsymbol{\delta}} \\ \phi^{yz,zx}_{-\boldsymbol{\delta}} & \pm i\xi_d/2 & \phi^{yz,yz}_{-\boldsymbol{\delta}} & \epsilon_d \end{pmatrix}. \tag{C.14c}$$

C.4.2 σ-bands

Below we introduce in detail the Hamiltonian under consideration in §4.5.2. The basis reads

$$\begin{aligned} \Psi^\dagger_{\mathbf{k}} = \Big\{ & a^\dagger_{\mathbf{k},p_z,+}\,,\ b^\dagger_{\mathbf{k},p_z,+}\,,\ a^\dagger_{\mathbf{k},p_z,-}\,,\ b^\dagger_{\mathbf{k},p_z,-}\,,\ a^\dagger_{\mathbf{k},s,+}\,,\ b^\dagger_{\mathbf{k},s,+}\,,\ a^\dagger_{\mathbf{k},s,-}\,,\ b^\dagger_{\mathbf{k},s,-}\,, \\ & a^\dagger_{\mathbf{k},p_x,+}\,,\ b^\dagger_{\mathbf{k},p_x,+}\,,\ a^\dagger_{\mathbf{k},p_x,-}\,,\ b^\dagger_{\mathbf{k},p_x,-}\,,\ a^\dagger_{\mathbf{k},p_y,+}\,,\ b^\dagger_{\mathbf{k},p_y,+}\,,\ a^\dagger_{\mathbf{k},p_y,-}\,,\ b^\dagger_{\mathbf{k},p_y,-} \Big\}, \end{aligned} \tag{C.15}$$

and the respective Hamiltonian can be written in the condensed form

$$\mathcal{H} = \begin{pmatrix} H_\pi & H_{\pi\sigma} \\ H^\dagger_{\pi\sigma} & H_\sigma \end{pmatrix}, \tag{C.16}$$

where the respective blocks read

$$H_\pi = \begin{pmatrix} \epsilon_p & \phi^{z,z}_{\boldsymbol{\delta}} \\ \phi^{z,z}_{-\boldsymbol{\delta}} & \epsilon_p \end{pmatrix} \otimes \mathbb{1}_\pm\,, \tag{C.17a}$$

where, π-bands have the standard nearest neighbour TB terms. The coupling block is linear in ξ_p

$$H_{\pi\sigma} = \begin{pmatrix} 0 & 0 & 0 & 0 & 0 & 0 & \xi_p & 0 & 0 & 0 & i\xi_p & 0 \\ 0 & 0 & 0 & 0 & 0 & 0 & 0 & \xi_p & 0 & 0 & 0 & i\xi_p \\ 0 & 0 & 0 & 0 & \xi_p & 0 & 0 & 0 & -i\xi_p & 0 & 0 & 0 \\ 0 & 0 & 0 & 0 & 0 & \xi_p & 0 & 0 & 0 & -i\xi_p & 0 & 0 \end{pmatrix}, \tag{C.17b}$$

and the σ-bands require yet another block matrix representation due to it large size.

$$H_\sigma = \begin{pmatrix} H_s & H_{sp} \\ H^\dagger_{sp} & H_p \end{pmatrix}, \tag{C.17c}$$

where the dispersion of the s-bands is ignored

$$H_s = \epsilon_s \mathbb{1}_4\,, \tag{C.17d}$$

but the coupling between s and p_x or p_y is taken into consideration

$$H_{sp} = \begin{pmatrix} 0 & \phi^{s,x}_{\boldsymbol{\delta}} & 0 & 0 & 0 & \phi^{s,y}_{\boldsymbol{\delta}} & 0 & 0 \\ \phi^{s,x}_{-\boldsymbol{\delta}} & 0 & 0 & 0 & \phi^{s,y}_{-\boldsymbol{\delta}} & 0 & 0 & 0 \\ 0 & 0 & 0 & \phi^{s,x}_{\boldsymbol{\delta}} & 0 & 0 & 0 & \phi^{s,y}_{\boldsymbol{\delta}} \\ 0 & 0 & \phi^{s,x}_{-\boldsymbol{\delta}} & 0 & 0 & \phi^{s,x}_{-\boldsymbol{\delta}} & 0 & 0 \end{pmatrix}, \tag{C.17e}$$

finally, by neglecting the dispersion of the p_x and p_y is the SOC coupling between these orbitals.

$$H_\sigma = \begin{pmatrix} \epsilon_p & 0 & 0 & 0 & i\xi_p & 0 & 0 & 0 \\ 0 & \epsilon_p & 0 & 0 & 0 & i\xi_p & 0 & 0 \\ 0 & 0 & \epsilon_p & 0 & 0 & 0 & -i\xi_p & 0 \\ 0 & 0 & 0 & \epsilon_p & 0 & 0 & 0 & -i\xi_p \\ -i\xi_p & 0 & 0 & 0 & \epsilon_p & 0 & 0 & 0 \\ 0 & -i\xi_p & 0 & 0 & 0 & \epsilon_p & 0 & 0 \\ 0 & 0 & i\xi_p & 0 & 0 & 0 & \epsilon_p & 0 \\ 0 & 0 & 0 & i\xi_p & 0 & 0 & 0 & \epsilon_p \end{pmatrix}. \tag{C.17f}$$

C.4.3 Buckled honeycomb

Below we introduce in detail the Hamiltonian under consideration in §4.5.3. The basis is the same as the basis used for the σ-bond Hamiltonian, equation C.15. The Hamiltonian lends it self to the same division in blocks, equation C.16. An additional subdivision is introduced, namely $H_{\pi\sigma} = \begin{pmatrix} H_{z,s} & H_{z,p} \end{pmatrix}$. Moreover, the distortion of the lattice requires the revision of the Slater–Koster hopping terms. The respective hopping terms are listed in equations C.6.

$$H_{z,s} = \begin{pmatrix} 0 & \phi^{z,s}_{\boldsymbol{\delta}} \\ \phi^{z,s}_{-\boldsymbol{\delta}} & 0 \end{pmatrix} \otimes \mathbb{1}_\pm \; ; \quad H_{z,p} = \begin{pmatrix} 0 & \phi^{z,x}_{\boldsymbol{\delta}} & \xi_p & 0 & 0 & \phi^{z,y}_{\boldsymbol{\delta}} & i\xi_p & 0 \\ \phi^{z,x}_{-\boldsymbol{\delta}} & 0 & 0 & \xi_p & \phi^{z,y}_{\boldsymbol{\delta}} & 0 & 0 & i\xi_p \\ \xi_p & 0 & 0 & \phi^{z,x}_{\boldsymbol{\delta}} & -i\xi_p & \phi^{z,z}_{\boldsymbol{\delta}} & 0 & 0 \\ \phi^{z,x}_{-\boldsymbol{\delta}} & \xi_p & 0 & 0 & 0 & -i\xi_p & \phi^{z,y}_{-\boldsymbol{\delta}} & 0 \end{pmatrix}. \tag{C.18a}$$

As in case of the flat honeycomb, the H_σ block must be split in four blocks

$$H_\sigma = \begin{pmatrix} H_s & H_{sp} \\ H^\dagger_{sp} & H_p \end{pmatrix}, \tag{C.18b}$$

where

$$H_s = \begin{pmatrix} \epsilon_s & \phi^{s,s}_{\boldsymbol{\delta}} \\ \phi^{s,s}_{-\boldsymbol{\delta}} & \epsilon_s \end{pmatrix} \otimes \mathbb{1}_\pm \; ; \quad H_{sp} = \begin{pmatrix} 0 & \phi^{s,x}_{\boldsymbol{\delta}} & 0 & 0 & 0 & \phi^{s,y}_{\boldsymbol{\delta}} & 0 & 0 \\ \phi^{s,x}_{-\boldsymbol{\delta}} & 0 & 0 & 0 & \phi^{s,y}_{-\boldsymbol{\delta}} & 0 & 0 & 0 \\ 0 & 0 & 0 & \phi^{s,x}_{\boldsymbol{\delta}} & 0 & 0 & 0 & \phi^{s,y}_{\boldsymbol{\delta}} \\ 0 & 0 & \phi^{s,x}_{-\boldsymbol{\delta}} & 0 & 0 & \phi^{s,x}_{-\boldsymbol{\delta}} & 0 & 0 \end{pmatrix}, \tag{C.18c}$$

and

$$H_p = \begin{pmatrix} \epsilon_p & \phi^{x,x}_{\boldsymbol{\delta}} & 0 & 0 & i\xi_p & \phi^{x,y}_{\boldsymbol{\delta}} & 0 & 0 \\ \phi^{x,x}_{-\boldsymbol{\delta}} & \epsilon_p & 0 & 0 & \phi^{x,y}_{-\boldsymbol{\delta}} & i\xi_p & 0 & 0 \\ 0 & 0 & \epsilon_p & \phi^{x,x}_{\boldsymbol{\delta}} & 0 & 0 & -i\xi_p & \phi^{x,y}_{\boldsymbol{\delta}} \\ 0 & 0 & \phi^{x,x}_{-\boldsymbol{\delta}} & \epsilon_p & 0 & 0 & \phi^{x,y}_{-\boldsymbol{\delta}} & -i\xi_p \\ -i\xi_p & \phi^{y,x}_{\boldsymbol{\delta}} & 0 & 0 & \epsilon_p & \phi^{y,y}_{\boldsymbol{\delta}} & 0 & 0 \\ \phi^{y,x}_{-\boldsymbol{\delta}} & -i\xi_p & 0 & 0 & \phi^{y,y}_{-\boldsymbol{\delta}} & \epsilon_p & 0 & 0 \\ 0 & 0 & i\xi_p & \phi^{y,x}_{\boldsymbol{\delta}} & 0 & 0 & \epsilon_p & \phi^{y,y}_{-\boldsymbol{\delta}} \\ 0 & 0 & \phi^{y,x}_{-\boldsymbol{\delta}} & i\xi_p & 0 & 0 & \phi^{y,y}_{\boldsymbol{\delta}} & \epsilon_p \end{pmatrix}. \tag{C.18d}$$